Ph.D. Thesis

Thermo-Hydro-Mechanical Impacts of Carbon Dioxide (CO_2) Injection in Deep Saline Aquifers.

by

Víctor Vilarrasa Riaño

Hydrogeology Group (GHS)

Department of Geotechnical Engineering and Geosciences,
Technical University of Catalonia (UPC-BarcelonaTech)

Institute of Environmental Assessment and Water Research (IDAEA),
Spanish Research Council (CSIC)

Supervised by:

Jesús Carrera

Sebastià Olivella

June, 2012

This thesis was funded by the Spanish Ministry of Science and Innovation (MCI), through the “Formación de Profesorado Universitario” Program, and the “Colegio de Ingenieros de Caminos, Canales y Puertos – Catalunya”; and was developed in the framework of two projects: the ALM/09/18 project of the Spanish Ministry of Industry, Energy and Tourism through the CIUDEN foundation (www.ciuden.es) and the “MUSTANG” project (from the European Community’s Seventh Framework Programme FP7/2007-2013 under grant agreement nº 227286; www.co2mustang.eu).

To my pillar

I. Abstract

Coupled thermo-hydro-mechanical effects related to geologic carbon storage should be understood and quantified in order to demonstrate to the public that carbon dioxide (CO_2) injection is safe. This Thesis aims to improve such understanding by developing methods to: (1) evaluate the CO_2 plume geometry and fluid pressure evolution; (2) define a field test to characterize the maximum sustainable injection pressure and the hydromechanical properties of the aquifer and the caprock; and (3) propose an energy efficient injection concept that improves the caprock mechanical stability in most geological settings due to thermo-mechanical effects.

First, we investigate numerically and analytically the effect of CO_2 density and viscosity variability on the position of the interface between the CO_2-rich phase and the formation brine. We introduce a correction to account for CO_2 compressibility (density variations) and viscosity variations in current analytical solutions. We find that the error in the interface position caused by neglecting CO_2 compressibility is relatively small when viscous forces dominate. However, it can become significant when gravity forces dominate, which is likely to occur at late times and/or far from the injection well.

Second, we develop a semianalytical solution for the CO_2 plume geometry and fluid pressure evolution, accounting for CO_2 compressibility and buoyancy effects in the injection well. We formulate the problem in terms of a CO_2 potential that facilitates solution in horizontal layers, in which we discretize the aquifer. We find that when a prescribed CO_2 mass flow rate is injected, CO_2 advances initially through the top portion of the aquifer. As CO_2 pressure builds up, CO_2 advances not only laterally, but also vertically downwards. However, the CO_2 plume does not necessarily occupy the whole thickness of the aquifer. Both CO_2 plume position and fluid pressure compare well with numerical simulations. Therefore, this solution facilitates quick evaluations of the CO_2 plume position and fluid pressure distribution when injecting supercritical CO_2 in a deep saline aquifer.

Third, we study potential failure mechanisms, which could lead to CO_2 leakage, in an axysimmetric horizontal aquifer-caprock system, using a viscoplastic approach.

Simulations illustrate that, depending on boundary conditions, the least favorable situation may occur at the beginning of injection. However, in the presence of low-permeability boundaries, fluid pressure continues to rise in the whole aquifer, which may compromise the caprock integrity in the long-term.

Next, we propose a hydromechanical characterization test to estimate the hydromechanical properties of the aquifer and caprock at the field scale. We obtain curves for overpressure and vertical displacement as a function of the volumetric strain term obtained from a dimensional analysis of the hydromechanical equations. We can then estimate the values of the Young's modulus and the Poisson ratio of the aquifer and the caprock by introducing field measurements in these plots. The results indicate that induced microseismicity is more likely to occur in the aquifer than in the caprock. The onset of microseismicity in the caprock can be used to define the maximum sustainable injection pressure to ensure a safe permanent CO_2 storage.

Finally, we analyze the thermodynamic evolution of CO_2 and the thermo-hydro-mechanical response of the formation and the caprock to liquid (cold) CO_2 injection. We find that injecting CO_2 in liquid state is energetically more efficient than in supercritical state because liquid CO_2 is denser than supercritical CO_2. Therefore, the pressure required at the wellhead for a given CO_2 pressure in the aquifer is much lower for liquid than for gas or supercritical injection. In fact, the overpressure required at the aquifer is also smaller because a smaller fluid volume is displaced. The temperature decrease close to the injection well induces a stress reduction due to thermal contraction of the media. This can lead to shear slip of pre-existing fractures in the aquifer for large temperature contrasts in stiff rocks, which could enhance injectivity. In contrast, the mechanical stability of the caprock is improved in stress regimes where the maximum principal stress is the vertical.

II. Resumen

Los procesos termo-hidro-mecánicos relacionados con el almacenamiento geológico de carbono deben ser entendidos y cuantificados para demostrar a la opinión pública de que la inyección de dióxido de carbono (CO_2) es segura. Esta Tesis tiene como objetivo mejorar dicho conocimiento mediante el desarrollo de métodos para: (1) evaluar la evolución tanto de la geometría de la pluma de CO_2 como de la presión de los fluidos; (2) definir un ensayo de campo que permita caracterizar la presión de inyección máxima sostenible y los parámetros hidromecánicos de las rocas sello y almacén; y (3) proponer un nuevo concepto de inyección que es energéticamente eficiente y que mejora la estabilidad de la roca sello en la mayoría de escenarios geológicos debido a efectos termo-mecánicos.

Primero, investigamos numérica y analíticamente los efectos de la variabilidad de la densidad y viscosidad del CO_2 en la posición de la interfaz entre la fase rica en CO_2 y la salmuera de la formación. Introducimos una corrección para tener en cuenta dicha variabilidad en las soluciones analíticas actuales. Encontramos que el error producido en la posición de la interfaz al despreciar la compresibilidad del CO_2 es relativamente pequeño cuando dominan las fuerzas viscosas. Sin embargo, puede ser significativo cuando dominan las fuerzas de gravedad, lo que ocurre para tiempos y/o distancias largas de inyección.

Segundo, desarrollamos una solución semianalítica para la evolución de la geometría de la pluma de CO_2 y la presión de fluido, teniendo en cuenta tanto la compresibilidad del CO_2 como los efectos de flotación dentro del pozo. Formulamos el problema en términos de un potencial de CO_2 que facilita la solución en capas horizontales, en las que hemos discretizado el acuífero. El CO_2 avanza inicialmente por la porción superior del acuífero. Pero a medida que aumenta la presión de CO_2, la pluma crece no solo lateralmente, sino también hacia abajo, aunque no tiene porqué llegar a ocupar todo el espesor del acuífero. Tanto la interfaz CO_2-salmuera como la presión de fluido muestran una buena comparación con las simulaciones numéricas.

En tercer lugar, estudiamos posibles mecanismos de rotura, que podrían llegar a producir fugas de CO_2, en un sistema acuífero-sello con simetría radial, utilizando un

modelo viscoplástico. Las simulaciones ilustran que, dependiendo de las condiciones de contorno, el momento más desfavorable ocurre al inicio de la inyección. Sin embargo, si los contornos son poco permeables, la presión de fluido continúa aumentando en todo el acuífero, lo que podría llegar a comprometer la estabilidad de la roca sello a largo plazo.

Para evaluar dichos problemas, proponemos un ensayo de caracterización hidromecánica a escala de campo para estimar las propiedades hidromecánicas de las rocas sello y almacén. Obtenemos curvas para la sobrepresión y el desplazamiento vertical en función del término de la deformación volumétrica obtenido del análisis adimensional de las ecuaciones hidromecánicas. Ajustando las medidas de campo a estas curvas se pueden estimar los valores del módulo de Young y el coeficiente de Poisson del acuífero y del sello. Los resultados indican que la microsismicidad inducida tiene más probabilidades de ocurrir en el acuífero que en el sello. El inicio de la microsismicidad en el sello marca la presión de inyección máxima sostenible para asegurar un almacenamiento permanente de CO_2 seguro.

Finalmente, analizamos la evolución termodinámica del CO_2 y la respuesta termo-hidro-mecánica de las rocas sello y almacén a la inyección de CO_2 líquido (frío). Encontramos que inyectar CO_2 en estado líquido es energéticamente más eficiente porque al ser más denso que el CO_2 supercrítico, requiere menor presión en cabeza de pozo para una presión dad en el acuífero. De hecho, esta presión también es menor en el almacén porque se desplaza un volumen menor de fluido. La disminución de temperatura en el entorno del pozo induce una reducción de tensiones debido a la contracción térmica del medio. Esto puede producir deslizamiento de fracturas existentes en acuíferos formados por rocas rígidas bajo contrastes de temperatura grandes, lo que podría incrementar la inyectividad de la roca almacén. Por otro lado, la estabilidad mecánica de la roca sello mejora cuando la tensión principal máxima es la vertical.

III. Resum

Els processos termo-hidro-mecànics relacionats amb l'emmagatzematge geològic de carboni han de ser entesos i quantificats per tal de demostrar a l'opinió pública de que la injecció de diòxid de carboni (CO_2) és segura. Aquesta Tesi té com a objectiu millorar aquest coneixement mitjançant el desenvolupament de mètodes per a: (1) avaluar l'evolució tant de la geometria del plomall de CO_2 com de la pressió dels fluids; (2) definir un assaig de camp que permeti caracteritzar la pressió d'injecció màxima sostenible i els paràmetres hidromecànics de les roques segell i magatzem; i (3) proposar un nou concepte d'injecció que és energèticament eficient i que millora l'estabilitat de la roca segell en la majoria d'escenaris geològics a causa d'efectes termo-mecànics.

Primer, investiguem numèricament i analítica els efectes de la variabilitat de la densitat i viscositat del CO_2 en la posició de la interfície entre la fase rica en CO_2 i la salmorra de la formació. Introduïm una correcció per tal de tenir en compte aquesta variabilitat en les solucions analítiques actuals. Trobem que l'error produït en la posició de la interfície en menysprear la compressibilitat del CO_2 és relativament petit quan dominen les forces viscoses. Malgrat això, l'error pot ser significatiu quan dominen les forces de gravetat, la qual cosa té lloc per a temps i/o distàncies llargues d'injecció.

Segon, desenvolupem una solució semianalítica per a l'evolució de la geometria del plomall de CO_2 i la pressió de fluid, tenint en compte tant la compressibilitat del CO_2 com els efectes de flotació dins del pou. Formulem el problema en termes d'un potencial de CO_2 que facilita la solució en capes horitzontals, en les quals hem discretitzat l'aqüífer. El CO_2 avança inicialment per la porció superior de l'aqüífer. Però a mesura que augmenta la pressió de CO_2, el plomall de CO_2 no només creix lateralment, sinó que també ho fa cap avall, encara que no té perquè arribar a ocupar tot el gruix de l'aqüífer. Tant la interfície CO_2-salmorra com la pressió de fluid mostren una bona comparació amb les simulacions numèriques.

En tercer lloc, estudiem possibles mecanismes de trencament, que podrien arribar a produir fugues de CO_2, en un sistema aqüífer-segell amb simetria radial, utilitzant un model viscoplàstic. Les simulacions il·lustren que, depenent de les condicions de

contorn, el moment més desfavorable té lloc a l'inici de la injecció. Tot i això, si els contorns són poc permeables, la pressió de fluid continua augmentant en tot l'aqüífer, la qual cosa podria arribar a comprometre l'estabilitat de la roca segell a llarg termini.

Per a avaluar aquests problemes, proposem un assaig de caracterització hidromecànica a escala de camp per a estimar les propietats hidromecàniques de les roques segell i magatzem. Obtenim corbes per a la sobrepressió i el desplaçament vertical en funció del terme de la deformació volumètrica obtingut de l'anàlisi adimensional de les equacions hidromecàniques. Ajustant les mesures de camp a aquestes corbes es poden estimar els valors del mòdul de Young i el coeficient de Poisson de l'aqüífer i del segell. Els resultats indiquen que la microsismicitat induïda té més probabilitats d'ocórrer en l'aqüífer que en el segell. L'inici de la microsismicitat en el segell marca la pressió d'injecció màxima sostenible per tal d'assegurar un emmagatzematge permanent de CO_2 segur.

Finalment, analitzem l'evolució termodinàmica del CO_2 i la resposta termo-hidro-mecànica de les roques segell i magatzem a la injecció de CO_2 líquid (fred). Trobem que injectar CO_2 en estat líquid és energèticament més eficient perquè al ser més dens que el CO_2 supercrític, requereix una pressió menor al cap de pou per a una pressió donada a l'aqüífer. De fet, aquesta pressió també és menor a l'aqüífer perquè es desplaça un volum menor de fluid. La disminució de temperatura a l'entorn del pou indueix una reducció de tensions a causa de la contracció tèrmica del medi. Això pot produir lliscament de fractures existents en aqüífers formats per roques rígides sota contrastos de temperatura grans, la qual cosa podria incrementar la injectivitat de la roca magatzem. D'altra banda, l'estabilitat mecànica de la roca segell millora quan la tensió principal màxima és la vertical.

IV. Acknowledgements

Many people have left a footprint in my work and myself during my PhD studies, each in their own special way. I would like to express my most sincere gratitude to all of them.

First of all, I would like to express my deepest gratitude to my supervisors Jesús Carrera and Sebastià Olivella for trusting me and letting me fly under their wise guidance. It has been a privilege and a pleasure to work with them and to continuously learn from them.

I greatly appreciate Orlando Silva for sharing his code of flow through pipes and for revising the implementation of the CO_2 thermal properties in CODE_BRIGHT.

I would also like to express my utmost gratitude to Prof. Hamdi Tchelepi for his supervision and guidance during my stay at Stanford University. I would also like to thank the people who made my stay there comfortable, especially to Maria Elenius, Juan Argote, Joan Murcia, Anna Borrell and Jihoon Kim. I am also thankful to Dr. Jens Birkholzer for giving me the opportunity to give a seminar at the Lawrence Berkeley Nacional Laboratory. I am grateful to Prof. Sally Benson, Dr. Jonny Rutqvist and Dr. Quanlin Zhou for fruitful discussion and their interest in my work.

I would like to express my most sincere gratitude to all the people with whom I have worked with during these years. A special mention is deserved to those scientists with whom I have the privilege to share the coauthorship of a publication: Diogo Bolster, Marco Dentz, Orlando Silva, Estanislao Pujades, Anna Jurado, Francesca de Gaspari, Silvia de Simone, Enric Vázquez-Suñé, Daniel Fernández-García, Xavier Sánchez-Vila, Daniel Tartakovsky, Tomofumi Koyama, Lanru Jing and Ivars Neretnieks.

Needless to say, I am deeply grateful to all my fellow students from the Civil Engineering School, but especially to my fellows of the Hydrogeology Group. I would also like to thank the people who work to make our life easier at University: Teresa García, Silvia Aranda, Ana Martínez. Thanks also to Jordi Cama's joy, who does not understand that love can coexist with the rivalry of Barça-Madrid supporters. I am

especially thankful to Alberto Herrero, Estanis Pujades, Albert Nardi, Daniele Pedretti, Joaquín Jiménez and Diogo Bolster for their friendship and sharing my worries.

I would like to thank the MUSTANG team, especially to Dr. Jacob Bear for his perseverance in improving the work, Dr. Auli Niemi for coordinating the project and Dr. Jacob Bensabat, Dr. Henry Power, Dr. Tore Torp for fruitful discussion.

I would also like to thank the CIUDEN team, especially to Dr. Andrés Pérez-Estaún, Dr. Ramón Carbonell, Dr. José Luís Fuentes, Dr. Jordi Bruno, Dr. Oriol Montserrat from whom I have learnt a lot. I am particularly grateful to Dr. Modesto Montoto for his interest in my research and encouraging me to be enterprising.

I would like to extend my special thanks to the friends I made at the Civil Engineering School of Barcelona: Oriol, Guillem, Jonatan, Pau, Núria, Marc, Quim, Ignasi, Edu, Jordi, with whom I have shared uncountable laughs, but unfortunately some worries lately because of the bad moments that our profession is undergoing these days.

I would like to express my special thanks to all my family, especially to my parents, who have always given me support and smoothed the way.

Last but not least, my dearest thanks to Pilar for all the good moments we have lived together and for her patience, understanding and unconditional support. Thanks for encouraging me in taking the hard decision of starting my PhD studies.

V. List of Contents

1. Introduction

1.1. Background and objectives

The combustion of fossil fuels has released huge amounts of carbon dioxide (CO_2) to the atmosphere ever since the industrial revolution. These emissions have led to a significant increase of CO_2 concentration in the atmosphere. Pre-industrial CO_2 concentrations were around 280 parts per million in volume (ppmv). Since then, CO_2 concentration has risen up to 392 ppmv in 2011, increasing at a rate of 2.0 ppm/yr during the last decade. Current predictions are that CO_2 emissions will continue increasing at similar rates over the coming years.

CO_2 is a greenhouse gas; it traps infrared radiation emitted by the Earth that otherwise would escape into space, warming the atmosphere. Thanks to greenhouse gases such as water vapor, CO_2 and methane, our planet displays a comfortable average temperature of 15 ºC, instead of the -18 ºC that would exist if no greenhouse gasses were present in the atmosphere. Nevertheless, the continuous anthropic emissions of CO_2 into the atmosphere will increase the Earth temperature further, thus altering atmospheric circulation and changing the climate. This is why a change in the sources of energy, an increase in the energy and power generation efficiency are necessary. However, the deployment of existing and new low-carbon technologies is not an immediate process and may take several decades. Therefore, bridge technologies are needed. Carbon Capture and Sequestration (CCS) may indeed be one of such bridge technologies that will permit the reduction of CO_2 emissions over the coming decades while a change in the energy market occurs (IEA, 2010).

CCS consists of three stages. The first is the CO_2 capture itself, the second is its transport and the third the injection and storage in deep geological formations. Various types of geological formations can be considered for CO_2 sequestration. These include unminable coal seams, depleted oil and gas reservoirs and deep saline aquifers. The latter have received particular attention due to their high CO_2 storage capacity and wide availability throughout the world (Bachu and Adams, 2003). The injection needs to be

done in aquifers with high permeability, so that the huge amounts of CO_2 that will be injected can flow relatively easily without generating large overpressures. The fact that the target aquifers are saline is because their formation water has no potential use and therefore no valuable water resources are lost by storing CO_2 there. Furthermore, these aquifers would ideally be deep to ensure that the stored CO_2 will be in a supercritical state (pressures greater than 7.38 MPa and temperatures above 31.04 °C) to ensure effective storage (high CO_2 density). This is achieved, in general, for depths greater than 800 m. At these depths, CO_2 reaches relatively high densities, but still lower than that of the resident brine. Thus, CO_2 will tend to float. For this reason, a low-permeability and high entry pressure rock, known as caprock, overlying the aquifer is required. This caprock provides a hydrodynamic trap for CO_2 that prevents CO_2 from migrating upwards (Figure 1.1). Apart from a liquid-like density, supercritical CO_2 has a low gas-like dynamic viscosity, which is around one order of magnitude lower than that of brine. Therefore, CO_2 flows more easily than brine. Additionally, since CO_2 is injected into a formation that is already saturated, fluid pressure builds up. Moreover, the injected CO_2 will not, in general, be in thermal equilibrium with the reservoir. Overpressure and temperature difference can alter effective stresses, and therefore induce deformations of the rock, which might compromise the caprock mechanical stability. Maintaining the mechanical stability of the caprock is crucial in order to prevent CO_2 leakage towards freshwater aquifers and eventually to the atmosphere.

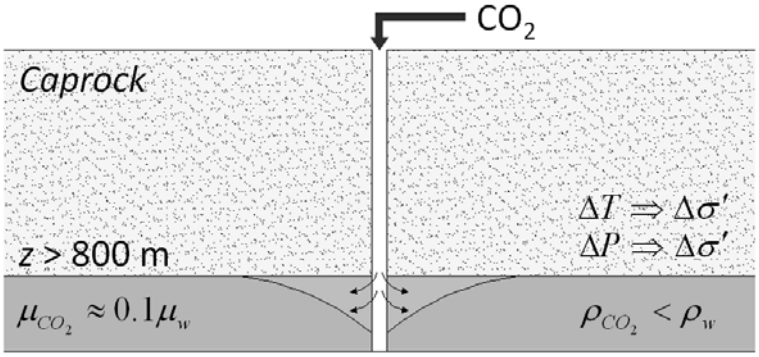

Figure 1.1 – Schematic description of CO_2 injection into deep saline aquifer. The depth of the aquifer must be greater than 800 m to ensure that the CO_2 stays in a supercritical state. In this state the density is relatively high, though lower than that of the formation brine, so CO_2 tends to float. Thus, a low-permeability formation, or caprock, is needed above the aquifer. The viscosity of supercritical CO_2 is one order of magnitude lower than that of brine and thus flows relatively easily. CO_2 injection induces an increase in fluid pressure and generates temperature differences, resulting in deformations of the rock.

Figure 1.2 illustrates a typical CO_2 plume in which CO_2 tends to flow preferentially through the top of the aquifer due to buoyancy. 2.5 Mt of CO_2 have been injected over 1 year through a single vertical well (located on the left side of Figure 1.2) in an aquifer at a depth between 1000 and 1100 m. The overpressure at the injection well reaches some 5 MPa (the initial pressure at the top of the aquifer is 10 MPa) (Figure 1.2b). These pressure variations affect CO_2 density significantly because CO_2 is highly compressible (Span and Wagner, 1996). This is reflected in Figure 1.2c, where we observe large variations of CO_2 density inside the CO_2 plume.

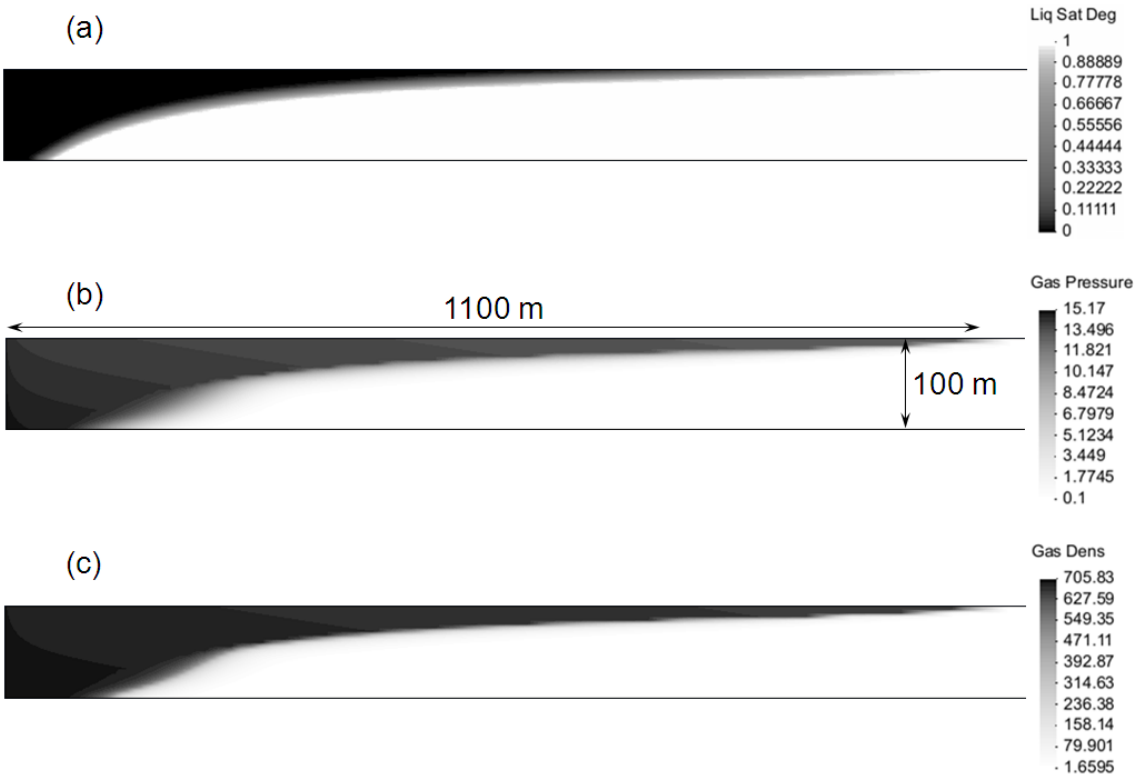

Figure 1.2 – CO_2 plume after 1 year of a radial injection of 2.5 Mt/yr of CO_2 at a depth between 1000 and 1100 m. (a) Water saturation degree, (b) CO_2 pressure and (c) CO_2 density.

Figure 1.3 shows how CO_2 density varies with depth under hydrostatic conditions and for an overpressure of 5 MPa generated by CO_2 injection for several geothermal gradients. Though CO_2 density can be calculated for a given pressure and temperature, the actual overpressure induced by CO_2 injection is difficult to determine due to inherent nonlinearities and the highly coupled nature of this problem. On the one hand, CO_2 density depends on fluid pressure. On the other hand, fluid pressure buildup is dependent on CO_2 density, because it determines the volume of displaced brine. An overpressure of 5 MPa may be typical for the amounts of CO_2 to be injected in deep

saline aquifers (e.g. Birkholzer *et al*., 2009). CO_2 density differences between hydrostatic pressure and an overpressure of 5 MPa decrease as the geothermal gradient becomes smaller (Figure 1.3). This difference also decreases for increasing depths. However, the majority of the aquifers in which CO_2 is being or will be injected range between 1000 and 1600 m (shaded zone in Figure 1.3) (Michael *et al*., 2010), where CO_2 density differences are greater than 100 kg/m^3. This density difference may result in large errors of the CO_2 plume position estimates if CO_2 compressibility is not taken into account.

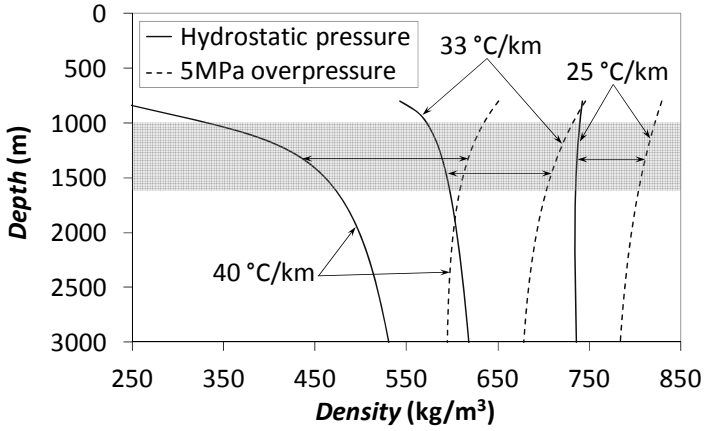

Figure 1.3 – CO_2 density as a function of depth for several geothermal gradients at hydrostatic conditions and for a 5 MPa overpressure generated by CO_2 injection. Surface temperature is of 5, 10 and 15 ºC for the geothermal gradients of 25, 33 and 40 ºC/km, respectively.

Buoyancy effects are rarely taken into account in the injection well. Instead, the well is often simulated as a prescribed (constant) flux boundary. However, this boundary condition plays a relevant role in determining the shape of the CO_2 plume. Since CO_2 is buoyant with respect to the formation brine, CO_2 tends to enter the aquifer preferentially along the top portion of the aquifer (Figure 1.4). The CO_2-brine interface develops maintaining pressure equilibrium, i.e. CO_2 pressure at the interface is equal to brine pressure plus the capillary entry pressure. Thus, the plume will advance according to pressure buildup. Aquifers with a high permeability offer low resistance to CO_2 advance. Therefore, the CO_2 plume will advance preferentially through the top of the aquifer, without occupying the whole thickness of the aquifer at the injection well. In contrast, lower permeability aquifers experience a higher pressure buildup. Consequently, the CO_2 plume will also advance downwards inside the injection well and may occupy the whole thickness of the aquifer at the injection well. Of course, once the CO_2 enters the aquifer, it will tend to flow upwards due to buoyancy.

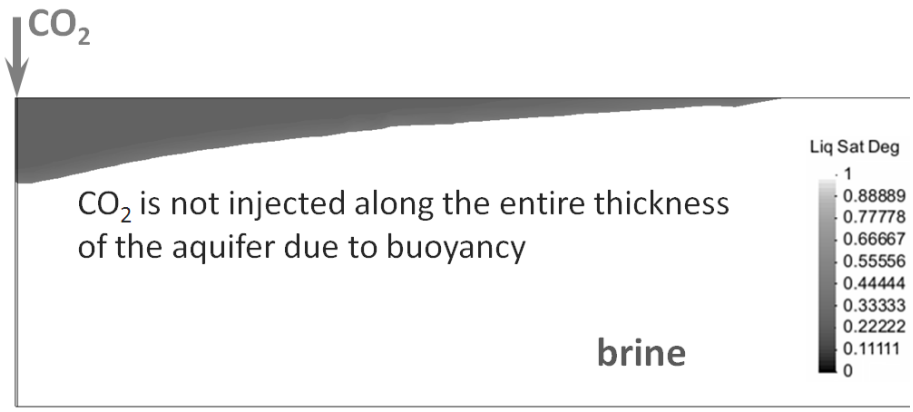

Figure 1.4 – Cross section of CO_2 injection through a vertical well in a deep saline aquifer. Note that CO_2 remains in the upper part of the aquifer because of buoyancy and it is not necessarily injected through the entire thickness of the aquifer.

Predictions of the CO_2 plume extent and the generated overpressure should be performed for each potential CO_2 storage site. Creating a numerical model for every one of these sites will be needed. Still, analytical solutions, which make simplifying assumptions, may help in the process of screening and decision making for initial site selection. Existing analytical solutions of the CO_2 plume position, i.e. those of Nordbotten *et al*. (2005) and Dentz and Tartakovsky (2009a) for the injection period and Hesse *et al*. (2007, 2008) and Juanes *et al*. (2010) for the post-injection period, assume that CO_2 is incompressible and that it is uniformly injected through the whole thickness of the aquifer. These two assumptions should be relaxed because they can induce large errors in the CO_2 plume position estimates. This leads to the first objective of this thesis, which consists in incorporating CO_2 compressibility into existing analytical solutions for the CO_2 plume position and propose a semianalytical solution for the CO_2 plume position and pressure distribution that accounts for CO_2 compressibility and buoyancy in the injection well.

The understanding of coupled hydromechanical effects, such as ground deformation, induced microseismicity and fault reactivation, will be crucial to convince the public that CCS is secure. Public fear to geological storage of CO_2 is one of the factors limiting the deployment of CCS. Fear is partly based on concerns about catastrophic failure, which seems unlikely to occur. Indeed, the most representative hydromechanical example may be the ground heave of 0.5 mm/yr on top of the CO_2 injection wells at the In Salah storage project in Algeria (Rutqvist *et al*., 2010). However, induced seismicity may have a greater impact on the long-term integrity of caprocks. Fluid pressure buildup reduces

effective stresses, which induces straining of the rock and can eventually trigger microseismic events. These can open fractures and reactivate faults, which might create flow paths through which CO_2 could migrate upwards. Furthermore, fault reactivation could potentially trigger a seismic event that could be felt by the local population (Cappa and Rutqvist, 2011b). A 3.4 magnitude injection induced seismic event triggered in Basel, Switzerland, during the hydraulic stimulation of a geothermal project motivated the shut-down of the project because of concerns by the local community (Häring *et al*., 2008). However, important differences exist between a geothermal stimulation and geologic CO_2 storage: CO_2 overpressure will be limited in order to avoid the opening of fractures, while geothermal stimulation aims precisely to open them; CO_2 will be injected in aquifers, while geothermal projects usually take place in low-permeability formations like granites. Hence, notable seismic events are not likely to occur in geologic CO_2 storage. Still, special attention has to be paid to hydromechanical coupled processes to avoid undesired phenomena such as fault reactivation, fracturing or well damage, which could lead to CO_2 leakage.

Coupled hydromechanical models can aid in defining the maximum sustainable injection pressure that guarantees that no CO_2 leakage will occur (Rutqvist *et al*., 2007). This maximum sustainable injection pressure coincides with the yield of the rock, which triggers microseismic events. CO_2 injection is intended to last for decades (30 to 50 years), so the pressure buildup cone caused by injection will propagate over large distances, reaching the boundaries of the aquifer. The nature of the boundary will influence fluid pressure evolution, which may affect caprock stability. Therefore, the second objective of this thesis is to understand fluid pressure evolution and how it is affected by boundary conditions as well as to investigate induced stress and strain (reversible and irreversible) during CO_2 injection to assess caprock stability.

The mechanical properties of the rocks are usually measured at the laboratory from core samples. However, the values that should be used in the models to reproduce the hydromechanical behaviour at the field scale differ significantly from those obtained from core samples (e.g. Verdon *et al*., 2011). This is mainly because rock masses contain not only the rock matrix tested at the laboratory, but also fractures that are not present in the cores. Therefore, field tests are needed to obtain representative values of the rock mechanical properties, to define the maximum sustainable injection pressure and to select suitable sequestration sites. The proposal of this test constitutes the third objective of this thesis.

Another issue of relevance is the way in which CO_2 is injected into the reservoir. In general, it is assumed that CO_2 will be injected in supercritical state because the pressure and temperature conditions of the target aquifers are such that CO_2 will remain in supercritical state. However, inflowing CO_2 may not be in thermal equilibrium with the aquifer because pressure and temperature injection conditions at the wellhead can have a very broad range and CO_2 will not equilibrate with the geothermal gradient if the flow rate is high. Temperature differences induce stress changes that can affect the mechanical stability of the caprock (Preisig and Prévost, 2011). This leads to the need for non-isothermal simulations of CO_2 injection in deformable porous media. Furthermore, other injection strategies may present a lower probability of CO_2 leakage or reduce the costs of supercritical CO_2 injection. For instance, pumping brine from the aquifer to reduce the overpressure and reinject it saturated in CO_2 avoids the presence of CO_2 in free phase and minimizes the risk of leakage because brine with dissolved CO_2 is denser than brine without CO_2, thus sinking. Hence, injection strategies other than the widely accepted supercritical CO_2 injection should also be considered to enhance proposed CCS projects. Thus, the final objective of this thesis is to propose a new injection strategy that minimizes energy consumption and to assess the caprock mechanical stability of this injection strategy considering thermo-hydro-mechanical couplings.

1.2. Thesis layout

This Thesis is organized in seven chapters, which coincide with papers already published in international scientific journals or in the process. Each chapter contains its own introduction and conclusions. A common reference list is included at the end of the document. The structure of the Thesis is as follows:

- *Chapter 2* deals with the effects of CO_2 compressibility on the prediction of the CO_2 plume position using existing analytical solutions; we present a correction to account for CO_2 compressibility in these analytical solutions. Fluid pressure is derived from these analytical solutions. The results from the analytical solutions are compared with numerical simulations. The contents of this chapter have given rise to the publication of Vilarrasa *et al*. (2010a) in the scientific journal Transport In Porous Media.

- *Chapter 3* presents a semianalytical solution for the CO_2 plume position and pressure evolution during injection of compressible CO_2 considering buoyancy effects in the injection well. The aquifer is discretized into horizontal layers through which CO_2 advances laterally and vertically downwards. CO_2 is not necessarily injected through the whole thickness of the aquifer because of its buoyancy. The contents of this chapter have been presented in a conference (Vilarrasa *et al*., 2010c) and it is planned to publish them in a scientific journal.
- *Chapter 4* focuses on the hydromechanical coupling of CO_2 sequestration in deep saline aquifers and how pressure buildup affects the mechanical caprock stability. Pressure evolution and the effect of the hydraulic boundary conditions are analyzed. The contents of this chapter have already been published in international scientific journals (Vilarrasa *et al*., 2010b; 2011b) and have been presented in several conferences (Vilarrasa *et al*., 2009; 2010d, e, f, g; 2011e).
- *Chapter 5* introduces a hydromechanical characterization test to assess the suitability of CO_2 injection sites to withstanding fluid pressure buildup. A literature review of the mechanical properties of the rocks involved in CO_2 sequestration is presented. The mechanical properties of the aquifer and caprock can be estimated from introducing the field measurements of the test (overpressure and vertical displacement) into the plots obtained from numerical simulations expressed in dimensionless variables. The onset of microseismicity defines the maximum sustainable injection pressure and microseismicity evolution can give information on the stress regime. The contents of this chapter have been presented in several conferences (Vilarrasa *et al*., 2011c, d; 2012a) and it is planned to publish them in a scientific journal.
- *Chapter 6* proposes a new CO_2 injection concept which consists in injecting CO_2 in liquid state. Injecting liquid CO_2 reduces fluid overpressure and improves caprock stability. To analyze this, simulations of non-isothermal two-phase flow in a deformable media are performed. The coupled thermo-hydro-mechanical processes occurring when injecting cold CO_2 are investigated. The contents of this chapter have been presented in several conferences (Vilarrasa *et al*., 2012b, c, d) and it is planned to publish them in a scientific journal.
- *Chapter 7* provides some general conclusions withdrawn from the previous chapters.

2. Effects of CO_2 Compressibility on CO_2 Storage in Deep Saline Aquifers

2.1. Introduction

Carbon dioxide (CO_2) sequestration in deep geological formations is considered a promising mitigation solution for reducing greenhouse gas emissions to the atmosphere. Although this technology is relatively new, wide experience is available in the field of multiphase fluid injection (e.g. the injection of CO_2 for enhanced oil recovery (Lake, 1989; Cantucci *et al*., 2009), production and storage of natural gas in aquifers (Dake, 1978; Katz and Lee, 1990), gravity currents (Huppert and Woods, 1995; Lyle *et al*., 2005) and disposal of liquid waste (Tsang *et al*., 2008)). Various types of geological formations can be considered for CO_2 sequestration. These include unminable coal seams, depleted oil and gas reservoirs and deep saline aquifers. The latter have received particular attention due to their high CO_2 storage capacity (Bachu and Adams, 2003). Viable saline aquifers are typically at depths greater than 800 m. Pressure and temperature conditions in such aquifers ensure that the density of CO_2 is relatively high (Hitchon *et al*., 1999).

Several sources of uncertainty associated with multiphase flows exist at these depths. These include those often encountered in other subsurface flows such as the impact of heterogeneity of geological media, e.g. (Neuweiller *et al*., 2003; Bolster *et al*., 2009b), variability and lack of knowledge of multiphase flow parameters (e.g. van Genuchten and Brooks-Corey models). Beyond these difficulties, the properties of supercritical CO_2, such as density and viscosity, can vary substantially (Garcia, 2003; Garcia and Pruess, 2003; Bachu, 2003) making the assumption of incompressibility questionable.

Two analytical solutions have been proposed for the position of the interface between the CO_2 rich phase and the formation brine: the Nordbotten *et al*. (2005) solution and

the Dentz and Tartakovsky (2009a) solution. Both assume an abrupt interface between phases. Both solutions neglect CO_2 dissolution into the brine, so the effect of convective cells (Ennis-king and Paterson, 2005; Hidalgo and Carrera, 2009; Riaz *et al*., 2006) on the front propagation is not taken into account. Each phase has constant density and viscosity. The shape of the solution by Nordbotten *et al*. (2005) depends on the viscosity of both CO_2 and brine, while the one derived by Dentz and Tartakovsky (2009a) depends on both the density and viscosity differences between the two phases. The validity of these sharp interface solutions has been discussed in, e.g., Dentz and Tartakovsky (2009a, b); Lu *et al*. (2009).

The injection of CO_2 causes an increase in fluid pressure and displaces the formation brine laterally. This brine can migrate out of the aquifer if the aquifer is open, causing salinization of other formations such as fresh water aquifers. In contrast, if the aquifer has very low-permeability boundaries, the storage capacity will be related exclusively to rock and fluid compressibility (Zhou *et al*., 2008). In the latter case, fluid pressure will increase dramatically and this can lead to geomechanical damage of the caprock (Rutqvist *et al*., 2007). Additionally, this pressure buildup during injection gives rise to a wide range of CO_2 density values within the CO_2 plume (Figure 2.1). As density changes are directly related to changes in volume, the interface position will be affected by compressibility. However, neither of the current analytical solutions for the interface location acknowledges changes in CO_2 density.

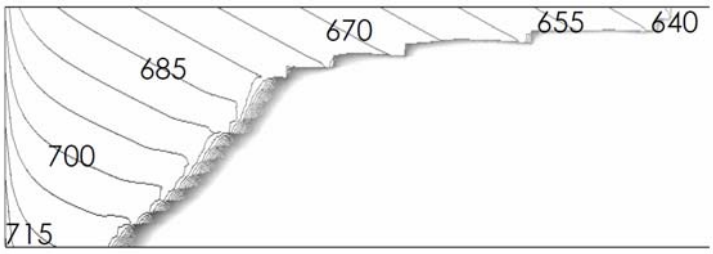

Figure 2.1 – CO_2 density (kg/m^3) within the CO_2 plume resulting from a numerical simulation that acknowledges CO_2 compressibility.

The evolution of fluid pressure during CO_2 injection has been studied by several authors, e.g. (Saripalli and McGrail, 2002; Mathias *et al*., 2009). Mathias *et al*., (2009) followed Nordbotten *et al*. (2005), calculating fluid pressure averaged over the thickness of the aquifer. They considered a slight compressibility in the fluids and geological formation, but still assumed constant fluid density values. Accounting for the

slight compressibility allows them to avoid the calculation of the radius of influence, which, as we propose later, can be determined by Cooper and Jacob (1946) method.

Typically CO_2 injection projects are intended to take place over several decades. This implies that the radius of the final CO_2 plume, which can be calculated with the above analytical solutions (Stauffer *et al*., 2009), may reach the kilometer scale. The omission of compressibility effects can result in a significant error in these estimates. This in turn reduces the reliability of risk assessments, where even simple models can provide a lot of useful information (e.g. Tartakovsky (2007); Bolster *et al*. (2009a)).

The nature of uncertainty in the density field is illustrated by the Sleipner Project (Korbol and Kaddour, 1995). There, around one million tons of CO_2 have been injected annually into the Utsira formation since 1996. Nooner *et al*. (2007) found that the best fit between the gravity measurements made in situ and models based on time-lapse 3D seismic data corresponds to an average in situ CO_2 density of 530 kg/m^3, with an uncertainty of ±65 kg/m^3. This uncertainty is significant in itself. However, prior to these measurements and calculations, the majority of the work on the site had assumed a range between 650-700 kg/m^3, which implies a significant error (> 20 %) in volume estimation.

Here we study the impact of CO_2 compressibility on the interface position, both numerically and analytically. We propose a simple method to account for compressibility effects (density variations) and viscosity variations and apply it to the analytical solutions of Nordbotten *et al*. (2005) and Dentz and Tartakovsky (2009a). First, we derive an expression for the fluid pressure distribution in the aquifer from the analytical solutions. Then, we propose an iterative method to determine the interface position that accounts for compressibility. Finally, we contrast these corrections with the results of numerical simulations and conclude with a discussion on the importance of considering CO_2 compressibility in the interface position.

2.2. Multiphase flow. The role of compressibility

Consider injection of supercritical CO_2 in a deep confined saline aquifer (see a schematic description in Figure 2.2). Momentum conservation is expressed using Darcy's law, which for phases CO_2, *c*, and brine, *w*, is given by

$$\mathbf{q}_\alpha = -\frac{kk_{r\alpha}}{\mu_\alpha}\left(\nabla P_\alpha + \rho_\alpha g \nabla z\right),\ \alpha = c, w, \tag{2.1}$$

where $\mathbf{q}_\alpha$ is the volumetric flux of α-phase, k is the intrinsic permeability, $k_{r\alpha}$ is the α-phase relative permeability, μ_α its viscosity, P_α its pressure, ρ_α its density, g is gravity and z is the vertical coordinate.

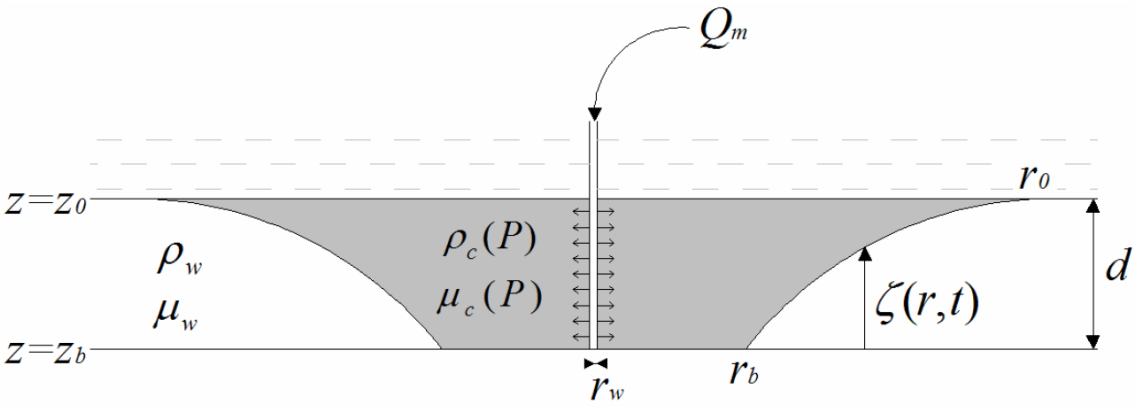

Figure 2.2 – Problem setup. Injection of compressible CO_2 in a homogeneous horizontal deep saline aquifer.

Mass conservation of these two immiscible fluids can be expressed as (Bear, 1972),

$$\frac{\partial\left(\rho_\alpha S_\alpha \varphi\right)}{\partial t} = -\nabla\cdot\left(\rho_\alpha \mathbf{q}_\alpha\right),\ \alpha = c, w, \tag{2.2}$$

where S_α is the saturation of the α-phase, φ is the porosity of the porous medium and t is time.

The left-hand side of Eq. (2.2) represents the time variation of the mass of α-phase per unit volume of porous medium. Assuming that there is no external loading, and that the grains of the porous medium are incompressible, but not stationary (Bear, 1972), the expansion of the partial derivative of this term results in

$$\frac{\partial\left(\rho_\alpha S_\alpha \varphi\right)}{\partial t} = S_\alpha \varphi \rho_\alpha c_\alpha \frac{\partial P_\alpha}{\partial t} + \rho_\alpha S_\alpha c_r \frac{\partial P_\alpha}{\partial t} + \rho_\alpha \varphi \frac{\partial S_\alpha}{\partial t}, \tag{2.3}$$

where $c_\alpha = \left(1/\rho_\alpha\right)\left(\mathrm{d}\rho_\alpha/\mathrm{d}P_\alpha\right)$ is fluid compressibility, $c_r = \mathrm{d}\varepsilon_v/\mathrm{d}\sigma'$ is rock compressibility, ε_v is the volumetric strain and σ' is the effective stress.

The first term in the right-hand side of Eq. (2.3) corresponds to changes in storage caused by the compressibility of fluid phases. The second term refers to rock

compressibility. The third term in the right-hand side of Eq. (2.3) represents changes in the mass of α caused by fluid saturation-desaturation processes (i.e., CO_2 plume advance). As such, it does not represent compressibility effects, although its actual value will be sensitive to pressure through the phase density, which controls the size of the CO_2 plume.

The relative importance of the first two terms depends on whether we are in the CO_2 or brine zones, because the compressibility of CO_2 is much larger than that of brine and rock. Typical rock compressibility values at depths of interest for CO_2 sequestration range from 10^{-11} to $5 \cdot 10^{-9}$ Pa^{-1} (Neuzil, 1986), but can be effectively larger if plastic deformation conditions are reached. Water compressibility is of the order of $4.5 \cdot 10^{-10}$ Pa^{-1}, which lies within the range of rock compressibility values. CO_2 compressibility ranges from 10^{-9} to 10^{-8} Pa^{-1} (Law and Bachu, 1996; Span and Wagner, 1996), one to two orders of magnitude greater than that of rock and water. Thus, CO_2 compressibility has a significant effect on the first term in the right-hand side of Eq. (2.3). However, the second term, which accounts for rock compressibility, can be neglected in the CO_2 rich zone, both because it is small and because the volume of rock occupied by CO_2 is orders of magnitude smaller than that affected by pressure buildup of the formation brine.

The situation is different in the region occupied by resident water. Water compressibility is at the low end of rock compressibilities at large depths. Moreover, its value is multiplied by porosity. Therefore, water compressibility will only play a relevant role in high porosity stiff rocks, which are rare. In any case, the two compressibility terms can be combined in the brine saturated zone, yielding

$$\rho_w g(\varphi c_w + c_r)\frac{\partial h_w}{\partial t} = S_s \frac{\partial h_w}{\partial t}, \qquad (2.4)$$

where h_w is the hydraulic head of water, S_s is the specific storage coefficient (Bear, 1972), which accounts for both brine and rock compressibility.

The specific storage coefficient controls, together with permeability, the radius of influence, R (i.e. the size of the pressure buildup cone caused by injection). In fact, assuming the aquifer to be large and for the purpose of calculating pressure buildup, this infinite compressible system can be replaced by an incompressible system whose radius grows as determined from the comparison between Thiem's solution (steady state) (Thiem, 1906) and Jacob's solution (transient) (Cooper and Jacob, 1946)

$$\Delta P_w = \frac{Q_0 \mu_w}{4\pi kd} \ln\left(\frac{R^2}{r^2}\right) = \frac{Q_0 \mu_w}{4\pi kd} \ln\left(\frac{2.25 k \rho_w g t}{\mu_w r^2 S_s}\right), \quad (2.5)$$

where Q_0 is the volumetric flow rate, d is the aquifer thickness and r is radial distance. The radius of influence can then be defined from Eq. (2.5) as

$$R = \sqrt{\frac{2.25 k \rho_w g t}{\mu_w S_s}}. \quad (2.6)$$

CO_2 is lighter than brine and density differences affect flow via buoyancy. To quantify the relative influence of buoyancy we define a gravity number, N, as the ratio of gravity to viscous forces. The latter can be represented by the horizontal pressure gradient ($Q_0 \mu / (2\pi krd)$), and the former by the buoyancy force ($\Delta \rho g$) in Darcy's law, expressed in terms of equivalent head. This would yield the traditional gravity number for incompressible flow (e.g. Lake, 1989). However, for compressible fluids, the boundary condition is usually expressed in terms of the mass flow rate, Q_m (Figure 2.2). Therefore, it is more appropriate to write Q_0 as Q_m / ρ. Hence, N becomes

$$N = \frac{2\pi k \Delta \rho g \bar{\rho}_c r_c d}{\mu_c Q_m}, \quad (2.7)$$

where $\Delta \rho = \rho_w - \rho_c$ is the difference between the fluid densities, $\bar{\rho}_c$ is a characteristic density, r_c is a characteristic length and Q_m is the CO_2 mass flow rate. Large gravity numbers (N >> 1) indicate that gravity forces dominate. Small gravity numbers (N << 1) indicate that viscous forces dominate. Gravity numbers close to one indicate that gravity and viscous forces are comparable.

The characteristic density can be chosen as the mean CO_2 density of the plume. The characteristic length depends on the scale of interest (Kopp *et al.*, 2009). The gravity number increases with the characteristic length, thus increasing the relative importance of gravity forces with respect to viscous forces (Tchelepi and Orr Jr., 1994). This implies that, as the CO_2 plume becomes large, gravity forces will dominate far from the injection well.

These equations can be solved numerically (e.g. Aziz and Settari, 2002; Chen *et al.*, 2006; Pruess *et al.*, 2004). However, creating a numerical model for each potential candidate site may require a significant cost. Alternatively, the problem can be solved analytically using some simplifications. The use of analytical solutions is useful because (i) they are instantaneous (Stauffer *et al.*, 2009), (ii) numerical solutions can

be coupled with analytical solutions to make them more efficient (Celia and Nordbotten, 2009) and (iii) they identify important scaling relationships that give insight into the balance of the physical driving mechanisms.

2.3. Analytical solutions

2.3.1. Abrupt interface approximation

The abrupt interface approximation considers that the two fluids, CO_2 and brine in this case, are immiscible and separated by a sharp interface. The saturation of each fluid is assumed constant in each fluid region and capillary effects are usually neglected. Neglecting compressibility and considering a quasi-steady (successive steady-states) description of moving fronts in Eq. (2.2) yields that the volumetric flux defined in (2.1) is divergence free. Additionally, if the Dupuit assumption is adopted in a horizontal radial aquifer and S_α is set to 1, i.e. the α-phase relative permeability equals 1, the following equation can be derived (Bear, 1972)

$$\frac{1}{r}\frac{\partial}{\partial r}\left[\varsigma\frac{Q_0-2\pi r\Delta\rho g\left(k/\mu_c\right)\left(d-\varsigma\right)\partial\varsigma/\partial r}{\varsigma+\left(d-\varsigma\right)\mu_w/\mu_c}\right]+2\pi\varphi\frac{\partial\varsigma}{\partial t}=0\,, \tag{2.8}$$

where ς is the distance from the base of the aquifer to the interface position. To account for a residual saturation of the formation brine, S_{rw}, behind the CO_2 front, one should replace μ_c by μ_c/k'_{rc} in Eq. (2.8) and below, where k'_{rc} is the CO_2 relative permeability evaluated at the residual brine saturation S_{rw}. Equation (2.8) can be expressed in dimensionless form using

$$r_D=\frac{r}{r_c},\quad \varsigma_D=\frac{\varsigma}{\varsigma_c},\quad t_D=\frac{t}{t_c},\quad M=\frac{k_{rw}/\mu_w}{k_{rc}/\mu_c},\quad N, \tag{2.9}$$

where M is the mobility ratio, N is the gravity number defined in Eq. (2.7), t_c is the characteristic time and the subscript D denotes a dimensionless variable, which yields

$$\frac{1}{r_D}\frac{\partial}{\partial r_D}\left[\varsigma_D\frac{1-r_DN\left(d/r_c\right)\left(1-\varsigma_D\right)\partial\varsigma_D/\partial r_D}{\varsigma_D+\left(1-\varsigma_D\right)/M}\right]+\frac{\partial\varsigma_D}{\partial t_D}=0\,. \tag{2.10}$$

Equation (2.10) shows that the problem depends on two parameters, N and M. The mobility ratio will have values around 0.1 for CO_2 sequestration, which will lead to the formation of a thin layer of CO_2 along the top of the aquifer (Hesse *et al*., 2007, 2008; Juanes *et al*., 2010). On the other hand, the gravity number can vary over several

orders of magnitude, depending on the aquifer permeability and the injection rate. Thus, the gravity number is the key parameter governing the interface position.

The analytical solutions of Nordbotten *et al*. (2005) and Dentz and Tartakovsky (2009a) to determine the interface position of the CO_2 plume when injecting supercritical CO_2 in a deep saline aquifer start from this approximation.

2.3.2. Nordbotten *et al*. (2005) approach

To find the interface position, Nordbotten *et al*. (2005) solve Eq. (2.8) neglecting the gravity term and approximating the transient system response to injection into an infinite aquifer by a solution to the steady-state problem with a moving outer boundary whose location increases in proportion to $\sqrt{t}$ in a radial geometry, i.e. the radius of influence defined in (2.6). In addition, they impose (i) volume balance, (ii) gravity override (CO_2 plume travels preferentially along the top) and (iii) they minimize energy at the well. The fluid pressure applies over the entire thickness of the aquifer and fluid properties are vertically averaged. The vertically averaged properties are defined as a linear weighting between the properties of the two phases. Nordbotten *et al*. (2005) write their solution as a function of the mobility, λ_α, defined as the ratio of relative permeability to viscosity, $\lambda_\alpha = k_{r\alpha} / \mu_\alpha$. For the case of an abrupt interface where both sides of the interface are fully saturated with the corresponding phase, the relative permeability is 1 and λ_α becomes the inverse of the viscosity of each phase. These viscosities are assumed constant.

Under these assumptions, Nordbotten *et al*. (2005) obtain the interface position as,

$$\varsigma_N(r,t) = d\left[1 - \frac{\mu_c}{\Delta\mu_w}\left(\sqrt{\frac{\mu_w V(t)}{\mu_c \varphi \pi d r^2}} - 1\right)\right], \tag{2.11}$$

where $V(t) = Q_0 \cdot t$ is the CO_2 volume assuming a constant CO_2 density and $\Delta\mu = \mu_w - \mu_c$ is the difference between fluid viscosities.

Integrating the flow equation and assuming vertically integrated properties of the fluid over the entire thickness of the formation, Nordbotten *et al*. (2005) provide the following expression for fluid pressure buildup

$$\bar{P}_N(r,t) - \bar{P}_0 = \frac{Q_0 \mu_w}{2\pi k} \int_r^R \frac{\mathrm{d}\, r}{r\left[(\Delta\mu / \mu_c)(d - \varsigma(r)) + d\right]}, \tag{2.12}$$

where $\bar{P}_N$ is the vertically averaged pressure and $\bar{P}_0$ is the vertically averaged initial pressure prior to injection.

2.3.3. Dentz and Tartakovsky (2009a) approach

Dentz and Tartakovsky (2009a) also consider an abrupt interface approximation. They include buoyancy effects, and the densities and viscosities of each phase are assumed constant.

They combine Darcy's law with the Dupuit assumption in radial coordinates. Imposing fluid pressure continuity at the interface they obtain

$$\varsigma_{DT}(r,t) = d\gamma_{cw} \ln\left(\frac{r}{r_b(t)}\right), \tag{2.13}$$

where r_b is the radius of the interface at the base of the aquifer and γ_{cw} is a dimensionless parameter that measures the relative importance of viscous and gravity forces

$$\gamma_{cw} = \frac{Q_0}{2\pi k d^2 g} \frac{\Delta\mu}{\Delta\rho}. \tag{2.14}$$

The interface radius at the base of the aquifer is obtained from volume balance as

$$r_b(t) = \sqrt{\frac{2Q_0 t}{\pi\varphi d\gamma_{cw}\left[\exp\left(\frac{2}{\gamma_{cw}}\right) - 1\right]^{-1}}}. \tag{2.15}$$

Note that the fluid viscosity contrast is treated differently in the two approaches (i.e. mobility ratio and viscosity difference). The mobility ratio is particularly relevant in multiphase flow when the two phases coexist. However, when one phase displaces the other, the viscosity difference governs the process (see Eq. (2.14) in Dentz and Tartakovsky (2009a) solution). An exception to this is the case when fluid properties are integrated vertically (Nordbotten *et al*., 2005), which can be thought of as a coexistence of phases.

2.4. Compressibility correction

Let us assume that we have an initial estimation of the mean CO_2 density and viscosity. With this we can calculate the interface position using either analytical solutions (2.11) or (2.13). Furthermore, the fluid pressure can be calculated from Darcy's law. Then, the density can be determined within the plume assuming that it is solely a function of pressure. Integrating the CO_2 density within the plume and dividing it by the volume of the plume, we obtain the mean CO_2 density

$$\overline{\rho}_c = \frac{1}{V}\int_0^d \int_0^{r(\varsigma)} 2\pi\varphi r \rho_c\left(P_c\right) \mathrm{d}r\,\mathrm{d}z\,, \tag{2.16}$$

where V is the volume occupied by the CO_2 plume and $r(\varsigma)$ is the distance from the well to the interface position from either Nordbotten *et al*. (2005) or Dentz and Tartakovsky (2009a).

Note here that we do not specify a priori a particular relationship between density and pressure. We only specify that density is solely a function of pressure. CO_2 density also depends on temperature (Garcia, 2003). However, we neglect thermal effects within the aquifer, and take the mean temperature of the aquifer as representative of the system. This assumption is commonly used in CO_2 injection simulations (e.g. Law and Bachu, 1996; Pruess and Garcia, 2002) and may be considered valid if CO_2 does not expand rapidly. If this happens, CO_2 will experience strong cooling due to the Joule-Thomson effect.

The relationship between pressure and density in Eq. (2.16) is in general nonlinear. Moreover, pressure varies in space. Notice that the dependence is two-way: CO_2 density depends explicitly on fluid pressure, but fluid pressure also depends on density, because density controls the plume volume, and thus the fluid pressure through the volume of water that needs to be displaced. Therefore, an iterative scheme is needed to solve this nonlinear problem. As density varies moderately with pressure, a Picard algorithm should converge, provided that the initial approximation is not too far from the solution.

The formulation of this iterative approach requires an expression for the spatial variability of fluid pressure for each of the two analytical solutions. In the approach of Nordbotten *et al*. (2005), we obtain an expression for the vertically averaged pressure by introducing (2.11) into (2.12) and integrating. The expression for pressure depends

on the region: close to the injection well, all fluid is CO_2; far away, all fluid is saline water; in between the two phases coexist with an abrupt interface between them,

$$\begin{aligned}
&r > r_0; \quad \overline{P}_N(r,t) = \overline{P}_0 + \frac{Q_0\mu_w}{2\pi kd}\ln\left(\frac{R}{r}\right), \\
&r_b \le r \le r_0; \quad \overline{P}_N(r,t) = \overline{P}_0 + \frac{Q_0\mu_w}{2\pi kd}\left[\ln\left(\frac{R}{r}\right) + \sqrt{\frac{\mu_c\varphi\pi d}{\mu_w V(t)}}(r_o - r)\right], \\
&r < r_b; \quad \overline{P}_N(r,t) = \overline{P}_0 + \frac{Q_0\mu_w}{2\pi kd}\left[\ln\left(\frac{R}{r}\right) + \sqrt{\frac{\mu_c\varphi\pi d}{\mu_w V(t)}}(r_o - r_b) + \frac{\mu_c}{\mu_w}\ln\left(\frac{r_b}{r}\right)\right],
\end{aligned} \tag{2.17}$$

where r_0 is the radial distance where the interface intersects the top of the aquifer, r_b is the radial distance where the interface intersects the bottom of the aquifer, $\overline{P}_0 = P_{t0} + \rho_w g d/2$ is the vertically averaged fluid pressure prior to injection, and P_{t0} is the initial pressure at the top of the aquifer. Mathias *et al*. (2009) come to a similar expression for fluid pressure, but they consider a slight compressibility in the fluids and rock instead of a radius of influence. The vertically averaged fluid pressure varies with the logarithm of the distance to the well in the regions where a single phase is present (CO_2 or brine). However, it varies linearly in the region where both phases coexist.

Fluid pressure can be obtained from the Dentz and Tartakovsky (2009a) approach by integrating (2.1), assuming hydrostatic pressure (Dupuit approximation) in the aquifer, and taking the interface position given by (2.13), which yields

$$\begin{aligned}
&r > r(\zeta_{DT}); \quad P_{DT}(r,z,t) = P_{t0} + \rho_w g(d - z) + \frac{Q_0\mu_w}{2\pi kd}\ln\left(\frac{R}{r}\right), \\
&r \le r(\zeta_{DT}); \quad P_{DT}(r,z,t) = P_{t0} + \rho_w g(d - z) \\
&\qquad\qquad + \frac{Q_0}{2\pi kd}\left[\mu_w \ln\left(\frac{R}{r_b}\right) + \mu_c \ln\left(\frac{r_b}{r}\right) - \Delta\mu\frac{z}{d\gamma_{cw}}\right].
\end{aligned} \tag{2.18}$$

Equation (2.18) can be averaged over the entire thickness of the aquifer to obtain an averaged pressure, which will be used to compare the two approaches. This averaged pressure is given by

$$
\begin{aligned}
&r > r_0; \quad \overline{P}_{DT}(r,t) = \overline{P}_0 + \frac{Q_0 \mu_w}{2\pi k d} \ln\left(\frac{R}{r}\right), \\
&r_b \le r \le r_0; \quad \overline{P}_{DT}(r,t) = \overline{P}_0 + \frac{Q_0}{2\pi k d}\left\{\mu_w\left[\ln\left(\frac{R}{r_b}\right) + \gamma_{cw}\ln\left(\frac{r}{r_b}\right)\ln\left(\frac{r_b}{r}\right)\right]\right. \\
&\qquad\qquad + \mu_c \ln\left(\frac{r_b}{r}\right)\left[1 - \gamma_{cw}\ln\left(\frac{r}{r_b}\right)\right] \\
&\qquad\qquad \left. - \frac{\Delta\mu}{2\gamma_{cw}}\left[1 - \gamma_{cw}^2\left(\ln\left(\frac{r}{r_b}\right)\right)^2\right]\right\}, \\
&r < r_b; \quad \overline{P}_{DT}(r,t) = \overline{P}_0 + \frac{Q_0}{2\pi k d}\left[\mu_w \ln\left(\frac{R}{r_b}\right) + \mu_c \ln\left(\frac{r_b}{r}\right) - \frac{\Delta\mu}{2\gamma_{cw}}\right].
\end{aligned}
\tag{2.19}
$$

Thus, the vertically averaged fluid pressure is defined in three regions in both approaches by Eqs. (2.17) and (2.19). Unsurprisingly, the two approaches have the same solution in the regions where only one phase exists. Differences appear in the region where CO_2 and the formation brine coexist. In the Nordbotten *et al*. (2005) approach, the vertically averaged pressure varies linearly with distance to the well. However, in Dentz and Tartakovsky (2009a), it changes logarithmically with distance to the well. As a result, the approach of Dentz and Tartakovsky (2009a) predicts higher fluid pressure values in this zone.

Equations (2.17) and (2.18) allow us to develop a simple iterative method for correcting the interface position. The method can be applied to both the Nordbotten *et al*. (2005) and Dentz and Tartakovsky (2009a) solutions as well as to any other future solutions that may emerge. The procedure is as follows

1) Take a reasonable initial approximation for mean CO_2 density and viscosity from the literature, e.g. Bachu (2003).
2) Determine the interface position using mean density and viscosity in analytical solutions (2.11) or (2.13).
3) Calculate the pressure distribution using (2.17) or (2.18).
4) Calculate the corresponding mean density and viscosity of the CO_2 using (2.16).
5) Repeat steps 2-4 until the solution converges to within some prespecified tolerance. Two different convergence criteria can be chosen: (i) changes in the interface position or (ii) changes in the mean CO_2 density.

The method is relatively easy to implement and can be programmed in a spreadsheet or any code of choice. The method converges rapidly, within a few iterations (typically less than 5) in all test cases. A calculation spreadsheet can be downloaded from GHS (2009).

2.5. Application

2.5.1. Injection scenarios

To illustrate the relevance of CO_2 compressibility effects, we consider three injection scenarios: (i) a regime in which viscous forces dominate gravity forces, (ii) one where both forces have a similar influence and (iii) a case where gravity forces dominate.

CO_2 thermodynamic properties have been widely investigated (e.g. Sovova and Prochazka, 1993; Span and Wagner, 1996; Garcia, 2003). The thermodynamic properties given by Span and Wagner (1996) are almost identical to the International Union of Pure and Applied Chemistry (IUPAC) (Angus *et al*., 1976) data sets over the *P-T* range of CO_2 sequestration interest (McPherson *et al*., 2008). However, the algorithm given by Span and Wagner (1996) for evaluating CO_2 properties has a very high computational cost. For the sake of simplicity and illustrative purposes, we assume a linear relationship between CO_2 density and pressure, given as

$$\rho_c = \rho_0 + \rho_1 \beta \left(P_c - P_{t0} \right), \tag{2.20}$$

where ρ_0 and ρ_1 are constants for the CO_2 density, β is CO_2 compressibility, P_c is CO_2 pressure and P_{t0} is the reference pressure for ρ_0. ρ_0, ρ_1 and β are obtained from data tables in Span and Wagner (1996). Appendix I contains the expressions for the mean CO_2 density using this linear approximation in (2.20) for both approaches.

CO_2 viscosity is calculated using an expression proposed by Altunin and Sakhabetdinov (1972). In this expression, the viscosity is a function of density and temperature. Thus the mean CO_2 viscosity is calculated from the mean CO_2 density. Figure 2.3 shows how the density varies within the CO_2 plume for one of our numerical simulations. The numerical simulations calculate CO_2 density assuming the Redlich-Kwong equation of state (Redlich and Kwong, 1949) using the parameters for CO_2 proposed by Spycher *et al*. (2003) and CO_2 viscosity using the expression of Altunin and Sakhabetdinov (1972) (see Appendix II). The maximum error encountered in this

study due to the linear CO_2 density approximation was around 8 %, which we deem acceptable for our illustrative purposes. Bachu (2003) shows vertical profiles of CO_2 density assuming hydrostatic pressure and different geothermal gradients. However, pressure buildup affects CO_2 properties. Hence, these vertical profiles can only be taken as a reference, for example, to obtain the initial approximation of CO_2 density and viscosity.

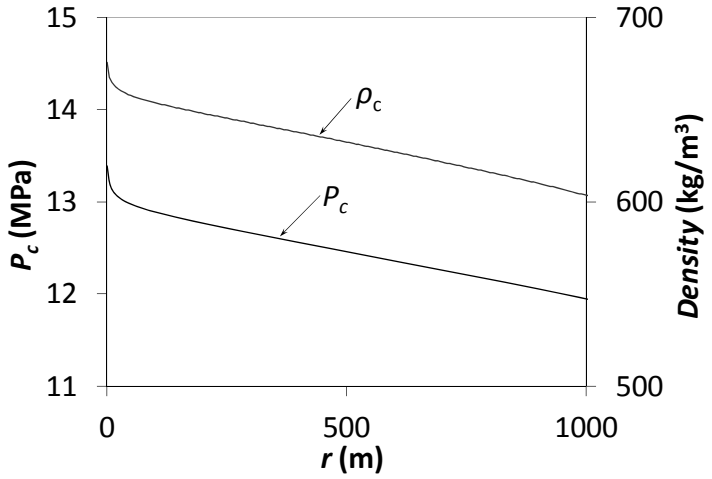

Figure 2.3 – CO_2 pressure and CO_2 density at the top of the aquifer resulting from a numerical simulation that acknowledges CO_2 compressibility.

We study a saline aquifer at a depth that ranges from 1000 to 1100 m. The temperature is assumed to be constant and equal to 320 K. For this depth and temperature, the initial CO_2 density is estimated as 730 kg/m^3 (Bachu, 2003). The corresponding CO_2 viscosity according to Altunin and Sakhabetdinov (1972) is 0.061 mPa·s.

For the numerical simulations we used the program CODE_BRIGHT (Olivella *et al.*, 1994; 1996) with the incorporation of the above defined constitutive equations for CO_2 density and viscosity. This code solves the mass balance of water and CO_2 (Eq. (2.2)) using the Finite Element Method and a Newton-Raphson scheme to solve the nonlinearities. The aquifer is represented by an axisymmetric model in which a constant CO_2 mass rate is injected uniformly in the whole vertical of a well with radius, r_p, 0.15 m. The aquifer is assumed infinite-acting, homogeneous and isotropic. In order to obtain a solution close to an abrupt interface, a van Genuchten retention curve (van Genuchten, 1980), with an entry pressure, P_{cc}, of 0.02 MPa and the shape

parameter m =0.8, was used. To approximate a sharp interface, linear relative permeability functions, for both the CO_2 and the brine, have been used (Table 2.1). This retention curve and relative permeability functions enable us to obtain a CO_2 rich zone with a saturation very close to 1, and a relatively narrow mixing zone. The CO_2 saturation 90 % isoline has been chosen to represent the position of the interface.

Table 2.1 – Parameters considered for the numerical simulations in the three injection scenarios.

	m	P_{cc} (MPa)	k (m^2)	$k_{r\alpha}$	Q_m (kg/s)	r_p (m)	S_s
Case 1			10^{-13}		120		
Case 2	0.8	0.02	10^{-12}	$S_{r\alpha}$	79	0.15	$1.76 \cdot 10^{-6}$
Case 3			10^{-12}		1		

2.5.2. Case 1: Viscous forces dominate

This first case consists of an injection with a gravity number of the order of 10^{-3} in the well. In this situation, the corrected mean CO_2 density (770 kg/m^3 for Nordbotten *et al*. (2005) and 803 kg/m^3 for Dentz and Tartakovsky (2009a)) is higher than that assumed initially (730 kg/m^3). The corresponding CO_2 viscosities are 0.067 and 0.073 mPa·s respectively. Therefore, the corrected interface position is located closer to the well than when we neglect variations in density. The Dentz and Tartakovsky (2009a) approach gives a higher value of the mean CO_2 density because fluid pressure grows exponentially, while it grows linearly in Nordbotten *et al*. (2005) approach, thus leading to lower fluid pressure values in the zone where CO_2 and brine coexist. We define relative error, E_{rel}, of the interface position as

$$E_{rel} = \frac{R_i - R_c}{R_i}, \tag{2.21}$$

where R_i is the radius of the CO_2 plume at the top of the aquifer for incompressible CO_2 and R_c is the radius of the CO_2 plume at the top of the aquifer for compressible CO_2.

Differences between the compressible and incompressible solutions are shown in Figure 2.4. For the Dentz and Tartakovsky (2009a) solution, the relative error increases slightly from the base to the top of the aquifer, presenting a maximum relative error of 6 % at the top of the aquifer. For the Nordbotten *et al*. (2005) solution the interface tilts, with the base of the interface located just 2 % further from the well than its initial

position, but the top positioned 7 % closer to the well. The difference in shape between the two analytical solutions results in a CO_2 plume that extends further along the top of the aquifer for Nordbotten *et al*. (2005) solution than Dentz and Tartakovsky (2009a) over time (Figure 2.4b). A similar behaviour can be seen in the numerical simulations (Figure 2.4a). In this case, the interface given by the numerical simulation compares favourably with that of Nordbotten *et al*. (2005).

Figure 2.4c displays a comparison between the vertically averaged fluid pressure given by both approaches. The fluid pressure given by Mathias *et al*. (2009) is identical to that obtained in Nordbotten *et al*. (2005) approach (Eq. (2.17)). This is because Mathias *et al*. (2009) assumed the Nordbotten *et al*. (2005) solution for the interface position and that the hypothesis made therein are valid. Thus, both expressions can be considered equivalent for the vertically averaged fluid pressure. Fluid pressure obtained from the numerical simulation is smaller than the other profiles inside the CO_2 plume region. This may reflect the larger energy dissipation produced by analytical solutions as a result of the Dupuit assumption.

2.5.3. Case 2: Comparable gravity and viscous forces

Here, the gravity number at the well is in the order of 10^{-1} (Note that the gravity number increases to 1 if we take a characteristic length only 1.5 m away from the injection well. In fact, it keeps increasing further away from the well, where gravity forces will eventually dominate (recall Section 3)). The density variations between the initial guess of 730 kg/m^3 and the corrected value can be large. The density reduces to 512 kg/m^3 (viscosity of 0.037 mPa·s) for Nordbotten *et al*. (2005) and to 493 kg/m^3 (viscosity of 0.036 mPa·s) for Dentz and Tartakovsky (2009a). This means that the error associated with neglecting CO_2 compressibility can become very large and should be reflected in the interface position (Figure 2.5a). For the Dentz and Tartakovsky (2009a) solution including compressibility leads to a 26 % error at the top of the aquifer. This relative error reaches 53 % in the Nordbotten *et al*. (2005) solution. Over a 30 year injection this could represent a potential error of 3 km in the interface position estimation (Figure 2.5b). Here, the numerical simulations also show the importance of considering CO_2 compressibility. The interface position from the simulations is similar to that of Nordbotten *et al*. (2005) in the lower half of the aquifer, where viscous forces may dominate, but it is similar to that of Dentz and Tartakovsky (2009a) in the upper part of the aquifer, where buoyancy begins to dominate.

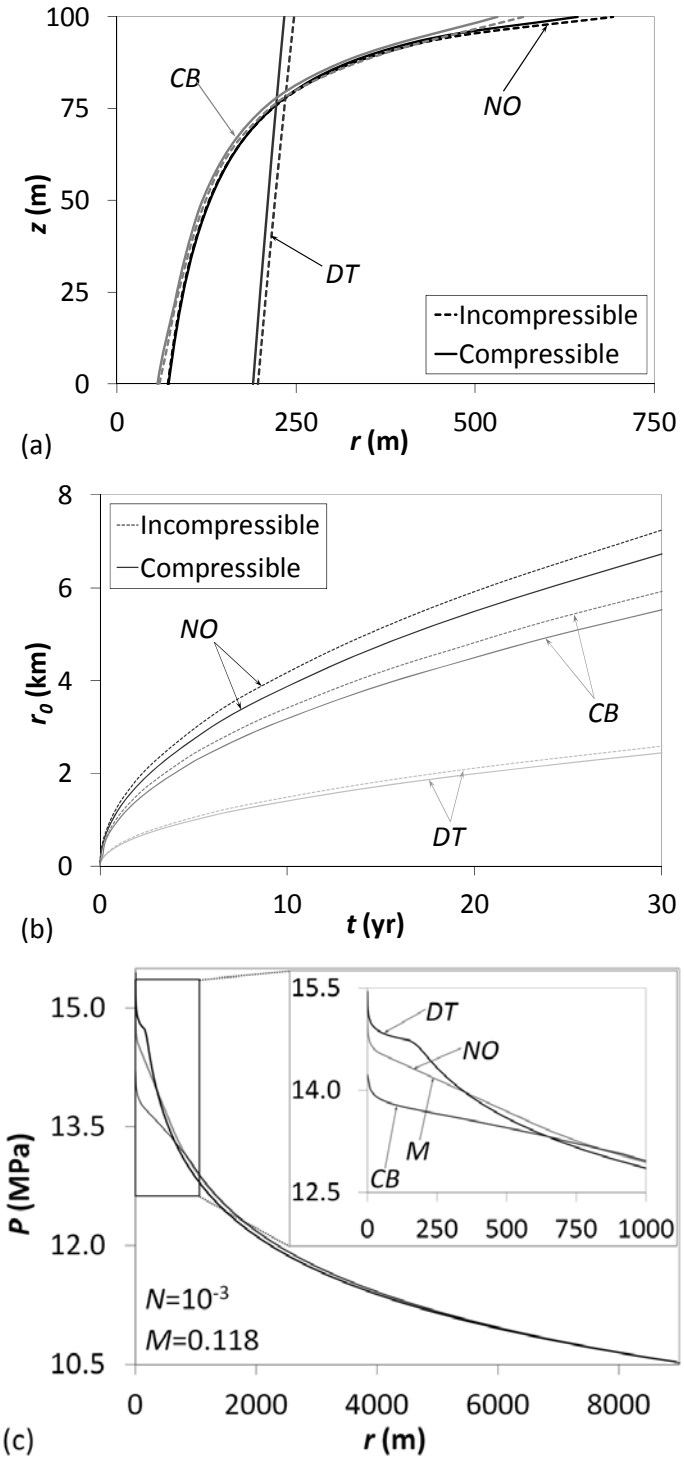

Figure 2.4 – Case 1: Viscous forces dominate. Gravity number, N, equals 10^{-3} in the well. (a) Abrupt interface position in a vertical cross section after 100 days of injection, (b) evolution of the CO_2 plume radius at the top of the aquifer and (c) vertically averaged fluid pressure with distance to the well after 100 days of injection, with a detail of the CO_2 rich zone. *NO* refers to Nordbotten *et al*. (2005) solution, *DT* to Dentz and Tartakovsky (2009a) solution, *CB* to the numerical solution of CODE_BRIGHT and *M* is the Mathias *et al*. (2009) solution for fluid pressure.

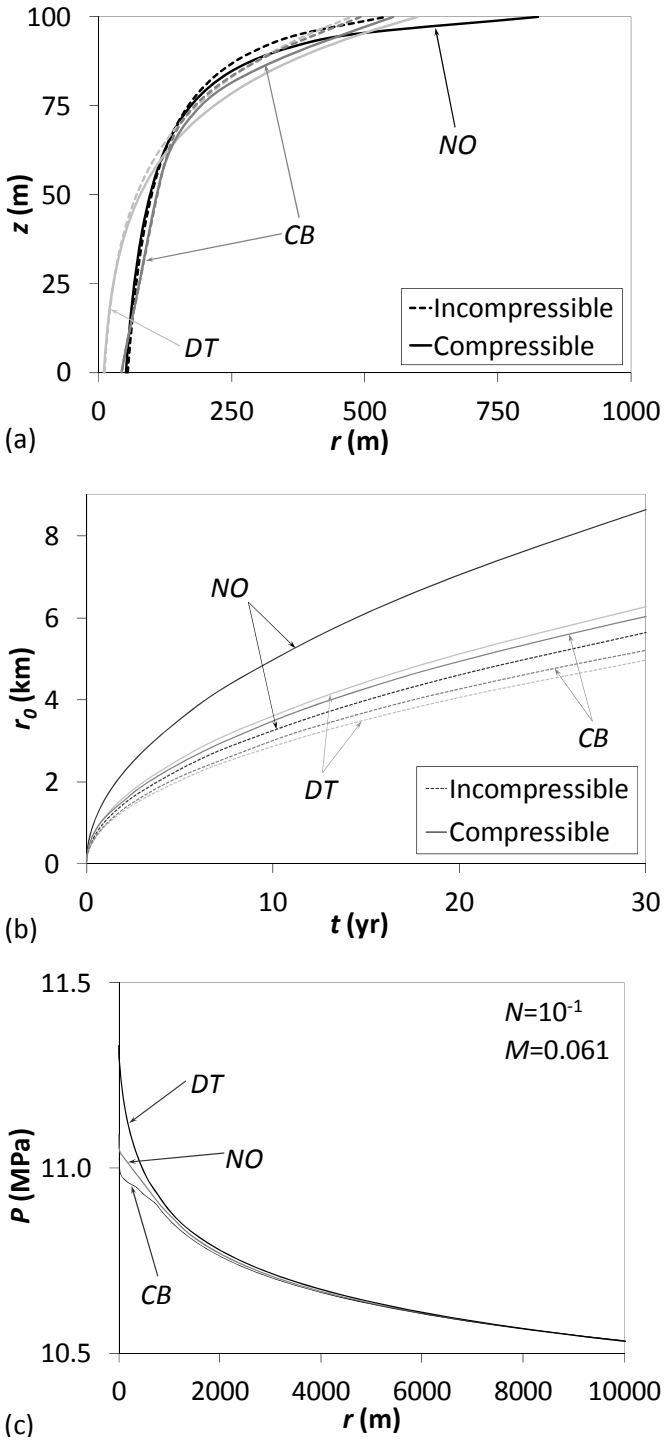

Figure 2.5 – Case 2: Comparable viscous and gravity forces. Gravity number, N, equals 10^{-1} in the well. (a) Abrupt interface position in a vertical cross section after 100 days of injection, (b) evolution of the CO_2 plume radius at the top of the aquifer and (c) vertically averaged fluid pressure with distance to the well after 100 days of injection. *NO* refers to Nordbotten *et al*. (2005) solution, *DT* to Dentz and Tartakovsky (2009a) solution and *CB* to the numerical solution of CODE_BRIGHT.

This dominant buoyancy flow may be significant when considering risks associated with potential leakage from the aquifer (Nordbotten *et al*., 2009) or mechanical damage of the caprock (Vilarrasa *et al*., 2010b), where the extent and pressure distribution of the CO_2 on the top of the aquifer plays a dominant role.

Unlike the previous case, the mean CO_2 density of Dentz and Tartakovsky (2009a) approach is lower than that of Nordbotten *et al*. (2005). This is because Nordbotten *et al*. (2005) consider the vertically averaged fluid pressure (Figure 2.5c). When gravity forces play an important role, the CO_2 plume largely extends at the top of the aquifer. CO_2 pressure at the top of the aquifer is lower than the vertically averaged fluid pressure, which considers CO_2 and the formation brine. Thus, the mean CO_2 density is overestimated when it is calculated from vertically averaged fluid pressure values.

2.5.4. Case 3: Gravity forces dominate

In this case, the gravity number is close to 10 at the well. Density deviations from our initial guess can be very large here. The mean density drops to 479 kg/m^3 for Nordbotten *et al*. (2005) and to 449 kg/m^3 for Dentz and Tartakovsky (2009a) solutions, which correspond to CO_2 viscosities of 0.035 and 0.032 mPa·s respectively. This means that the interface position at the top of the aquifer will extend much further than when not considering CO_2 compressibility. The Dentz and Tartakovsky (2009a) solution clearly reflects buoyancy and the CO_2 advances through a very thin layer at the top of the aquifer (Figure 2.6a). In contrast, the Nordbotten *et al*. (2005) interface cannot represent this strong buoyancy effect because this solution does not account for gravitational forces. The relative error of the interface position at the top of the aquifer is of 30 % for Dentz and Tartakovsky (2009a) solution, and of 64 % for Nordbotten *et al*. (2005). In this case, the numerical simulation compares more favourably with the Dentz and Tartakovsky (2009a) solution.

The vertically averaged pressure from Dentz and Tartakovsky (2009a) is similar to that of the numerical simulation because gravity forces dominate (Figure 2.6c). In this case, Nordbotten *et al*. (2005) predict a very small pressure buildup, which reflects their linear variation with distance. In addition, the zone with only CO_2, where fluid pressure grows logarithmically, is very limited.

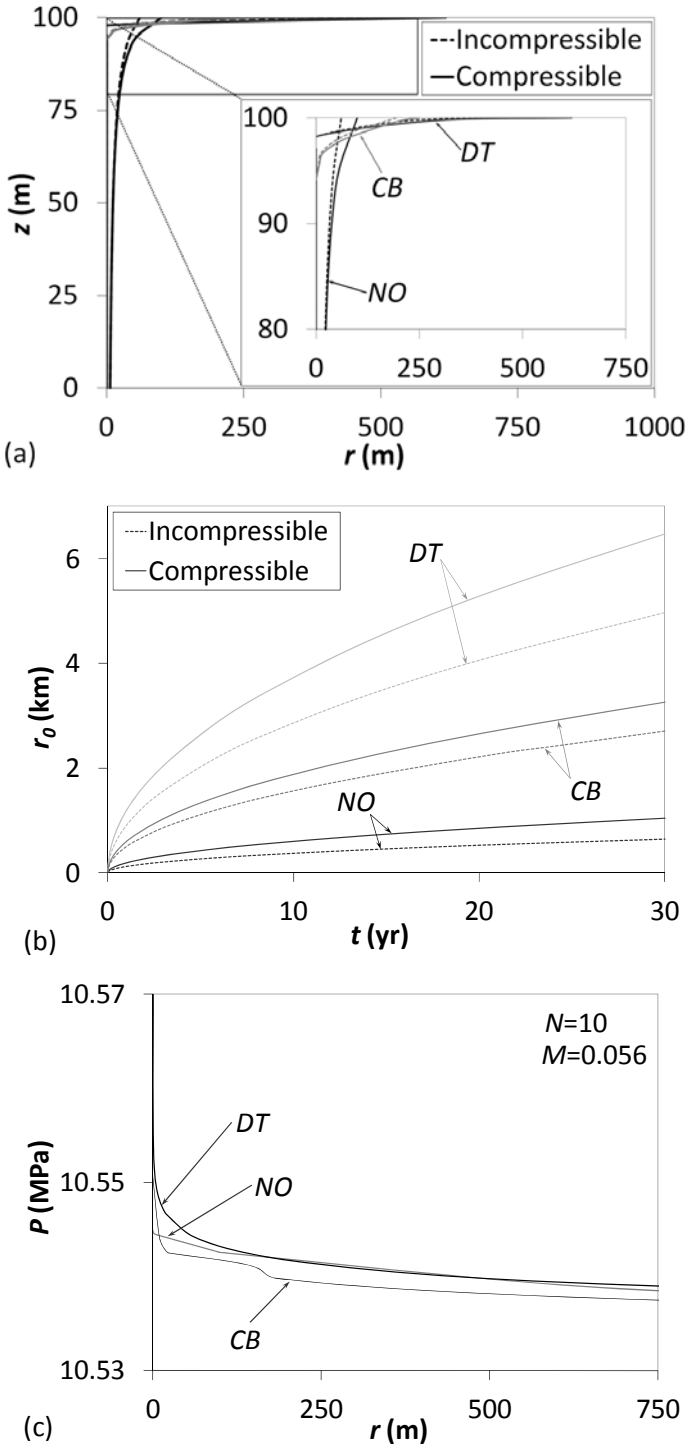

Figure 2.6 – Case 3: Gravity forces dominate. Gravity number, N, equals 10 in the well. (a) Abrupt interface position in a vertical cross section after 100 days of injection, (b) evolution of the CO_2 plume radius at the top of the aquifer and (c) vertically averaged fluid pressure with distance to the well after 100 days of injection. *NO* refers to Nordbotten *et al*. (2005) solution, *DT* to Dentz and Tartakovsky (2009a) solution and *CB* to the numerical solution of CODE_BRIGHT.

Finally, we consider the influence of the gravity number on CO_2 compressibility effects. Figure 2.7 displays the relative error (Eq. (2.21)) of the interface position at the top of the aquifer as a function of the gravity number, computed at the injection well. Negative relative errors mean that the interface position extends further when considering CO_2 compressibility. Both analytical solutions, i.e. Nordbotten *et al*. (2005) and Dentz and Tartakovsky (2009a), present a similar behaviour, but Nordbotten *et al*. (2005) has a bigger error. This is mainly because they vertically average fluid pressure, which leads to unrealistic CO_2 properties in the zone where both CO_2 and brine exist. For gravity numbers greater than 1, the mean CO_2 density tends to a constant value because fluid pressure buildup in the well is very small. For this reason, the relative error remains constant for this range of gravity numbers. However, the absolute relative error decreases until the mean CO_2 density equals that of the initial approximation for gravity numbers lower than 1. The closer the initial CO_2 density approximation is to the actual density, the smaller is the error in the interface position.

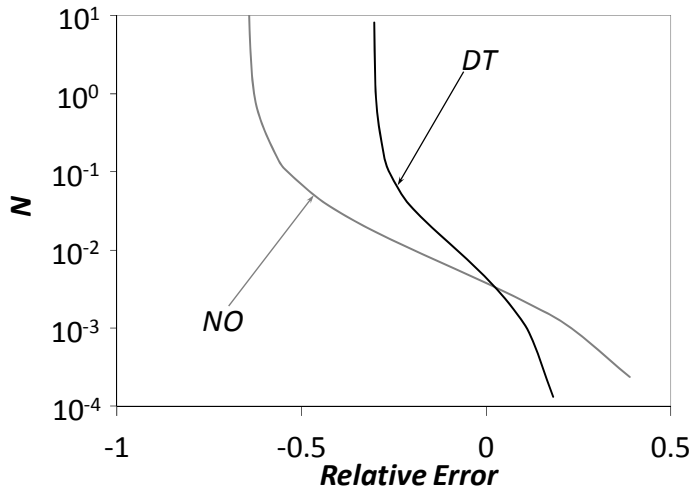

Figure 2.7 – Relative error (Eq. (2.21)) of the interface position at the top of the aquifer made when CO_2 compressibility is not considered as a function of the gravity number for both analytical solutions. *NO* refers to Nordbotten *et al*. (2005) solution and *DT* to Dentz and Tartakovsky (2009a) solution.

Figure 2.8 displays the mean CO_2 density as a function of the gravity number computed in the well for the cases discussed here. Differences arise between the two analytical approaches. The most relevant difference occurs at high gravity numbers. For gravity numbers greater than $5 \cdot 10^{-2}$, Nordbotten *et al*. (2005) yield a higher CO_2 density because fluid pressure is averaged over the whole vertical. Thus, fluid pressure in the zone where CO_2 and brine exist is overestimated, resulting in higher CO_2 density

values. For gravity numbers lower than $5 \cdot 10^{-2}$, CO_2 density given by Dentz and Tartakovsky (2009a) is slightly higher than that of Nordbotten *et al*. (2005) because the former predicts higher fluid pressure values in the CO_2 rich zone, as explained previously. However, both approaches present similar mean CO_2 density values for low gravity numbers.

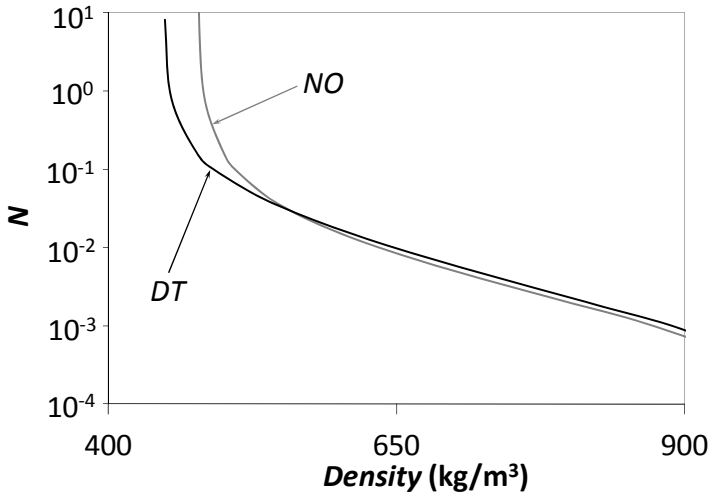

Figure 2.8 – Mean CO_2 density as a function of the gravity number in the cases discussed here for both analytical solutions. *NO* refers to Nordbotten *et al*. (2005) solution and *DT* to Dentz and Tartakovsky (2009a) solution.

2.6. Conclusions

CO_2 compressibility effects may play an important role in determining the size and geometry of the CO_2 plume that will develop when supercritical CO_2 is injected in an aquifer. Here, we have studied the effect that accounting for CO_2 compressibility (density variations and corresponding changes in viscosity) exerts on the shape of the plume computed by two abrupt interface analytical solutions. To this end, we have presented a simple method to correct the initial estimation of the CO_2 density and viscosity and hence use more realistic values. These corrected values give a more accurate prediction for the interface position of the CO_2 plume.

The error associated with neglecting compressibility increases dramatically when gravity forces dominate, which is likely to occur at late injection times. This is relevant because the relative importance of buoyancy forces increases with distance to the injection well. Thus gravity forces will ultimately dominate in most CO_2 sequestration

projects. As such incorporating CO_2 compressibility is critical for determining the interface position.

Comparison with numerical simulations suggests that the solution by Nordbotten *et al*. (2005) gives good predictions when viscous forces dominate, while the Dentz and Tartakovsky (2009a) solution provides good estimates of the CO_2 plume position when gravity forces dominate.

3. Semianalytical Solution for CO_2 Plume Shape and Pressure Evolution during CO_2 Injection in Deep Saline Aquifers

3.1. Introduction

Greenhouse gas emissions to the atmosphere can be reduced through the injection of supercritical carbon dioxide (CO_2) in deep saline aquifers. Under injection conditions, the density of CO_2 (450-900 kg/m^3) is highly dependent on pressure and temperature (Garcia, 2003). This density is sufficiently high for storage purposes, but it is much lower than that of typical resident waters (1020-1200 kg/m^3). Thus, the CO_2 plume tends to float above the resident brine and its thickness progressively increases as CO_2 pressure builds up (Figure 3.1).

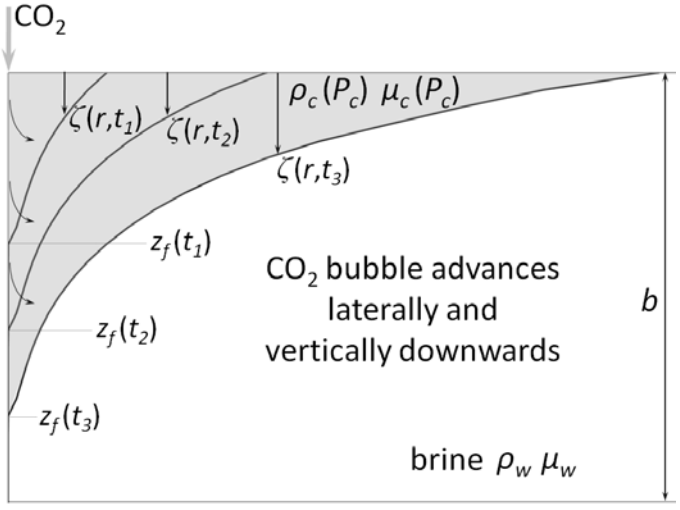

Figure 3.1 – CO_2 injection in a deep saline aquifer. The CO_2 plume thickness at the injection well progressively increases with time as CO_2 pressure builds up. CO_2 density and viscosity are dependent on pressure. Note that CO_2 remains in the upper part of the aquifer because of buoyancy and it is not necessarily injected through the whole thickness of the aquifer.

Supercritical CO_2 is very compressible and determining its density in the reservoir is complicated because of the highly nonlinear and coupled relationships. On the one hand, CO_2 density depends on fluid pressure. On the other hand, fluid pressure buildup during injection depends on CO_2 density, because it determines the volume of displaced brine. Pressure buildup is also controlled by other factors, like the the caprock permeability (Birkholzer *et al*., 2009) or the nature of the aquifer boundaries (Zhou *et al*., 2008). The resident brine can easily migrate out laterally in open aquifers. This limits pressure buildup, but may salinize adjacent freshwater bodies. In contrast, fluid and rock compressibility may limit storage capacity in the presence of low-permeability boundaries (Zhou *et al*., 2008; Mathias *et al*., 2011). Estimating CO_2 density is nontrivial because of the inherent nonlinearities and highly coupled nature of this problem, as evidenced both in situ (Nooner *et al*., 2007) and analytically (Vilarrasa *et al*., 2010a). Errors in CO_2 density estimates will lead to errors in the CO_2 plume volume estimates. For instance, while 3D seismic data gave an average in situ CO_2 density of 530 ± 65 kg/m^3 at the Utsira formation (Sleipner, Norway), the CO_2 density estimates prior to the measurements ranged from 650 to 700 kg/m^3 (Nooner *et al*., 2007). CO_2 density, which is a priori unknown, has to be chosen when using some analytical solutions for determining the CO_2 plume position. Neglecting CO_2 compressibility can lead to errors greater than 50 % in the CO_2 plume position at the top of the aquifer (Vilarrasa *et al*., 2010a).

Existing analytical solutions also assume that the injection takes place uniformly along the whole thickness of the aquifer (Saripalli and McGrail, 2002; Nordbotten *et al*., 2005; Nordbotten and Celia, 2006; Dentz and Tartakovsky, 2009a; Manceau and Rohmer, 2011; Houseworth, 2012). This assumption is also unrealistic. Instead, one should expect that most CO_2 flows through the top portion of the aquifer, where the difference between CO_2 and resident water pressures are largest. In fact, the CO_2 plume may never reach the aquifer bottom (Figure 3.1). Even analytical solutions that predict the CO_2 plume evolution in the post-injection period consider that the CO_2 plume occupies the whole thickness of the aquifer at the end of the injection period (Hesse *et al*., 2007, 2008; Juanes *et al*., 2010). This may underestimate the CO_2 volume in free-phase at late times because the shape of the CO_2 plume at the end of injection affects its post-injection behaviour when capillary trapping is considered (MacMinn and Juanes, 2009).

In addition to the evolution of the CO_2 plume, it is important to understand the evolution of its pressure. Pressure affects the required compression energy, the CO_2 density and the mechanical stability of the caprock (Rutqvist *et al*., 2007; Ferronato *et al*., 2010;

Vilarrasa *et al*., 2010b). Mathias *et al*. (2009) assumed the Nordbotten *et al*. (2005) solution for the CO_2 plume position to calculate a vertical average of the fluid pressure in the aquifer. The same result was obtained by Vilarrasa *et al*. (2010a), who extended the computation to the solution of Dentz and Tartakovsky (2009a) and to calculate fluid pressure at every point of the aquifer. However, fluid pressure obtained from these analytical solutions differs significantly from that of numerical solutions (Vilarrasa *et al*., 2010a).

This paper aims to develop a semianalytical solution that gives the CO_2 plume position and fluid pressure evolution accounting for CO_2 compressibility and buoyancy effects in the injection well. Thus, the extent and the thickness of the CO_2 plume as well as the overpressure can be quickly assessed. We formulate the problem and present the methodology for solving it when the CO_2 mass flow rate or the CO_2 pressure are prescribed at the injection well. Finally, we present an application of this methodology and compare the results with full numerical simulations.

3.2. Problem formulation

Consider the injection of compressible CO_2 through a vertical well in a deep homogeneous horizontal confined brine aquifer. Mass conservation of these two fluids can be expressed as (Bear, 1972)

$$\frac{\partial(\rho_\alpha S_\alpha \varphi)}{\partial t} = -\nabla \cdot (\rho_\alpha \mathbf{q}_\alpha), \ \alpha = c, w, \tag{3.1}$$

where ρ_α is fluid density of the α-phase, S_α is the saturation of the α-phase, φ is porosity, t is time and $\mathbf{q}_\alpha$ is the volumetric flux of the α-phase, which can be either c, the CO_2 rich phase, or w, the aqueous phase.

Momentum conservation is expressed using Darcy's law

$$\mathbf{q}_\alpha = -\frac{k k_{r\alpha}}{\mu_\alpha}(\nabla P_\alpha + \rho_\alpha g \nabla z), \ \alpha = c, w, \tag{3.2}$$

where k is intrinsic permeability, $k_{r\alpha}$ is relative permeability of the α-phase, μ_α is viscosity, P_α is fluid pressure, g is gravity and z is the vertical coordinate (positive upwards).

This two-phase flow is affected by buoyancy effects because CO_2 is lighter than brine. To quantify the relative influence of buoyancy we define a gravity number, N_g, as the ratio of gravity to viscous forces. Gravity forces can be represented by the buoyancy force ($\Delta\rho g$, where $\Delta\rho$ is the difference between fluids density) in Darcy's law, expressed in terms of equivalent head. Viscous dissipation forces correspond to the horizontal pressure gradient, which can be approximated as $(Q_0\mu/(2\pi rbkk_{r\alpha}))$, where Q_0 is the volumetric flow rate, r is radial distance and b is aquifer thickness). However, since CO_2 is compressible, it is more appropriate to express the volumetric flow rate in terms of the mass flow rate, Q_m, as $Q_0 = Q_m/\rho$. Thus, N_g becomes

$$N_g = \frac{2\pi r_{ch} bkk_{rc}\Delta\rho g\rho_{ch}}{\mu_c Q_m}, \tag{3.3}$$

where ρ_{ch} is a characteristic density and r_{ch} is a characteristic distance. Large values of the gravity number ($N_g >> 1$) indicate that buoyancy forces dominate. On the other hand, small gravity numbers ($N_g << 1$) indicate that viscous forces dominate. Notice that buoyancy forces will always dominate far from the injection well, where r_{ch} is sufficiently large, whereas the opposite will be true near the well.

Assuming that fluid density depends only on fluid pressure, the head of the α-phase is defined as (Bear, 1972)

$$h_\alpha = z - z_0 + \frac{1}{g}\int_{P_0}^{P_\alpha} \frac{\mathrm{d}P'_\alpha}{\rho_\alpha(P'_\alpha)}, \tag{3.4}$$

where h_α is head of the α-phase, z_0 is a reference depth and P_0 is the hydrostatic fluid pressure corresponding to depth z_0.

Darcy's law can be expressed in terms of head provided that density is not affected by other variables (i.e. under isothermal conditions) by combining Eq. (3.2) and (3.4)

$$\mathbf{q}_\alpha = -\frac{kk_{r\alpha}}{\mu_\alpha}\rho_\alpha g\nabla h_\alpha . \tag{3.5}$$

When flow rate is prescribed at the injection well, CO_2 will penetrate initially along the top portion of the aquifer because its pressure is not sufficient to displace brine along the entire aquifer thickness. The CO_2 plume advances both laterally and vertically downwards as pressure builds up. CO_2 occupies the portion of the well where CO_2

pressure is higher than brine pressure (Figure 3.1). Brine and CO_2 pressures are related at the porous medium interface via the capillary entry pressure

$$P_c(r_i, z) = P_w(r_i, z) + P_{cc}, \tag{3.6}$$

where P_{cc} is the capillary entry pressure and r_i is the radial position of the interface at depth z.

Neglecting mass transfer across the interface, the problem is defined by the two differential equations in (3.1), one for each phase, which are coupled by the equilibrium equation in (3.6) and by the continuity of flux at the interface

$$\mathbf{q}_c(r_i, z) = \mathbf{q}_w(r_i, z). \tag{3.7}$$

The boundary condition at the injection well is a prescribed CO_2 mass flow rate or CO_2 pressure. As for the outer boundary, we consider an infinite aquifer.

3.3. Semianalytical solution

3.3.1. Radial injection of compressible CO_2

To address the problem of CO_2 injection defined in the previous section we assume that the CO_2 rich phase and the formation brine are separated by a sharp interface. This assumption is reasonable from an analytical perspective in the context of CO_2 sequestration (Nordbotten *et al*., 2005; Dentz and Tartakovsky, 2009a, 2009b; Lu *et al*., 2009). Capillary pressure is considered at the interface between the CO_2 rich phase and the formation brine (Eq. (3.6)). Thus, there is a jump in fluid pressure at the interface equal to the entry pressure. CO_2 dissolution into the brine, which may induce density-driven convective cells (Lindeberg and Wessel-Berg, 1997; Riaz *et al*., 2006; Hidalgo and Carrera, 2009; Pau *et al*., 2010), is not considered.

We solve the problem by vertically discretizing the aquifer into n layers of thickness $d = b/n$ (Figure 3.2). The time evolution of the problem is solved using discrete time steps to overcome nonlinearities and coupling difficulties. The interface advances laterally in the layers that contain CO_2, but also moves vertically downwards as fluid pressure builds up. CO_2 at the bottom of the CO_2 plume may fill the thickness of a layer only partially. Once the CO_2 plume reaches a thickness equal to md, where m is the number of layers filled with CO_2, the following layer $m+1$, previously devoid of CO_2,

begins to fill up with CO_2. The part occupied by CO_2 in this new layer has a thickness equal to $b_c - md$, where b_c is the CO_2 plume thickness at the well (Figure 3.2).

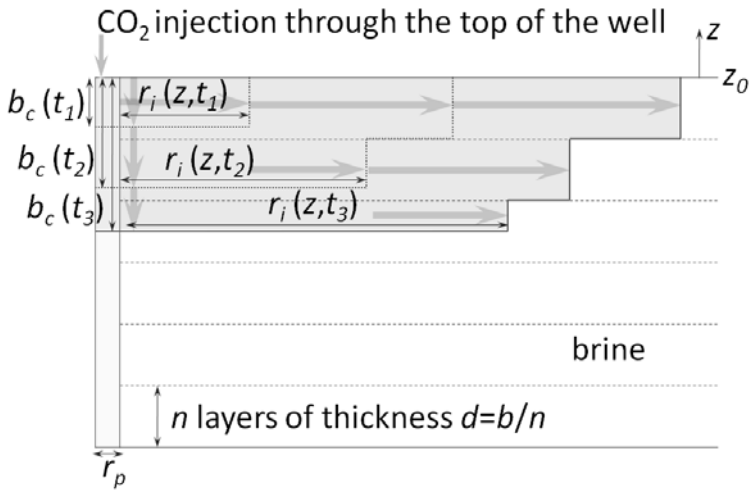

Figure 3.2 – Schematic representation of CO_2 injection evolution taking into account that CO_2 first enters through the top of the aquifer because of buoyancy. The aquifer is divided into n layers through which CO_2 advances laterally and vertically downwards. The CO_2 plume reaches, at every time step, the depth at which CO_2 pressure equals brine pressure plus the capillary entry pressure.

To calculate the CO_2 plume thickness in the injection well, we assume hydrostatic conditions in it,

$$\frac{\mathrm{d}P_\alpha}{\mathrm{d}z} = -g\rho_\alpha\left(P_\alpha\right),\ \alpha = c, w\,. \tag{3.8}$$

To calculate the lateral advance of CO_2 in each layer, we assume that the hydraulic response within the CO_2 plume is much shorter than transport of the front. Therefore, we consider a quasi-steady (sequence of steady-states) description of the moving fronts in Eq. (3.1). Hence, the left-hand side of Eq. (3.1) cancels. Additionally, we make the Dupuit approximation of horizontal flow. Furthermore, the density of the CO_2 phase will vary in space because so will the CO_2 pressure and because of the high compressibility of CO_2. Therefore, conservation should not be expressed in terms of volumetric fluxes, but mass fluxes. The total mass flow rate, per unit aquifer thickness, in a radial injection varies with depth but is constant at a given z within each phase

$$J_\alpha = 2\pi r \rho_\alpha q_{r\alpha}\,, \tag{3.9}$$

where J_α is the mass flow rate per unit thickness of α-phase and $q_{r\alpha}$ is the horizontal component of the volumetric flux of α-phase. This mass flow rate per unit thickness will vary from layer to layer. At the interface in each layer, we impose continuity of flux in the radial direction

$$q_{rc}(r_j, z) = q_{rw}(r_j, z), \tag{3.10}$$

where r_j is the radius of the interface in layer j.

Since we adopt a sharp interface approximation, the saturation in the CO_2 rich phase is taken as constant. Thus, the interface position advances as

$$\frac{dr_j}{dt} = \frac{q_{r\alpha}(r_j)}{\varphi(1 - S_{rw})}, \tag{3.11}$$

where S_{rw} is the residual degree of saturation of brine.

To eliminate the complexities associated to nonlinearity, we define the following potential to formulate the problem assuming that relative permeability and fluid density are solely a function of fluid pressure

$$\Phi_\alpha(h_\alpha) = \int_0^{h_\alpha} 2\pi g k k_{r\alpha}(h'_\alpha) \frac{\left(\rho^*_\alpha(h'_\alpha)\right)^2}{\mu_\alpha} \mathrm{d}h'_\alpha , \tag{3.12}$$

where $\rho^*_\alpha(h'_\alpha) = \rho^*_\alpha(P_\alpha(h'_\alpha))$.

Combining Eq. (3.5), (3.9) and (3.12), flow rate in the layer becomes

$$r \frac{\mathrm{d}\Phi_\alpha}{\mathrm{d}r} = -J_\alpha . \tag{3.13}$$

Though we make the Dupuit approximation of horizontal flow within a layer, we acknowledge the vertical CO_2 leakage between layers. Acknowledging that flow towards the aquifer top is largely buoyancy driven, we impose that the vertical mass flow rates between layers occur punctually, for simplicity. The distance at which the vertical flow rates are injected to the adjacent layer depends on the gravity number computed in the vicinity of the injection well (Eq. (3.3)). This is because vertical flow rates are expected to occur when gravity forces dominate, i.e. large gravity numbers. Then, vertical flow rates will occur close to the injection well for large gravity numbers. On the other hand, vertical flow rates will occur far from the injection well for small gravity numbers computed close to the injection well. Therefore, the distance at which

the vertical flow rates occur is inversely proportional to the gravity number. The vertical mass flow rate of a layer to its adjacent one is given by

$$J_{cz,j} = \int_{r_p}^{\bar{r}_j} 2\pi\rho_c q_{zc}\,\mathrm{d}r\,, \tag{3.14}$$

where r_p is the radius of the well and q_{zc} is the vertical component of the volumetric CO_2 flux. We will inject this flow rate at a radius $\bar{r}_j = \min\left(r_{j+1}, b/(2N_g)\right)$. The term $b/(2N_g)$ is somewhat arbitrary, and can be chosen case specifically. For simplicity, we have adopted r_{j+1} as $\bar{r}_j$. Introducing Eq. (3.5) into Eq. (3.14) and assuming that the CO_2 head varies linearly with the logarithm of distance to the well, after some algebra, yields

$$J_{cz,j} = \frac{2\pi k k_{rc}\rho_c^2 g}{\mu_c \Delta z_j}\left(u_j - u_{j+1}\right)\left(r_{j+1} - r_p - r_{j+1}\ln\frac{r_{j+1}}{r_p}\right), \tag{3.15}$$

where u_j is the logarithmic slope of the CO_2 head in layer j, Δz_j is the thickness of the layer j and CO_2 density is evaluated at the point of the vertical flow rate injection. Note that the subscript of the layers increases with depth, i.e. layer j is placed above layer $j+1$.

The integration of Eq. (3.13), accounting for the fact that now J_c is a function of the radial distance due to the vertical flow rates, yields the solution of the problem

$$\Phi_{w,j} = \Phi_R + J_{w,j}\ln\left(\frac{R}{r}\right), \qquad r \geq r_j \tag{3.16a}$$

$$\Phi_{c,j} = \Phi_j + \left(J_{c,j} + J_{cz,j+1}\right)\ln\left(\frac{r_j}{r}\right), \qquad r_{j+1} < r < r_j \tag{3.16b}$$

$$\Phi_{c,j} = \Phi_j + J_{c,j}\ln\left(\frac{r_j}{r}\right) + J_{cz,j+1}\ln\left(\frac{r_j}{r_{j+1}}\right), \qquad r < r_{j+1} \tag{3.16c}$$

where Φ_R is the potential at the radius of influence, R is the radius of influence, the subscript after the comma indicates the layer (e.g. , j indicates layer j) and Φ_j is the potential at the interface in layer j . Φ_R is known and constant because it refers to the initial fluid pressure in the aquifer. Φ_j can be determined by evaluating Eq. (3.16a) at the interface. The radius of influence corresponds to the distance affected by the pressure buildup cone caused by injection and grows with the square root of time as

$$R = \sqrt{\frac{2.25k\rho_w gt}{\mu_w S_s}}, \tag{3.17}$$

where S_s is the specific storage coefficient.

The CO_2 mass flow rate at the injection well for layer j can be determined from Eq. (3.16c) as

$$J_{c,j} = \frac{\Phi_{c,j}(r_p) - \Phi_j - J_{cz,j+1}\ln(r_j/r_{j+1})}{\ln(r_j/r_p)}. \tag{3.18}$$

This CO_2 mass flow rate will change with time as the CO_2 plume grows. The evolution of the CO_2 plume is calculated using a time stepping algorithm. Integrating Eq. (3.11) and using Eq. (3.9) yields the interface position for a given time step

$$r_j^{l+1}(z) = \sqrt{\left(r_j^l\right)^2 + \frac{J_{c,j}^l(r_j)\Delta t^{l+1}}{\pi\varphi(1-S_{rw})\rho_{ci,j}^l}}, \tag{3.19}$$

where the superscript l denotes the time step, Δt is increment of time between step l and step $l+1$ and $\rho_{ci,j}$ is the CO_2 density at the interface in layer j.

The volumetric flow rate of brine, Q_w, at a radial distance r from the well can be calculated once the interface position is known. Due to the continuity of fluxes at the interface, we obtain

$$Q_w(r) = \int_{z_f}^{z_0-\zeta(r)} \frac{J_c(r)}{\rho_c(r)}\,\mathrm{d}z, \tag{3.20}$$

where z_f is the depth of the bottom of the CO_2 plume and ζ is the vertical position of the CO_2 plume from the top of the aquifer.

The volume of displaced brine at radius r is equal to the volume of injected CO_2. The flow rate of brine is driven by the overpressure produced by the injected CO_2, which is assumed to be distributed through the portion of the aquifer thickness occupied by the formation brine

$$Q_w(r) = -\int_{z_0-b}^{z_0-\zeta(r)} 2\pi r \frac{k}{\mu_w}\frac{\partial P_w}{\partial r}\,\mathrm{d}z. \tag{3.21}$$

Integrating Eq. (3.21) yields the following expression for brine pressure

$$P_w - P_0 = \frac{\mu_w Q_w(r)}{2\pi k\left(b - \zeta(r)\right)} \ln \frac{R}{r} . \tag{3.22}$$

The problem accepts two possible boundary conditions at the injection well. Either a prescribed CO_2 mass flow rate or a prescribed CO_2 pressure can be imposed.

3.3.2. Prescribed CO_2 mass flow rate

When injecting a prescribed CO_2 mass flow rate, the CO_2 plume advances both laterally and vertically downwards as CO_2 pressure builds up. Since this problem presents two unknowns at every time step, i.e. the CO_2 head at the well and the thickness of the CO_2 plume at the well, two conditions are needed. First, hydrostatic conditions are assumed in the well (Eq. (3.8)) accounting for the capillary entry pressure at the CO_2-brine interface (Eq. (3.6)). And second, mass balance must be satisfied. The mass inlet at a given time step corresponds to the mass flow rate multiplied by the time increment. This mass is distributed through the layers containing CO_2 proportionally to the mass flow rate per unit thickness and the thickness of each layer. Furthermore, the mass that occupies the volume corresponding to the increment of the plume thickness in each time step has to be accounted for, resulting in

$$Q_m = \sum_{j=1}^{m} J_{c,j} \Delta z_j + \overline{\rho}_c \pi r_{if}^2 \varphi \left(1 - S_{rw}\right) \frac{\Delta z_f}{\Delta t} , \tag{3.23}$$

where Q_m is the prescribed CO_2 mass flow rate, m is the total number of layers in which CO_2 is present, $\overline{\rho}_c$ is the mean CO_2 density in the layer that coincides with the bottom of the CO_2 plume, r_{if} is the interface position at the bottom of the CO_2 plume and Δz_f is the increment of the CO_2 plume thickness at the well at a given time step.

3.3.3. Prescribed CO_2 pressure

Since the head at the well is known when imposing the CO_2 pressure, there is only one unknown: the thickness of the CO_2 plume at the well. Hence, imposing hydrostatic conditions in the well (Eq. (3.8)) and that the thickness of the CO_2 plume in the well is such that the CO_2 pressure equals the brine pressure plus the capillary entry pressure (Eq. (3.6)) allows solving the problem.

3.4. Algorithm

The evolution of the position of the CO_2 plume is calculated using a time stepping algorithm. The process is very similar for the two possible injection boundary conditions and is repeated for each time step (Figure 3.3). The procedure has to be initialized, using a small time increment, as follows

- The CO_2 plume is assumed to grow slightly in the top layer, i.e. the interface position advances laterally a fraction of the well radius and the thickness of the CO_2 plume is a fraction of d .
- The volumetric flow rate is assumed equal to the mass flow rate divided by density at the reference CO_2 pressure.

These two assumptions allow initializing the overpressure (using Eq. (3.22) and the volumetric flow rate), the potential at the interface (using Eq. (3.12)), the depth that reaches the CO_2 plume, the head at the injection well and the potential at the well (using Eq. (3.12)). No vertical flow rates exist in this initialization. The time stepping algorithm can then be used after obtaining these data. It is as follows

1) Determine the vertical CO_2 mass flow rate (Eq. (3.15)) and the horizontal CO_2 mass flow rate in each layer evaluating Eq. (3.18) at the well. We use the potential at the interface and at the well and the interface position evaluated at the previous time step.
2) Calculate the new interface position in every layer using Eq. (3.19). The CO_2 mass flow rate is the one calculated in step 1 and the CO_2 density at the interface is the one evaluated at the previous time step.
3) Calculate the potential at the interface (Eq. (3.12)), using Eq. (3.20) to calculate the volumetric flow rate and Eq. (3.22) to calculate the brine pressure, and Eq. (3.6) to calculate the CO_2 pressure at the interface.

4.1) Impose a prescribed CO_2 mass flow rate: solve the system of two equations (Eqs. (3.23) and (3.8) accounting for the capillary entry pressure in (3.6)) and determine the CO_2 head at the well and the thickness of the CO_2 plume at the well.

4.2) Impose a prescribed CO_2 pressure: the head at the well can be determined by using Eq. (3.4) and the thickness of the CO_2 plume at the well can be calculated by imposing Eq. (3.8) accounting for the capillary entry pressure in (3.6).

5) Based on the head at the well calculated in step 4, compute the potential at the well using Eq. (3.12).

These five steps are repeated, applying a time increment after every loop, until CO_2 injection is completed.

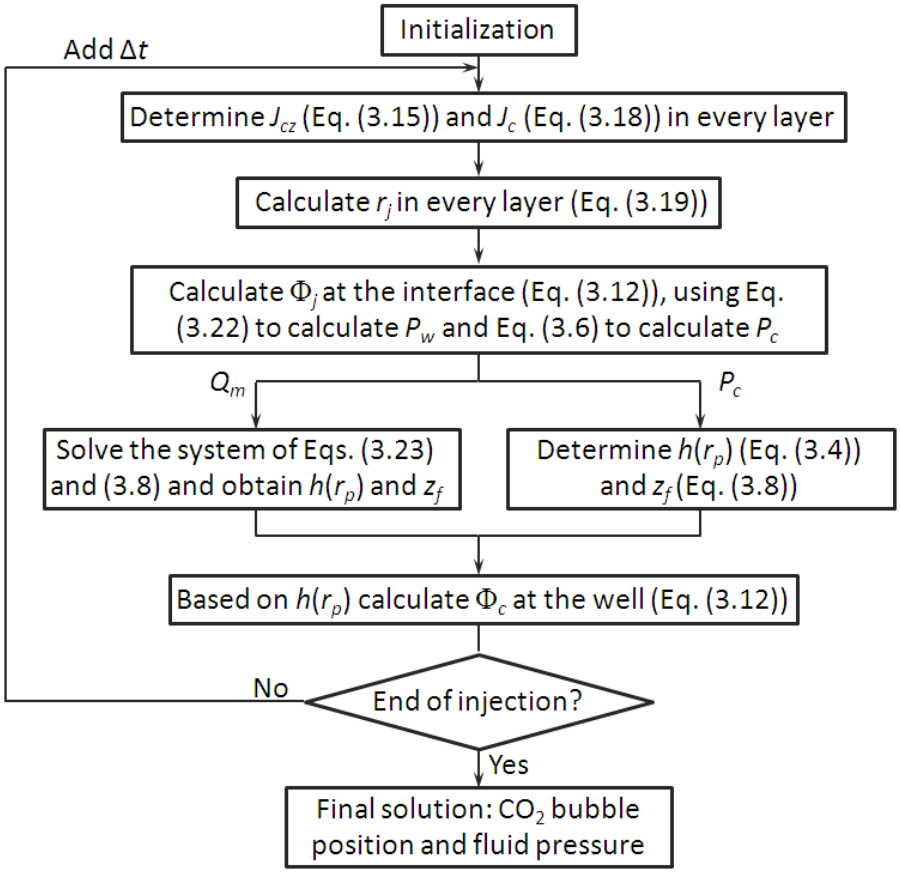

Figure 3.3 – Time stepping algorithm to calculate the position of the CO_2 plume and the fluid pressure.

3.5. Application

3.5.1. Spreadsheet programming

In order to evaluate this methodology, we programmed it in a spreadsheet that can be downloaded from GHS (2012). We programmed it this way to highlight ease of implementation and use by non-expert programmers. This spreadsheet considers 25 layers, a prescribed mass flow rate, constant properties of the brine (density and viscosity), constant CO_2 viscosity and the CO_2 density is defined to vary linearly with CO_2 pressure

$$\rho_c = \rho_0 + \beta\left(P_c - P_0\right), \tag{3.24}$$

where ρ_0 is the reference density for the reference pressure P_0 and β is CO_2 compressibility. These values were taken from the data tables given by Span and Wagner (1996).

With this linear approximation of the CO_2 density, the potential for the CO_2 can be obtained by integrating Eq. (3.12), which yields (see Appendix III)

$$\Phi_c = \frac{\pi k \rho_0^2}{\mu_c \beta} e^{-2g\beta(z-z_0)}\left(e^{2g\beta h_c} - 1\right). \tag{3.25}$$

Furthermore, CO_2 pressure can be expressed as a function of the potential (Appendix III)

$$P_c - P_0 = \sqrt{\frac{\mu_c}{\pi k \beta}\Phi_c + \frac{\rho_0^2}{\beta^2} e^{-2g\beta(z-z_0)}} - \frac{\rho_0}{\beta}. \tag{3.26}$$

Note that CO_2 overpressure varies with the square root of the logarithm of the distance to the injection well (see the form of the potential Φ_c in Eq. (3.16b,c)).

The solution of the system of two equations (Eqs. (3.8) and (3.23)) for finding the CO_2 head and the thickness of the CO_2 plume at the well is shown in Appendix IV. The mean density appearing in Eq. (3.23) is calculated in Appendix V.

3.5.2. Model setup

We represent a 100 m thick saline aquifer whose top is located at a depth of 1000 m. The aquifer is assumed to be infinite-acting, homogeneous and isotropic. The permeability of the aquifer is either 10^{-12} or 10^{-13} m^2, its porosity is 0.1 and the rock compressibility is $1.2 \cdot 10^{-10}$ Pa^{-1}. The temperature is assumed to be constant and equal to 320 K. The density of brine is 1087.5 kg/m^3, its viscosity is 0.6 mPa·s and its compressibility is $4.5 \cdot 10^{-10}$ Pa^{-1}. Thus, the specific storage coefficient yields a value of $1.76 \cdot 10^{-6}$ m^{-1}. The reference CO_2 density ρ_0, corresponding to the reference pressure P_0=10 MPa (hydrostatic pressure at the top of the aquifer), is 448.28 kg/m^3 and its compressibility β is $5.56 \cdot 10^{-5}$ $kg/m^3 \cdot Pa^{-1}$ (Span and Wagner, 1996). β is the product of the actual CO_2 compressibility and a density. The actual CO_2 compressibility at the pressure and temperature of the aquifer is $1.48 \cdot 10^{-7}$ Pa^{-1}. Note that CO_2 compressibility, for the range of pressure and temperature of this study, is three orders

of magnitude higher than that of brine. The CO_2 viscosity is calculated using the expression proposed by Altunin and Sakhabetdinov (1972). Though constant, CO_2 viscosity is case specific and depends on the overpressure, so that a representative value can be adopted according to the mean CO_2 density. The entry pressure equals 0.02 MPa and the residual degree of saturation of brine is 0.025. The injected mass flow rate is 1.0 Mt/yr. An injection ramp is used to progressively increase the mass flow rate from zero to the desired mass flow rate. Doing so, the increments in the CO_2 plume thickness are small. This injection ramp lasts less than 50 s, so its effect can be considered as negligible for practical purposes.

The finite element numerical code CODE_BRIGHT (Olivella *et al*., 1994; 1996), extended for CO_2 sequestration (Appendix II), has been used to validate the results of this semianalytical solution with those of numerical results. The aquifer is represented by an axisymmetric model, with a radius of 100 km, in which CO_2 is injected at the top of the injection well. The radius of the injection well is 0.5 m. The well is modelled assigning a porosity equal to 1 and a high permeability. The grid is structured and has 25 elements in the vertical coordinate in order to represent the 25 layers adopted in the application of the semianalytical solution. We used a van Genuchten retention curve (van Genuchten, 1980), with an entry pressure of 0.02 MPa and a shape parameter of 0.8. The relative permeability functions, for both the CO_2 and the brine, are linear with the degree of saturation of each phase. These retention curve and relative permeability functions produce a CO_2 plume with an almost constant CO_2 saturation and a narrow capillary fringe. Thus, the numerical solutions are close to the assumption of the abrupt interface approximation assumed for the semianalytical solution. The CO_2 saturation 90 % isoline has been chosen to represent the position of the CO_2-brine interface.

3.5.3. Validation of the semianalytical solution

We compare the results of the semianalytical solution with those of the numerical solution. Additionally, the analytical solutions of Nordbotten *et al*. (2005) and Dentz and Tartakovsky (2009a) using the method proposed by Vilarrasa *et al*. (2010a) to account for CO_2 compressibility are presented for comparative purposes. These analytical solutions inject CO_2 uniformly in the whole thickness of the aquifer, which may not be realistic.

Figure 3.4 displays the CO_2 plume position for the analytical, semianalytical and numerical solutions after 1 yr of injecting 1 Mt/yr of CO_2 for two aquifer permeabilities.

We consider a case with high permeability (k =10^{-12} m^2) in which gravity forces dominate and another case with low permeability (k =10^{-13} m^2) in which viscous forces dominate. The semianalytical solution compares well with the numerical solution in both cases. The CO_2 plume occupies only the top portion of the aquifer when gravity forces dominate (CO_2 is injected into the aquifer through the top 32 m) (Figure 3.4a). On the other hand, the CO_2 plume reaches the bottom of the aquifer when viscous forces dominate (Figure 3.4b). The Nordbotten *et al*. (2005) solution gives a better approximation when viscous forces dominate, while the Dentz and Tartakovsky (2009a) solution predicts a better CO_2 plume position when gravity forces dominate. However, both analytical solutions differ from the numerical solution at the bottom of the CO_2 plume due to the fact that they consider a uniform injection along the whole thickness of the aquifer.

Figure 3.5 compares fluid overpressure at the top of the aquifer as a function of the distance to the injection well resulting from the semianalytical, numerical and analytical solutions when injecting 1.0 Mt/yr in an aquifer with a permeability of 10^{-13} m^2. Fluid overpressure obtained from the semianalytical solution compares well with that of the numerical solution, presenting the same slope in the region occupied by CO_2 close to the injection well. The pressure drop increases sharply at the distance where CO_2 from the second layer is injected in the top layer. This is in contrast with the numerical solution, where the gradient increases smoothly. As a result, our solution is somewhat more abrupt than the numerical solution near the interface. Existing analytical solutions, i.e. those of Nordbotten *et al*. (2005) and Dentz and Tartakovsky (2009a), fail to give good fluid pressure predictions. First, they predict a lower brine overpressure because they underestimate the volumetric flow rate of brine. This is because CO_2 is injected along the whole thickness of the aquifer and since CO_2 density increases with depth, the mean CO_2 density becomes higher than in the semianalytical and numerical solutions. Additionally, the slopes of fluid pressure inside the CO_2 plume are lower than that of numerical simulations. In contrast, the slope of the semianalytical solution is the same as that of the numerical solution close to the injection well in the region occupied by CO_2. Hence, it can be concluded from this semianalytical solution that while brine overpressure is proportional to the logarithm of distance from the injection well, CO_2 overpressure is proportional to the square root of the logarithm of the distance from the injection well (recall Eq. (3.26)).

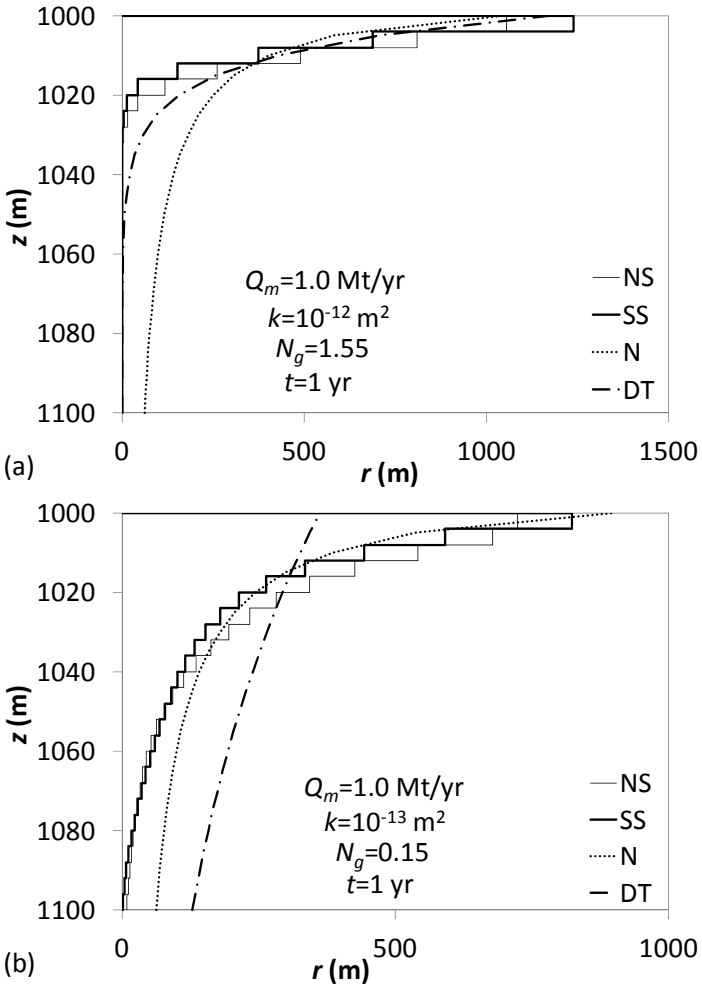

Figure 3.4 – Comparison of the CO_2 plume position between semianalytical (SS) and numerical solution (NS) after 1 yr of injection of 1 Mt/yr, and permeabilities, k, (a) k =10^{-12} m^2 and (b) k =10^{-13} m^2. Additionally, the analytical solutions of Nordbotten *et al*. (2005) (N) and Dentz and Tartakovsky (2009a) (DT) after using the method of Vilarrasa *et al*. (2010a) to account for CO_2 compressibility are presented for comparison. Note that these analytical solutions inject CO_2 uniformly along the whole thickness of the aquifer.

Figure 3.6 displays the evolution of the overpressure at the injection well when injecting 1.0 Mt/yr in an aquifer with a permeability of 10^{-13} m^2. While the overpressure predicted by the analytical solutions of Nordbotten *et al*. (2005) and Dentz and Tartakovsky (2009a) increases continuously, fluid overpressure decreases after reaching a maximum at the beginning of injection for the semianalytical and numerical solutions. Mukhopadhyay *et al*. (2012) found that overpressure increases continuously when injecting CO_2 in depleted gas reservoirs, whose fluid pressure is significantly below hydrostatic conditions. However, a pressure drop after the initial pressure build up was observed in situ in the Ketsin test site, Germany (Henninges *et al*., 2011) and

numerically by Vilarrasa *et al*. (2010b), who argued that pressure drops because the overpressure that occurs in the capillary fringe due to relative permeability reduction is distributed over a larger area as the CO_2 plume increases and because the viscosity of the CO_2 is much lower than that of the brine.

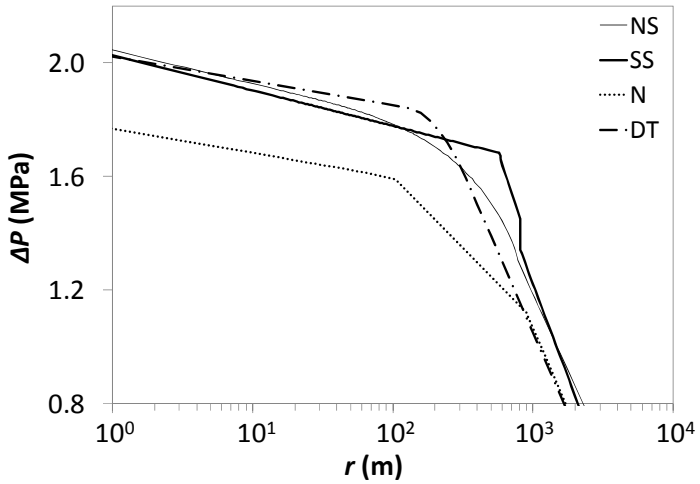

Figure 3.5 – Comparison of the fluid overpressure at the top of the aquifer between analytical, semianalytical (SS) and numerical solutions (NS) after 1 yr injecting 1.0 Mt/yr in an aquifer with a permeability of 10^{-13} m^2. The analytical solutions of Nordbotten *et al*. (2005) (N) and Dentz and Tartakovsky (2009a) (DT) after using the method of Vilarrasa *et al*. (2010a) to account for CO_2 compressibility are presented for comparison. The first change in slope beginning from the right hand side of the figure indicates the CO_2-brine interface position for each solution.

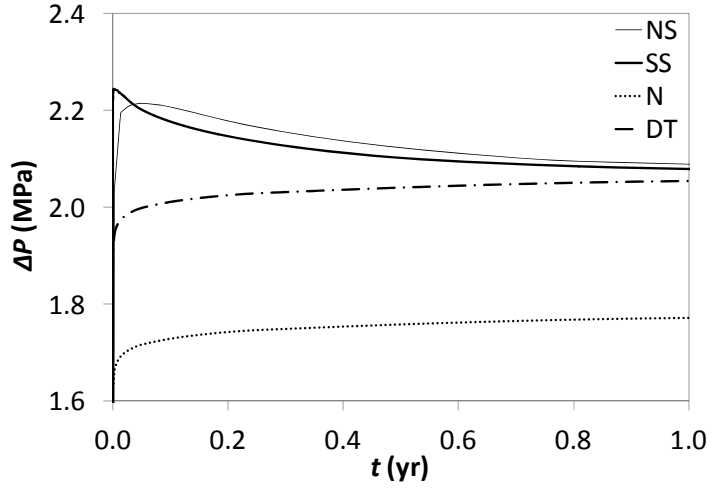

Figure 3.6 – Comparison of the time evolution of the injection pressure at the top of the aquifer between analytical, semianalytical (SS) and numerical solutions (NS) when injecting 1.0 Mt/yr in an aquifer with a permeability of 10^{-13} m^2. The analytical solutions of Nordbotten *et al*. (2005) (N) and Dentz and Tartakovsky (2009a) (DT) after using the method of Vilarrasa *et al*. (2010a) to account for CO_2 compressibility are presented for comparison.

3.5.4. CO_2 plume thickness

Figure 3.7 shows the CO_2 plume position evolution for several injection times given by the semianalytical solution when injecting 1.0 Mt/yr in an aquifer with a permeability of 10^{-13} m^2. CO_2 advances laterally and vertically downwards as pressure builds up. Note that the CO_2 plume advances preferentially through the top of the aquifer for increasing injection times. This is because gravity forces become dominant as CO_2 flows away from the injection well. Note that in this case the CO_2 plume reaches the aquifer bottom for an injection time longer than 30 days (actually, it occurs after 162.6 days of injection). However, the CO_2 plume would not reach the bottom of the aquifer in a more permeable aquifer, like the one presented in Figure 3.4a.

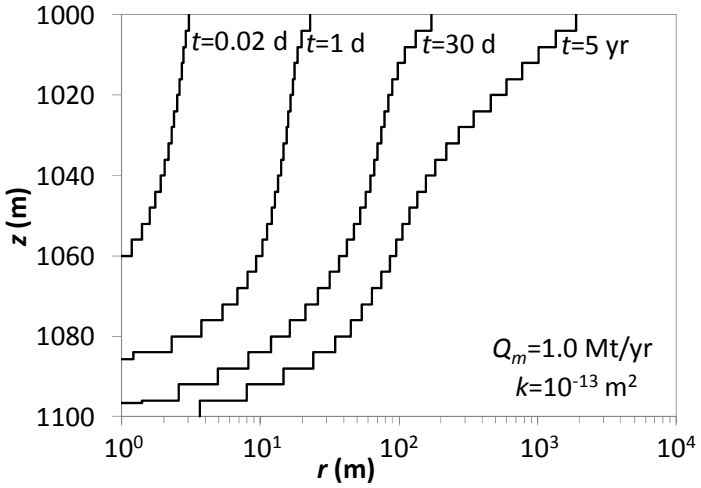

Figure 3.7 – CO_2 plume evolution given by the semianalytical solution for several injection times when injecting 1.0 Mt/yr in a 100 m thick aquifer with a permeability of 10^{-13} m^2. Note that the thickness of the CO_2 plume progressively increases with injection time.

Figure 3.8 displays the CO_2 plume thickness at the well after 1 yr of injection as a function of the gravity number computed at 1 m from the injection well (Eq (3.3)) for several aquifer permeabilities. The curves are obtained by varying the mass flow rate. The logarithm of the CO_2 plume thickness decreases linearly with the logarithm of the gravity number, presenting a slope of -0.5. The CO_2 plume is thinner than the aquifer thickness for high gravity numbers (buoyancy forces dominate). In contrast, it reaches the bottom of the aquifer for gravity numbers lower than 0.15 (viscous forces dominate). The effect of the permeability is small, but not negligible because permeability affects fluid overpressure and thus CO_2 density. These curves are useful for quickly estimating the CO_2 thickness at the well of a CO_2 injection project.

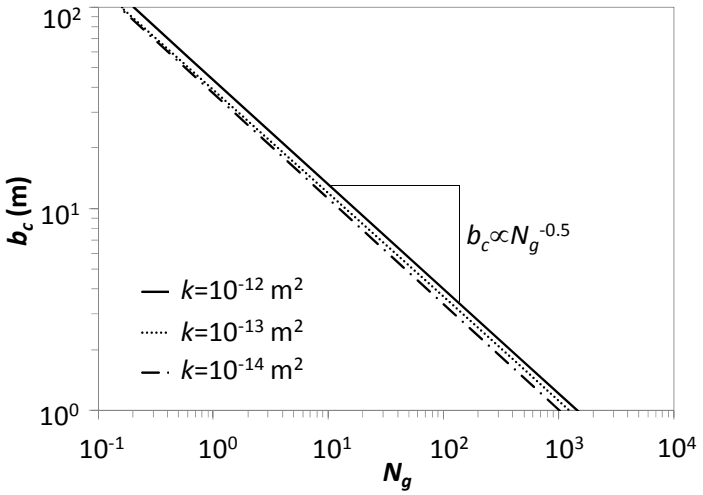

Figure 3.8 – CO_2 plume thickness at the injection well after 1 yr of injection as a function of the gravity number for several aquifer permeabilities. Note that the logarithm of the CO_2 plume thickness decreases linearly with the logarithm of the gravity number.

3.6. Discussion and conclusions

Both CO_2 plume position and fluid pressure obtained from the proposed semianalytical solution are comparable to those given by numerical simulations. Analytical solutions give acceptable results of the CO_2 plume position depending on the gravity number (Vilarrasa *et al*., 2010a). However, the semianalytical solution gives good estimates regardless of the gravity number. Furthermore, the approximation of the semianalytical solution has a clear advantage in front of numerical solutions in terms of the time required for calculation. One should bear in mind that simulating CO_2 injection through the well instead of injecting it uniformly along the whole thickness of the aquifer implies a high computational cost. Note that, in contrast, the semianalytical solution gives immediate results. Furthermore, analytical and semianalytical solutions can be coupled with numerical models in order to speed up their calculations (Celia and Nordbotten, 2009; McDermott *et al*., 2011).

This solution facilitates quick evaluations of the lateral extension and thickness of the CO_2 plume for a given injection time. The calculation of the CO_2 plume thickness is very innovative because it is commonly accepted that the CO_2 plume occupies the whole aquifer thickness. The CO_2 plume thickness is a function of the gravity number (see Figure 3.8). This knowledge can be useful to support decision making concerning the operation of CO_2 injection projects. Additionally, this solution can be helpful in

designing and interpreting CO_2 injection tests in pilot projects. In this context, it is important to bear in mind that, from a storage point of view, it is desirable to inject over the whole aquifer thickness to maximize the use of pore space. As we have seen, this goal is limited by buoyancy, which dominates far from the injection well. Still, even near the well, injecting over a partial thickness may be profitable during early stages because it promotes CO_2 dissolution into the brine, which in turn may cause CO_2 dissolution and stimulation quite far from the injection well. For such goal, our solution, generalized for varying permeability, would be extremely useful.

Finally, the slope of CO_2 pressure as a function of the logarithm of distance from the well calculated with the semianalytical solution is the same as that of the numerical solution. In the semianalytical solution, the CO_2 overpressure varies with the square root of the logarithm of the distance to the injection well (Eq. (3.26)). This is interesting because this variation with distance to the well differs from those of existing analytical solutions. Additionally, the semianalytical solution reproduces a CO_2 injection pressure evolution similar to the one observed in numerical solutions and at the field, i.e. fluid pressure drops after an initial abrupt fluid pressure buildup. This behaviour, which appears naturally in this semianalytical solution, is not reflected by other existing analytical solutions.

4. Coupled Hydromechanical Modeling of CO_2 Sequestration in Deep Saline Aquifers

4.1. Introduction

Carbon dioxide (CO_2) sequestration in deep saline aquifers is considered a promising mitigation option for the reduction of CO_2 emissions to the atmosphere. Injecting CO_2 into aquifers at depths greater than 800 m brings CO_2 to a supercritical state where its density is large enough to ensure an efficient use of pore space (Hitchon *et al*., 1999). Although the density of CO_2 can reach values as high as 900 kg/m^3, it will always be lighter than the resident brine. Consequently, it will flow along the top of the aquifer because of buoyancy. Thus, suitable aquifers should be capped by a low-permeability rock to avoid CO_2 migration to upper aquifers and the surface. Caprock discontinuities, such as fractured zones, may favor upwards CO_2 migration. Additionally, CO_2 injection can result in significant pressure buildup, which affects the stress field and may induce large deformations. These can eventually damage the caprock and open up new flow paths. These interactions between fluid flow and rock mechanics are known as hydromechanical coupling.

Hydromechanical (HM) processes generally play an important role in geological media, and in particular during CO_2 injection into deep saline aquifers. These formations are usually fluid-saturated fractured rock masses. Therefore, they can deform either as a result of changes in external loads or internal pore pressures. This can be explained with direct and indirect HM coupling mechanisms (Rutqvist and Stephansson, 2003). Direct HM coupling consists of two phenomena: a solid-to-fluid coupling in which a variation in the applied load induces a change in porosity and thus in fluid pressure or mass; and a fluid-to-solid coupling that takes place when a change in fluid pressure or fluid mass causes a variation in the volume of the geological media. On the other hand,

indirect HM coupling refers to changes in hydraulic or mechanical properties in response to strain.

In practice, using HM couplings allows us to determine conditions under which mechanical failure (shear failure or hydraulic fracture) could occur so that injection pressures can be limited below a fracturing threshold. Rutqvist *et al*. (2008) found that shear failure usually occurs at a lower injection pressure than hydro fracturing. When horizontal stress is greater than vertical stress ($\sigma_h > \sigma_v$), shear failure will occur preferentially in gently dipping fractures, without damage to the upper part of the caprock. However, when vertical stress is greater than horizontal stress ($\sigma_h < \sigma_v$) the propagation of fractures is most likely to occur in the form of steeply dipping fractures which could penetrate the entire caprock.

Existing simplified analytical solutions for determining the maximum sustainable pressure often predict incorrect values (Rutqvist *et al*., 2007, Vidal-Gilbert *et al*., 2008), suggesting that the fully coupled problem should be solved. Nonetheless, the majority of CO_2 injection simulations only model the multiphase flow problem (e.g. Doughty and Pruess, 2004; Ide *et al*., 2007), without mechanical coupling. Some of these numerical studies reproduce pilot CO_2 injection tests (Doughty *et al*., 2006; Ghomian *et al*., 2008). Given that small quantities of CO_2 are usually injected in pilot tests, rock stability is not a concern. The computational burden is much higher using the hydromechanical coupling than the hydraulic problem (Tran *et al*., 2004). Nevertheless, coupling strategies are available to avoid the full coupling (i.e. solving the flow and mechanical problem together), such as explicit or iterative coupling or, even, decoupling. These schemes allow reducing the computational burden, but at the expense of some loss of accuracy (Mainguy and Longuemare, 2002; Settari and Walters, 1999).

The vast majority of rocks present very small yield stresses (Cristescu, 1989). As pressure buildup caused by CO_2 injection will affect a large extension of the aquifer and caprock over several decades, irreversible strains are expected to occur. However, poroelasticity is usually adopted to resolve the mechanical problem (Rutqvist *et al*., 2008, Vidal-Gilbert *et al*., 2008). Although this approach gives a good approximation, an elasto-plastic constitutive model provides more precise results (Settari and Walters, 1999).

Strains are induced by fluid pressure evolution, which depends on the hydraulic

boundary conditions. Aquifers are sometimes assumed to be infinite (Rutqvist *et al*., 2008; van der Meer and van Wees, 2006). In modeling practice, this means that the boundary is placed far enough to ensure that it does not affect fluid flow. In fact, deep saline aquifers for CO_2 sequestration may extend tens or even hundreds of kilometers (McPherson and Cole, 2000; Zhang *et al*., 2009). However, CO_2 sequestration projects will span several decades. Therefore, the radius of influence ($R = \sqrt{2.25k\rho_w gt/(\mu_w S_s)}$, where k is the intrinsic permeability, ρ_w is water density, g is gravity, t is time, μ_w is water viscosity and S_s is the specific storage coefficient of the aquifer) propagates over large distances, reaching the boundaries much earlier than the end of operations (Birkholzer *et al*., 2009). In such cases, the infinite acting aquifer assumption may not be appropriate and the nature of the boundary may have to be addressed. Aquifers can be classified as open and semi-closed, depending on the nature of the boundaries. Open aquifers can be modeled with a constant head boundary condition (Lucier and Zoback, 2008), and semi-closed aquifers with a leakage coefficient. In open aquifers brine could escape and salinize fresh water bodies (Birkholzer and Zhou, 2009). In closed and semi-closed aquifers, the CO_2 storage capacity is basically controlled by rock and fluid compressibility (Vilarrasa *et al*., 2010a; Zhou *et al*., 2008). Given that a low-permeability boundary can be modeled with a leakage coefficient, the role of such a boundary condition should be evaluated. The effect that a low-permeability boundary has on fluid flow has been studied in hydrogeology (e.g. Wheatcraft and Winterberg, 1985; Butler, 1988). Although these studies deal with single phase flows, they can be helpful and valid in two phase flows (e.g. Neuweiler *et al*., 2003; Bolster *et al*., 2009b). The other boundary condition that affects fluid pressure corresponds to that at the injection well. Various injection schemes have been studied using hydromechanical coupling, such as two-dimensional models that conceptually represent a large line of injection wells (e.g. Rutqvist and Tsang, 2002) and even a 3-D model simulating horizontal wells (Rutqvist *et al*., 2010). However, a single injection well with a radial flow, which can be represented by an axysimmetric model, has to our knowledge not yet been studied.

The aim of the present study is to investigate stress and strain during CO_2 injection in a single well using an axysimmetric model to assess caprock integrity. The relevance of plastic strains is examined along with the influence of the boundary conditions on fluid pressure evolution.

4.2. Methods

4.2.1. Geometry

An ideal homogeneous horizontal aquifer-caprock system is considered for this study (Figure 4.1). The top of the 100 m thick aquifer is located at a depth of 1000 m. A 400 m thick low-permeability caprock overlies the aquifer and the caprock is covered by 600 m of media with low shear strength. These media do not need to be included in the model. The system is axysimmetric and extends laterally up to 1 km. An injection well with a radius of 0.15 m is placed at the centre of the domain.

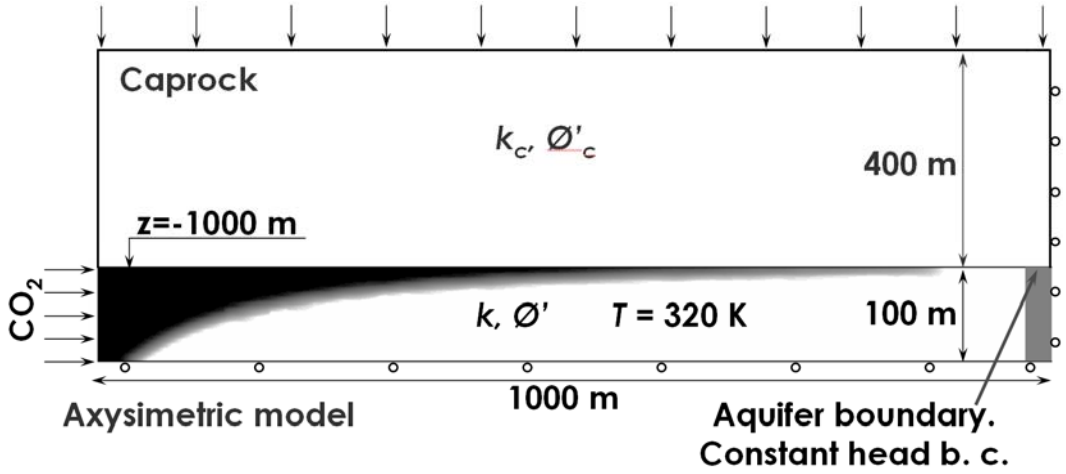

Figure 4.1 – Schematic of description model geometry and boundary conditions.

4.2.2. Fluid mechanics

The properties of the aquifer and caprock correspond to those of permeable sandstone (Dana and Skoczylas, 2002) and low-strength shale (Rutqvist *et al*., 2008), respectively (Table 4.1). Relative permeability follows a power law of saturation for both phases. In the aquifer it is a cubic law, while in the low-permeability caprock the power is 6. Retention curves follow the van Genuchten (1980) model (e.g. Rutqvist and Tsang, 2002; Zhou *et al*., 2008) (see Appendix VI for the governing equations). We consider the aquifer to be a sandstone with homogeneous grain size. Therefore, the entry pressure is low and the shape parameter is high. These parameters favor CO_2 flow through the aquifer without a dramatic pressure buildup. On the other hand, caprock entry pressure is high, which hinders CO_2 migration.

Table 4.1 – Material properties used in the hydromechanical analysis of the aquifer-caprock system.

Property	**Aquifer**	**Caprock**
Young's modulus, E (MPa)	$1 \cdot 10^4$	$5 \cdot 10^3$
Poisson's ratio, ν (–)	0.3	0.3
Porosity, φ (–)	0.1	0.01
Cohesion, c' (MPa)	0.01	0.01
Parameter M (–)	1.2	0.65 *
Parameter β (–)	2.08	2.12
Permeability, k (m^2)	10^{-13}	10^{-16}
Relative liquid permeability, k_{rl} (–)	S_l^3	S_l^6
Relative gas permeability, k_{rg} (–)	S_g^3	S_g^6
Gas entry pressure, P_{cc} (MPa)	0.02	0.6
van Genuchten m (–)	0.8	0.5

*: Low value taken to obtain irreversible strain

The initial conditions are hydrostatic pressure and constant temperature of T =320 K. A constant head boundary condition is imposed on the outer boundary.

In order to determine the influence of the outer boundary condition on fluid pressure evolution, two purely hydraulic models were used. One that simulates an infinitely acting aquifer in which the lateral extent of the model is sufficient to ensure that flow is independent of the nature of the boundary. The other consists of a low-permeability boundary placed 5 km from the injection well. The low-permeability boundary is imposed with a mixed or Cauchy boundary condition, which reads

$$Q = \alpha\left(P_0 - P\right), \tag{4.1}$$

where Q is the flow rate, α is the leakage coefficient, P_0 is the pressure of the external water body into which the aquifer leaks and P is fluid pressure. Three leakage coefficients, of 16, 32 and 64, are used to evaluate the effect of this low-permeability boundary. The lower the value of the leakage coefficient, the less permeable the outer boundary.

CO_2 is injected uniformly throughout the entire thickness of the aquifer at a constant rate of 79 kg/s (2.5 Mt/yr) and 113 kg/s (3.6 Mt/yr) for the purely hydraulic and the

coupled hydromechanical simulations, respectively. The latter falls within the range of the CO_2 generated by a 400 MW coal-fired power plant.

As for the fluid properties, the formation brine, at the aquifer depths considered, has an initial density of 1087.5 kg/m^3 and a viscosity of $6 \cdot 10^{-4}$ Pa·s. Brine density depends on pressure, temperature and the amount of dissolved CO_2 in the brine. Brine viscosity depends only on temperature and is therefore constant for the isothermal case presented here. CO_2 density is calculated using the formulas of Span and Wagner (1996) and can vary significantly with pressure at the considered temperature T =320 K. The viscosity of CO_2 depends on temperature and CO_2 density (pressure). In this study, it is calculated with an expression proposed by Altunin and Sakhabetdinov (1972).

4.2.3. Geomechanics

The initial stress field displays a greater vertical than horizontal stress, $\sigma'_h = 0.65\sigma'_v$, where σ'_v is the lithostatic effective stress. The mechanical boundary conditions are no displacement normal to the bottom and outer boundary. A constant, vertical lithostatic stress is imposed at the top of the caprock. We account for direct HM coupling, but we do not include strain dependent hydraulic properties.

The viscoplastic constitutive model adopted here is conceptually appropriate and computationally advantageous (Zienkiewicz and Cormeau, 1974; Zienkiewicz and Taylor, 2000). Most rocks present a very small yield stress. Furthermore, a significant pressure buildup will take place during CO_2 sequestration. Therefore, irreversible strains are expected to occur. This leads to the division of total strain into two parts

$$\mathrm{d}\boldsymbol{\varepsilon} = \mathrm{d}\boldsymbol{\varepsilon}^e + \mathrm{d}\boldsymbol{\varepsilon}^i, \tag{4.2}$$

where $\boldsymbol{\varepsilon}^e$ is the elastic strain tensor and $\boldsymbol{\varepsilon}^i$ is the inelastic strain tensor.

The yield criterion is formulated in terms of invariants of the effective stress tensor

$$p' = \frac{1}{3}\left(\sigma'_x + \sigma'_y + \sigma'_z\right) = p - P_f \tag{4.3}$$

and

$$J_2 = \frac{1}{2}\mathrm{tr}\left(\mathbf{s}^{\mathrm{t}} : \mathbf{s}\right) = \frac{1}{3}q^2, \tag{4.4}$$

where p' is the mean effective stress, p is the mean stress, $P_f = \max(P_g, P_w)$ is fluid pressure, P_g is the gas pressure, P_w the water pressure and σ' denotes the effective stress. J_2 is the second invariant of $\mathbf{s} = \boldsymbol{\sigma}' - p'\mathbf{I}$ and then q is the equivalent deviatoric stress. The superscript t denotes transpose. The sign convention of soil mechanics is adopted, i.e. $p > 0$ represents compression.

The elastic strain increments can be decomposed into a volumetric strain and a deviatoric strain

$$\mathrm{d}\,\varepsilon_v^e = \frac{\mathrm{d}\,p'}{K}, \tag{4.5a}$$

$$\mathrm{d}\,\varepsilon_d^e = \frac{\mathrm{d}\,q}{3G}, \tag{4.5b}$$

where ε_v^e and ε_d^e are the elastic volumetric strain and elastic deviatoric strain respectively, $K = E/(3(1-2\nu))$ is the bulk modulus, E is Young's modulus, ν is the Poisson ratio and $G = E/(2(1+\nu))$ is the shear modulus.

For the viscoplastic model, we adopted a Drucker-Prager yield function, F, defined as

$$F = q - Mp' - c\beta, \tag{4.6}$$

where c is the cohesion and parameters M and β depend on the initial stress. For compression ($\sigma_1 > \sigma_2 = \sigma_3$)

$$M = \frac{6\sin\phi'}{3-\sin\phi'} \qquad \beta = \frac{6\cos\phi'}{3-\sin\phi'} \tag{4.7}$$

and for extension ($\sigma_1 = \sigma_2 > \sigma_3$)

$$M = \frac{6\sin\phi'}{3+\sin\phi'} \qquad \beta = \frac{6\cos\phi'}{3+\sin\phi'}, \tag{4.8}$$

where ϕ' is the internal friction angle and c the cohesion, using the analogy with the Mohr-Coulomb yield criterion. $F < 0$ denotes elastic behaviour, and $F \geq 0$ implies viscoplastic strain, which are defined as

$$\frac{d\boldsymbol{\varepsilon}^i}{dt} = \Gamma\langle\Phi(F)\rangle\frac{\partial G}{\partial \boldsymbol{\sigma}'}, \tag{4.9}$$

where t is time, Γ is a viscosity parameter, $\Phi(F)$ is a stress function, $\boldsymbol{\sigma}'$ is the effective stress tensor and G is the flow rule, which is given by

$$G = q - \alpha(Mp' + c\beta), \tag{4.10}$$

where α is a non-associativity parameter. The non-associativity parameter α can vary between 0 and 1. When α is zero, there is no dilatancy, and when α equals one, the model is associated and gives large dilatancy. In this study we consider α =0.3.

Finally, the stress function is defined as

$$\Phi(F) = F^m , \tag{4.11}$$

where m is a constant power, which has been chosen as 3 for this study. It should be pointed out that both Γ and m are arbitrary in the sense that we are looking for an irreversible strain, which is not time dependent, and which essentially depends on the failure criteria. The analogy between viscoplasticity and plasticity is obtained from

$$d\boldsymbol{\varepsilon}^i = \Gamma\langle\Phi(F)\rangle dt \frac{\partial G}{\partial \boldsymbol{\sigma}'} = \Lambda \frac{\partial G}{\partial \boldsymbol{\sigma}'} , \tag{4.12}$$

where Λ would be the plastic multiplier. So, for a sufficiently large Γ, the plasticity solution is recovered.

Mechanical failure can be assessed once the evolution of fluid pressure and related changes in the stress field are known. As stated in the introduction, two failure mechanisms can occur: hydraulic fracture and shear slip of pre-existing fractures. Hydraulic fracture occurs when fluid pressure exceeds the least compressive principal stress. This is a conservative assumption (Rutqvist *et al*., 2008) allowing for a safety factor. Thus, the critical pressure for hydrofracturing would be for a fracture with tension strength equal to zero

$$P_f \geq \sigma_3 . \tag{4.13}$$

As for the onset of shear slip, if a fracture of random orientation exists at any point, shear initiates plasticity when the deviatoric invariant q exceeds the yield function, i.e.

$$q \geq Mp' + c\beta . \tag{4.14}$$

The two conditions can also be put together for an existing fracture without cohesion using the following condition

$$F = q - Mp' \geq 0 . \tag{4.15}$$

4.2.4. Numerical solution

The injection of CO_2 into a homogeneous saline aquifer is simulated using the finite element numerical code CODE_BRIGHT (Olivella *et al*., 1994, 1996) modified for CO_2 injection. Quadrilateral elements are used to enable the calculation of the mechanical problem. The mesh, which is unstructured, consists of elements 10 m by 10 m located close to the injection well, both in the aquifer and the caprock. The size of element increases progressively away from the well up to a size of 30 m by 30 m at the outer boundary. As a first step, a steady-state calculation is carried out to ensure equilibrium for the pressure and stress fields.

4.3. Fluid pressure evolution

4.3.1. Infinitely acting aquifer

Figure 4.2 displays the evolution of fluid pressure at the top of the injection well for an infinitely acting aquifer. The magnitude of the pressure buildup is inversely proportional to the permeability of the aquifer. Thus, the permeability of the aquifer may be a limiting factor. Injection pressure increases sharply when CO_2 injection starts. This sharp increase is maintained while a capillary fringe is being formed. This is because the relative permeability becomes very small when the porous media begins to desaturate. Once the capillary fringe is fully developed, pressure begins to drop (see Appendix VII). At this stage, the pores in the vicinity of the well are filled with CO_2. Thus the fluid can flow more easily, because CO_2 viscosity is one order of magnitude smaller than that of brine. The less viscous CO_2 displaces the brine and the capillary fringe laterally. The overpressure caused by the permeability reduction within the capillary fringe due to desaturation decreases with distance from the injection well (Figure 4.3). This results in a drop in fluid pressure buildup. This tendency is maintained until the CO_2-water interface is far enough so that the pressure drop due to the capillary fringe does not influence injection. This may occur for very long injection times (see Appendix VII). Thereafter, fluid pressure starts increasing slightly.

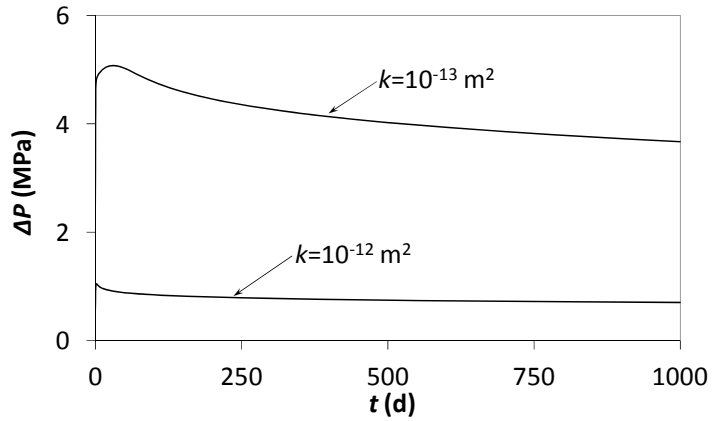

Figure 4.2 – Injection pressure at the top of the aquifer for a 1000 day injection period, for two intrinsic permeabilities of the aquifer. Injection pressure drops because of the lower CO_2 viscosity with respect to that of brine.

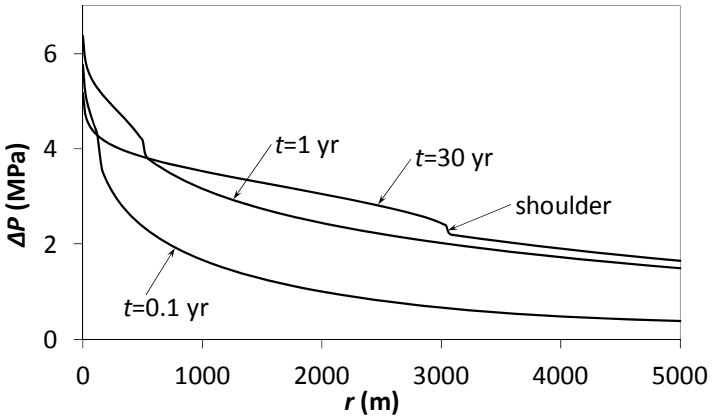

Figure 4.3 – Fluid overpressure at the top of the aquifer as a function of the distance from the injection well for different injection times when the aquifer presents a low-permeability boundary at 5 km from the injection well. Note the shoulder in pressure observed near the CO_2-water interface. The pressure drop across this interface decreases with distance from the well because the overall permeability drops in response to partial desaturation.

4.3.2. Radial aquifer with a low-permeability boundary

The fluid pressure profile at the aquifer top for the case of a leakage coefficient equal to 16 is presented for several injection times in Figure 4.3. These profiles show the maximum pressure of either the CO_2 or the brine, i.e. the gas pressure in the CO_2 rich phase and the liquid pressure in the region occupied by the formation brine. A shoulder can be observed in all fluid pressure profiles. This increment corresponds to the edge of the CO_2 plume and is due to both capillary pressure and the overall reduction in permeability within the capillary fringe. Fluid pressure at the injection well decreases

after long injection times, as illustrated by comparing the curve after 1 year with that after 30 years of injection. However, note that fluid pressure increases in the entire aquifer. The pressure profile flattens and slowly increases its magnitude with time. Fluid pressure undergoes an increase of nearly 2 MPa at the low-permeability boundary during the first year of injection. It continues to increase for longer injection times, but at a very small rate.

Figure 4.4 displays the additional pressure increase for different values of the leakage coefficient, α, of the aquifer border. For a sufficiently high value of α, a constant head boundary condition is obtained. To maintain the flux for the imposed Cauchy boundary condition at the outer boundary of the aquifer, the product between the leakage coefficient and the pressure gradient has to be constant (Equation (4.1)). For this reason, the lower the leakage coefficient, the greater the pressure gradient. Note that for the case where α=16 the pressure increase with respect to the constant head boundary condition is 1 MPa, which may be sufficient to induce mechanical failure. The overpressure in the presence of a permeable boundary with a constant head is lower because once the radius of influence reaches it, the growth of brine back pressure is stopped. From there on, injection pressure drops down because the displaced brine is more viscous than the invading CO_2. These are not necessarily good news, because it implies that a volume of brine equal to that of injected CO_2 is leaving the system, possibly to an adjacent freshwater body.

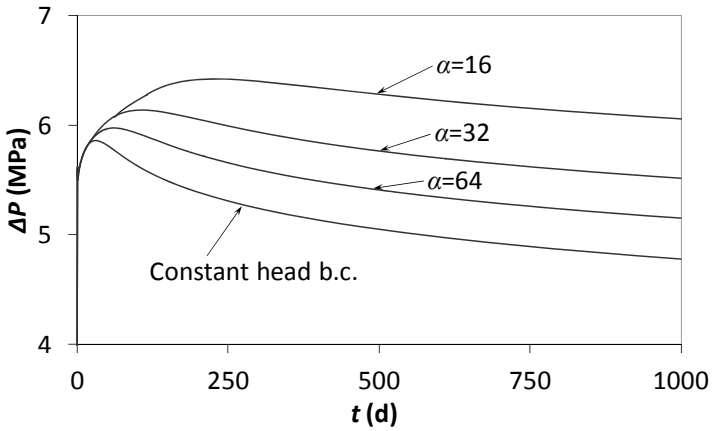

Figure 4.4 – Overpressure at the injection well at the top of the aquifer for a 1000 day injection period for different leakage coefficients of the aquifer boundary placed 5 km away from the injection well.

For a low-permeability boundary located at a distance greater than the one considered here, this fluid pressure increase behaviour would happen in the same manner, but delayed a time equal to $\mu_w S_s R^2/(2.25k\rho_w g)$, where R is the distance at which the low-permeability boundary is located. If the low-permeability boundary was located at a considerable distance from the injection well, the injection pressure would drop after the initial increase (Figure 4.2). However, once the radius of influence of the injection reached the low-permeability boundary, fluid pressure would increase in the whole aquifer (Figure 4.3). In particular, fluid pressure would also increase again at the injection well.

4.4. Hydromechanical coupling

CO_2 injection causes fluid pressure to increase, thus changing the effective stress tensor. The latter produces deformations of the medium, and these deformations exert an influence on the evolution of fluid pressure. Figure 4.5 compares a purely hydraulic simulation (H) with a coupled hydromechanical (HM) simulation of the model presented in Figure 4.1. This coupled HM simulation uses the viscoplastic constitutive model outlined in Section 4.2.3. The difference between the purely hydraulic and the coupled hydromechanical simulations is small in the aquifer (Figure 4.5a). The two curves are almost parallel, with comparable asymptotic values of the pressures, and can be corrected by a translation, which depends on the storage coefficient selected. However, it is not easy to assign storativity values because the real relationship between stress and volumetric strain is very sensitive to strain mechanisms. Furthermore, HM simulation captures porosity changes due to rock strain (not only volumetric) in contrast to H simulation, which only considers a storage coefficient that includes fluid and rock compressibility (Mainguy and Longuemare, 2002). Thus, the two curves are not exactly parallel. Interestingly, the difference becomes significant in the caprock (Figure 4.5b). Hydraulic simulations do not capture the drop in the initial fluid pressure because of mechanical effects, such as dilatancy or bending of the caprock due to CO_2 injection. Thus, measuring fluid pressure in the caprock plays a major role in identifying the hydromechanical processes.

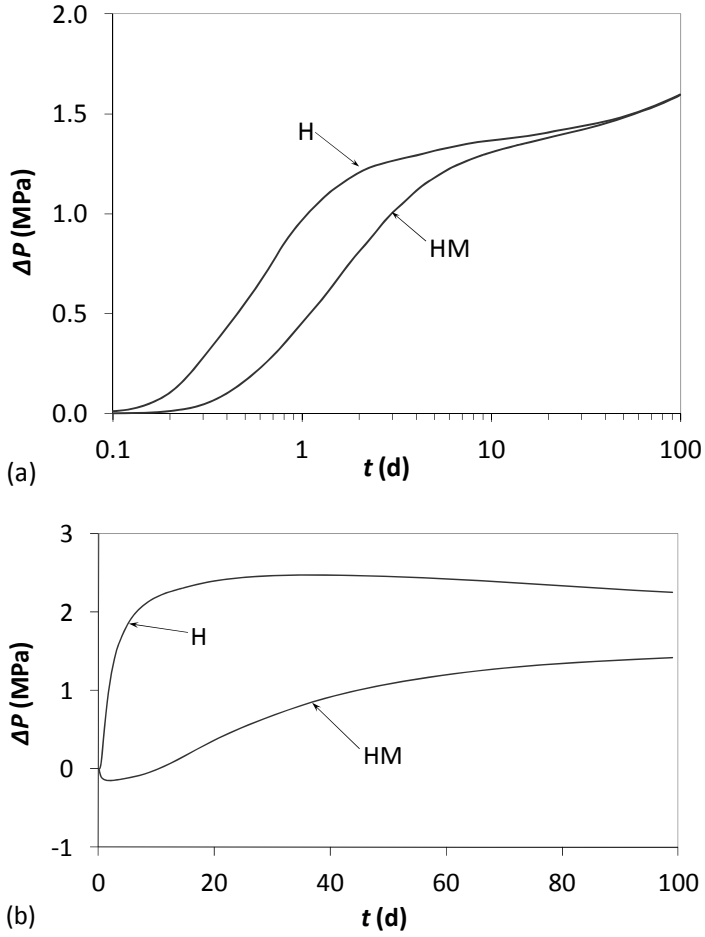

Figure 4.5 – Fluid overpressure for a 100 days injection period, comparing pure hydraulic (H) with coupled hydromechanical (HM) simulation in (a) the aquifer at the contact between the aquifer and the caprock 400 m from the injection well and (b) in the caprock 50 m above the aquifer and 50 m away the injection well.

Figure 4.6 displays the evolution of stresses and pressures at the beginning of the injection. Fluid pressure in the aquifer and the caprock increases dramatically in response to the injection. Once the reservoir begins to desaturate, the gas and liquid pressure increase sharply, both in the reservoir and the caprock. As a result, the mean effective stress is reduced, which produces an expansion of the pore volume. Unlike the mean effective stress, the deviatoric stress is only slightly reduced, which compromises caprock integrity. This is the most critical period, as indicated by the maximum in the ratio between the deviatoric and the mean effective stresses. However, after the increase in the initial fluid pressure (and consequent decrease in the mean effective stress), the liquid pressure will tend to stabilize. Thereafter, there is a decrease in gas and liquid pressure. As a result, the mean effective stress increases, but the deviatoric stress remains constant, and the ratio decreases. Therefore, for the

conditions of our simulation, CO_2 injection becomes safer from the mechanical point of view as the injection time increases.

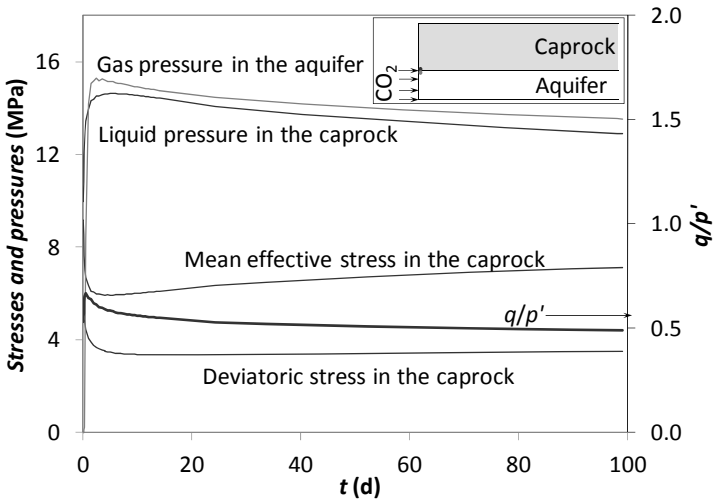

Figure 4.6 – Stress and pressure evolution with time at the beginning of CO_2 injection at the base of the caprock next to the injection well (see location in inset).

We consider the deviatoric stress q over a vertical section located in the vicinity of the injection well after 4 days of injection to study the risk of mechanical failure in the caprock (Figure 4.7) provided that parameters for a low-strength caprock are considered. The rock plastifies if the q exceeds the critical value, q_{critic}, which is obtained from Eq. (4.6) for F =0. Simulation results show that the rock plastifies at the contact point between the aquifer and the caprock. Similarly, the Mohr circle after 4 days of injection becomes tangent to the Mohr-Coulomb yield criterion (Figure 4.8). This implies that the caprock is damaged. The Mohr circle is displaced to the left over time, as expected because of increases in fluid pressure. Interestingly though, it shrinks, because horizontal stresses increase as horizontal strain is limited in the horizontal plane. Thus, lateral confinement ensures that the system becomes safer with time, i.e. if damage does not occur early it is unlikely to occur subsequently.

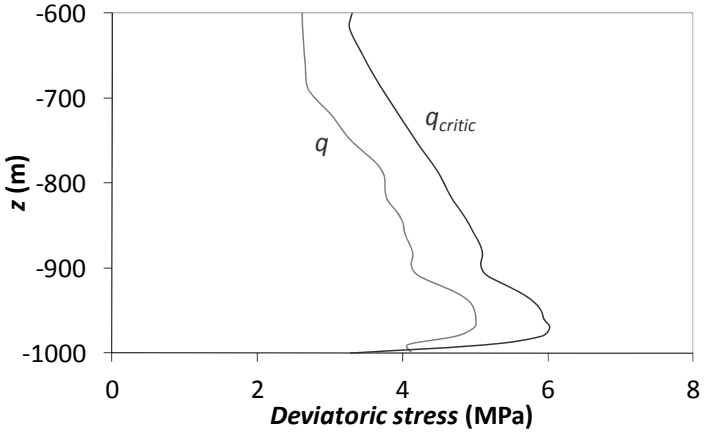

Figure 4.7 – A vertical section of the caprock in the vicinity of the well, with the deviatoric stress, q, and critical the deviatoric stress, q_{critic}, after 4 days of injection. Note that q exceeds q_{critic} in the contact between the caprock and the aquifer, thus causing the caprock to plastify.

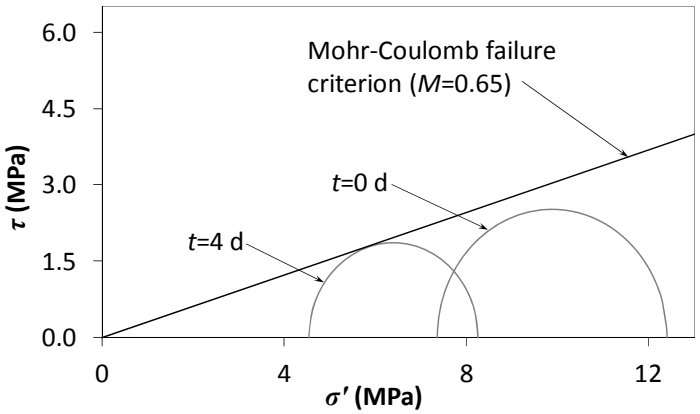

Figure 4.8 – Mohr circles at the initial state and after 4 days of injection. The parameters of the Mohr-Coulomb failure criterion are c=0 and ϕ'=17.2º (low value taken to obtain irreversible strain). The Mohr circle after 4 days of injection is displaced to the left (reduction in p') and is reduced in size (reduction in q).

This behaviour is also observed in the (q, p') plane for a point at the base of the caprock close to the well over an injection period of 100 days (Figure 4.9). Prior to injection (point A), the caprock is in the safe zone, at some distance from the plastic regime. Once injection begins, the mean effective stress decreases much more drastically than the deviatoric stress and the Mohr-Coulomb yield envelope is rapidly reached (point B). At this point, the rock begins to behave plastically. Thus, strain occurs plastically for a few days, until it reaches point C after 5 days of injection. Then,

the deviatoric stress decreases at a higher rate than for the period between point B and C, and the caprock ceases to plastify. Finally, the mean effective stress increases, reaching a safe situation again (point D) after 100 days of injection. In this particular case the rock plastifies, but there will be injection scenarios in which the (q, p') trajectory will not reach the Mohr-Coulomb yield envelope. In these situations, the mobilized angle of friction of the caprock, i.e. the angle of friction that triggers plasticity can be determined. This mobilized angle of friction yields an estimate for the likelihood of mechanical failure in a given situation. This leads to the definition of a safety factor (SF) that is defined as follows

$$SF = \frac{\tan \phi'_{real}}{\tan \phi'_{mobilized}}, \tag{4.16}$$

where in this particular case of injection, the mobilized angle of friction is 17.2º. Whenever the actual angle of friction of the caprock is higher than this mobilized angle of friction, the injection safety factor is higher than one, indicating that it will be safe.

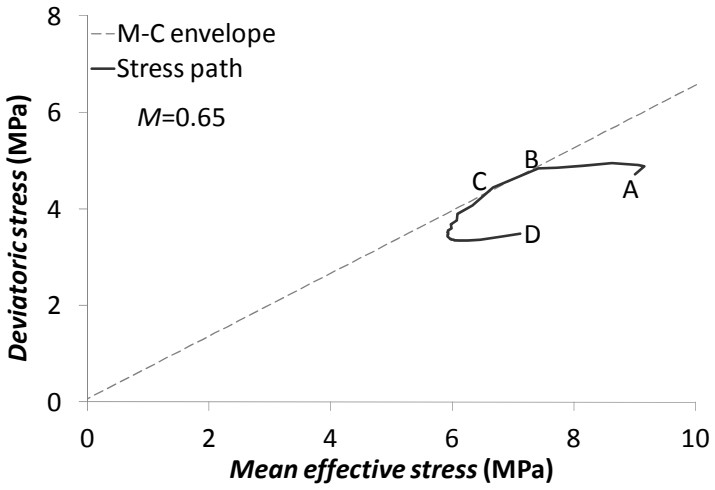

Figure 4.9 – (q, p') trajectory for a 100 day injection. The initial and final states are represented by A and D, respectively. The onset of plasticity takes place during early times (B-C), but plastic behaviour eventually stops.

Figure 4.10 shows the plastic strain in the caprock in the vicinity of the injection well and the corresponding CO_2 plume for different times close to the beginning of injection. Plastic strains evolve as CO_2 advances, but they stabilize after 5 days of injection. This is because a safe situation is reached, as shown by the (q, p') trajectory in Figure 4.9. The plastic region propagates upwards and to the right with time as the CO_2 plume increases in size, presenting a marked trend of maximum strain following a direction of

approximately 45º to the ground surface. Once this plastic region stabilizes, it reaches horizontally a distance of 175 m from the injection well and 125 m above the base of the caprock. Note that the induced plastic strains are small (0.04 %), which suggests that the integrity of the caprock will not be compromised here.

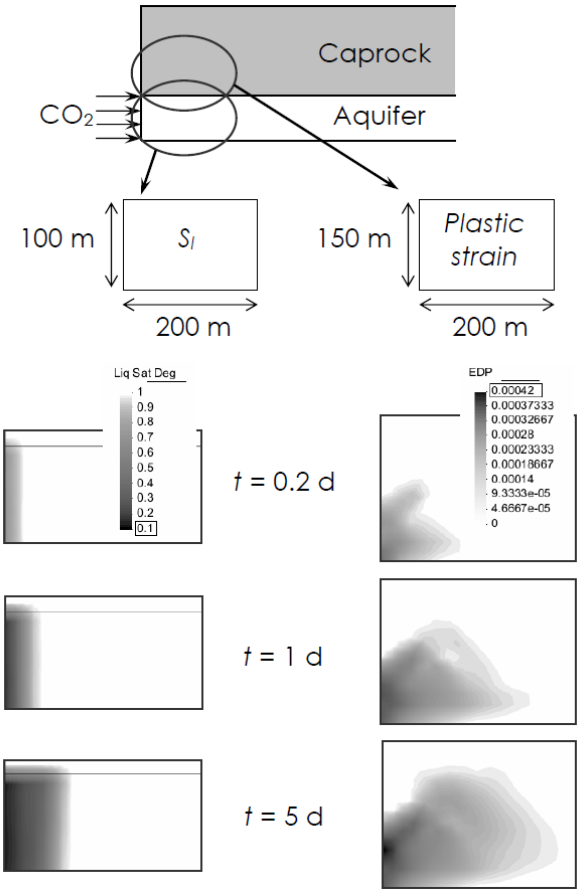

Figure 4.10 – Plastic strain (EDP) in the caprock (left) and liquid saturation degree, S_l, in the aquifer (right) for different injection times. Plastic strain propagates as CO_2 advances at the beginning of injection.

Unlike horizontal displacements, vertical displacements can be significant (Vasco *et al.*, 2008; Rutqvist *et al.*, 2010). Figure 4.11 shows the vertical displacement that takes place at the top of the caprock, at a depth of 600 m, as a function of the distance from the injection well at different injection times. The vertical displacement has a typical bell shape. The magnitude of the uplift gradually increases with time, reaching a maximum of several centimeters next to the injection well after 100 days of injection. This particular model does not simulate the upper 600 m of rock, but the vertical displacement should follow a similar trend, which means that a significant uplift of the ground could take place (Morris *et al.*, 2009).

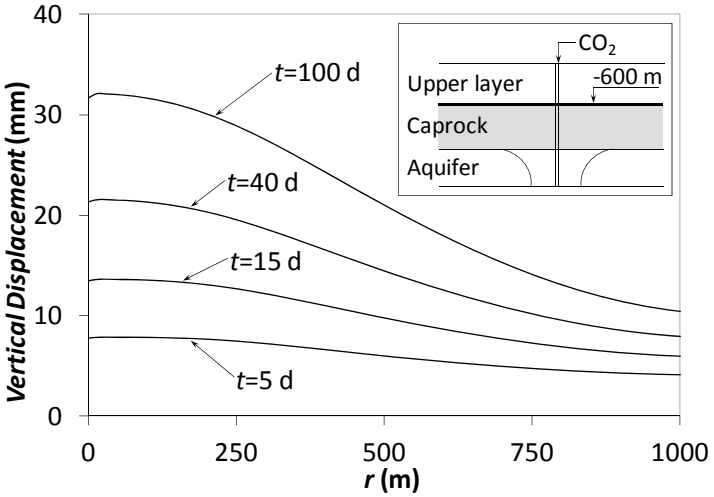

Figure 4.11 – Vertical displacement as a function of distance from the well for different injection times at the top of the caprock (z = -600 m).

4.5. Discussion and conclusions

We conducted simulations of CO_2 injection into a deep saline aquifer to study the risk of caprock mechanical failure. The specific scenario we model is meant to reflect a real world scenario. In particular, we assumed the material to be viscoplastic and the initial stress tensor to be axysimmetric with the vertical stress greater than the horizontal ones.

Given that instability is caused by fluid pressure buildup, we carried out hydraulic simulations of an infinitely acting aquifer and a circular aquifer with a low-permeability boundary to study the influence of the boundary condition. Exclusion of the mechanical component allowed us to run the simulations at a reasonably low computational cost. We found that after an initial sharp increase, the fluid pressure drops. This occurs because the less viscous CO_2 displaces brine and the capillary fringe laterally. This capillary fringe produces an overpressure because of permeability reduction due to desaturation. This overpressure decreases with distance from the injection well. Thus, fluid pressure decreases with time. This drop in fluid pressure may allow the injection of an additional amount of CO_2 without compromising the caprock stability. Furthermore, the measurement of this fluid pressure drop in field tests (with constant injection mass rate) can give valuable information about the capillary fringe.

If the aquifer has a low-permeability boundary, fluid pressure can rise again once the

radius of influence reaches this boundary. This increase takes place in the whole aquifer. This additional overpressure may induce rock failure in the long term. In most CO_2 sequestration projects, the boundaries of the basins will play a role in the injection since CO_2 sequestration projects are planned to take place over long periods of time (several decades). Over such timescales the radius of influence will reach tens and even hundreds of kilometers, depending on the permeability of the aquifer. Thus, the geometry and hydraulic properties of the aquifer boundaries should be characterized in detail.

Full coupling in hydromechanical simulations leads to lower increases in fluid pressure than the use of purely hydraulic simulations. This occurs because of rock deformations. The difference can be small in the aquifer if a good estimate of the storage coefficient is used. However, the evolution of fluid pressure is completely different in the caprock because of mechanical effects such as dilatancy and bending of the caprock due to CO_2 injection. In these coupled simulations we consider direct HM couplings, but not indirect HM ones (such as changes in permeability due to porosity changes (Rutqvist and Tsang, 2002)). The incorporation of indirect HM couplings might lead to significant differences in the results. On the other hand, direct HM couplings consider rock strain and changes in the stress field (Figure 4.8). CO_2 injection increases fluid pressure and as a result the rock deforms leading to changes in the porosity. This deformation increases the pore volume, resulting in a drop in fluid pressure. Despite this drop in fluid pressure, a sufficiently large overpressure occurs in the reservoir, inducing plastic strain in the caprock at the beginning of the injection. In this work, the caprock mechanical strength was intentionally chosen so that the rock plastifies as our goal was to determine failure mechanisms that could serve as an escape route for CO_2.

In practice, it is essential to determine the in situ stress field. The failure mechanisms discussed here could be expected for cases where the vertical stress is greater than the horizontal stresses. From a mechanical perspective, the analysis of the (q, p') trajectories illustrates that the most critical period occurs in the early stages for a constant injection rate. The stress state can be close to failure during this period. Failure will occur when the yield surface is reached, giving rise to plastic strain, which may result in microfracturing (i.e. detectable by a local seismic network). Yield is local, so that the breakup of caprock is unlikely. Nonetheless, monitoring caprock integrity at the beginning of the injection is crucial to ensure a safe injection. As shown in Figure 4.10, the caprock could yield at the beginning of the injection and the damage could propagate through a portion of the caprock. Furthermore, if a weak zone was already

present in the caprock, the damage would be greater and preferential paths could be created, allowing the CO_2 to migrate up to shallow aquifers or even the ground surface. If the CO_2 can penetrate into the caprock, geochemical interactions will take place due to its acidity.

To limit local failure at the beginning of injection, a good characterization of the caprock is necessary. If the strength of the rock was known, numerical simulations would enable us to determine a sustainable injection pressure. This may be achieved by determining the mobilized angle of friction and by ensuring that it does not exceed the real friction angle of the rock even in weak zones. The use of a safety factor (Equation (4.16)) can be valuable in probabilistic risk assessment (e.g. Tartakovsky, 2007; Bolster *et al*., 2009a; Jurado *et al*., 2012).

In this study, a homogeneous caprock is considered. Heterogeneities in the caprock, such as weak zones, fractured zones or discontinuities, are likely to be present in most injection areas. Furthermore, given that CO_2 injection projects are planned to last decades, the CO_2 plume will span several kilometers. Therefore, future studies should address the influence of mechanical and hydraulic heterogeneities in the caprock in order to simulate more realistic situations.

We modified and used the program CODE_BRIGHT to study the coupled hydromechanical evolution in an aquifer-caprock system during CO_2 sequestration in deep saline aquifers. In summary, the main conclusions drawn from this study are:

- Fluid pressure begins to drop once the capillary fringe is fully developed. The overpressure produced within the capillary fringe (because of permeability reduction due to desaturation) decreases with the distance from the well. Measuring this fluid pressure drop in field tests can give valuable information about the capillary fringe. Furthermore, an additional amount of CO_2 may be injected with a small increase in fluid pressure.
- If the aquifer has a low-permeability boundary, fluid pressure can rise once the radius of influence reaches the outer boundary. As a result of this, the mechanical integrity of the caprock could be compromised in the long term.
- The lower zone of the caprock presents the largest hydromechanical changes, presenting the greatest risk of rock failure, particularly in the early stages of injection.

- Slowly increasing the injection rate at the beginning of injection is recommendable in order to reduce possible damage to the caprock. Furthermore, measuring fluid pressure in the caprock is essential for identifying hydromechanical processes.

Numerical simulations allow us to estimate the maximum sustainable injection pressure given the strength of the caprock. A safety factor can be defined by determining the mobilized angle of friction.

5. Hydromechanical Characterization of CO_2 Injection Sites

5.1. Introduction

Coupled hydromechanical effects, such as ground deformation, induced microseismicity and fault reactivation, should be understood and quantified to demonstrate to the public that geologic carbon storage is safe. The most representative example of a coupled hydromechanical effect may be the ground heave of 0.5 mm/yr on top of the carbon dioxide (CO_2) injection wells at the In Salah storage project in Algeria (Rutqvist *et al*., 2010; Vasco *et al*., 2010). Other relevant examples are related to induced microseismicity and seismicity. Induced microseismic events were detected at Otsego County, Michigan Basin, US, due to CO_2 leakage around wells (Bohnhoff *et al*., 2010) and in the Weyburn field, Saskatchewan, Canada (Verdon *et al*., 2011). Cappa and Rutqvist (2011b) estimated through numerical simulations that CO_2 injection in a deep aquifer bounded by a low-permeability fault can trigger earthquakes with magnitude up to 4.5. Additionally, a natural high pressure CO_2 source is believed to have driven, after the occurrence of two earthquakes, thousands of aftershocks in the Northern Apennines, Italy, during more than 30 days, including four events with moment magnitudes ranging from 5 to 6 (Miller *et al*., 2004). Thus, hydromechanical processes need to be well understood to ensure stable permanent CO_2 storage in deep geological formations.

Hydromechanical studies have focused on several aspects, including the estimation of maximum sustainable injection pressure (Streit and Hillis, 2004; Rutqvist *et al*., 2007), evaluating fault reactivation due to production of gas/oil fields (Ferronato *et al*., 2008; Soltanzadeh and Hawkes, 2009) and due to CO_2 injection (Ferronato *et al*., 2010; Cappa and Rutqvist, 2011a). Fault reactivation occurs once the fault yields, in which case induced microsesimicity will be triggered. This microseismicity is usually due to shear-slip and produces changes in the fault aperture in the order of microns (Guglielmi *et al*. 2008). Thus, fracture permeability is enhanced, especially in the direction

perpendicular to shear (Barton *et al*., 1985; Yeo *et al*., 1998; Mallikamas and Rajaram, 2005). Phillips *et al*. (2002) present three examples of induced microseismicity in sedimentary basins in which the events concentrate on the contact between layers of different mechanical properties or stress states. The evolution of the yielding region depends on the stress tensor and may propagate upwards when vertical stress is greater than horizontal stresses (Rutqvist *et al*., 2008; Vilarrasa *et al*., 2011b). To quantify these coupled hydromechanical effects, the mechanical properties of the rocks should be measured.

Mechanical properties of rocks are usually inferred from core samples at the laboratory. However, these values might be representative at the field scale because of the existence of joints or fractures. This is illustrated by the difference between the values of the Young's modulus obtained from laboratory tests and from back-analysis of convergence measurements in underground excavations. Its value from laboratory tests is always higher than that resulting from back-analysis because fractures are more deformable than the rock matrix (e.g. Ledesma *et al*., 1996; Zhang *et al*., 2006; Cai *et al*., 2007). However, the large-scale geomechanical properties are difficult to quantify (Rutqvist, 2012). This is why it is necessary to develop a field test to characterize the macroscopic mechanical properties of the rock layers involved in CO_2 storage in deep geological formations, i.e. the reservoir and the caprock.

Pilot projects are an excellent opportunity to perform new tests that will be useful for CO_2 injection at the industrial scale. However, little hydromechanical field data is available in pilot projects (Kikuta *et al*., 2005; Michael *et al*., 2010) and the related studies are mainly conceptual (Chiaramonte *et al*., 2008; Smith *et al*., 2009; Vidal-Gilbert *et al*., 2010). Because of this lack of hydromechanical tests at the field scale, we propose a hydromechanical characterization test to obtain the macroscopic hydraulic and mechanical properties of the reservoir and the caprock and to evaluate the maximum sustainable injection pressure. This test will be performed at the pilot site of Hontomin (Carrera *et al*., 2011a), Spain, which is the injection site of the CO_2 storage Technology Demonstration Plant (TDP) of the Compostilla OXYCFB300 project, operated by Energy City Foundation (CIUDEN). Hontomin is a dome-like structure situated 30 km to the north of the city of Burgos, Spain. The reservoir is a dolomitized level located at 1450 m depth, overlaid by a caprock made of marls. A large number of experiments are planned both for site characterization and for injection technology development.

5.2. Mechanical properties of rocks

Sedimentary rocks (sandstone, limestone and dolomite) are potential host rocks for CO_2 storage. On the other hand, low-permeability, high-entry pressure formations, such as shale, marl and claystone, can form the caprock. Mechanical properties of these rock types (Figures 5.1 and 5.2) can take a wide range of values.

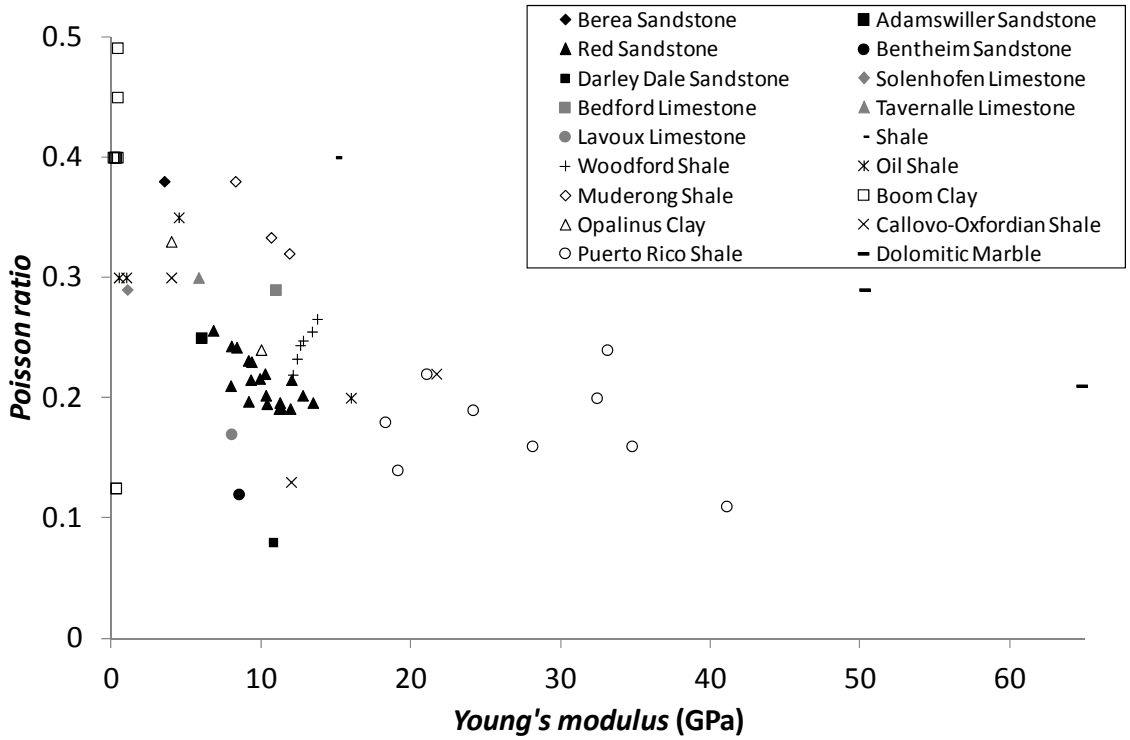

Figure 5.1 – Literature review of matrix Young's modulus and Poisson ratio for several sandstones, limestones, dolomitic marble and shales.

The variation in rock properties depends on the rock type. For example, the Young's modulus of sandstones and limestones ranges only from 1 to 20 GPa (Goodman, 1989; Abousleiman *et al*., 2010; Heap *et al*., 2010; Hu *et al*., 2010; Rimmele *et al*., 2010). Instead, reported Young's moduli of shales range over two orders of magnitude. Soft shales, like the Boom Clay, display Young's moduli in the order of 0.1-0.4 GPa (Giraud and Rousset, 1996; Mertens *et al*., 2004; Dehandschutter *et al*., 2005; François *et al*., 2009). Stiff clays, like one from Puerto Rico, have got Young's moduli in the order of 20-40 GPa (Shalabi *et al*., 2007). Other shales (Ortega *et al*., 2010), such as oil shales (Eseme *et al*., 2007), Opalinus Clay (Thury, 2002; Gens *et al*., 2007) and Callovo-Oxfordian argillite (Zhang and Rothfuchs, 2004; Saurot *et al*., 2007; Wileveau and Bernier, 2008), have intermediate Young's modulus values, ranging from 1 to 20

GPa. The actual value of the Young's modulus increases with the mean effective stress (Dodds *et al*., 2007; Shalabi *et al*., 2007; Hu *et al*., 2010).

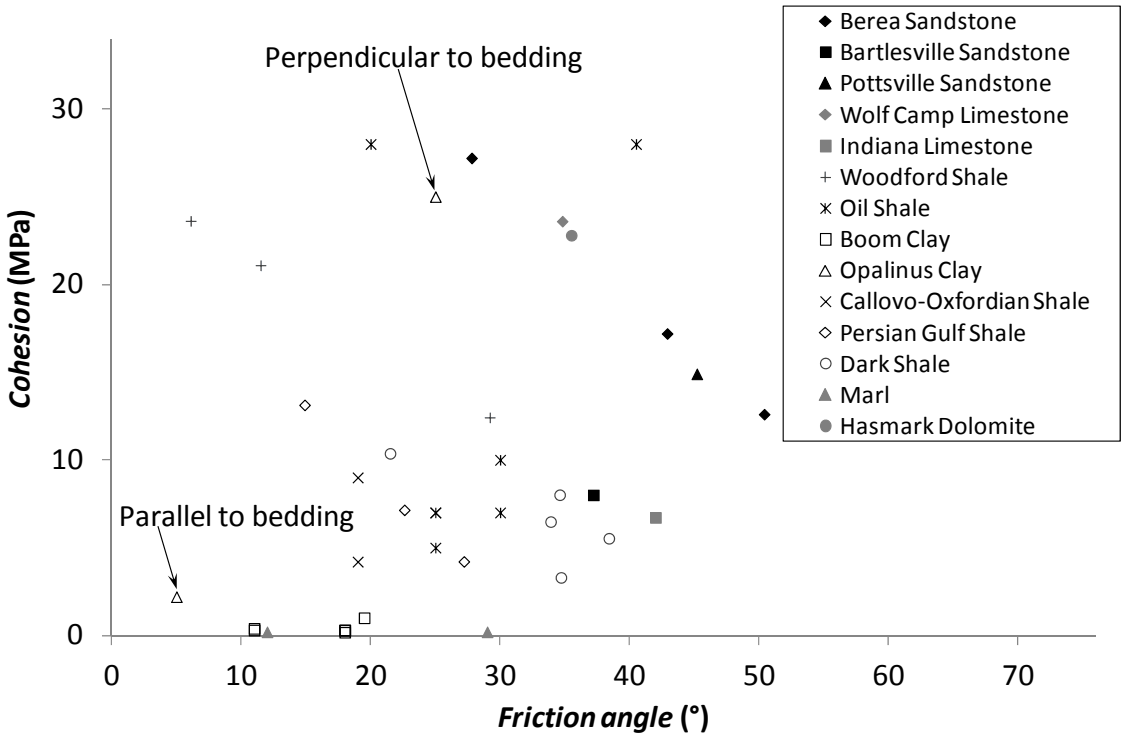

Figure 5.2 – Literature review of cohesion and friction angle for several sandstones, limestones, marls, dolomite and shales.

Poisson ratios range from 0.15 to 0.25 for the vast majority of rock samples (Figure 5.1). Some values close to 0.5 (incompressible) are reported in low-permeability rocks. These values are due to undrained conditions, but they are not representative of the real Poisson ratio of the rock.

The friction angle of existing fractures is important because it controls the occurrence of microseismic events. Sedimentary formations, which are formed after depositional sequences, present a high anisotropy in the directions parallel and perpendicular to bedding (Thury, 2002; Gens *et al*., 2007; Saurot *et al*., 2007). Friction angles as low as 5° (Figure 5.2) have been found in the direction parallel to bedding in clay-rich materials (Gens *et al*., 2007) or when the rock has been weakened due to demineralization (Abousleiman *et al*., 2010). Related to this, the percentage of carbonate in the clay-size material of marls affects the residual friction angle. Low carbonate content (<11%) yields residual friction angles around 12°. High carbonate content (>30%) yields residual friction angles around 30° (Frydman *et al*., 2007).

Figures 5.1 and 5.2 illustrate that the mechanical properties of sedimentary rocks are highly variable. Additionally, these properties are difficult to estimate at the field scale, which is the scale of interest for CO_2 sequestration. Hydromechanical numerical studies usually take the values obtained from samples tested at the laboratory as the values of the formation. However, laboratory tests are representative of the rock matrix, but not of the formation as a whole. This is because the formation is fractured. The value of the Young's modulus of the formation can differ in more than one order of magnitude with respect to that of the matrix. For example, Verdon *et al*. (2011) had to reduce the Young's modulus of the aquifer from 14.5 (value obtained from laboratory tests) to 0.5 GPa in order to adjust their model to the observed microseismicity in the Weyburn field, Saskatchewan, Canada.

5.3. Hydromechanical characterization test

5.3.1. Test description

We propose a test to characterize the hydromechanical parameters of the aquifer and caprock at the field scale. The test consists in injecting water at high pressure and flow rate, while monitoring fluid pressure, rock deformation and induced microseismicity (Figure 5.3). The overpressure (several MPa) is proportional to the flow rate, which can be high if the aquifer transmissivity is high. The injected water can be obtained from surface sources, e.g. rivers or lakes. However, aquifer brine must be used if geochemical alteration is not desired. In this case, brine is pumped and stored at the surface prior to the injetion test. Therefore, the duration of the injection will be conditioned by storage capacity.

The overpressure should be progressively increased until the elastic limit is reached and microseismicity occurs. Microseisms can take place both in the reservoir and the caprock. Since microseisms open up fractures, enhancing their transmissivity, microseismicity will be benificial while it occurs within the aquifer. However, if it occurs in the caprock, the maximum sustainable injection pressure is reached, indicating the overpressure that must not be exceeded during the operational stage of CO_2 injection.

Instrumentation for the test consists of equipments to measure fluid pressure, vertical displacement and microseismicity. Fluid pressure and vertical displacement measurements are taken in the injection and observation wells, both in the reservoir

and the caprock (Figure 5.3). In the case that vertical displacement measurements are not available, strain should be measured. An array of geophones should be placed in the observation well at depth to detect microseismic events of magnitudes as low as -3. Additionally, a network of geophones in surface can complement the microseismicity measurements and help to localize the events. Microseismicity measurements are essential to guarantee the caprock integrity and avoid leakage of future CO_2 injection tests in the same site.

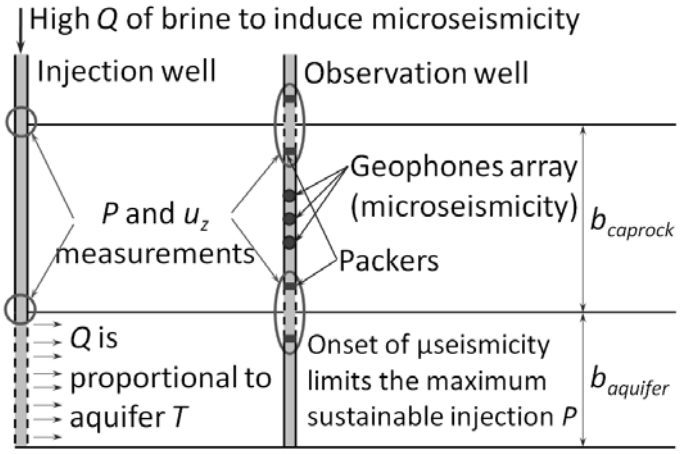

Figure 5.3 – Schematic representation of the hydromechanical characterization test. A sufficiently high water flow rate so as to reach the maximum sustainable injection pressure is injected for several hours. Fluid pressure and displacements or strains are monitored in the aquifer and caprock in as many places as possible (preferably in both the injection and the observation well, but at least in one well).

5.3.2. Problem formulation

a) Elasticity in porous media

Fluid injection induces strain in the aquifer-caprock system, which will be elastic while failure conditions are not reached. Hooke's law gives the relationship between elastic strain and effective stress, which can be written either as (Zimmerman, 2000)

$$\boldsymbol{\varepsilon} = \frac{\sigma'_m}{3K}\mathbf{I} + \frac{1}{2G}\left(\boldsymbol{\sigma}' - p'\mathbf{I}\right), \tag{5.1a}$$

or as

$$\boldsymbol{\sigma}' = K\varepsilon_v\mathbf{I} + 2G\left(\boldsymbol{\varepsilon} - \frac{\varepsilon_v}{3}\mathbf{I}\right), \tag{5.1b}$$

where $\boldsymbol{\varepsilon}$ is the elastic strain tensor, $\boldsymbol{\sigma}'$ is the effective stress tensor, $\sigma'_m = \left(\sigma'_x + \sigma'_y + \sigma'_z\right)/3$ is the mean effective stress, $\mathbf{I}$ is the identity matrix, $K = E/\left(3\left(1-2\nu\right)\right)$ is the bulk modulus, $G = E/\left(2\left(1+\nu\right)\right)$ is the shear modulus, E is the Young's modulus, ν the Poisson ratio and ε_v is volumetric strain.

Elastic strain can be decomposed into a volumetric and a deviatoric strain

$$\varepsilon_v = \frac{\sigma'_m}{K} \tag{5.2a}$$

$$\varepsilon_d = \frac{q}{3G} \tag{5.2b}$$

where ε_d is deviatoric strain, $q = \sqrt{3J_{2_D}}$ is deviatoric stress and $J_{2_D} = \left(1/2\right)\mathrm{tr}\left(\mathbf{s}^T : \mathbf{s}\right)$ is the second invariant of $\mathbf{s} = \boldsymbol{\sigma}' - \sigma'_m\mathbf{I}$. Note that Eq. (5.1a) and (5.1b) are related through Eq. (5.2a).

Considering the sign criterion of continuum mechanics, i.e. stress is positive in tension and fluid pressure is positive in compression, the effective stress tensor is defined as

$$\boldsymbol{\sigma}' = \boldsymbol{\sigma} + p\mathbf{I}\,, \tag{5.3}$$

where $\boldsymbol{\sigma}$ is the total stress tensor and p is fluid pressure.

To solve the mechanical problem, the momentum balance of the porous media has to be satisfied. If the inertial terms are neglected, it reduces to the equilibrium of stresses

$$\nabla\cdot\boldsymbol{\sigma} + \mathbf{b} = \mathbf{0}\,, \tag{5.4}$$

where $\mathbf{b}$ is the vector of body forces.

Introducing Eq. (5.1b) and (5.3) in Eq. (5.4) gives the equilibrium of stresses in terms of strain as

$$\left(K - \frac{2}{3}G\right)\nabla\varepsilon_v + 2G\nabla\cdot\boldsymbol{\varepsilon} - \nabla p + \mathbf{b} = \mathbf{0}\,. \tag{5.5}$$

The compatibility relationship that relates strain to displacements reads

$$\boldsymbol{\varepsilon} = \frac{1}{2}\left(\nabla\mathbf{u} + \left(\nabla\mathbf{u}\right)^T\right), \tag{5.6}$$

where $\mathbf{u}$ is the displacement vector and the superscript T denotes transpose.

The volumetric strain can be also expressed as the divergence of the displacement vector

$$\varepsilon_v = \nabla \cdot \mathbf{u} \,. \tag{5.7}$$

The stress equilibrium can be expressed in terms of displacements by introducing Eq. (5.6) and (5.7) in Eq. (5.5), which yields a non-homogeneous Navier equation of linear elasticity with a non-homogeneous term given by the gradient of the fluid pressure

$$G\nabla^2\mathbf{u} + \frac{3K}{2(1+\nu)}\nabla(\nabla \cdot \mathbf{u}) - \nabla p + \mathbf{b} = \mathbf{0} \,. \tag{5.8}$$

Equation (5.8) is coupled with the flow equation through the fluid pressure (third term). Assuming that there is no external loading and that the grains are incompressible, the mass conservation of the fluid can be written as (see Appendix VIII)

$$\phi\beta\frac{\partial p}{\partial t} + \frac{\mathrm{d}}{\mathrm{d}\,t}(\nabla \cdot \mathbf{u}) + \nabla \cdot \mathbf{q} = 0 \tag{5.9}$$

where ϕ is porosity, β is the compressibility of water, t is time and $\mathbf{q}$ is the water flux. Note that the flow equation (Eq. (5.9)) is also coupled with the mechanical equation (Eq. (5.8)) through the volumetric strain, i.e. the divergence of the displacements (second term).

The water flux is given by Darcy's law

$$\mathbf{q} = -\frac{k}{\mu}(\nabla p + \rho g \nabla z) \,, \tag{5.10}$$

where k is intrinsic permeability, μ is fluid viscosity, ρ is fluid density, g is gravity and z is the vertical coordinate.

Water compressibility is defined as

$$\beta = \frac{1}{\rho}\frac{\mathrm{d}\,\rho}{\mathrm{d}\,p} \,. \tag{5.11}$$

Integrating Eq. (5.11) gives an exponential variation of water density with respect to fluid pressure increments

$$\rho = \rho_0 \exp(\beta(p - p_0)) \,, \tag{5.12}$$

where p_0 is a reference pressure and ρ_0 is the water density corresponding to the reference pressure p_0.

If density is only a function of pressure, the hydraulic head is defined as (Bear, 1972)

$$h = \int_{p_0}^{p} \frac{\mathrm{d}\, p'}{\rho(p')g} + z\,. \tag{5.13}$$

Darcy's law (Eq. (5.10)) can be expressed as a function of the hydraulic head by using the definition that appears in Eq. (5.13). Thus, introducing Eq. (5.10) in Eq. (5.9) and using Eq. (5.13) yields

$$\phi\beta\frac{\partial p}{\partial t} + \frac{\mathrm{d}}{\mathrm{d}\, t}\left(\nabla\cdot\mathbf{u}\right) = \nabla\cdot\left(\kappa\nabla h\right), \tag{5.14}$$

where $\kappa = k\rho g/\mu$ is the hydraulic conductivity.

Since the mechanical equation (Eq. (5.8)) and the flow equation (Eq. (5.14)) are coupled, they can be combined. Deriving Eq. (5.8) with respect to time, assuming that the loads are stationary, and using Eq. (5.14) for $\partial p/\partial t$ yields

$$G\frac{\partial}{\partial t}\nabla^2\mathbf{u} + \left(\frac{G}{3} + K + \frac{1}{\phi\beta}\right)\frac{\partial}{\partial t}\nabla\left(\nabla\cdot\mathbf{u}\right) - \frac{1}{\phi\beta}\nabla\left(\nabla\cdot\left(\kappa\nabla h\right)\right) = \mathbf{0}\,. \tag{5.15}$$

Alternatively, Eq. (5.15) can be obtained by applying the gradient operator to Eq. (5.14) and substitute in it the fluid pressure gradient given by Eq. (5.8).

We generalize the problem by performing a dimensional analysis. The dimensionless variables of the problem are

$$t_D = \frac{t}{t_c};\ h_D = \frac{h}{h_c};\ \mathbf{u}_D = \frac{\mathbf{u}}{u_c};\ r_D = \frac{r}{L} \text{ and } \kappa_D = \frac{\kappa}{\kappa_c} \tag{5.16}$$

where r is the radial coordinate, L is a characteristic distance and the subscripts D and c denote dimensionless and characteristic variables, respectively. The characteristic variables can be taken as the values of each variable in the aquifer. Thus, the value of the variables in the caprock will be expressed as the ratio with respect to the value of the variable in the aquifer. As for the definition of the characteristic length, which is usually a difficult choice (Kopp *et al.*, 2009), can be chosen as the aquifer thickness.

Using the dimensionless variables of Eq. (5.16), after some algebra, Eq. (5.15) can be written as

$$\frac{G_i u_c \phi_i \beta L}{t_c \kappa_c h_c} G_D \frac{\partial}{\partial t_D}\nabla_D{}^2\mathbf{u}_D + \left(\frac{G_i}{3} + K_i + \frac{1}{\phi_i\beta}\right)\frac{u_c\phi_i\beta L}{t_c\kappa_c h_c}\frac{\partial}{\partial t_D}\nabla_D\left(\nabla_D\cdot\mathbf{u}_D\right) - \nabla_D\left(\nabla_D\cdot\left(\kappa_D\nabla_D h_D\right)\right) = \mathbf{0}\,, \tag{5.17}$$

where the subscript i can be either aq for the aquifer or cap for the caprock.

The characteristic head can be defined from the hydraulic boundary conditions. Since the flow rate is $Q = 2\pi r_w b_{aq} \kappa \left(\partial h / \partial r\right)\big|_{r=r_w}$, where r_w is the radius of the well and b_{aq} is the thickness of the aquifer; its dimensionless form reads

$$\kappa_D r_{w_D} \frac{\partial h_D}{\partial r_D} = \frac{Q}{2\pi b_{aq} \kappa_c h_c}. \tag{5.18}$$

By imposing that the right hand side of Eq. (5.18) equals 1, the characteristic head yields

$$h_c = \frac{Q}{2\pi b_{aq} \kappa_c}, \tag{5.19}$$

where the characteristic hydraulic conductivity can be chosen as the geometric mean of hydraulic conductivities of the aquifer measured at several wells.

The mechanical boundary conditions of this problem are no displacement perpendicular to the bottom and outer boundary. The characteristic displacement u_c can be chosen as the vertical displacement in the aquifer induced by injection. Assuming no horizontal strain in the aquifer, it can be written as

$$u_c = h_c S_s b_{aq} = \frac{Q \rho_0 g \left(\phi_c \beta + \alpha_c\right)}{2\pi \kappa_c} \tag{5.20}$$

where S_s is the specific storage coefficient and $\alpha_c = 1/K_c$ is the compressibility of the aquifer.

The characteristic time can be defined from the flow equation (Eq. (5.14)), yielding the characteristic time of a diffusion equation

$$t_c = \frac{L^2 S_s}{\kappa_c} = \frac{L^2 \rho_0 g \left(\phi_c \beta + \alpha_c\right)}{\kappa_c}. \tag{5.21}$$

Thus, Eq. (5.17) can be written in dimensionless form as

$$G_i' \frac{\partial}{\partial t_D} \nabla_D{}^2 \mathbf{u}_D + \left(\frac{G_i'}{3} + \frac{1}{Le_i} \right) \frac{\partial}{\partial t_D} \nabla_D \left(\nabla_D \cdot \mathbf{u}_D \right) - \nabla_D \left(\nabla_D \cdot \left(\kappa_D \nabla_D h_D \right) \right) = \mathbf{0}, \tag{5.22}$$

where

$$G_i' = G_i \phi_i \beta \tag{5.23a}$$

and

$$Le_i = \frac{\alpha_i}{\phi_i \beta + \alpha_i} \tag{5.23b}$$

are the two dimensionless groups that govern the hydromechanical problem. The dimensionless number appearing in Eq. (5.23b) is the loading efficiency, which represents the ratio of change of fluid pressure to change of mean stress (van der Kamp and Gale, 1983; Hsieh *et al*., 1988).

b) Elasticity in porous media with dilatancy

Frictional materials usually show a change in volumetric strain due to changes in deviatoric stress (Verruijt, 1969; van der Kamp and Gale, 1983). This is because of dilatancy (Barton *et al*., 1985). Later, we perform numerical simulations in which plasticity contains dilatancy, but for the sake of simplicity, here we account for dilatancy as a first approximation by adding to the volumetric strain a term that accounts for volumetric strain due to changes in deviatoric stress

$$\varepsilon_v = \frac{\sigma'_m}{K} + Dq \,, \tag{5.24}$$

where D is a dilatancy coefficient.

Therefore, Hooke's law adopts the following form

$$\boldsymbol{\varepsilon} = \left(\frac{\sigma'_m}{3K} + \frac{D}{3} q \right) \mathbf{I} + \frac{1}{2G} \left(\boldsymbol{\sigma}' - p' \mathbf{I} \right), \tag{5.25a}$$

$$\boldsymbol{\sigma}' = K \left(\varepsilon_v - D' \varepsilon_d \right) \mathbf{I} + 2G \left(\boldsymbol{\varepsilon} - \frac{\varepsilon_v}{3} \mathbf{I} \right), \tag{5.25b}$$

where the dilatancy parameter D' can be related to the parameters $D' = 3DG = \tan\psi$ and ψ is the dilatancy angle.

Then, we proceed in the same manner as in the previous section. But, the dimensionless equation that is obtained for the hydromechanical problem has an additional term for the dilatancy in comparison with Eq. (5.22)

$$G'_i \frac{\partial}{\partial t_D} \nabla_D{}^2 \mathbf{u}_D + \left(\frac{G'_i}{3} + \frac{1}{Le_i} \right) \frac{\partial}{\partial t_D} \nabla_D \left(\nabla_D \cdot \mathbf{u}_D \right) - N_D \frac{\partial}{\partial t_D} \nabla_D \varepsilon_{dD} - \nabla_D \left(\nabla_D \cdot \left(\boldsymbol{\kappa}_D \nabla_D h_D \right) \right) = \mathbf{0} \,, \tag{5.26}$$

where the dimensionless number in the dilatancy term is

$$N_D = \frac{2\pi b_{aq} k_{aq}}{Q\mu} \varepsilon_c K_i \tan\psi \left(1 - Le_i \right), \tag{5.27}$$

where ε_c is a characteristic deviatoric strain.

The main difference between this dimensionless number and the other two is that the hydraulic variables, i.e. permeability and flow rate, appear in the dimensionless number of the dilatancy term.

c) Onset of microseismicity

Induced microseismicity occurs if the stress state is under yield conditions. To determine this, a failure criterion has to be defined. We adopt the Mohr-Coulomb failure criterion (Figure 5.4)

$$\tau = c' + \sigma_n' \tan\phi' , \tag{5.28}$$

where τ is the shear stress, σ_n' is the normal effective stress, c' is cohesion and ϕ' is the friction angle. Fluid pressure increases due to fluid injection, which displaces the Mohr circle to the left. Shear failure, leading to slip along the planes of a fracture, occurs when the Mohr circle becomes tangent to the failure envelope. This can occur in a favorably oriented cohesionless pre-existing fracture (Mohr circle with center *C'* in Figure 5.4) or in intact rock if the deviatoric stress (difference between the maximum and the minimum principal stresses) is sufficiently large to make the Mohr circle becomes tangent to the failure envelope. Alternatively, if the least principal stress equals the rock tensile strength, σ_t', a hydrofracture will be created perpendicular to the least principal stress (Mohr circle with center *C''* in Figure 5.4). If the least principal stress is horizontal, hydrofractures will be vertical. But if the least principal stress is vertical, hydrofractures will be horizontal (Klee *et al*., 2011). Generally, shear failure in pre-existing fractures occur before failure of intact rock, even when they are not favorably oriented (Rutledge and Phillips, 2003).

The style of faulting is a consequence of the pre-existing stress tensor. There are three cases depending on the relative magnitude of the vertical stress with respect to the two horizontal principal stresses: normal, strike slip and reverse faulting. Normal faulting occurs when the vertical stress is the maximum principal stress; strike slip faulting occurs when the vertical stress is the intermediate principal stress and reverse faulting occurs when the vertical stress is the minimum principal stress. The latter may take place in compressional regimes where lateral deformation is constrained in the direction perpendicular to compression. A compilation of the present-day stress field was carried out by the World Stress Map Project (Zoback, 1992).

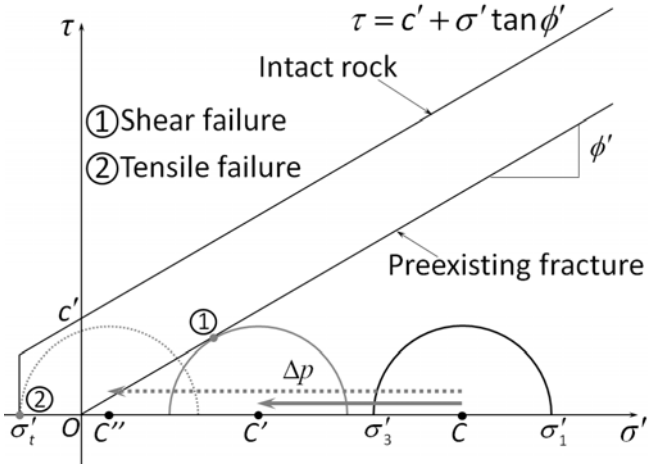

Figure 5.4 – Mohr-Coulomb failure criterion. Fluid pressure increases due to fluid injection, displacing the Mohr circle to the left. In a favorably oriented cohesionless pre-existing fracture, slip occurs when the Mohr circle becomes tangent to the failure envelope (Mohr circle with center *C'*). In intact rock, if the least principal stress equals the rock tensile strength, a hydrofracture will be created perpendicular to its direction (Mohr circle with center *C''*). Alternatively, if deviatoric stress increases and the Mohr circle becomes tangent to the failure envelope, the intact rock will fail along a shear plane.

5.3.3. Numerical solution

a) Elastic models

The hydromechanical characterization test is simulated using the fully coupled finite element code CODE_BRIGHT (Olivella *et al*., 1994, 1996). An ideal homogeneous horizontal aquifer–caprock system with the geometrical distribution of the Hontomin pilot test is considered (Figure 5.3). The aquifer has a thickness of 100 m, which we define as the characteristic length of the problem. The top of the aquifer is located at a depth of 1500 m. The aquifer is overlaid by a low-permeability caprock. Several thicknesses of the caprock have been considered: from 50 to 1500 m. The caprock is covered by a low shear strength media, which do not need to be included in the model. The system is axisymmetric and extends laterally up to 20 km. An injection well with a radius of 0.15 m is placed at the centre of the domain and the observation well is placed 50 m away. A structured mesh of quadrilateral elements has been used. The element size grows progressively from the injection well to the outer boundary. As a first step, a steady-state calculation is carried out to ensure equilibrium for the pressure and stress fields prior to injection.

b) Plastic models

Microseismicity propagation patterns are investigated by making an analogy between plastic strain and microseismic events. Since plastic strain occurs when a seism takes place, the region where seismic events would occur can be assessed by tracking the evolution of plastic strain. Thus, we simulate fluid injection using a viscoplasticity constitutive law in 3D models that represent the three possible stress regimes, i.e. normal, strike slip and reverse faulting. The details of the viscoplastic constitutive law can be found in Vilarrasa *et al*. (2010b). The geometry of these models is analogous to the axisymmetric models, but in 3D. We only model one fourth of the domain because of symmetry. The stress ratio $\sigma'_v : \sigma'_H : \sigma'_h$, where σ'_v is the vertical effective stress, σ'_H is the maximum horizontal principal effective stress and σ'_h is the minimum horizontal principal effective stress, is 1:0.65:0.4 for normal faulting, 1:1.1:0.45 for strike slip faulting and 1:1.95:1.1 for reverse faulting. The friction angle has been set to 30º for the aquifer and to 22º for the caprock.

5.4. Results

5.4.1. Hydromechanical behaviour

When injecting a fluid in an aquifer, fluid pressure increases, changing the effective stress field. This produces an expansion of the aquifer. As a result, the caprock is also deformed (Figure 5.5a). But the pressure buildup propagation from the injected aquifer into the caprock is orders of magnitude slower than that of the aquifer due to the permeability contrast between the two formations. This means that the overpressure caused by injection only affects the first meters of the lower part of the caprock. However, fluid pressure changes occur in the caprock. In fact, fluid pressure decreases in the upper part of the caprock. These fluid pressure changes in the caprock are due to volumetric strain variations caused by caprock deformation (Figure 5.5). Fluid pressure drops in the parts of the caprock where the pore volume increases (extension occurs). This is because the pore space becomes bigger while the mass of fluid remains constant and thus fluid pressure is reduced. In contrast, fluid pressure increases in the parts of the caprock where the pore volume decreases (compression occurs). This is because the pore space becomes smaller for a constant mass of fluid and thus fluid pressure increases.

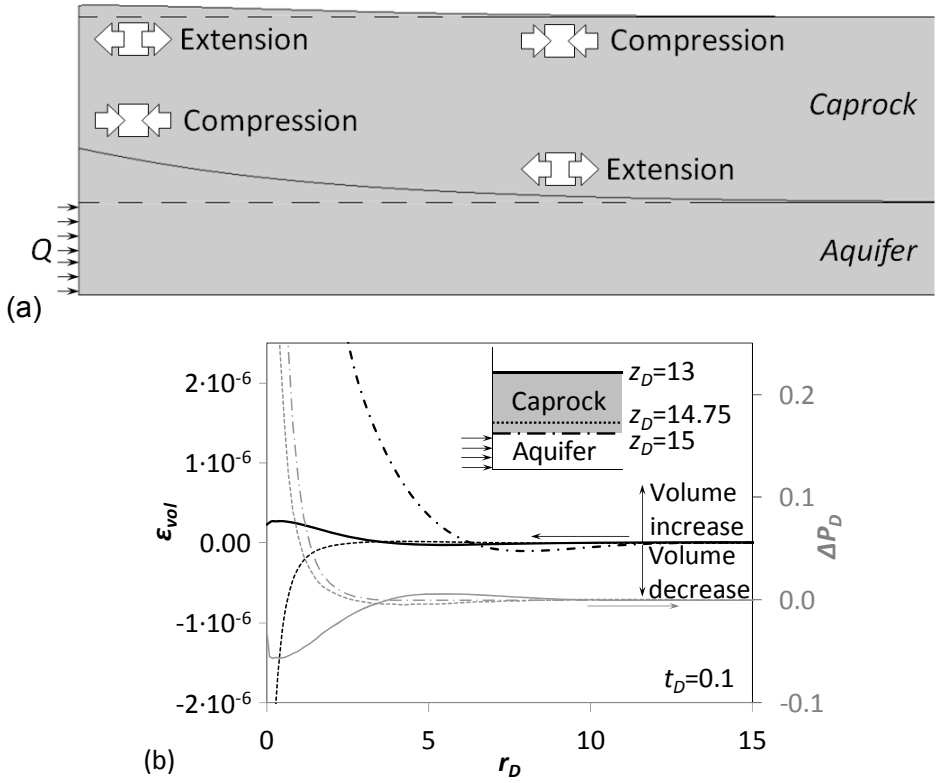

Figure 5.5 – (a) Original (dashed lines) and deformed form of the aquifer and caprock when injecting a fluid in the aquifer. The uplift at the top of the aquifer generates compression in the lower part of the caprock close to the injection well and extension far from it. However, extensions appear in the upper part of the caprock close to the well and compressions far from it. (b) Volumetric strain and dimensionless fluid pressure change versus dimensionless distance from the injection well at several dimensionless depths. The pore volume decreases close to the well in the lower part of the caprock because the aquifer uplift compresses it. The pore volume increases close to the well at the top of the caprock due to extension. Fluid pressure in the caprock is inversely proportional to the volumetric strain change. Thus, fluid pressure increases where the pore volume decreases and decreases where the pore volume increases.

Figure 5.5a displays the original and deformed form of the aquifer and caprock as a consequence of fluid injection in the aquifer. Vertical displacement presents a shape similar to that of fluid overpressure at the top of the aquifer, which decreases logarithmically with distance. However, vertical displacement becomes smoother at the top of the caprock. The uplift at the top of the aquifer generates compression in the lower part of the caprock close to the injection well, so fluid pressure increases. However, extensions appear at the top of the caprock close to the well, which increases the pore volume and thus fluid pressure decreases (Figure 5.5b). This leads to a reverse-water level fluctuation, which is well-documented in confined aquifers. When fluid is pumped, hydraulic heads in adjacent aquitards rise after pumping starts

(Rodrigues, 1983; Hsieh, 1995; Kim and Parizek, 1997). This phenomenon is known as “reverse-water level fluctuation” or “Noordbergum effect”, because it was observed for the first time in the village of Noordbergum, the Netherlands (Verruijt, 1969). However, since in CO_2 sequestration a fluid is injected, it occurs the opposite response that the one observed in Noordbergum, i.e. fluid pressure drops in the upper part of caprock close to the injection well (Vilarrasa *et al*., 2010b). The contrary occurs far away from the injection well, i.e. extensions at the lower part of the caprock and compressions at its top. However, these are small compared to those close to the well.

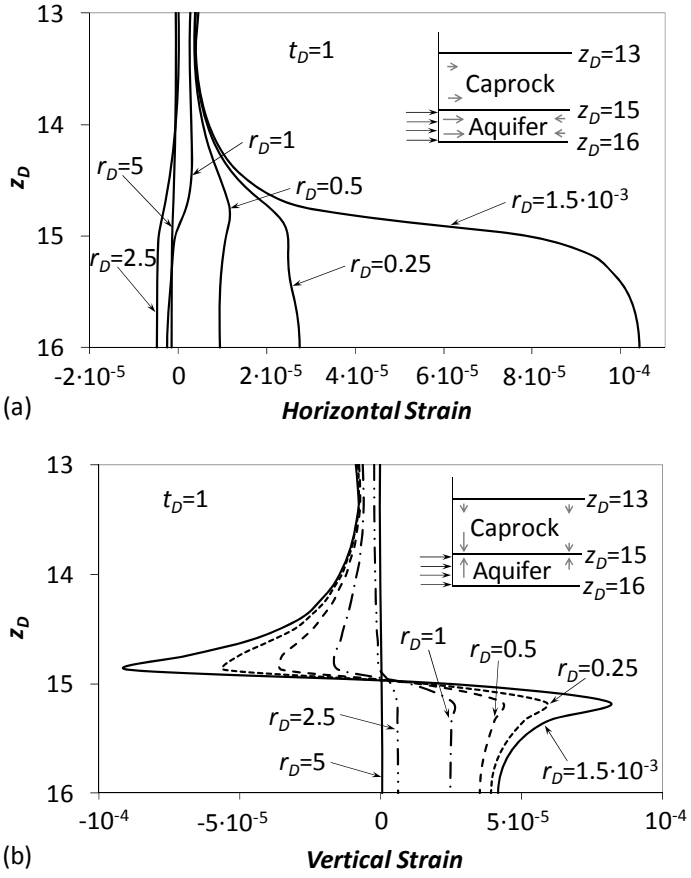

Figure 5.6 – (a) Horizontal strain as a function of dimensionless depth at several dimensionless radial distances from the injection well. The injected water displaces the aquifer laterally. The horizontal strain mainly concentrates in the aquifer. Relative displacements between the aquifer and the caprock may occur in the presence of a clay-rich layer with a low friction angle. (b) Vertical strain as a function of dimensionless depth at several dimensionless radial distances from the injection well. The vertical strain is high in the aquifer, where the injected water expands the pore volume, lifting the formation. The caprock, which is pushed upwards, acts as a spring, mitigating the uplift. The grey arrows in the inlets indicate the direction of the strain.

Fluid injection produces both a vertical and a horizontal displacement of the aquifer. The aquifer is horizontally displaced away from the injection well (Figure 5.6a) and pushed upwards (Figure 5.6b). The horizontal strain can even become negative at a certain distance from the well. The deformation of the aquifer produces deformation of the caprock, with the condition that displacements are continuous at the aquifer-caprock interface. The caprock acts as a spring, dissipating the deformation of the aquifer. Hence, horizontal strain decreases rapidly at the lower part of the caprock (Figura 5.6a) and vertical strain is negative in the caprock (Figura 5.6b), which means that its thickness becomes smaller. The high gradient of horizontal strain at the aquifer-caprock contact suggests that relative displacements between the two formations might occur in the presence of a clay-rich layer with a low friction angle (see Figure 5.2). If this occurred, microseismic events would be triggered.

5.4.2. Sensitivity analysis

a) Aquifer

The mechanical properties of the rocks that form the reservoir and the caprock in potential CO_2 storage sites are highly variable (see Section 5.2). We analyze the sensitivity to the mechanical properties within each geological formation separately. We start by varying the mechanical properties of the aquifer while maintaining those of the caprock constant. The ratio of the caprock to aquifer thickness is set to 2.

Figure 5.7 displays the dimensionless overpressure and vertical displacement as a function of the dimensionless group of the volumetric strain term $\Gamma_{aq} = G'_{aq}/3 + 1/Le_{aq}$ (second term in the left hand side of Eq. (5.22)) at the top of the aquifer and the top of the caprock. The results correspond to a dimensionless time equal to 1 and a dimensionless distance from the injection well of 0.5. The most relevant variables in this analysis are listed in Table 5.1. The dimensionless group of the volumetric strain term Γ_{aq} is a measure of the stiffness of the rock. High values of Γ_{aq} indicate a stiff rock and low values of Γ_{aq} indicate a soft rock. Dimensionless fluid overpressure in the aquifer decreases slightly as the aquifer becomes stiffer and the effect of the Poisson ratio has little effect (Figure 5.7a). The reverse-water level fluctuation is more pronounced for soft aquifers, which can lead to a fluid pressure drop at the top of the caprock almost as high as the overpressure in the aquifer. However, fluid pressure

variations at the top of the caprock are almost negligible when injecting in very stiff aquifers. Note that the curves of pressure drop at the top of the caprock coincide regardless of the Poisson ratio. This means that the Poisson ratio of the aquifer has no effect on the overpressure at the top of the caprock when plotting the results as a function of the dimensionless group of the volumetric strain term Γ_{aq}.

Table 5.1 – Variable definition

Variable	Definition
$\Gamma_i = \frac{G_i'}{3} + \frac{1}{Le_i}$	Dimensionless group of the volumetric strain term of the hydromechanical equation. Summation of one third of the pore rigidity ratio and the inverse of the loading efficiency. Subscript i indicates either the aquifer, aq, or the caprock, cap
$G_i' = G_i \phi_i \beta$	Pore rigidity ratio. Product of rock shear modulus, rock porosity and water compressibility, where i indicates either aquifer, aq, or caprock, cap.
$Le_i = \frac{\alpha_i}{(\alpha_i + \phi_i \beta)}$	Loading efficiency. Ratio of rock compressibility to rock compressibility plus water compressibility multiplied by porosity. The subscript i indicates either aquifer, aq, or caprock, cap.
$L = b_{aq}$	The characteristic length has been chosen as the thickness of the aquifer.
$t_D = \frac{\kappa_{aq} t}{L^2 S_s}$	Dimensionless time. Ratio of the product of aquifer hydraulic conductivity and time to the product of the square of the characteristic length and the specific storage coefficient.
$S_s = \rho g (\phi\beta + \alpha)$	Specific storage coefficient. Product of fluid density, gravity and the sum of rock compressibility and water compressibility multiplied by porosity.
$r_D = \frac{r}{L} = \frac{r}{b_{aq}}$	Dimensionless radial distance. Ratio of the radial distance to the characteristic length.
$u_{z_D} = \frac{u_z}{h_c S_s b_{aq}}$	Dimensionless vertical displacement. Ratio of the vertical displacement to the product of characteristic head, specific storage coefficient and aquifer thickness.

$h_c = \dfrac{Q}{2\pi b_{aq}\kappa_{aq}}$ Characteristic head. Ratio of the flow rate to the product of 2π, aquifer thickness and aquifer hydraulic conductivity.

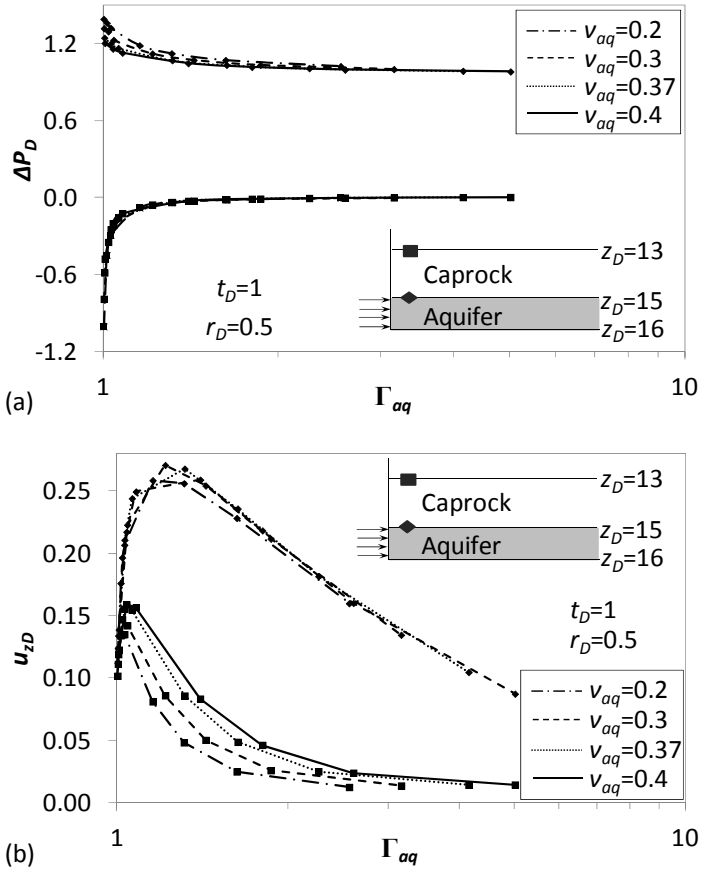

Figure 5.7 – (a) Dimensionless overpressure and (b) dimensionless vertical displacement as a function of the dimensionless group of the volumetric strain term Γ_{aq} at a dimensionless time equal to 1 at the top of the aquifer. Measurements are taken at an observation well placed at a dimensionless distance of 0.5 from the injection well.

Similarly, the dimensionless vertical displacement at the top of the aquifer is independent of the aquifer Poisson ratio when plotted as a function of the dimensionless group of the volumetric strain term Γ_{aq} (Figure 5.7b). However, it has some effect at the top of the caprock, which can help to characterize the aquifer's Poisson ratio. The dimensionless vertical displacement is small for very soft aquifers. It increases both at the top of the aquifer and the caprock as the aquifer becomes stiffer, until it reaches a maximum and then decreases (Figure 5.7b). This behaviour can be explained by the fact that as the aquifer becomes stiffer, its loading efficiency (Eq. (5.23b)) decreases. The loading efficiency measures the part of a load that is taken by

the pore-water with respect to the solid skeleton of a soil or rock. While water takes almost all the load in soft soils, stiff rocks have a compressibility comparable to that of water multiplied by porosity, so the load distributes between the solid skeleton and the water. Thus, the dimensionless vertical displacement presents its maximum when a non-negligible part of the load is taken by the solid skeleton of the porous media. The difference between the vertical displacement at the top of the caprock and at the top of the aquifer is the amount of displacement absorbed by the caprock.

Field measurements of fluid pressure and vertical displacement can be used to characterize the mechanical properties of the aquifer and caprock. Figure 5.8 shows possible combinations of fluid overpressure and vertical displacement at the top of the aquifer as a function of the aquifer mechanical properties at a dimensionless distance of 0.5 from the injection well. Thus, the mechanical properties of the aquifer can be determined by introducing field measurements (fluid overpressure and vertical displacement) in Figure 5.8.

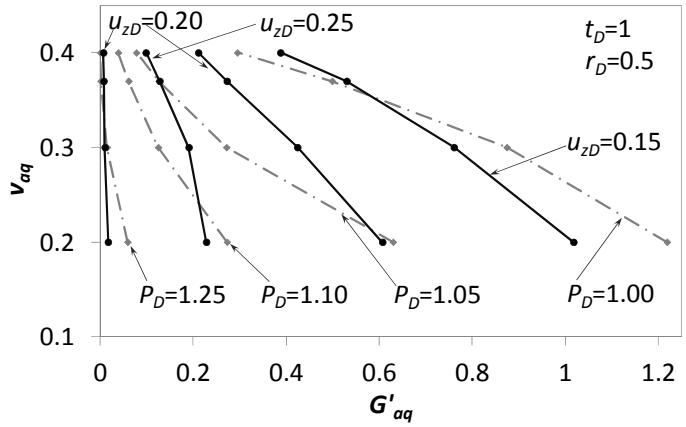

Figure 5.8 – Aquifer Poisson ratio ν_{aq} versus aquifer pore rigidity ratio G'_{aq} for several dimensionless overpressure and dimensionless vertical displacement at the top of the aquifer. Results for a dimensionless time equal to 1 and a dimensionless distance of 0.5 from the injection well. The intersections are possible combinations of the aquifer mechanical properties.

The proposed test can also be used as a conventional hydraulic test to characterize the hydraulic properties of the aquifer. The interpretation of fluid pressure evolution of the injection test gives the aquifer transmissivity and storage coefficient (Cooper and Jacob, 1946). The mechanical properties of the aquifer have little effect on fluid overpressure evolution in the aquifer when plotted in dimensionless variables (Figure 5.9a). In actual dimensions, pressure buildup is delayed in soft aquifers and for small Poisson ratios because of their higher storativity. On the other hand, pressure drop at

the top of the caprock becomes bigger for softer aquifers (Figure 5.9b). Note the difference between hydromechanical simulations and a purely hydraulic simulation (denoted by *H* in Figure 5.9). Although the difference is small in the aquifer, the reverse-water level fluctuation does not occur in the caprock. Thus, hydromechanical simulations are essential for understanding the processes undergoing in the caprock during fluid injection.

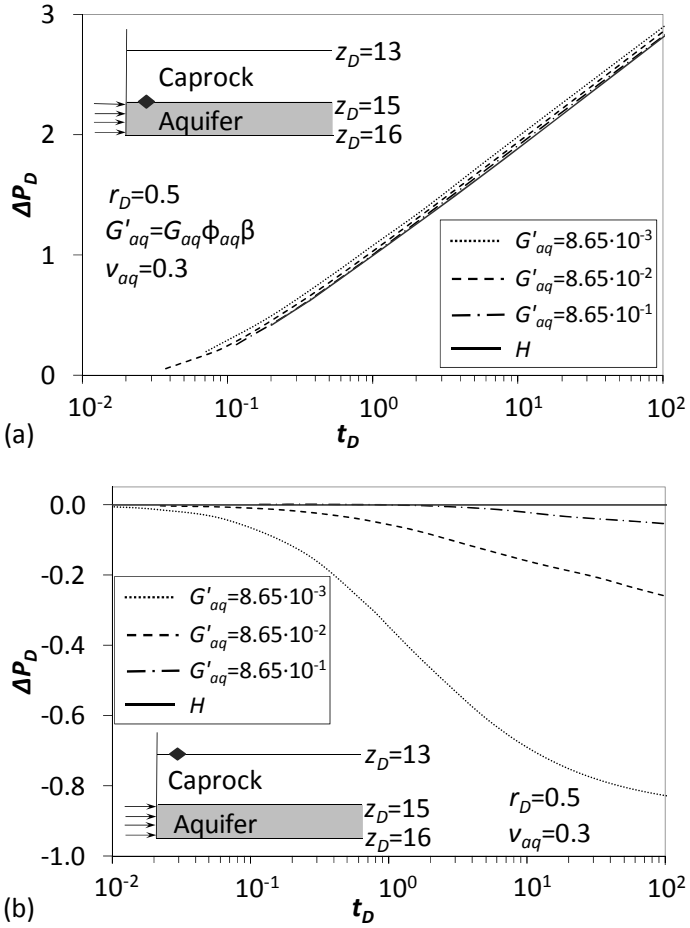

Figure 5.9 – Dimensionless overpressure as a function of the logarithm of dimensionless time at a dimensionless distance of 0.5 from the injection well for several mechanical dimensionless numbers and purely hydraulic simulation (*H*) (a) at the top of the aquifer and (b) at the top of the caprock.

b) Caprock

Next, we change the caprock mechanical properties while maintaining those of the aquifer constant. Here, the effect of the caprock thickness is also examined. Figure 5.10 shows the dimensionless overpressure at the top of the aquifer as a function of the dimensionless group of the volumetric strain term Γ_{cap} for a dimensionless time

equal to 1 and a dimensionless distance from the injection well of 0.5. The overpressure increases slightly as the caprock becomes stiffer. This was also observed by Yin *et al*. (2009), but considering that the reservoir is closed, i.e. it is completely surrounded by a low-permeability formation. The thickness of the caprock has a greater effect in stiff caprocks than in soft ones. The thicker the caprock, the higher the overpressure at the top of the aquifer. This is because stiff thick caprocks control de rigidity of the aquifer-caprock system, increasing the stiffness of the aquifer. This affects the storage coefficient, reducing it and therefore the pressure buildup occurs before than in the presence of a thin soft caprock.

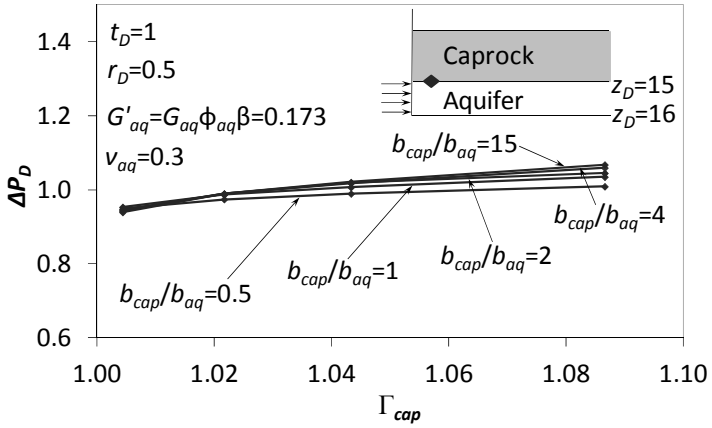

Figure 5.10 – Dimensionless overpressure at the top of the aquifer as a function of the dimensionless group of the volumetric strain term Γ_{cap} at a dimensionless time equal to 1 at a dimensionless distance of 0.5 from the injection well for several ratios of the caprock to aquifer thickness. The properties of the aquifer are constant. The stiffness and thickness of the caprock alter the aquifer storage coefficient. Stiff thick caprocks lead to a lower aquifer storage coefficient than soft thin caprocks, which advances the pressure buildup response to fluid injection.

The variation of the mechanical properties and thickness of the caprock has a greater effect on the vertical displacement (Figure 5.11) than on the overpressure (Figure 5.10). Although the caprock's Poisson ratio has a negligible effect both on fluid overpressure and vertical displacement (results not shown), the stiffness of the caprock does have an effect. Vertical displacement at the top of the aquifer decreases as the caprock becomes stiffer and thicker because they increase the bending moment of the caprock, which opposes to vertical displacement. In contrast, vertical displacement at the top of the caprock increases as the caprock becomes stiffer. This is because the stiffer the caprock, the lesser deformation it absorbs. Furthermore, vertical displacement decreases as the thickness of the caprock increases because a greater

deformation can be absorbed within the caprock. This leads to the extreme case of thick soft caprocks that can yield subsidence at the top of the caprock (Figure 5.11). The dashed lines reproduce the vertical displacement of a caprock that reaches the surface at the depths of the top of all the considered caprocks. The vertical displacement is similar at all depths when the caprocks are soft. However, the deformation within the caprock is significantly different for stiff caprocks, in part because the vertical displacement at the top of the aquifer is controlled by the caprock thickness.

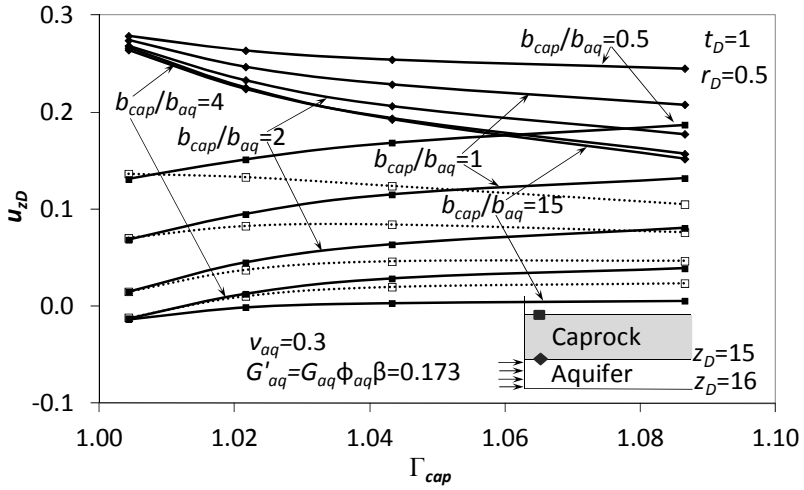

Figure 5.11 – Dimensionless vertical displacement at the top of the aquifer and the caprock as a function of the dimensionless group of the volumetric strain term Γ_{cap} at a dimensionless time equal to 1 at a dimensionless distance of 0.5 from the injection well for several ratios of the caprock to aquifer thickness. The properties of the aquifer are constant. Thick caprocks with low-rigidity can yield subsidence.

5.4.3. Induced microseismicity analysis

a) Elastic models

Figure 5.12 displays the mobilized friction angle at the top of both the aquifer and the caprock as a function of the dip angle of a pre-existing cohesionless fracture for a dimensionless time equal to 1. The vertical stress is the maximum principal stress and the horizontal stresses are equal due to axysimmetry in this slip tendency analysis. Soft aquifers yield a higher mobilized friction angle than stiff aquifers. However, the stiffness of the aquifer has little effect on the mobilized friction angle. On the other hand, the stiffness of the caprock has a negligible effect on the mobilized friction angle. The maximum mobilized friction angles at the top of the aquifer are in the order of 25-30°

for steep fractures with a dip angle around 60°; and in the order of 15-17° for fractures with a dip angle around 55° at the top of the caprock.

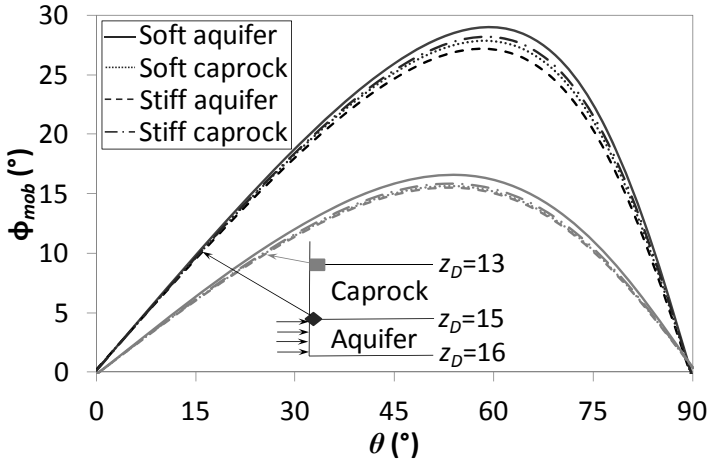

Figure 5.12 – Mobilized friction angle at the injection well in the aquifer-caprock contact and at the top of the caprock as a function of the dip angle for soft and stiff aquifers and caprocks for a dimensionless time equal to 1.

Figure 5.13 shows the mobilized friction angle at the top of the aquifer as a function of time. Soft aquifers yield a higher mobilized friction angle than stiff aquifers for a dimensionless time equal to 1. However, this relationship is inverted for later times of injection. The mobilized friction angles increases linearly with the logarithm of time in stiff aquifers, which will lead to failure conditions in long injection periods. The effect of the Poisson ratio is non-negligible. This is because the changes in horizontal stresses induced by fluid injection depend on the Poisson ratio (e.g. Rutqvist, 2012) in such a way that the smaller the Poisson ratio, the higher the horizontal stress increment. Therefore, the Mohr circle becomes smaller for small Poisson ratios, leading to a lower mobilized friction angle.

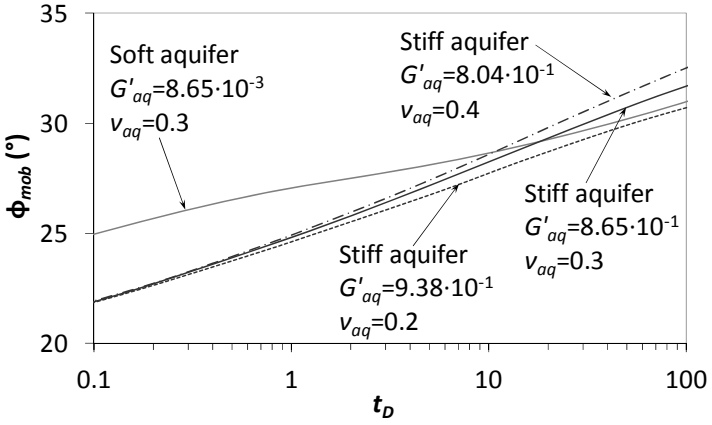

Figure 5.13 – Mobilized friction angle at the injection well at the top of the aquifer as a function of time.

The fact that the dip angle corresponding to the maximum mobilized friction angle varies from the aquifer to the caprock (Figure 5.12) is not a coincidence. In fact, the dip angle corresponding to the maximum mobilized friction angle can be obtained geometrically, as shown in Figure 5.14, and is equal to

$$\delta = \frac{\pi}{4} + \frac{\phi'_{mob}}{2}, \tag{5.29}$$

where δ is the angle with respect to the horizontal of the critically oriented fracture and ϕ'_{mob} is the mobilized friction angle. The mobilized friction angle is such that the Mohr-Coulomb envelope is tangent to the Mohr circle. The pole (denoted by *P* in Figure 5.14) of the Mohr circle coincides with the minimum principal stress in a stress field where the maximum principal stress is vertical. Though fluid injection produces a slight rotation of the stress tensor, it is very small and can be neglected. Recall that any straight line drawn from the pole will intersect the Mohr circle at a point that represents the stress state on a plane inclined at the same orientation in space as that line. Thus, the line that joins the pole with point *A*, i.e. the point of tangency between the Mohr circle and the Mohr-Coulomb envelope, gives the inclination of the critically oriented fracture. Hence, the higher the mobilized friction angle, the steeper the critically oriented fracture. Replacing the maximum mobilized friction angles in the aquifer and caprock in Equation (5.29) gives the dip angles of the critically oriented fractures for triggering induced microseismicity shown in Figure 5.12.

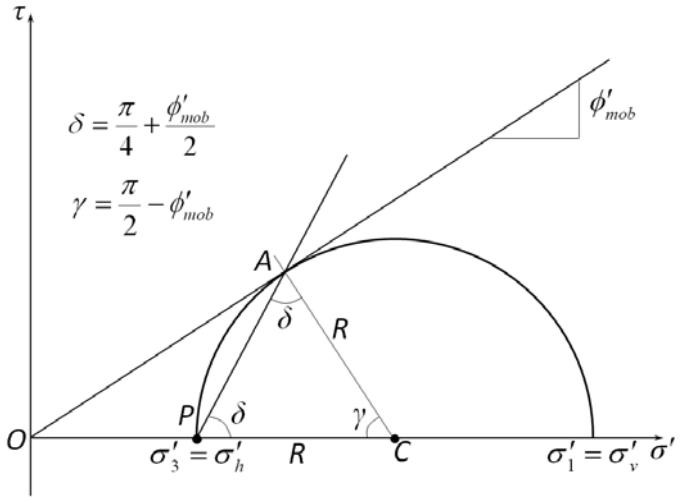

Figure 5.14 – Mohr circle representing the stress state of a point. The mobilized friction angle is related to the dip angle of critically oriented fracture, δ, through geometric properties of triangles.

b) Plastic models

The type of faulting is determined by the stress tensor. In a normal faulting stress regime, rock fails along steep shear planes (Figure 5.15b, c). The numerical model reproduces very well the plastic propagation, which follows an angle equal to $\pi/4+\phi'/2$ (Figure 5.15c). Note that this is the same stress regime as the one analysed in the previous section. The fact that the rock has some cohesion does not affect the angle in which shear occurs because the proportions between the triangles in the Mohr-Coulomb failure analysis are maintained (Figure 5.15a).

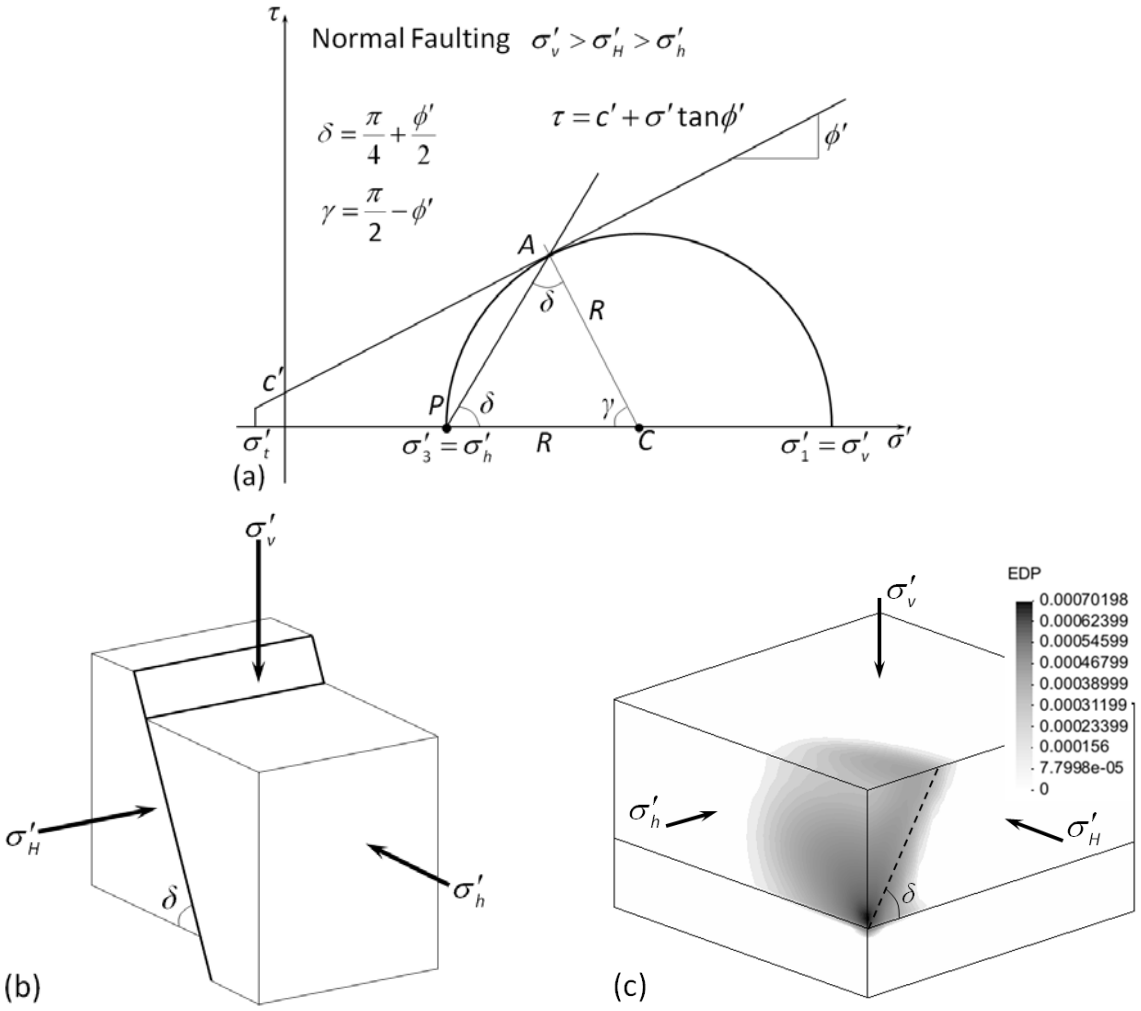

Figure 5.15 – Normal faulting stress regime. (a) Mohr circle at failure, (b) schematic representation of the failure mechanism and (c) plastic deformation obtained from a numerical simulation.

In a strike slip stress regime, vertical shear planes are formed (Figure 5.16b). The situation of the pole is somewhat arbitrary in this stress regime. The pole coincides with the maximum horizontal principal effective stress in Figure 5.16a. However, if the pole

had coincided with the minimum horizontal principal effective stress, the angle with respect to this direction in which shear occurs would have been the complimentary of the one shown in Figure 5.16a, i.e., $\pi/4+\phi'/2$, leading to the same orientation of the shear plane shown in Figure 5.16b. Numerical results show that plastic deformation is vertical and perpendicular to the maximum horizontal stress (Figure 5.16c). The region that presents plastic deformations is relatively wide because viscoplasticity regularizes and does not localize the failure mechanism.

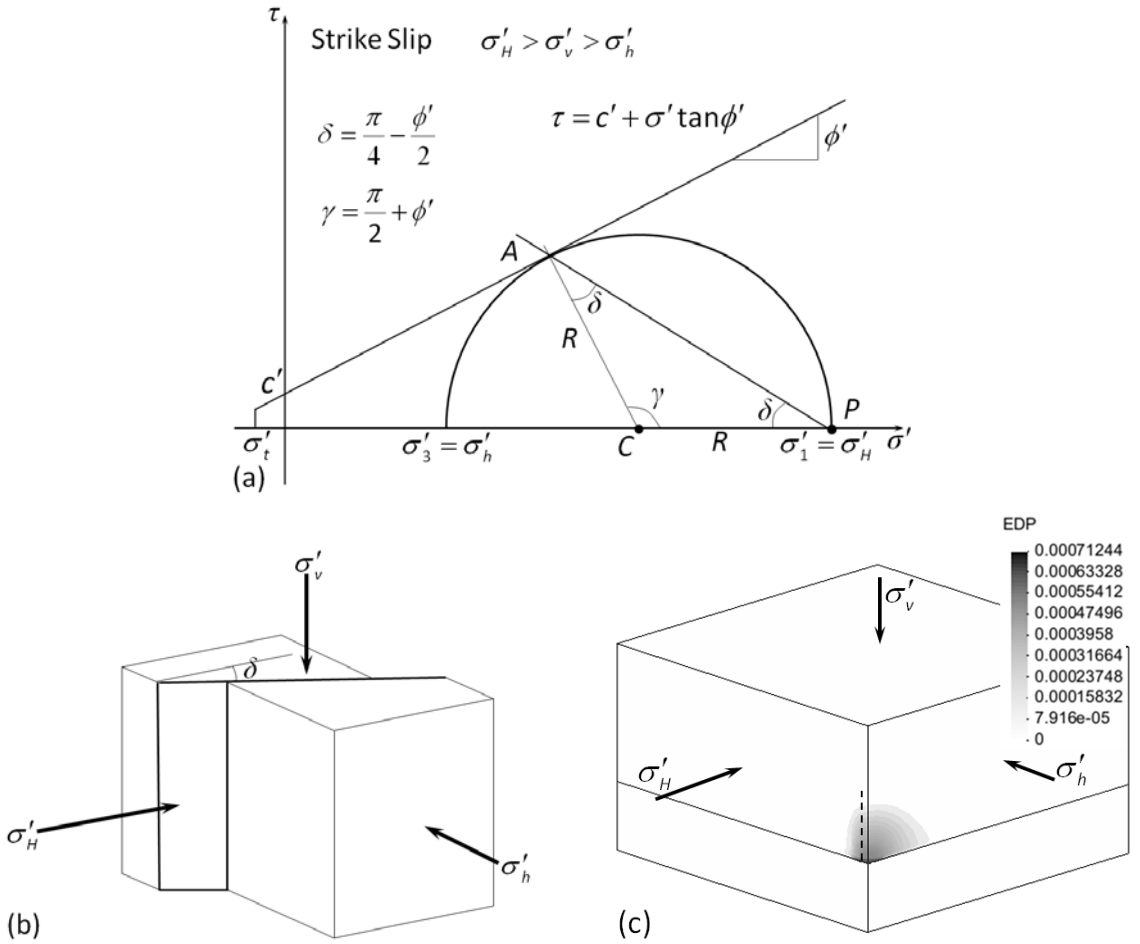

Figure 5.16 – Strike slip faulting stress regime. (a) Mohr circle at failure, (b) schematic representation of the failure mechanism and (c) plastic deformation obtained from a numerical simulation.

In a reverse faulting stress regime, rock fails along shallowly dipping shear planes (Figure 5.17b, c). In this case, the pole coincides with the maximum horizontal principal effective stress and thus the failure plane (line *P-A*) presents a dip angle equal to $\pi/4-\phi'/2$, which is lower than 45º (Figure 5.17a). Figure 5.17c shows plastic deformations occurring subhorizontally. Microseismicity monitoring can give a clue of

the existing stress tensor at the site by identifying the propagation pattern with one of these types of faulting.

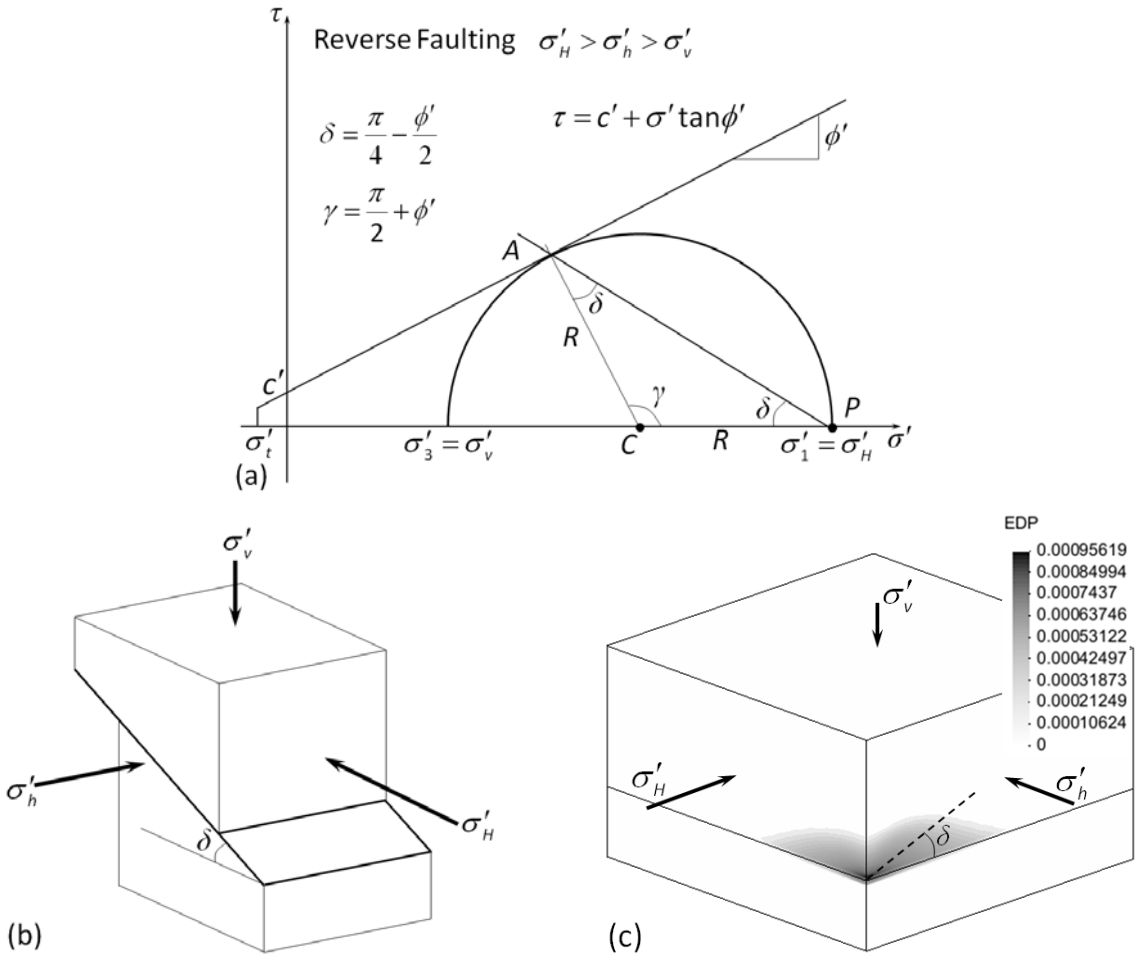

Figure 5.17 – Reverse faulting stress regime. (a) Mohr circle at failure, (b) schematic representation of the failure mechanism and (c) plastic deformation obtained from a numerical simulation.

Figure 5.18 displays deviatoric versus mean effective stresses trajectories of the three stress regimes at a point of the caprock placed 25 m away from the top of the injection well in all directions. All the trajectories start inside the failure envelope (elastic behaviour). However, the trajectories shift to the left because of fluid pressure increase once fluid injection starts. Finally, all trajectories touch the failure envelope, meaning that the caprock yields and microseismic events occur.

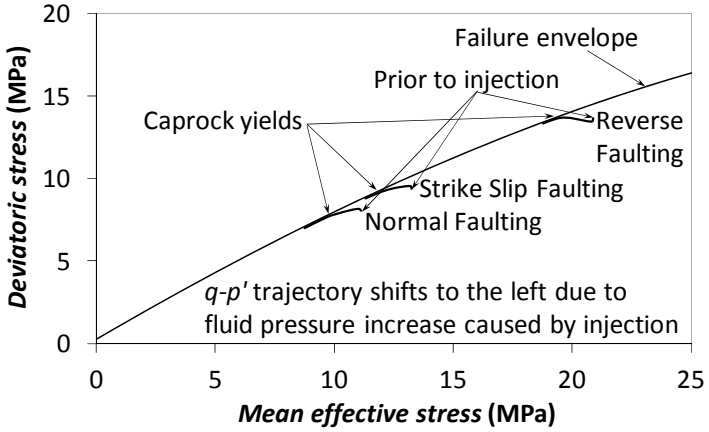

Figure 5.18 – Deviatoric versus mean effective stresses trajectories of a point of the caprock placed 25 m away from the top of the injection well in all directions for a normal, a strike slip and a reverse faulting stress regime.

5.5. Discussion

We propose a hydromechanical characterization test that will permit estimating representative values of the hydromechanical properties at the field scale. These values can be used as input data in numerical models, enabling to obtaining good fittings with measured data.

Not only does this injection test give information on the hydraulic properties of the aquifer, but also on the hydraulic properties of the caprock and boundaries. A first estimate of the aquifer transmissivity can be obtained from Earth tide analysis by monitoring fluid pressure fluctuations and Earth tide dilation of the aquifer prior to the injection (Hsieh *et al*., 1987). Furthermore, the injection will last several hours and up to a few days, so the drawdown evolution curve will suffer several changes in its slope in a semilog plot. These changes in slope give information on the permeability of the caprock (Hantush, 1956; Neuzil, 1986) or the existence of faults that may act either as a flow barrier or constant head boundaries (Hsieh and Bredehoeft, 1981). If the pressure buildup cone reaches these faults, their nature can be determined. Apart from this, if the open up of fractures occurs in the aquifer (triggering microseismic events) as a response to high pressure injection, permeability can be enhanced, which would reduce the slope of the drawdown evolution curve in the semilog plot. This can be accommodated in numerical models by using stress dependent permeability models.

Additionally, this field test can be used as a means of measuring the caprock stability to fluid injection at high pressure. We suggest injecting water, but CO_2 can be used as well, because it has been observed that water and CO_2 have a similar effect on fracture stimulation (Verdon *et al*., 2010). Microseismicity monitoring should allow to the location of the induced microseismic events (Xuan and Sava, 2010). The minimum detectable magnitude depends on the depth at which an array of geophones can be placed. Small events, of magnitude ranging from -3 to -2, can be detected only if the geophones are placed in a nearby borehole at a similar depth than the aquifer-caprock system (Moeck *et al*., 2009; Bohnhoff *et al*., 2010). The fracture slip likelihood as a function of fracture orientation can be determined from a slip tendency analysis (Segall and Fitzgerald, 1998; Moeck and Backers, 2011). The mobilized friction angle is higher in the aquifer than in the caprock (Figure 5.12) because the overpressure induced by injection translates the Mohr circle to the left (recall Figure 5.4). However, the likelihood of microseismic events occurrence depends on the actual friction angle of each formation. For instance, shear failure can occur in the caprock in critically oriented fractures with low-friction angles (Figure 5.2). The onset of microseismicity in the caprock can be used to define the maximum sustainable injection pressure. The value of this sustainable pressure will be a measure of the suitability of a specific site for permanent CO_2 storage. Low values of the maximum sustainable injection pressure are indicative that the site can undergo large plastic deformations and may reactivate faults (Rutqvist *et al*., 2008) through which CO_2 could migrate towards freshwater aquifers or even the surface.

The stress tensor plays an important role in assessing the suitability of a specific site for permanent CO_2 storage. Shear planes are subhorizontal in reverse faulting stress regime, but they are subvertical in normal faulting stress regime, as shown theoretically and numerically (Figures 5.15 and 5.17). Thus, it is more likely that the CO_2 finds a migration path that crosses the whole caprock in a normal faulting than in a reverse faulting stress regime. But, strike slip stress regime seems even more unfavorable, because shear planes are vertical (Figures 5.16). However, the size of earthquakes depends on the stress regime. Schorlemmer *et al*. (2005) found that the largest earthquakes occur in reverse faulting stress regime; normal faulting stress regime presents a larger proportion of small earthquakes and strike slip faulting stress regime has an intermediate behaviour. Hence, the propensity for larger earthquakes in a reverse faulting stress regime counterbalances the less unfavorable orientation of shear planes. However, the stress regime should not be a limiting factor if a careful

monitoring of the hydromechanical response is performed, as evidenced in In Salah (Rutqvist, 2012), where a strike slip stress regime exists.

The stress tensor can be determined from observation of breakouts, tensile fractures and induced hydrofractures in wells (Zoback *et al*., 2003). Alternatively, the observation of similar patterns in microseismic events (e.g. doublets, multiplets, wavelength, slip direction) can give clues to determine the stress tensor (Rubin *et al*., 1999; Tezuka and Niitsuma, 2000; Pytharouli *et al*., 2011). The stress tensor determination is not easy and may change with depth (Plenefisch and Bonjer, 1997; Klee *et al*., 2011). Nevertheless, the magnitude and orientation of the principal stresses should be, at least, delimited in order to have some confidence on the existing stress tensor and how far or close it is from failure. The latter can be assessed by the interpretation of the proposed hydromechanical characterization test.

The dimensional analysis of the hydromechanical equations shows that the problem is governed by two parameters: the loading efficiency and another that we have called the pore rigidity ratio. However, the later can be expressed as a function of the loading efficiency and the Poisson ratio as

$$G' = \left(\frac{1}{Le} - 1 \right) \frac{3(1-2\nu)}{2(1+\nu)}. \tag{5.30}$$

Note that the ratio where the Poisson ratio appears is the shear to bulk modulus ratio, i.e. G/K . The dimensionless curves of fluid pressure and vertical displacement as a function of these parameters permit the estimation of the mechanical properties of the aquifer and caprock. The dimensional analysis considers the possibility that the rock presents dilatancy. Its effect should be considered as a possible contributing term when analyzing hydromechanical measurements. Though real potential storage sites will present a complex geometry, each site may be idealized as one similar to the ones studied here. Thus, the results presented here will permit to gain insight on the relevant hydromechanical processes occurring in each site.

One of the more interesting hydromechanical processes occurring during fluid injection in an aquifer overlaid by a caprock is the reverse-water level fluctuation. These can only be observed numerically if hydromechanical coupled simulations are performed (see Figure 5.9). We use this effect, which is more pronounced in soft aquifers, to determine the geomechanical properties of the rocks. This effect can be difficult to measure in situ if the aquifer is stiff because it will lead to small fluid pressure changes, which will only be detectable if the measuring equipment is very accurate.

Vertical displacement is not easy to measure in deep boreholes. Strain measurements with fiber optic may be an alternative. However, it cannot be said for sure what deformation is being measured. Is it measuring the strain of the rock? Or is it measuring that of the casing? The measuring equipment will be embedded in the cement between the casing and the rock, which are of different stiffness, and thus deform differently. If the cement-rock contact becomes a sliding surface, then the measuring equipment will measure the casing strain. This would give the impression that the rock is much stiffer than it actually is. However, the combined interpretation of fluid pressure and vertical displacement measurements will help in deciding whether some measurements are or not representative of the aquifer or caprock. Overall, the hydromechanical parameters of the aquifer and caprock at the field scale can be estimated from the interpretation of the proposed hydromechanical characterization field test.

5.6. Conclusion

We propose a hydromechanical characterization test for determining the aquifer and caprock hydromechanical properties at the field scale. Additionally, the maximum sustainable CO_2 injection pressure can be determined by monitoring induced microseismicity. This will help to assess the suitability of specific sites for permanent CO_2 storage in deep saline formations.

We obtain the parameters that govern the problem through a dimensional analysis. We present the dimensionless overpressure and vertical displacement as a function of these parameters, which yields a family of curves for several Poisson ratio. Except for the vertical displacement at the top of the caprock, which depends on the Poisson ratio, all the curves collapse in one single curve when plotting the results as a function of the dimensionless group of the volumetric strain term Γ_{aq}. Not only do these curves show the behaviour of the aquifer-caprock system when injecting a fluid, but also can they be used for parameter estimation from field measurements.

The coupled hydromechanical simulations of fluid injection show a reverse-water level fluctuation in the caprock, i.e. fluid pressure drops in the caprock when injecting in the subjacent aquifer. This phenomenon cannot be observed when running purely

hydraulic simulations. Thus, coupled hydromechanical simulations should be performed when the processes that the caprock undergoes during fluid injection are of interest.

Induced microseismic events are of concern when occurring in the caprock. Although the mobilized friction angle is lower in the caprock than in the aquifer, rich-clay materials, like the ones that form the caprock, present low-friction angles, especially in the direction parallel to bedding. Thus, monitoring microseismicity can give confidence on the caprock integrity.

6. Liquid CO_2 Injection for Geological Storage in Deep Saline Aquifers

6.1. Introduction

Pressure (p) and temperature (T) conditions of deep geological formations suitable for storing CO_2 are such that this greenhouse gas remains in supercritical (SC) state, i.e. p >7.382 MPa and T >31.04 ºC (e.g. Bachu, 2003). Thus, it is usually assumed that CO_2 will reach the aquifer in SC conditions (e.g. Pruess and Garcia, 2002). However, injecting CO_2 in SC state may not be the best option. Several engineering methodologies have been proposed as alternatives to the concept of injecting SC CO_2. They focus on accelerating CO_2 dissolution to minimize the risk of leakage of free-phase mobile CO_2 by means of dissolving CO_2 at surface (Burton and Bryant, 2009; Jain and Bryant, 2011; Zendehboudi *et al*., 2011) or at depth (Carrera *et al*., 2011b), by injecting brine at some distance from the CO_2 injection well that mixes with the CO_2 plume enhancing dissolution (Hassanzadeh *et al*., 2009) or by injecting CO_2 under temporal pressure fluctuations, which enhances CO_2 dissolution (Bolster *et al*., 2009b). On the other hand, a few studies suggest that cold CO_2 (and therefore in liquid state) injection may have some advantageous implications for CO_2 storage (Rayward-Smith and Woods, 2011; Silva *et al*., 2011). However, these studies are approximations that do not take into account the whole coupling of the thermo-hydro-mechanical effects inherent to cold CO_2 injection.

It can be conjectured that injecting CO_2 in liquid state is energetically more efficient than doing so in SC state and more optimal from a storage engineering point of view because liquid CO_2 is denser than SC CO_2. Therefore, for a given mass of CO_2, a smaller volume of formation fluid will be displaced, leading to a lower overpressure in the reservoir. More importantly, the increased weight of liquid CO_2 in the injection well implies that a far lower pressure is required at the wellhead. Additionally, CO_2 is usually transported in liquid state (pressure above 8.5 MPa and ambient temperatures (Figure 6.1)) (McCoy and Rubin, 2008). Thus, it can be injected at the conditions in which it

arrives to the wellhead, without having to perform throttling or heating operations. In fact, since pressure at the wellhead is reduced, it may be smaller than transport pressure, which may allow recovering some energy from the incoming CO_2. Furthermore, if pressure needs to be increased, a smaller compression work has to be done to inject liquid CO_2 because liquid CO_2 is less compressible than SC CO_2. This compression can be performed by means of pumps without having to use compressors, which are much harder to operate. Despite these apparent advantages, liquid CO_2 injection has not been considered in the scientific literature and it has not been attempted in practice. This may reflect the fact that so far industrial operations have been associated to oil industry, where CO_2 is obtained in gas form. It may also reflect fear to phase transitions in the injection equipment or in the formation, or to thermal stresses associated to a cold fluid injection.

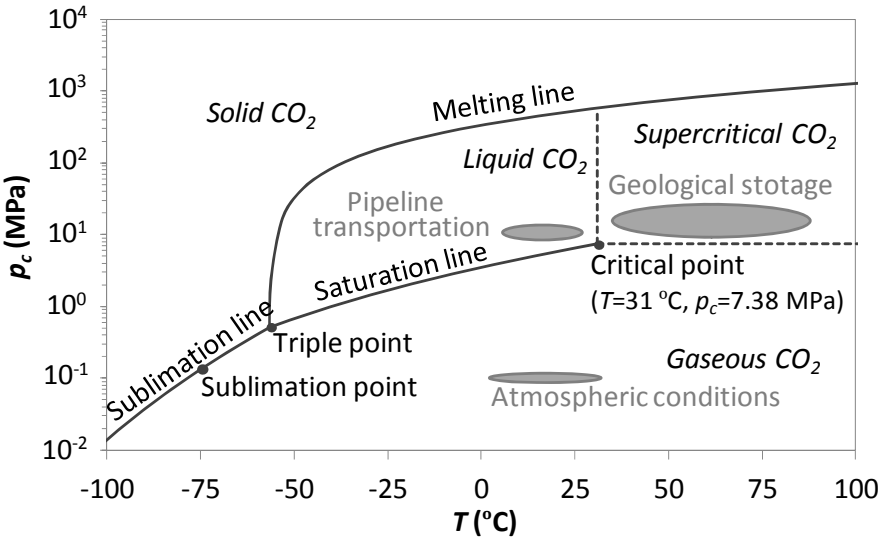

Figure 6.1 – CO_2 phase diagram. CO_2 is a gas in the atmosphere. Pipeline transportation is done in liquid CO_2 conditions and geological storage stays in supercritical CO_2 conditions.

Hydromechanical, but not thermomechanical, effects have been widely investigated in the context of geological storage of CO_2 (e.g. Rutqvist *et al*., 2007; Ferronato *et al*., 2010; Vilarrasa *et al*., 2010b; Goerke *et al*., 2011; Rutqvist, 2012). The main concern is to guarantee that the mechanical stability of the caprock will not be compromised in order to prevent CO_2 leakage. Nimtz *et al*. (2010) argue that when injecting liquid CO_2 the overpressure at the bottom of the well will be too high because CO_2 pressure at the wellhead has to be enough to ensure liquid conditions; and the hydrostatic pressure in the well will be also high because liquid CO_2 has a density around 900 kg/m^3. However,

they do not perform any hydromechanical simulation to confirm their hypothesis. Moreover, they do not consider reducing temperature, which ensures liquid conditions with moderate pressures. Note that an excessive overpressure can induce microseismicity (Phillips *et al*., 2002; Guglielmi *et al*., 2008; Cappa and Rutqvist, 2011b), which may open up migration paths for CO_2. However, since liquid CO_2 is colder than the formations where it will be injected, liquid CO_2 injection implies a combination of hydromechanical and thermomechanical effects that should be studied simultaneously to properly evaluate the caprock mechanical stability.

The injection of a cold fluid induces a thermal contraction of the rock, leading to a reduction of the effective stresses (Segall and Fitzgerald, 1998). In general, the smaller the effective stresses, the closer to failure conditions. Thermomechanical effects have been studied specially in geothermal reservoir stimulation (Ghassemi *et al*., 2007; Majer *et al*., 2007). In geological storage of CO_2, Preisig and Prévost (2011) studied the thermomechanical effects of injecting CO_2 at a colder temperature than that of the reservoir at In Salah (Algeria), but assuming constant CO_2 properties, which may not be realistic (see Appendix II). On the other hand, non-isothermal CO_2 flow simulations considering the actual CO_2 properties have been performed, but without considering the mechanical coupling and always in supercritical conditions (Han *et al*., 2010; Singh *et al*., 2011). Therefore, the thermomechanical effects of liquid CO_2 injection remain to be studied.

We propose to inject CO_2 in liquid state as a new engineering methodology for minimizing energy costs and CO_2 phase changes in the capture-transport-injection chain, and improving the short- and long-term storage efficiency of CO_2. This injection concept will be tested at the pilot site of Hontomín (Carrera *et al*., 2011a), Burgos, Spain, which is the injection site of the CO_2 storage Technology Demonstration Plant (TDP) of the Compostilla OXYCFB300 project (EU funded: European Energy Programme for Recovery), operated by Fundación Ciudad de la Energía (CIUDEN). Hontomín is a dome-like structure with a dolomitized reservoir located at 1450 m depth, which is overlaid by a caprock made of marls. A large number of experiments are planned both for site characterization and for injection technology development (Carrera *et al*., 2011a).

The objective of this chapter is to analyze liquid CO_2 injection into a deep aquifer in terms of (1) the energetic efficiency and (2) caprock mechanical stability. This represents a first step towards the design of the liquid CO_2 injection test that will be

performed at the Hontomín pilot test. We calculate CO_2 flow in both an injection well and a deep saline formation. We perform simulations of non-isothermal two-phase flow in a deformable porous media to evaluate the caprock mechanical stability.

6.2. Mathematical and numerical methods

We first solve CO_2 injection in a vertical injection well and afterwards in a saline formation. The geometry of the problem consists in a homogeneous 100 m thick horizontal aquifer that is overlaid and underlain by a seal. The system is axisymmetric and extends laterally 20 km. The nature of the outer hydraulic boundary condition does not affect the results because the radius of the pressure perturbation cone is smaller than the radius of the domain for the injection time scales presented here. Therefore, the model behaves as an infinitely acting aquifer. The top of the aquifer is located at a depth of 1500 m, which corresponds to the depth of the reservoir at the Hontomín test site. The seals that overlay and underlie the aquifer have a thickness of 200 m. The seal that is placed on top of the aquifer, i.e. the caprock, is covered by a 1300 m thick low shear strength media that do not need to be included in the model. An injection well with a radius of 0.15 m is placed in the center of the domain.

6.2.1. Non-isothermal flow in the injection pipe

Flow of CO_2, or any fluid, and its mixtures in non-isothermal wells involves solving the partial differential equation (PDE) that express energy, mass and momentum conservation. These PDEs are coupled through the equations of state (EOS) governing fluid and thermodynamic properties. Several authors describe numerical procedures to solve these equations (Lu and Connell, 2008; Paterson *et al*., 2008; Pan *et al*., 2009; Han *et al*., 2010).

Here, we adopted the approach of Lu and Connell (2008). They presented a methodology to solve steady state non-isothermal multiphase flow of CO_2 in an injection well, in which the flow equations are based on the averaged-flow model (e.g. Brill and Mukherjee, 1999; Hasan and Kabir, 2002). We assume that the steady state assumption describes reasonably well the operation after the initial stages. This leads to a system of one dimensional ordinary differential equation (ODE) along the vertical coordinate z. The number of equations of such system is five for single-phase

conditions or twelve for two-phase conditions. The corresponding vectors of unknown state variables are $\mathbf{x} = (\rho, v, p, h, T)^t$ or $\mathbf{x} = (\theta_l, \rho_l, \rho_g, v, p, h, T, X, s_l, s_g, h_l^{sat}, h_g^{sat})^t$, respectively, where ρ is density, v is velocity of the fluid mixture, p is pressure, h is specific enthalpy, T is temperature, θ_l is volumetric liquid content, X is gas mass fraction and s is entropy. Subscript l and g stand for liquid and gas phases, respectively; and superscript sat and t refer to saturation conditions and to transpose, respectively.

Because solubility of gas into water is neglected, this approach is restricted to pure CO_2 or a multi-component gaseous mixture rich in CO_2, but not a fluid mixture of water and gas. As explained by Lu and Connell (2008), the phase equilibrium condition is checked to identify the state of the fluid at a given point when solving the system of equations. If more than one root of the EOS exists and the Gibbs equilibrium condition applies, then the fluid is identified to be in a two-phase coexistence state and the size of the system is 12. Otherwise, the fluid is in single-phase conditions and the size of the system is 5. It should be noted that the above model simplifies considerably when simulating the injection of liquid CO_2, because single-phase conditions (liquid and/or supercritical) prevail along the entire wellbore.

In the approach of Lu and Connell (2008) the fluid in the injection pipe exchanges heat laterally with its surroundings. The heat exchange term is represented by

$$Q = -2\pi R_p U_\infty \left(T - T_{geo}(z)\right), \tag{6.1}$$

where U_∞ is the overall heat transfer coefficient for the injection well comprising the thermal properties of all the materials from which it is composed (the injection fluid, the injection pipe wall, the brine in the annulus between injection pipe and the casing wall, the casing wall and the cement), R_p is the radius of the injection pipe and $T_{geo}(z)$ is the geothermal temperature along the wellbore. We assumed a geothermal gradient of 0.033 ºC/m and a formation temperature at surface of 5 ºC in all the simulations. The internal diameter of the injection pipe is set at 9 and 15.24 cm. The bottom of the injection pipe is located at 1500 m, coinciding with the top of the aquifer for CO_2 storage.

To solve the system of flow equations, we need to specify 3 boundary conditions related to the primary physical quantities p, T and v. Additionally, the gas mass

fraction X or the volumetric liquid content θ_l need to be specified if injecting two-phase CO_2. Common operational conditions of an injection well are specifying the pressure and/or the flow rate and the temperature at the wellhead. If a pressure-controlled injection condition is assumed at the wellhead, a boundary condition relating the flow rate and the reservoir pressure at the bottom of the well can be specified. In fact, this boundary condition allows to address the coupling between the flow through the injection well and that in the reservoir. We study flow through the injection well and flow in the formation separately to explain the processes occurring in each of them in a clear way. However, we couple them by choosing a pressure and temperature conditions at the wellhead, such that the resulting pressure and temperature conditions at the bottom of the well coincide with the boundary conditions of the two-phase flow simulations in the reservoir.

As far as fluid properties are concerned, density was calculated assuming the Redlich-Kwong EOS (Redlich and Kwong, 1949) using the parameters proposed for CO_2 by Spycher *et al*. (2003) (see Appendix II). Viscosity was calculated according to the correlation of Altunin and Sakhabetdinov (1972) (see Appendix II). The friction factor of the fluid through the injection pipe was calculated according to the Blasius equation (Brill and Mukherjee, 1999; Hassan and Kabir, 2002). Turbulent flow regime can be also calculated using other empirical correlations that include rugosity of the pipe (e.g., Colebrook, 1939; Zigrang and Sylvester, 1985).

The steady state non-isothermal multiphase flow governing equations in the injection pipe were programmed in MatLab (Silva *et al*., 2011). These equations are solved using a variable order method for solving stiff differential equations.

6.2.2. Non-isothermal two-phase flow in a deformable porous media

Consider CO_2 injection in a deep confined deformable saline formation. In general, the injected CO_2 will not be in thermal equilibrium with the reservoir, especially at high flow rates (Paterson *et al*., 2008). To account for these processes, thermo-hydro-mechanical couplings should be taken into account. Therefore, mass conservation of each phase, energy balance and momentum balance have to be solved simultaneously.

a) Fluid mass conservation equation

Mass conservation of each phase can be expressed as (Bear 1972),

$$\frac{\partial(\varphi S_\alpha \rho_\alpha)}{\partial t} + \nabla \cdot (\rho_\alpha \mathbf{q}_\alpha) = r_\alpha, \qquad \alpha = c, w, \tag{6.2}$$

where φ is porosity, S_α is saturation of the α-phase, ρ_α is density, t is time, $\mathbf{q}_\alpha$ is the volumetric flux, r_α is the phase change term (i.e. CO_2 dissolution into water and water evaporation into CO_2) and α is either CO_2 rich phase, *c*, or aqueous phase, *w*. For the sake of simplicity we neglect evaporation of water into CO_2, i.e., r_w = 0.

Momentum conservation is expressed using Darcy's law, written as

$$\mathbf{q}_\alpha = -\frac{k k_{r\alpha}}{\mu_\alpha}(\nabla p_\alpha + \rho_\alpha g \nabla z), \qquad \alpha = c, w, \tag{6.3}$$

where k is intrinsic permeability, $k_{r\alpha}$ is the α-phase relative permeability, μ_α its viscosity, p_α its pressure and g is gravity.

The properties of the aquifer and seals correspond to those of limestone and shale, respectively (Vilarrasa *et al*., 2010b) and are detailed in Table 6.1. We consider the aquifer to be a permeable limestone with homogeneous grain size. Therefore, the entry pressure is low and the shape parameter of the van Genuchten (1980) retention curve is high. On the other hand, seal entry pressure is high, which hinders CO_2 migration. Relative permeabilities follow a power law of saturation for both phases: the limestone has a cubic law, while the power in the seals is 6. CO_2 density and viscosity, which are highly dependent on p and T conditions, are detailed in Appendix II.

Buoyancy effects are relevant in the CO_2 plume evolution, regardless of injection conditions. However, when injecting liquid CO_2 the density contrast between CO_2 and brine is smaller than when injecting SC CO_2. Additionally, liquid CO_2 viscosity is higher than SC CO_2 viscosity. Thus, viscous forces gain strength in front of gravity forces. This can be quantified through the gravity number (Vilarrasa *et al*., 2010a)

$$N_g = \frac{2\pi r_c b k k_{r\alpha} \Delta\rho g \rho_c}{Q_m \mu_c}, \tag{6.4}$$

where r_c is a characteristic length, b is aquifer thickness, $\Delta\rho$ is the difference between CO_2 and water density and Q_m is the CO_2 mass flow rate.

Table 6.1 – Material properties used in the thermo-hydro-mechanical analysis of liquid CO_2 injection.

Property	**Aquifer**	**Seal**
Permeability, k (m^2)	10^{-13}	10^{-18}
Relative water permeability, k_{rw}	S_w^3	S_w^6
Relative CO_2 permeability, k_{rc}	S_c^3	S_c^6
Gas entry pressure, p_0 (MPa)	0.02	0.6
van Genuchten, m	0.8	0.5
Porosity, φ	0.1	0.01
Young's modulus, E (GPa)	2.5	5.0
Poisson ratio, ν	0.3	0.3
Thermal conductivity, λ (W/m/K)	1.5	1.5
Thermal expansion coefficient, α_T ($ºC^{-1}$)	10^{-5}	10^{-5}

b) Energy conservation equation

Energy conservation can be written as (Faust and Mercer, 1979)

$$\frac{\partial\left(\left(1-\varphi\right)\rho_s h_s + \varphi\rho_w S_w h_w + \varphi\rho_c S_c h_c\right)}{\partial t} - \frac{\partial\left(\varphi S_w p_w + \varphi S_c p_c\right)}{\partial t} + \nabla\cdot\left(-\lambda\nabla T + \rho_w h_w \mathbf{q}_w + \rho_c h_c \mathbf{q}_c\right) = 0 \quad (6.5)$$

where ρ_s is solid density, h_α is enthalpy of α-phase ($\alpha = c, w, s$; s for solid) and λ is thermal conductivity.

Eq. (6.5) includes non-isothermal processes, such as Joule-Thomson effect (Tsang *et al*., 2008), heat of CO_2 dissolution and water evaporation (Han *et al*., 2010) and compression work due to the high compressibility of CO_2. We consider all these processes, except water evaporation.

c) Thermoelasticity in porous media

To solve the mechanical problem, the momentum balance of the porous media has to be satisfied. If inertial terms are neglected, it reduces to the equilibrium of stresses

$$\nabla\cdot\boldsymbol{\sigma} + \mathbf{b} = \mathbf{0}\,, \quad (6.6)$$

where $\boldsymbol{\sigma}$ is the stress tensor and $\mathbf{b}$ is the body forces vector.

Furthermore, we assume that the medium behaves elastically. In fact, we use linear thermoelasticity to acknowledge the effect of changes in fluid pressure and temperature. Therefore, elastic strain depends on total stress, overpressure and temperature as (Biot, 1956)

$$\boldsymbol{\varepsilon} = \frac{1+\nu}{E}\boldsymbol{\sigma} - \frac{3\nu}{E}\sigma_m \mathbf{I} - \frac{1-2\nu}{E}\Delta p \mathbf{I} - \frac{1+\nu}{3(1-2\nu)}\alpha_T \Delta T \mathbf{I}\,, \tag{6.7}$$

where $\boldsymbol{\varepsilon}$ is the strain tensor, $\sigma_m = (\sigma_x + \sigma_y + \sigma_z)/3$ is the mean stress, $\mathbf{I}$ is the identity matrix, E is the Young's modulus, ν is Poisson ratio and α_T is the linear thermal expansion coefficient. Here, the sign criterion of geomechanics is adopted, i.e. strain is positive in compression and negative in extension.

Simulations suggest that the temperature perturbation is localized within a relatively small volume of the formation close to the injection well, thus acting spherically. However, the fluid pressure perturbation propagates a long distance in the direction of the aquifer, but not in the perpendicular, thus acting anisotropically. Therefore, it may be assumed that stresses vary isotropically with temperature changes and that no horizontal strain is allowed in the outer boundary as a result of lateral confinement. This leads to a variation of the vertical and horizontal stresses as a result of fluid pressure and temperature variations as

$$\Delta\sigma_v = \frac{E(1-\nu)}{3(1-2\nu)^2}\alpha_T \Delta T\,, \tag{6.8a}$$

$$\Delta\sigma_h = \frac{1-2\nu}{1-\nu}\Delta p + \frac{E(1-\nu)}{3(1-2\nu)^2}\alpha_T \Delta T\,, \tag{6.8b}$$

where σ_v is the vertical stress and σ_h is the horizontal stress.

Eq. (6.8b) shows that an increase in pore pressure and/or temperature, which produces an expansion of the porous media, causes an increase of horizontal stresses because of lateral confinement that opposes to the induced expansion. On the other hand, a decrease in pressure and/or temperature, which produces a contraction of the porous media, causes a decrease of horizontal stresses.

d) Model setup

The initial conditions are hydrostatic pressure; temperature following a geothermal gradient of 0.033 ºC/m, with a surface temperature of 5 ºC; a vertical stress gradient of 0.023 MPa/m and horizontal effective stresses corresponding to a lateral earth pressure coefficient of either 0.5 (vertical stress higher than horizontal stresses) or 2.0

(horizontal stresses higher than vertical stress). As a first step, a steady-state calculation is carried out to ensure consistent initial conditions in equilibrium for the pressure, temperature and stress fields.

The hydraulic boundary conditions are a prescribed CO_2 mass flow rate at the injection well (1.0 Mt/yr) and a constant pressure on the outer boundary. The thermal boundary conditions are constant temperature at the top and bottom boundaries of the domain. The thermal perturbation does not reach these boundaries, so the nature of the boundary condition does not affect the results. The mechanical boundary conditions are no displacement normal to the bottom, outer and injection well boundaries. A constant, vertical lithostatic stress is imposed at the top of the caprock.

The mesh is made of structured quadrilateral elements. Laterally, the size of the elements is of tens of cm close to the injection well and increases exponentially up to a longitudinal size of 400 m next to the outer boundary. Vertically, the elements within the aquifer are of 5 m. In the caprock, close to the aquifer-seal contacts the size is of 5 m and far away from the contact the size grows up to 25 m.

Non-isothermal CO_2 injection in a deformable porous media is simulated using the finite element numerical code CODE_BRIGHT (Olivella *et al*., 1994, 1996). We have implemented CO_2 properties, such as density, viscosity, enthalpy and heat capacity (Appendix II) in order to simulate CO_2 storage. Furthermore, we have incorporated in the energy conservation the term of CO_2 volumetric compression due to pressure changes (second term of Eq. (6.5)), maintaining temperature as the state variable.

6.2.3. Mechanical stability

To determine whether a pre-existing fracture is stable or not a failure criterion has to be defined. The medium is stable and behaves elastically while the stress state falls inside the failure envelope. However, if the stress state touches the failure envelope, the rock yields, producing a microseismic event. We adopt the Mohr-Coulomb failure criterion

$$\tau = c' + \sigma'_n \tan \phi' , \qquad (6.9)$$

where τ is the shear stress, σ'_n is the normal effective stress, c' is cohesion and ϕ' is the friction angle.

The effective stress tensor, considering the sign criterion of geomechanics, i.e. stress and fluid pressure are positive in compression, is defined as

$$\boldsymbol{\sigma}' = \boldsymbol{\sigma} - p\mathbf{I}, \tag{6.10}$$

where $\boldsymbol{\sigma}'$ is the effective stress tensor and $p = \max(p_w, p_c)$ is fluid pressure.

We assume an axisymmetric stress state in which the horizontal effective stress is

$$\sigma'_h = k_0 \sigma'_v, \tag{6.11}$$

where k_0 is the lateral earth pressure coefficient. The stress regime has a great effect on the caprock failure mechanisms (Rutqvist *et al*., 2008; Vilarrasa *et al*., 2011b). Therefore, the effect of k_0 should be investigated.

Let us assume that a fracture exists with a dip angle θ (Figure 6.2). If we assume that the fracture is cohesionless, the mobilized friction angle can be calculated from Eq. (6.9) considering the stress changes induced by overpressure and temperature changes (Eq. (6.8)) in the normal effective stress and the shear stress that act on this pre-existing fracture

$$\tan\phi'_{mob} = \frac{0.5\left(\sigma'_{v0}\left(1-k_0\right)-\left(1-2\nu\right)/\left(1-\nu\right)\Delta p\right)\sin 2\theta}{\sigma'_{v0}\left(1-\left(1-k_0\right)\sin^2\theta\right)+\left(\left(1-2\nu\right)/\left(1-\nu\right)\sin^2\theta-1\right)\Delta p + E\left(1+\nu\right)\alpha_T\Delta T/\left(3\left(1-2\nu\right)^2\right)} \tag{6.12}$$

where σ'_{v0} is the original vertical effective stress, i.e. prior to pore pressure and temperature changes. The mobilized friction angle is a measure of how close to failure is the fracture. The closer the mobilized friction angle is to the actual friction angle, the closer to failure is the fracture.

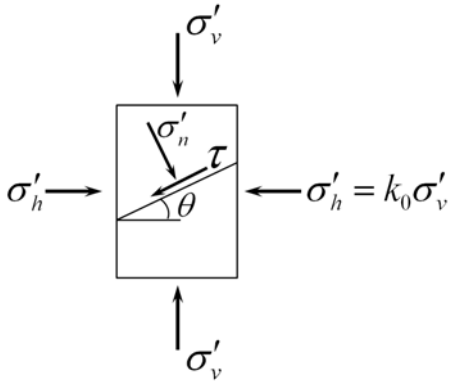

Figure 6.2 – An arbitrary pre-existing fracture in a porous media under an axisymmetric stress state.

It can be demonstrated geometrically by using the Mohr circle to represent the stress state that the dip angle of the most critically oriented fracture, θ_{cr}, is related to the friction angle of the fracture by

$$\theta_{cr} = \frac{\pi}{4} + \frac{\phi'}{2}, \quad \text{if } k_0 < 1, \tag{6.13a}$$

$$\theta_{cr} = \frac{\pi}{4} - \frac{\phi'}{2}, \quad \text{if } k_0 > 1. \tag{6.13b}$$

Assuming that a cohesionless fracture exists in the critical dip angle, the overpressure that will produce failure of this pre-existing fracture for a given friction angle, depth, lateral earth pressure coefficient and temperature change is

$$\begin{aligned}
&\frac{\Delta p}{\sigma'_{v0}} = \frac{2(1-\nu)}{1-2\nu-\sin\phi'}\left[1-0.5(1+k_0)(1+\sin\phi')-\frac{E(1-\nu)}{3(1-2\nu)^2\sigma'_{v0}}\alpha_T\Delta T\sin\phi'\right], \\
&\text{if } k_0 < 1-\frac{1-2\nu}{1-\nu}\frac{\Delta p}{\sigma'_{v0}} \\
&\frac{\Delta p}{\sigma'_{v0}} = \frac{2(1-\nu)}{1-2\nu+\sin\phi'}\left[1-0.5(1+k_0)(1-\sin\phi')+\frac{E(1-\nu)}{3(1-2\nu)^2\sigma'_{v0}}\alpha_T\Delta T\sin\phi'\right], \\
&\text{if } k_0 > 1-\frac{1-2\nu}{1-\nu}\frac{\Delta p}{\sigma'_{v0}}
\end{aligned} \tag{6.14}$$

Alternatively, the temperature change that will produce failure of this pre-existing cohesionless fracture for a given friction angle, depth, lateral earth pressure coefficient and overpressure is

$$\begin{aligned}
&\Delta T = \frac{3(1-2\nu)^2\sigma'_{v0}}{E(1-\nu)\alpha_T\sin\phi'}\left[1-0.5(1+k_0)(1+\sin\phi')-\frac{1-2\nu-\sin\phi'}{2(1-\nu)}\frac{\Delta p}{\sigma'_{v0}}\right], \\
&\text{if } k_0 < 1-\frac{1-2\nu}{1-\nu}\frac{\Delta p}{\sigma'_{v0}} \\
&\Delta T = \frac{3(1-2\nu)^2\sigma'_{v0}}{E(1-\nu)\alpha_T\sin\phi'}\left[-1+0.5(1+k_0)(1-\sin\phi')+\frac{1-2\nu+\sin\phi'}{2(1-\nu)}\frac{\Delta p}{\sigma'_{v0}}\right], \\
&\text{if } k_0 > 1-\frac{1-2\nu}{1-\nu}\frac{\Delta p}{\sigma'_{v0}}
\end{aligned} \tag{6.15}$$

6.3. CO_2 behaviour in the injection well

We consider several operational conditions at the wellhead to compare the feasibility and energy consumption of the proposed injection concept with other schemes. We use the methodology of Section 6.2 to simulate CO_2 injection through the injection well in gas, supercritical and liquid-state. Table 6.2 displays the pressure and temperature values for five injection conditions at the wellhead: gas-phase, near-critical point, supercritical phase, liquid-phase at high pressure and temperature and liquid-phase at low pressure and temperature. A mass flow rate of 1.5 kg/s and an overall heat transfer coefficient of $U_\infty = 10$ W m^{-2} K^{-1} were considered in the simulations. Figure 6.3 shows the temperature, pressure and density profiles obtained for each injection conditions.

Table 6.2 – Several CO_2 injection conditions at the wellhead (Q_{inj} = 1.5 kg/s, geothermal gradient = 0.033 ºC/m, R_p = 4.5 cm, U_∞ = 10 W m^{-2} K^{-1}) and their estimated energy consumption.

Injection conditions at the wellhead	T **, ºC**	p **, MPa**	**Energy consumption, kW**
Gas-phase	35	6.5	409.6
Near-critical point	31	7.0	368.2
Supercritical phase	40	8.0	361.9
Liquid-phase (high *T* and *p*)	25	8.0	154.7
Liquid-phase (low *T* and *p*)	5	4.2	83.6

Figure 6.3 shows that injection in gas-phase and supercritical phase conditions causes a distribution of low densities along the wellbore. Injecting gaseous CO_2 in near-critical point conditions causes a two-phase flow pattern within the injection pipe near the surface (in the first 50 m). It should be noted that phase changes always lead to higher head losses in pipes. This two-phase flow behaviour is associated with a change in the slope of the temperature profile when the fluid becomes supercritical. The resulting change of phase leads to higher densities through the injection pipe than those obtained when injecting in gas and supercritical phase conditions.

In contrast, the injection of CO_2 in liquid-phase conditions leads to a high CO_2 density, which is comparable to that of brine, along the entire injection pipe. CO_2 temperature keeps nearly constant through a long section of the pipe and then increases slightly

due to the heat exchange between the fluid and the surroundings. Actually, when injecting at high pressure and temperature, the fluid undergoes a small cooling because of the heat exchange with the geological media. On the other hand, CO_2 pressure at the bottom of the well becomes very high, around 20 MPa for this particular injection conditions, because the injection at the wellhead is made at high pressure. However, a smaller overpressure can be obtained at the bottom of the well by injecting liquid CO_2 at low pressure and temperature, resulting in a CO_2 pressure similar to that obtained when injecting in near-critical conditions, i.e. around 17 MPa.

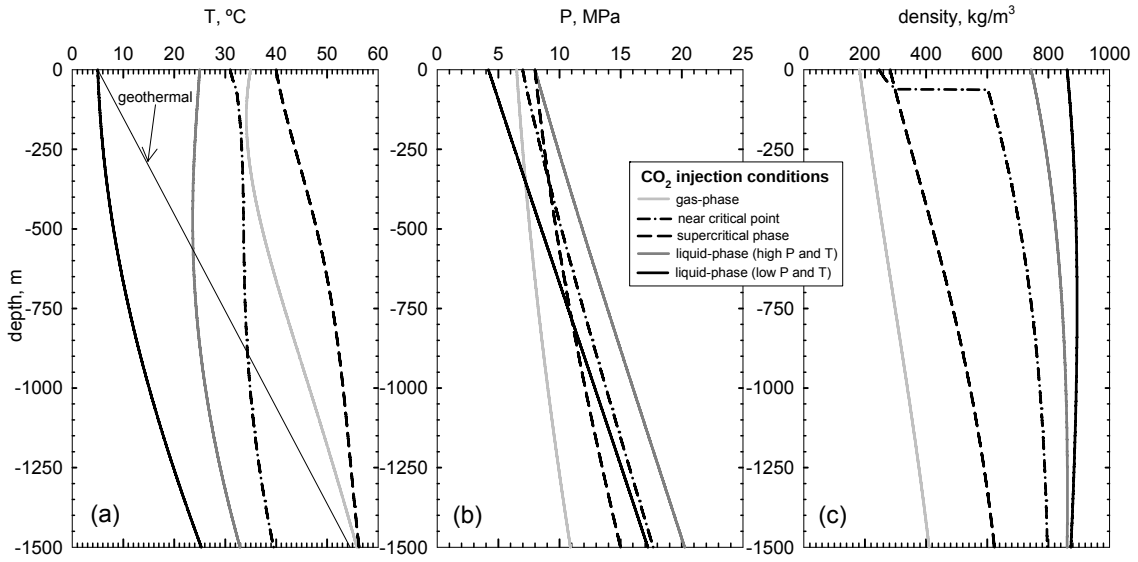

Figure 6.3 – Non-isothermal flow of CO_2 through an injection well: temperature (a), pressure (b) and density (c) profiles. Comparison between different injection conditions at the wellhead (gas-, supercritical- and liquid-phase) (Q_{inj} = 1.5 kg/s, geothermal gradient = 0.033 ºC/m, R_p = 4.5 cm, U_∞ = 10 W m^{-2} K^{-1}).

At pilot sites, CO_2 is often stored in vessels at very low temperatures (≈ -20 ºC) and pressures in the order of 2.0 MPa. The energy consumption associated to surface conditioning operations, such as compression, pumping and heating, will vary for each injection mode. Normally, to obtain the desired pressure and temperature conditions for injection, CO_2 is first pumped/compressed and then heated. To analyze the energy consumption of these operations we can use macroscopic energy balances. For negligible heat transfer with the surroundings and no appreciable kinetic and potential energy effects, the mass and energy rate balances reduce, at steady state, to give the work input per unit of mass flowing through a compressor or a pump as the specific enthalpy difference between the exit and the inlet of the compressor/pump (Moran *et*

al., 2011). A similar estimation can be done to calculate the energy demand during heating. Therefore, the total energy consumed to reach the injection conditions can be roughly estimated by the difference of specific enthalpy between wellhead and storage vessel conditions. Table 6.2 also includes the energy consumption of the five injection modes, calculated assuming that the pressure and temperature of the storage vessel are 2.0 MPa and -20 ºC, respectively. Table 6.2 shows that the energy consumption is higher when injecting CO_2 in gas-phase, near-critical and supercritical conditions at the wellhead. On the other hand, and as expected, injecting CO_2 in liquid-phase at the wellhead reduces the energy consumption because pumping/compression is easier and heating is minor. The injection of liquid CO_2 at low temperature and pressure involves the lowest energy consumption.

The overall heat transfer coefficient can take a wide range of values depending on the materials used for the injection tubing, e.g. cement or casing. Therefore, we make a sensitivity analysis on the overall heat transfer coefficient to study the effect of heat exchange between the wellbore and its surroundings. Injection temperature and pressure were set at 5 ºC and 4.2 MPa, respectively. Figure 6.4 displays the results obtained from varying U_∞ between 0.1 and 1000 W m^{-2} K^{-1}. Conditions reached by the fluid at the bottom of the well are supercritical for high values of the overall heat transfer coefficient (U_∞ = 100, 1000 W m^{-2} K^{-1}), which induce a thermal equilibrium between the fluid and the geological media. It is evident that the fluid within the injection pipe receives less heat from its surroundings by enhancing the thermal insulation of the wellbore, i.e. reducing U_∞. This helps keeping low temperatures through the injection pipe (Figure 6.4a), leading to CO_2 density values that approach those of water density (Figure 6.4c).

Figure 6.5 depicts the temperature, pressure and density distributions along the injection well for five injection temperatures and a wellhead pressure of 4.2 MPa. The overall heat transfer coefficient and the CO_2 mass flow rate were set at 10.0 W m^{-2} K^{-1} and 1.5 kg/s, respectively. A reduction in the injection temperature of 25 ºC (with respect to 5 ºC) causes a density increase of only 7% at the bottom of the injection pipe, while the pressure increase is lower than 2.0 MPa. Furthermore, energy consumption due to heating at surface decreases as the wellhead temperature decreases (considering a storage temperature of -20 ºC). Figure 6.6 shows that, at pilot scale, injecting at low temperatures may involve an energy saving in the order of 300 %.

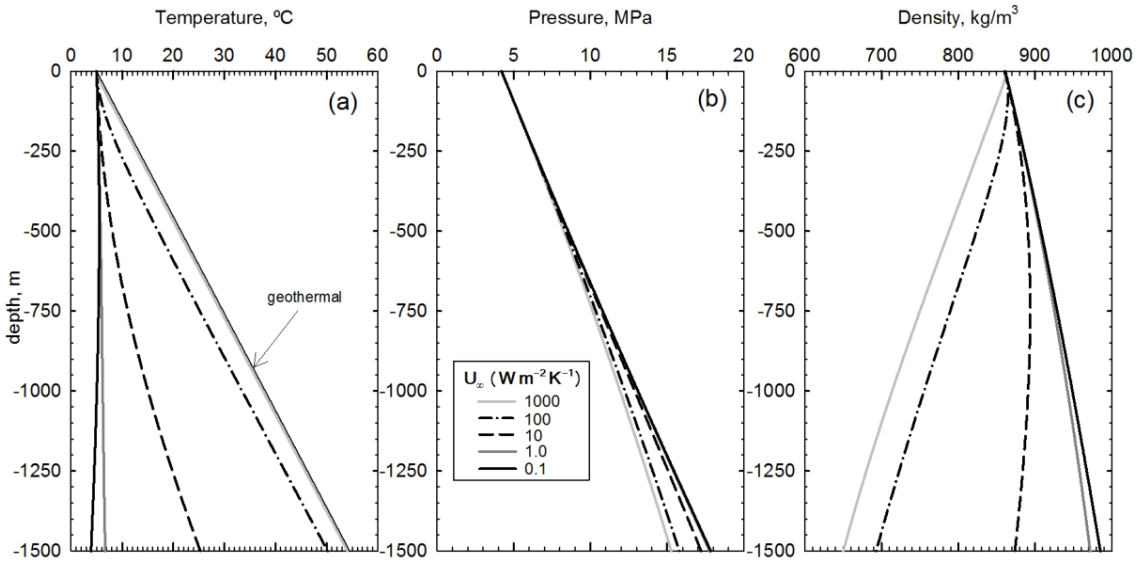

Figure 6.4 – CO_2 injection in liquid-phase at the wellhead. Sensitivity analysis to the overall heat transfer coefficient U_∞. Temperature (a), pressure (b) and density (c) profiles. (Q_{inj} = 1.5 kg/s, geothermal gradient = 0.033 ºC/m, R_p = 4.5 cm, T_{inj} =5.0 ºC, P_{inj} = 4.2 MPa).

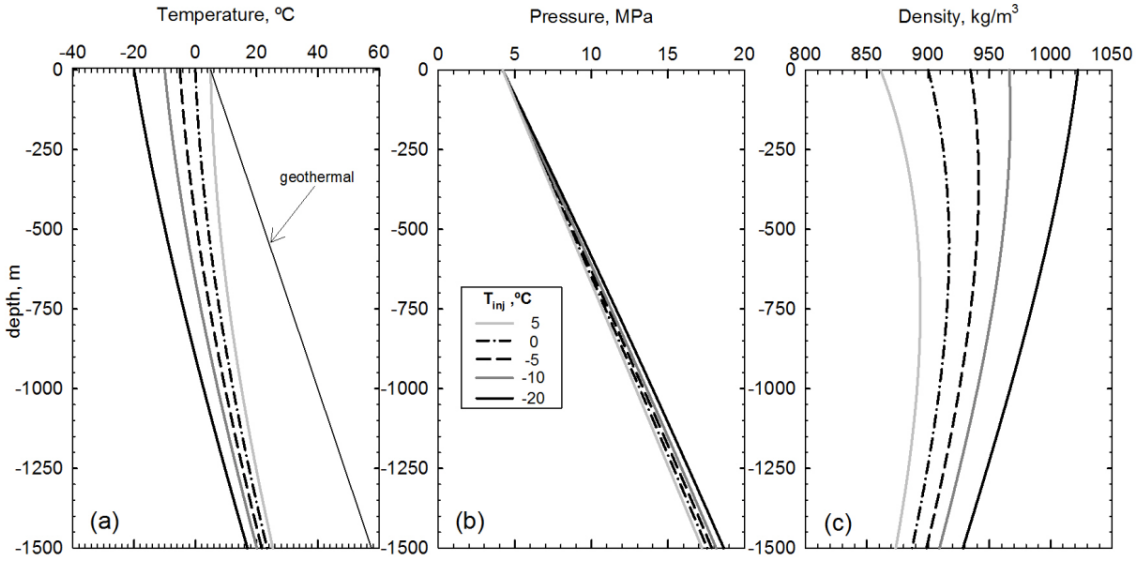

Figure 6.5 – Effect of injection temperature on liquid-phase CO_2 injection. Distributions of temperature (a), pressure (b) and density (c).

To compare SC CO_2 injection with injection of liquid CO_2 at industrial scale we also run two additional simulations for a CO_2 injection mass flow rate of 1.0 Mt/yr. Operational conditions and parameters for each case are shown in Table 6.3. The differences in the overall heat transfer coefficient are representative of different dimensions of the wellbore (e.g. diameter of injection pipe), different construction materials, different type of cements, use of isolating mechanisms, and variations induced by the dynamic of the

operation before achieving the steady state conditions. The pressure, temperature and density profiles obtained for each injection strategy are shown in Figure 6.7. When injecting SC CO_2 the temperature at the bottom of the well is around 56 ºC, which corresponds to the mean temperature of the aquifer placed at 1500 m depth considered in our simulations. In contrast, injecting CO_2 in liquid conditions along the entire injection pipe yields a temperature at the bottom of the well around 20 ºC. Pressure at the bottom of the well is approximately 17 MPa in both cases, but SC CO_2 injection produces a slightly higher overpressure than injecting liquid CO_2. These downhole fluid conditions are consistent with the boundary conditions in the simulation of non-isothermal CO_2 injection in a deformable porous media that is presented in Section 6.4.

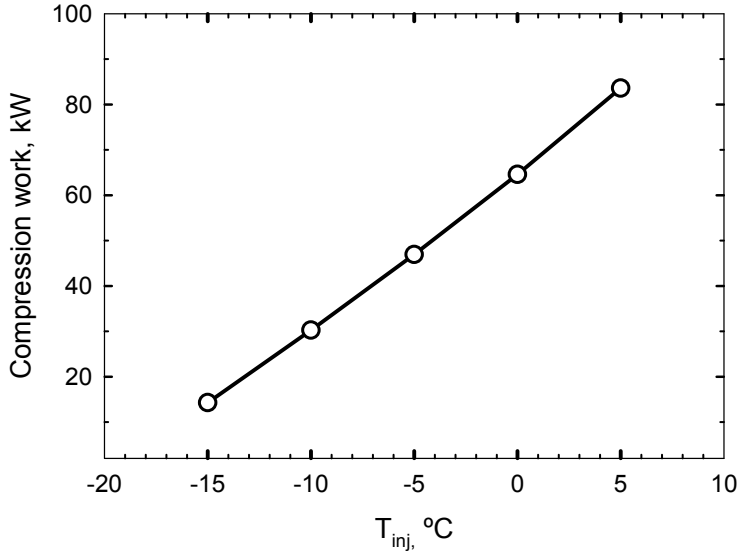

Figure 6.6 – Energy consumption to get the temperature of injection T_{inj} for CO_2 injection in liquid-phase (Q_{inj} = 1.5 kg/s, P_{inj} = 4.2 MPa) when CO_2 is stored in vessels at -20 ºC and 2.0 MPa.

Table 6.3 – Operational conditions and parameters for CO_2 injection in SC and liquid state at industrial scale (1.0 Mt/yr)

Variable or parameter	SC CO_2 injection	Liquid CO_2 injection
p, MPa	7.5	2.7
T, ºC	37.0	-10.0
R_p, cm	4.5	7.62
U_∞, W m^{-2} K^{-1}	300.0	125.0

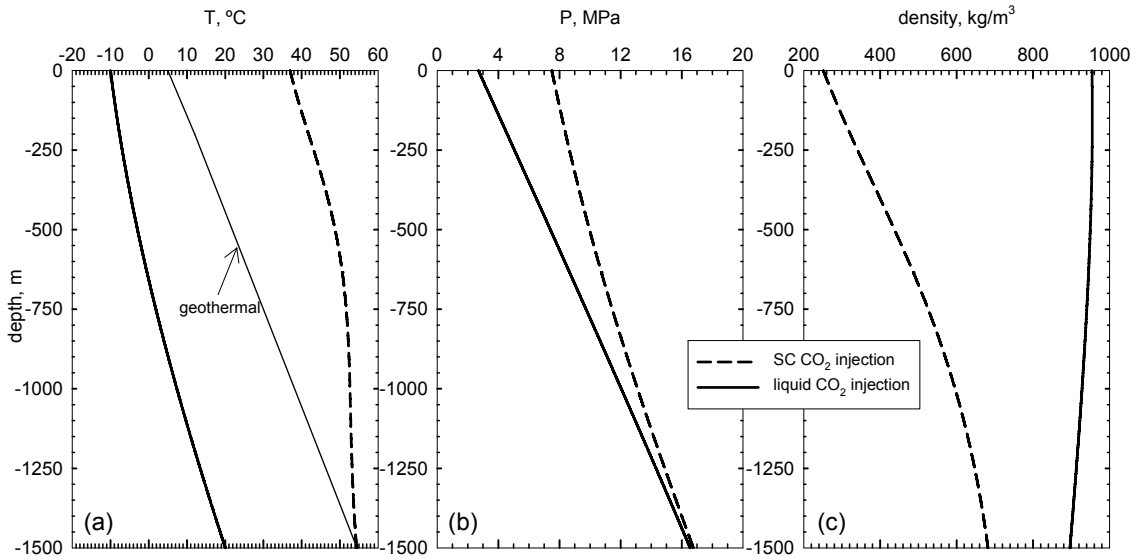

Figure 6.7 – Comparison between SC CO_2 injection (red) and liquid CO_2 injection at industrial scale (1.0 Mt CO_2/yr). Distributions of temperature (a), pressure (b) and density (c).

The energy consumption for a CO_2 mass flow rate of 1.0 Mt/yr, assuming the surface storage pressure and temperature conditions of the pilot test site of Hontomín (2.0 MPa and -20 ºC), is 7910 kW for SC CO_2 injection, while it is just of 675 kW for liquid CO_2 injection. However, a fairer comparison for such a high mass flow rate should consider pressure and temperature values resulting from transport through a long CO_2 pipeline. CO_2 transport and injection scenarios simulated by Nimtz *et al*. (2010) showed that CO_2 can arrive at the injection site at 8.5 MPa and 12 ºC. Thus, to get the injection conditions shown in Table 6.3, SC CO_2 injection would require a combination of heating and throttling, while cold CO_2 injection would require cooling and expansion (see Figure 6.8). Furthermore, energy could be produced in the CO_2 expansion by passing the expanding CO_2 through a turbine. Based on these hypothetical conditioning operations, the resulting energy cost is 5820 kW and -1415 kW for SC and liquid CO_2 injection, respectively (the negative sign is due to cooling and indicates that energy can be produced). Interestingly, if CO_2 is injected at the wellhead conditions proposed by Nimtz *et al*. (2010) in their application, i.e. 8.5 MPa and 12 ºC at the end of the pipeline and a mass flow rate of 117.3 kg/s distributed in 60 injection wells (1.95 kg/s in each well), CO_2 would reach the aquifer at 17.5 MPa and 35 ºC. Since the bottom hole pressure is similar to that of the reservoir simulation (see Section 6.4), CO_2 could be injected directly from the pipeline without any conditioning operation. Therefore, both at pilot and industrial scales injecting CO_2 in liquid phase conditions leads to a much lower energy demand.

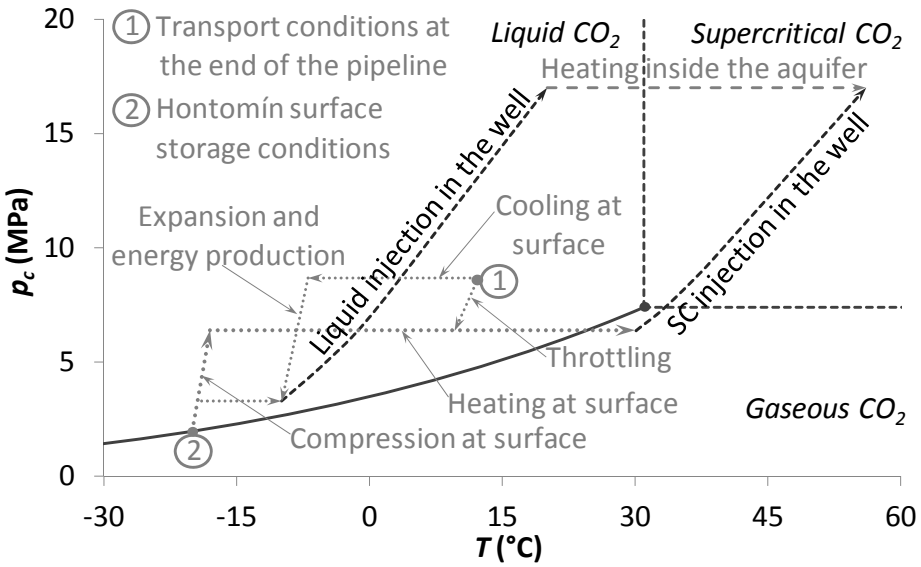

Figure 6.8 – CO_2 diagram with the pressure-temperature trajectories of the surface operations, in the injection well and inside the aquifer for the Hontomín surface storage conditions and for a hypothetical CO_2 transportation in a pipeline at industrial scale with an injection rate of 1 Mt/yr.

The results of the simulations presented in this section show that it is possible to inject CO_2 in dense liquid-phase by controlling the operational variables, which could lead to a reduction of the reservoir overpressure and, theoretically, of the operational energetic costs.

6.4. Thermo-hydro-mechanical effects of liquid CO_2 injection

6.4.1. Thermal effects on CO_2 plume evolution

Liquid CO_2 is denser and less viscous than SC CO_2. This means that gravity forces lose strength in front of viscous forces, which leads to a steeper CO_2-brine interface close to the injection well (Figure 6.9), where CO_2 remains in liquid state (Figure 6.10a). Further away, where CO_2 reaches SC conditions, the CO_2 plume evolution is characterized by gravity override (Nordbotten *et al*. 2005; Dentz and Tartakovsky, 2009a; Vilarrasa *et al*., 2010a) (Figure 6.9). The thermal transition is abrupt (Figure 6.10b). Once cold liquid CO_2 enters in the aquifer, it heats up until thermal equilibrium is reached, so that CO_2 evolves to SC conditions as it flows away from the well. Therefore, the liquid CO_2 region is much smaller than the whole CO_2 region. This leads to a steep liquid CO_2 front (where viscous forces dominate gravity forces) that

advances behind the typical CO_2 plume interface (where gravity forces dominate viscous forces).

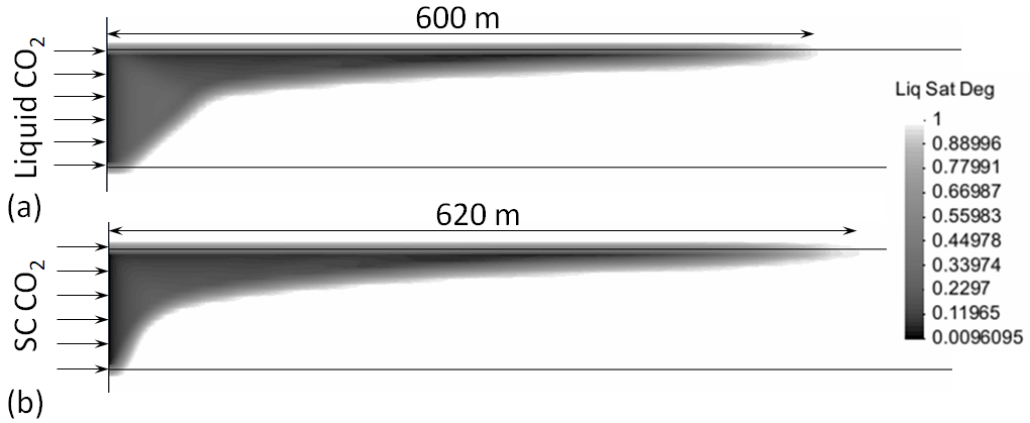

Figure 6.9 – CO_2 plume after 1 year of injecting 1 Mt/yr of CO_2 in (a) liquid and (b) supercritical state.

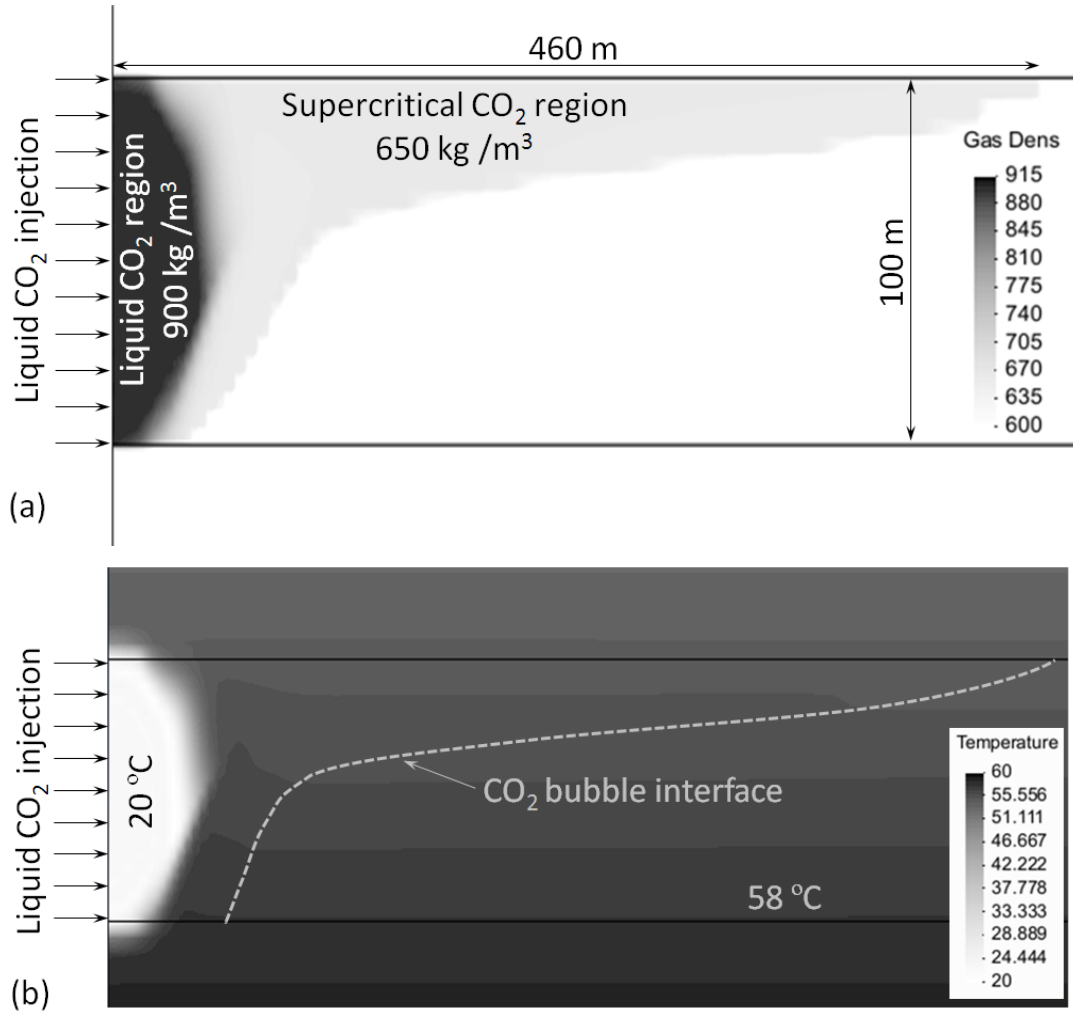

Figure 6.10 – (a) CO_2 density and (b) temperature after 8 months of liquid CO_2 injection. CO_2 remains in liquid state close to the injection well, leading to a steep front because viscous forces dominate gravity forces. Once the CO_2 thermally equilibrates with the medium (in a sharp front), CO_2 stays in SC state, leading to a CO_2 plume interface dominated by gravity forces.

Apart from the cold CO_2 injection, several processes affect the temperature distribution of the CO_2 plume. There is an interaction between: (1) the warmer CO_2 placed at the bottom of the aquifer flows upwards along the interface, (2) the colder brine placed at the top of the aquifer flows downwards along the interface, (3) CO_2 cools down as it advances away from the injection well due to the Joule-Thomson effect and (4) temperature increases due to the exothermal reaction of CO_2 dissolution into the brine. The net result of these processes is a slight temperature increase in the region of the CO_2 plume where CO_2 stays in SC state (Figure 6.10b).

Figure 6.11a shows that injection pressure for liquid CO_2 is slightly smaller than that of SC CO_2 because a higher CO_2 density reduces the volumetric flow rate and therefore the pressure buildup around the well. This is energetically advantageous, because a smaller compression work has to be done to inject the same amount of CO_2. Furthermore, the overpressure in the whole aquifer becomes smaller (Figure 6.11b), which improves the mechanical stability of the caprock.

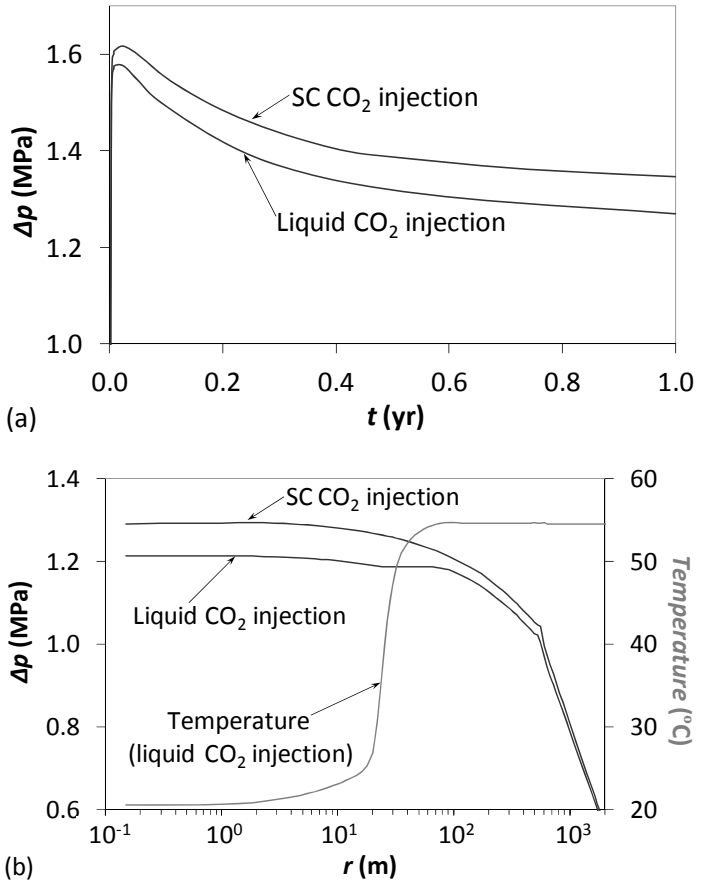

Figure 6.11 – (a) Injection pressure evolution at the top of the aquifer for liquid and SC CO_2 injection and (b) fluid pressure at the top of the aquifer as a function of radial distance from the injection well after 1 yr of injection.

6.4.2. Mechanical response to liquid CO_2 injection

These pressure and temperature changes induce strain and stress changes. Figure 6.12 displays the horizontal and vertical displacements of SC and liquid CO_2 injection. Since fluid pressure distribution is quite similar in both injections (recall Figure 6.11), the differences in displacements will be due to thermal effects. SC CO_2 injection (isothermal) produces a vertical expansion of the aquifer, pushing upwards the caprock and slightly downwards the seal placed below the aquifer. Laterally, SC CO_2 injection pushes the aquifer away from the injection well. However, liquid CO_2 injection generates a cold region around the injection well than undergoes thermal contraction. This is reflected in both the vertical and horizontal displacement. Vertically, the caprock moves downwards and the seal below the aquifer moves upwards close to the injection well. Similarly, the aquifer is displaced towards the injection well in the cold region, presenting the maximum negative horizontal displacement at the cold temperature front. Nevertheless, the thermal effect occurs close to the injection well, where cold CO_2 stays in liquid state (recall Figure 6.10b). Further away, the aquifer expands, both vertically and horizontally, due to overpressure.

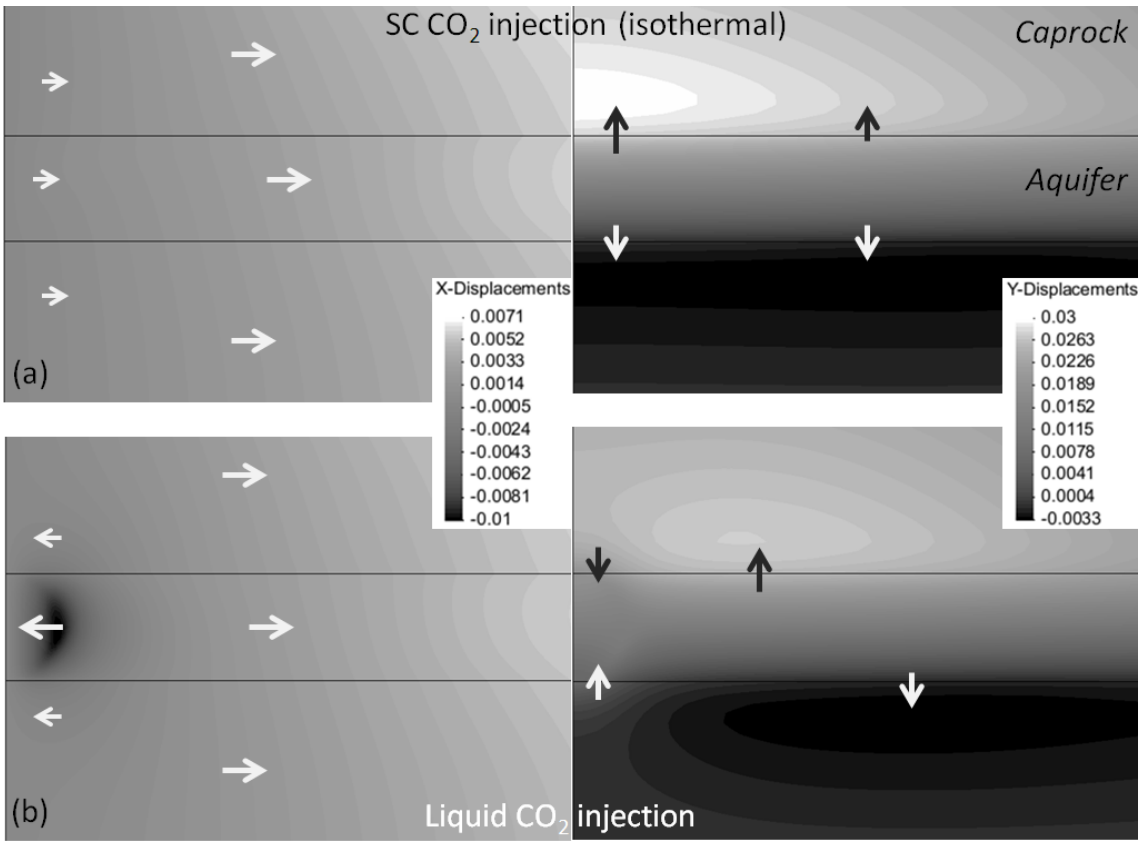

Figure 6.12 – Horizontal and vertical displacements of (a) supercritical and (b) liquid CO_2 injection. Fluid injection pushes the formation laterally and expands it vertically. When injecting cold CO_2, the thermal contraction of the rock is superimposed to the hydraulic effect. The arrows indicate the direction of the displacement.

Figure 6.13 displays total stress changes as a function of depth 3 m away from the injection well when injecting liquid and SC CO_2. The stress change is almost symmetric with respect to the middle of the aquifer. The vertical stress remains practically unaltered when injecting SC CO_2. However, it is reduced as a result of temperature drop when injecting liquid CO_2, with the maximum stress reduction in the middle of the aquifer. The stress reduction is also significant in the region of the seals affected by the temperature reduction (recall Figure 6.10b). The horizontal stresses increase in the aquifer because of lateral confinement that opposes to the expansion caused by CO_2 injection. The stress reduction due to thermal contraction of the rock superimposes to this horizontal stress increment, resulting in a stress reduction in the aquifer. The stress reduction due to thermal contraction of the rock is similar in magnitude in the vertical and horizontal directions. The fact that vertical stresses decrease in the aquifer produces an increase of the horizontal stresses in the seals close to their contact with the aquifer. This can be explained by an arch effect that is formed around the volume with vertical stress reduction to be able to support the overburden on top of the aquifer.

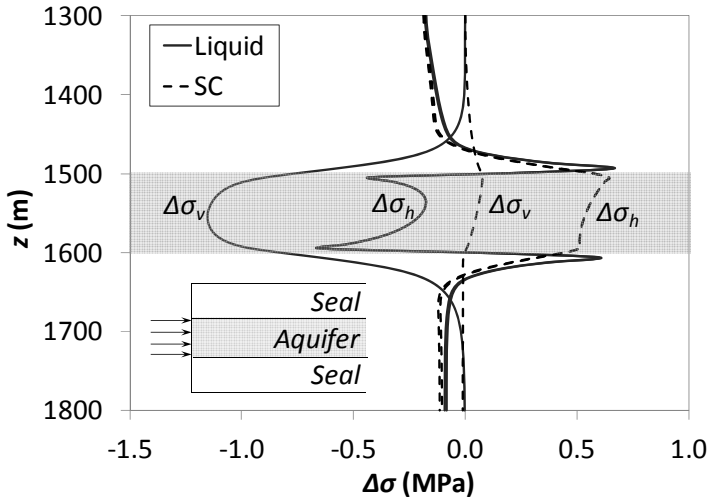

Figure 6.13 – Stress changes as a function of depth 3 m away from the injection well for liquid and SC CO_2 injection after 8 months of injection.

The volume where CO_2 stays in liquid state has equilibrated with the rock and formation water, thus displaying a homogeneous temperature and the transition to the geothermal temperature of the aquifer is abrupt (Figure 6.10b). Therefore, the rock affected by the effective stress reduction due to thermal contraction of the rock presents a homogeneous stress reduction (Figure 6.13) that is proportional to the temperature drop, the linear thermal expansion coefficient and the bulk modulus of the

rock (Eq. (6.8)). Thus, the thermal effect will dominate for large temperature contrasts and in stiff rocks.

6.4.3. Mechanical stability related to liquid CO_2 injection

Fluid injection induces an effective stress reduction that brings the stress state closer to the failure envelope. Furthermore, if the fluid is colder than the formation, a thermal contraction of the rock will occur, reducing even more the effective stresses. However, liquid CO_2 injection benefits from a lower overpressure for a given mass flow rate (Figure 6.11). Therefore, coupled thermo-hydro-mechanical effects of liquid CO_2 injection should be evaluated simultaneously to properly assess the mechanical stability of the aquifer and the caprock.

Figure 6.14 compares the mobilized friction angle along the vertical at a radial distance of 3 m away from the injection well when injecting liquid and SC CO_2 for two values of the lateral earth pressure coefficient. The mobilized friction angle in the aquifer is higher for liquid CO_2 injection than for SC CO_2 injection. However, the opposite occurs at the seals close to their contact with the aquifer when injecting liquid CO_2 for a lateral earth pressure coefficient of 0.5 (Figure 6.14a). This is because when the lateral earth pressure coefficient is lower than 1.0, the maximum principal stress is the vertical. Therefore, if the vertical stress is reduced and the horizontal stress increases (recall Figure 6.13), the Mohr circle becomes smaller, leading to a more stable situation with a smaller mobilized friction angle. The opposite occurs in the aquifer, where the vertical and horizontal stresses are reduced and therefore the Mohr circle shifts to the left, mobilizing higher friction angles. On the other hand, a lateral earth pressure coefficient higher than 1.0 implies a vertical stress smaller than the horizontal stresses. In this situation, a decrease in the vertical stress higher than in the horizontal stress makes the Mohr circle bigger, mobilizing higher friction angles (Figure 6.14b). This trend is only altered in the aquifer close to the contact with the seals, where the reduction in horizontal stress is higher than in vertical stress, leading to a local minimum of the mobilized friction angle in the aquifer.

If the mobilized friction angle becomes higher than the actual friction angle, shear slip of critically oriented pre-existing fractures will occur, which would trigger microseismic events. The effect of shear slip can be advantageous while it takes place within the aquifer, because it can enhance permeability, especially in the direction perpendicular to shear due to dilatancy (Yeo *et al*., 1998; Mallikamas and Rajaram, 2005; Vilarrasa *et*

al., 2011a), and thus injectivity increases. However, if it extends to the caprock, the open-up of fractures can lead to CO_2 leakage. Liquid CO_2 injection increases significantly the mobilized friction angle in the aquifer (Figure 6.14), but it improves caprock stability. This could be even advantageous for the energetic efficiency of this injection concept, because an increase in injectivity due to shearing of pre-existing fractures would lead to a lower injection pressure. Nevertheless, caprock stability should be carefully investigated for large temperature contrasts and in stiff rocks because fracture instability could propagate from the aquifer to the lower part of the caprock.

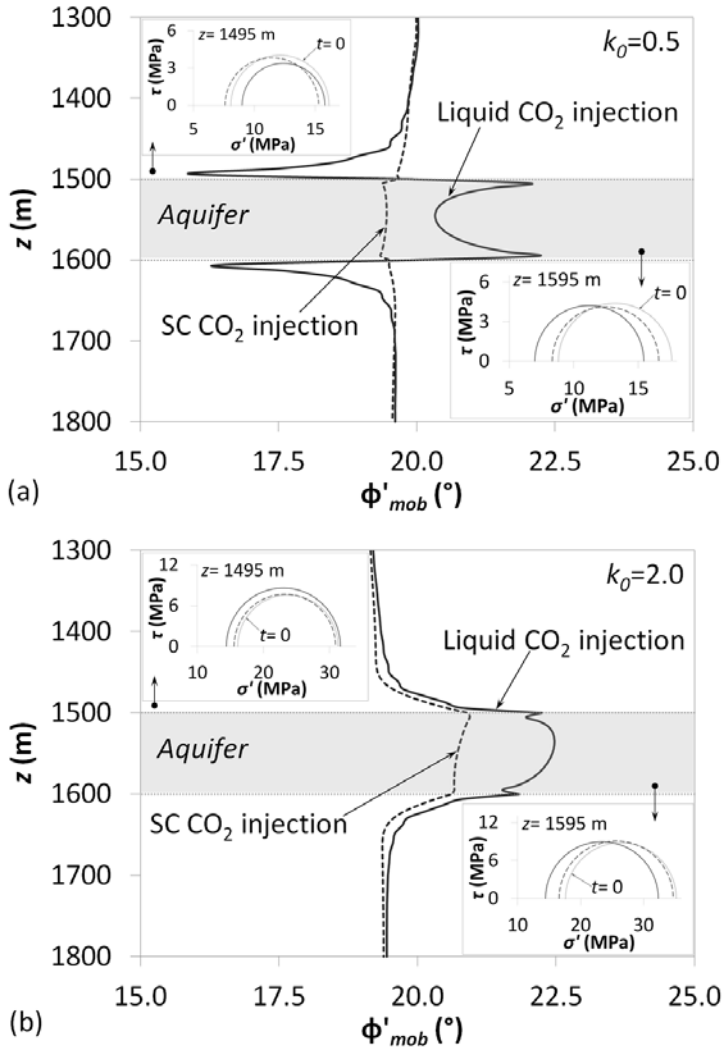

Figure 6.14 – Mobilized friction angle along the vertical for liquid and SC CO_2 injection 3 m away from the injection well after 8 months of injection for a lateral earth pressure coefficient of (a) 0.5 and (b) 2.0. The Mohr circles at depths 1495 m (caprock) and 1595 m (aquifer) are included.

Since thermo-hydro-mechanical simulations have an extremely high computational cost, it is unfeasible to carry out a large number of these simulations. Therefore, the analytical expressions of Eqs. (6.14) and (6.15) can give insight into the injection conditions that can yield fracture instability in the contact between the aquifer and the caprock. Figure 6.15a displays the overpressure normalized by the effective lithostatic stress that is needed to induce a microseismic event at the top of an aquifer placed at 1500 m depth when injecting cold CO_2 as a function of the friction angle for several temperature changes for a lateral earth pressure coefficient of 0.5 and a Poisson ratio of 0.3 using Eq. (6.14). The aquifer can support higher overpressures as its friction angle increases. But the sustainable overpressure decreases for increasing temperature contrasts because the stresses are reduced (Eq. 6.8). Furthermore, the stiffer the rock, the lower the overpressure needed to reach the failure envelope for a given temperature change.

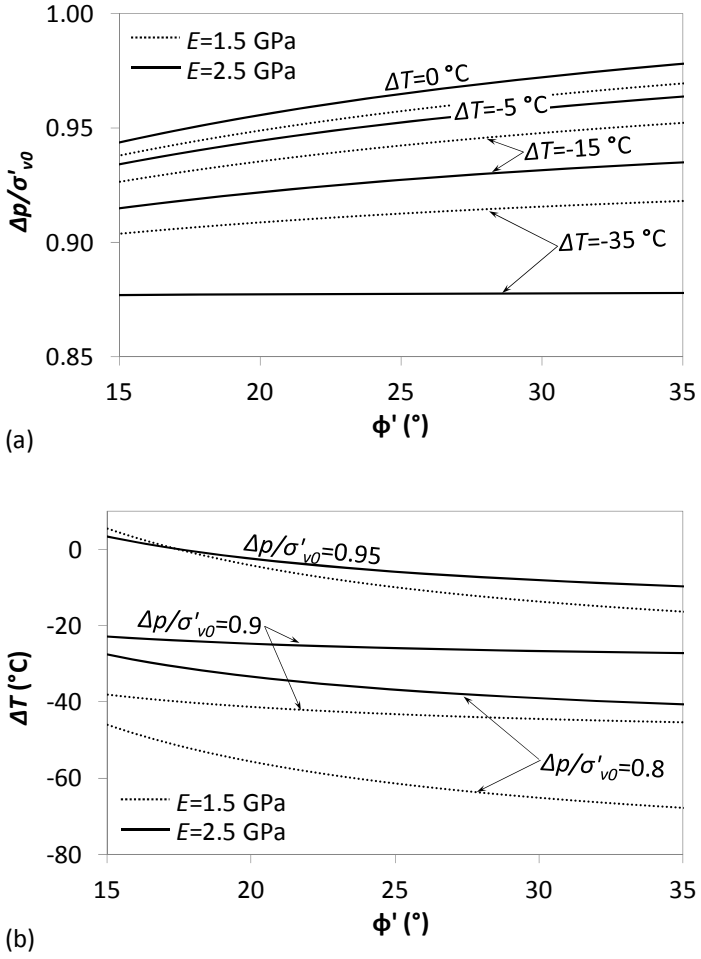

Figure 6.15 – (a) Overpressure normalized by the effective lithostatic stress and (b) temperature drop that is needed to induce a microseismic event at the top of an aquifer placed at 1500 m depth when injecting CO_2 at several temperatures and overpressures, respectively, as a

function of the friction angle for a lateral earth pressure coefficient of 0.5 and a Poisson ratio of 0.3 given by Eq. (6.14) and (6.15) respectively.

Figure 6.15b displays the temperature change that is needed to induce a microseismic event at the top of an aquifer placed at 1500 m depth when injecting cold CO_2 as a function of the friction angle for several overpressures for a lateral earth pressure coefficient of 0.5 and a Poisson ratio of 0.3 using Eq. (6.15). The maximum acceptable temperature change becomes higher for a given overpressure as the friction angle increases. Furthermore, the stiffer the rock, the smaller the temperature change required for inducing microseismicity for a given overpressure. Figure 6.15 can be used as a reference to assess the feasibility of injecting liquid CO_2 at a given site, once the rigidity of the rock and the temperature change are known. Since there are 3D effects that have not been considered in the analytical treatment of the problem, Figure 6.15 should be used only for guidance. However, its use is strongly recommended as a preliminary analysis of the suitability of liquid CO_2 injection at a given site because they avoid performing coupled thermo-hydro-mechanical simulations, which imply a high computational cost.

6.5. Conclusions

We propose to inject CO_2 in liquid state. This is favourable for several reasons: (1) this injection strategy is energetically advantageous, (2) no transformation operation or low energy consumption conditioning operations are necessary, (3) a smaller compression work is necessary because of the smaller compressibility of liquid CO_2, (4) since liquid CO_2 is denser than SC CO_2, liquid CO_2 injection induces a lower overpressure because a smaller amount of fluid is displaced and (5) the caprock mechanical stability is improved.

Although relatively simple as a concept, the implementation of the operation may require a thoroughly design of conditioning systems (e.g. throttling, heating or cooling) to get the injection conditions. Nevertheless, the system is relatively easy to control because direct control variables are the injection temperature and pressure. Additionally, the system may be indirectly controlled by a suitable design of the wellbore materials (e.g. cement, casing) to reduce the heat transfer between the pipe and the surroundings, thus ensuring that the CO_2 remains in liquid state along the entire injection pipe. Since, in general, the temperature at which CO_2 will reach the

aquifer will be different than that of the aquifer, non-isothermal simulations should be performed to reproduce realistic injection conditions.

As for the mechanical stability of the rocks, the thermal effect is more pronounced for large temperature contrasts and in stiff rocks. Thermal contraction mobilizes higher friction angles in the aquifer, which could lead to shear slip of pre-existing fractures. The effect of shear slip can be advantageous while it takes place within the aquifer, because it enhances permeability and thus CO_2 injectivity. Interestingly, the mobilized friction angle in the seals is not increased when injecting liquid CO_2 and it is even reduced in stress regimes where the maximum principal stress is the vertical.

7. Conclusions

This Thesis deals with several coupled effects related to CO_2 sequestration, including two-phase flow, hydromechanical coupling and thermo-hydro-mechanical coupling. The main conclusions drawn from this Thesis are summarized below.

Analytical solutions are useful because they provide a quick solution and help identify relevant parameters pertaining to a particular problem. However, current analytical solutions for the geometry of a CO_2 plume make several oversimplifying assumptions that we attempt to relax. These include the incompressibility of CO_2 and the uniform injection of CO_2 along the entire thickness of the aquifer. We have relaxed the former assumption by introducing an iterative method that corrects the initial estimate of CO_2 density and viscosity and hence ends up using more realistic values. We have found that the error associated with neglecting compressibility increases dramatically when gravity forces dominate, which is likely to occur at late times of injection. Comparison with numerical simulations suggests that the previously published solution of Nordbotten *et al*. (2005) gives good predictions for the CO_2 plume position when viscous forces dominate, while the solution of Dentz and Tartakovsky (2009a) provides better estimates when gravity forces dominate. Additionally, we have developed a semianalytical solution that takes into account both CO_2 compressibility and buoyancy effects within the injection well. Therefore, CO_2 is not necessarily injected along the entire thickness of the aquifer. The CO_2 plume geometry and fluid overpressure obtained from the semianalytical solution are in good agreement with high resolution numerical solutions. However, the computational cost and time to complete the calculations is minimal compared to these numerical solutions.

Fluid overpressure induces deformations of the aquifer and the caprock. When injecting a constant CO_2 mass flow rate in a vertical well, fluid pressure builds up sharply at the beginning of injection both because the viscosity of the displaced brine is high and because the permeability to brine is reduced due to desaturation. However, once CO_2 fills the pores in the vicinity of the injection well and a capillary fringe is fully developed, the pressure within the CO_2 plume slowly decreases both because the flux

across the fringe is reduced (it is inversely proportional to the radius of the capillary fringe) and because the viscosity of CO_2 is much lower than that of the brine. As a result, mechanical stability tends to improve. However, in the presence of a low-permeability boundary, brine pressure rises once the radius of influence reaches the outer boundary, which causes the CO_2 pressure to rise and could compromise the mechanical integrity of the caprock in the long-term. A conclusion from this analysis is that the risk of damage to the caprock is reduced if the injection rate is progressively increased at the beginning of injection.

The mechanical response of the aquifer and caprock to the fluid pressure perturbations depends on their mechanical properties, i.e. the Young's modulus and the Poisson ratio. These parameters are usually measured at the laboratory. However, values measured at the laboratory scale may not be representative of effective values at the field scale. Thus, we propose a hydromechanical characterization test to determine the aquifer and caprock hydromechanical properties at the field scale. This test permits also the determination of the maximum sustainable injection pressure, defined as the pressure that causes the onset of microseismicity in the caprock. We obtain curves for overpressure and vertical displacement as a function of the volumetric strain term obtained from a dimensional analysis of the hydromechanical equations. These curves show the hydromechanical behaviour of the aquifer-caprock system when injecting a fluid, but more importantly, they can also be used for parameter estimation from field measurements. Overall, this test will help assess the suitability of specific CO_2 storage sites and will allow practitioners to obtain representative effective values of hydromechanical parameters at the field scale.

We also propose a new injection strategy that is energetically advantageous and that improves the caprock mechanical stability in some situations, which consists of injecting CO_2 in liquid state. Liquid (cold) CO_2 is denser than supercritical CO_2. Therefore, the pressure required at the wellhead for a given CO_2 pressure at the aquifer is much lower for liquid than for gas or supercritical injection. Actually, the overpressure required at the aquifer is also smaller because a smaller fluid volume is displaced. Furthermore, since CO_2 is transported through pipelines in liquid state, CO_2 could be injected directly as it arrives to the wellhead or after conditioning operations of low energy cost. Thus, this injection strategy is energetically efficient. Apart from this, the injected liquid CO_2 will cool the reservoir around the injection well, inducing a stress reduction due to thermal contraction of the rock. The thermal effect becomes greater for larger temperature contrasts and for stiffer rocks. The thermal contraction of the

rock mobilizes higher friction angles, which could lead to shear slip of pre-existing fractures. Shear slip enhances fracture permeability, which is advantageous for CO_2 injection while it occurs within the aquifer. This is likely to occur when injecting liquid CO_2, because, interestingly, the mobilized friction angle in the caprock is not increased and is even reduced in stress regimes where the maximum principal stress is the vertical.

Appendices

I. Mean CO_2 density

Here, the mean CO_2 density defined in Eq. (2.16) is calculated using the linear approximation of CO_2 density with respect to pressure presented in Eq. (2.20) for both approaches, i.e. Nordbotten *et al*. (2005) and Dentz and Tartakovsky (2009a).

With the Nordbotten *et al*. (2005) approach, the mean CO_2 density is calculated by introducing (2.11) and (2.17) into (2.16), which leads to

$$\overline{\rho}_{cN} = \frac{2\pi\varphi}{V}\left\{\rho_0 \frac{d}{2} r_0 r_b + \rho_1 \beta\left[\frac{r_0 r_b}{4}\rho_w g d^2 + \frac{Q_0 \mu_w}{2\pi k}\left[r_0 r_b\left(\frac{1}{2}\ln\left(\frac{R}{r_0}\right)+\frac{1}{3}\right) - \frac{r_b^2}{6}\left(1-\frac{1}{2}\frac{\mu_c}{\mu_w}\right)\right]\right]\right\}. \tag{I.1}$$

Similarly, introducing (2.13) and (2.18) into (2.16), and integrating, yields the expression for the mean CO_2 density for the Dentz and Tartakovsky (2009a) approach,

$$\overline{\rho}_{cDT} = \frac{2\pi\varphi}{V}\left\{\left[\exp\left(\frac{2}{\gamma_{cw}}\right)-1\right]\frac{r_b^2}{4} d\gamma_{cw}\left[\rho_0 + \rho_1\beta\left(\frac{d\gamma_{cw}}{2}\rho_w g + \frac{Q_0}{2\pi k d}\left(\mu_w \ln\left(\frac{R}{r_b}\right) + \frac{\mu_w+\mu_c}{2}\right)\right)\right] - \frac{r_b^2}{4} d^2 \gamma_{cw}\rho_1\beta\rho_w g - \exp\left(\frac{2}{\gamma_{cw}}\right)\frac{r_b^2}{4} d\rho_1\beta\frac{Q_0}{2\pi k d}\mu_w\right\} \tag{I.2}$$

II. Implementation of CO_2 properties in CODE_BRIGHT

CODE_BRIGHT has been extended to simulate non-isothermal CO_2 injection. To do so, the Redlich and Kwong (1949) equation of state with the parameters proposed for CO_2 by Spycher *et al*. (2003) has been implemented. This equation of state is a cubic equation of the molar volume

$$V^3 - \left(\frac{RT}{p_c}\right)V^2 - \left(\frac{RTb}{p_c} - \frac{a}{p_c\sqrt{T}} + b^2\right)V - \left(\frac{ab}{p_c\sqrt{T}}\right) = 0\,, \qquad \text{(II.1)}$$

where V is molar volume, R is the gas constant, T is temperature, p_c is CO_2 pressure and a and b represent measures of intermolecular attraction and repulsion, respectively. Note that if $a = b$ = 0, the ideal gas law is recovered.

Spycher *et al*. (2003) assumed that

$$a = a_0 + a_1 T\,, \qquad \text{(II.2)}$$

and adjust a_0, a_1 and b to experimental $p_c - V - T$ data. For pure CO_2 these constants are

$$a_0 = 7.54\ \text{Pa}\cdot\text{m}^6\cdot\text{K}^{0.5}/\text{mol}^2\,, \qquad \text{(II.3a)}$$

$$a_1 = -4.13\cdot10^{-3}\ \text{Pa}\cdot\text{m}^6/\text{K}^{0.5}/\text{mol}^2\,, \qquad \text{(II.3b)}$$

$$b = 2.78\cdot10^{-5}\ \text{m}^3/\text{mol}\,. \qquad \text{(II.3c)}$$

Given a CO_2 pressure p_c and a temperature T, the cubic equation Eq. (II.1) can be solved directly for V by following a method like the one proposed by Nickalls (1993). Once the molar volume V is known, CO_2 density, ρ_c, is calculated as

$$\rho_c = \frac{M_{CO2}}{V}\,, \qquad \text{(II.4)}$$

where M_{CO2} = 0.044 kg/mol is the CO_2 molecular weight. Figure II.1 shows CO_2 density calculated according to this equation of state for several temperatures (sub and supercritical) and up to 40 MPa.

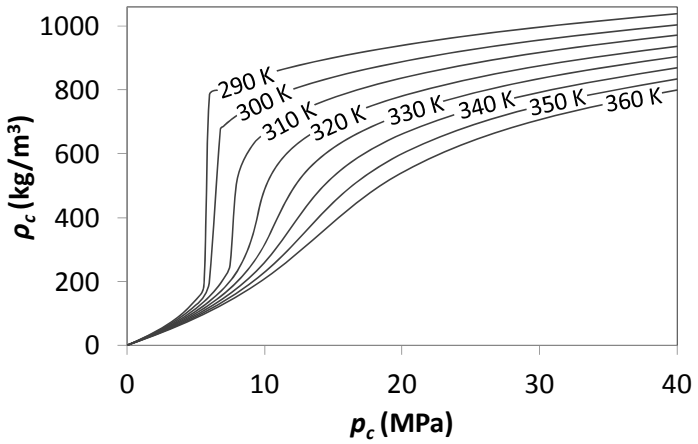

Figure II.1 – CO_2 density calculated according to the Redlich-Kwong equation of state with the parameters proposed by Spycher *et al*. (2003).

CO_2 viscosity, μ_c, has been taken from the empirical expression proposed by Altunin and Sakhabetdinov (1972), which according to Sovova and Prochazka (1993) is the most precise expression for CO_2 viscosity

$$\mu_c = \mu_0 \exp\left(\sum_{i=1}^{4}\sum_{j=0}^{1} \frac{a_{ij}\rho_R^i}{T_R^j}\right), \qquad \text{(II.5)}$$

where $\rho_R = \rho_c / \rho_{cr}$ and $T_R = T / T_{cr}$ are the reduced density and temperature, respectively, ρ_{cr} = 468 kg/m^3 and T_{cr} = 304 K. The coefficients a_{10} = 0.248566120, a_{11} = 0.004894942, a_{20} = -0.373300660, a_{21} = 1.22753488, a_{30} = 0.363854523, a_{31} = -0.774229021, a_{40} = -0.0639070755 and a_{41} = 0.142507049 were obtained from adjusting nine experimental data sets of CO_2 viscosity in the range of temperatures from 220 to 1300 K and up to a pressure of 120 MPa. μ_0, expressed in μPa·s, is a function of temperature and is given by

$$\mu_0 = T_R^{0.5}\left(27.2246461 - \frac{16.6346068}{T_R} + \frac{4.66920556}{T_R^2}\right). \qquad \text{(II.6)}$$

CO_2 density appearing in Eq. (II.5) is evaluated using the Redlich-Kwong equation of state (Eqs. II.1 – II.4). Figure II.2 displays CO_2 viscosity calculated according to this empirical relationship for several temperatures and up to a pressure of 40 MPa.

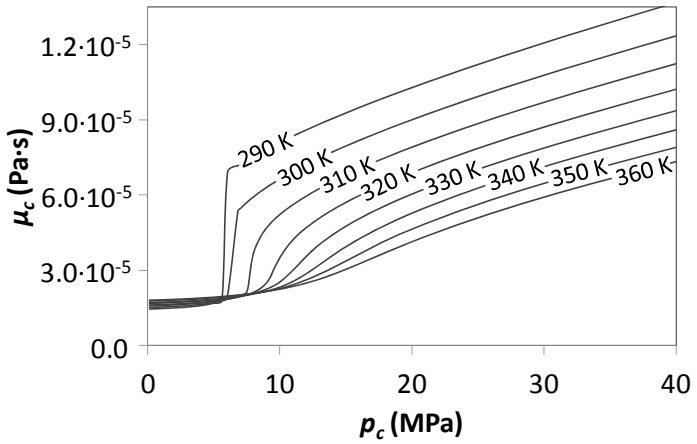

Figure II.2 – CO_2 viscosity calculated according to the empirical expression proposed by Altunin and Sakhabetdinov (1972).

Additionally, water density increment due to CO_2 dissolution has been implemented following the methodology proposed by Garcia (2003). Water density, ρ_w, is proportional to the dissolved CO_2 and a coefficient δ that accounts for the fact that the dissolved CO_2 occupies a certain volume

$$\rho_w = \rho_{w0} \exp\left(\beta\left(p_w - p_{w0}\right) + \alpha_w T\right)\left(1 + \delta\omega_l^c\right), \tag{II.7}$$

where ρ_{w0} is a reference water density corresponding to the reference water pressure p_{w0}, β is water compressibility, p_w is water pressure, α_w is water volumetric thermal expansion coefficient, ω_l^c is the CO_2 mass fraction in liquid and δ is

$$\delta = 1 - \rho_{w0} \exp\left(\beta\left(p_w - p_{w0}\right) + \alpha_w T\right)\frac{V_\phi}{M_{CO_2}}, \tag{II.8}$$

where V_ϕ is the apparent molar volume of dissolved CO_2. V_ϕ, expressed in m^3/mol, is a function of temperature (in ºC) and is equal to

$$V_\phi = \left(37.51 - 9.585 \cdot 10^{-2} T + 8.74 \cdot 10^{-4} T^2 - 5.044 \cdot 10^{-7} T^3\right) 10^{-6}. \tag{II.9}$$

The specific enthalpy of CO_2, h_c, can be evaluated integrating the fundamental thermodynamic relationship

$$dh_c = c_p dT + \left[V - T\left(\frac{\partial V}{\partial T}\right)_p\right] dp_c, \tag{II.10}$$

where c_p is the specific heat capacity at constant pressure, and the molar volume of CO_2, V, can be calculated using the Redlich-Kwong equation of state of Eqs. (II.1) to (II.4). At constant temperature, Eq. (II.10) reduces to

$$dh_c = \left[V - T\left(\frac{\partial V}{\partial T}\right)_p \right] dp_c \,. \tag{II.11}$$

Integrating Eq. (II.11) between a reference pressure, e.g. atmospheric pressure, and a CO_2 pressure p_c yields

$$h_c(p_c,T) - h_c^*(T) = \int_0^{p_c} \left[V - T\left(\frac{\partial V}{\partial T}\right)_p \right] dp_c \,, \tag{II.12a}$$

or

$$h_c(p_c,T) - h_c^*(T) = RT(Z-1) + \int_\infty^V \left[T\left(\frac{\partial p_c}{\partial T}\right)_V - p_c \right] dV \,, \tag{II.12b}$$

where h_c^* is the enthalpy of an ideal gas at atmospheric pressure, which only depends on temperature and Z is the compressibility factor. Adopting the Redlich-Kwong equation of state with the parameters proposed by Spycher *et al*. (2003), Eq. (II.12) becomes

$$h_c(p_c,T) - h_c^*(p_0,T) = \left(p_c V - RT - \frac{1.5a - a_1 T}{\sqrt{T}\,b} \ln\left(1 + \frac{b}{V}\right) \right) \Big/ M_{CO2} \,, \tag{II.13}$$

where temperature expressed in K, molar volume in m^3/mol and gas pressure in Pa gives enthalpy in J/kg. Figure II.3 shows the CO_2 enthalpy calculated from Eq. (II.13) for several temperatures up to a CO_2 pressure of 40 MPa.

Once the CO_2 enthalpy is determined through Eq. (II.13), the CO_2 specific heat capacity can be calculated from its definition

$$c_p = \left(\frac{\partial h_c}{\partial T}\right)_p \,. \tag{II.14}$$

Applying Eq. (II.14) with the expression of the enthalpy given by Eq. (II.13) yields

$$c_p = \frac{\partial h^*(p_0,T)}{\partial T} + \left(p_c \frac{\partial V}{\partial T} - R + \frac{0.75a}{b\sqrt{T^3}} \ln\left(1 + \frac{b}{V}\right) + \frac{1.5a - a_1 T}{\sqrt{T}(V+b)V} \frac{\partial V}{\partial T} \right) \Big/ M_{CO2} \,, \tag{II.15}$$

where

$$\frac{\partial V}{\partial T} = \frac{RV^2 + V\left(Rb - (0.5a - a_1 T)/\sqrt{T^3}\right) - b(0.5a - a_1 T)/\sqrt{T^3}}{3V^2 p_c + 2VRT + RTb - a/\sqrt{T} + b^2 p_c} \,, \tag{II.16}$$

where temperature expressed in K, molar volume in m^3/mol and gas pressure in Pa gives the specific heat capacity in J/kg/K. Figure II.4 displays the CO_2 specific heat capacity calculated from Eq. (II.15) and (II.16).

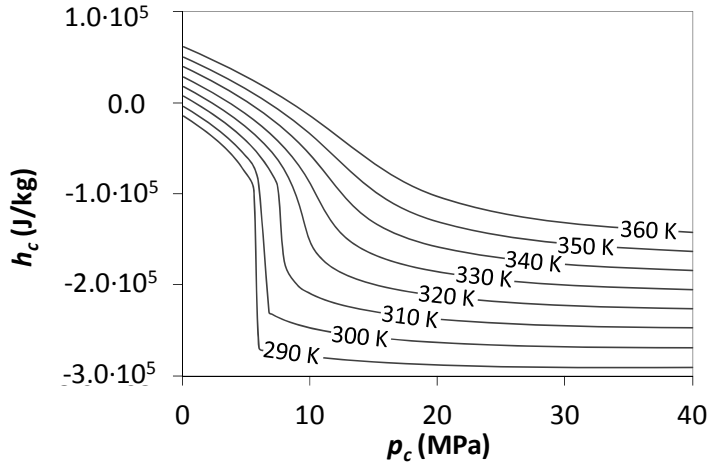

Figure II.3 – CO_2 enthalpy calculated from the Redlich-Kwong equation of state with the parameters proposed by Spycher *et al*. (2003).

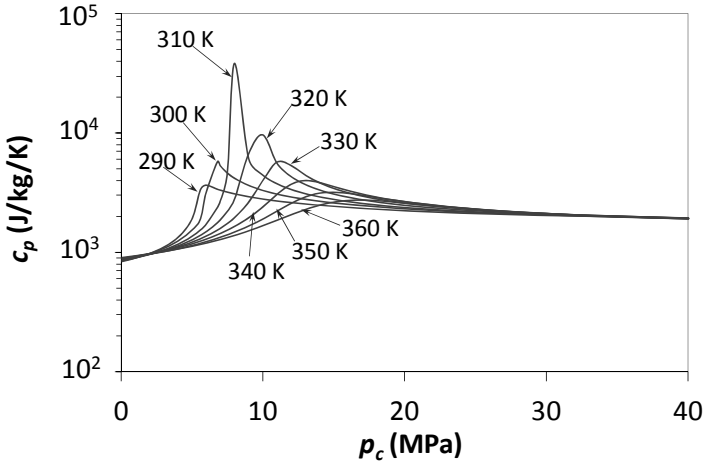

Figure II.4 – Specific heat capacity calculated from the Redlich-Kwong equation of state with the parameters proposed by Spycher *et al*. (2003).

We also account for the enthalpy of dissolved CO_2. According to Han *et al*. (2010), the enthalpy of dissolved CO_2, expressed in J/kg, is a function of temperature (in K),

$$h_l^c(T) = \left(106.56 - \frac{6.2634 \cdot 10^4}{T} + \frac{7.475 \cdot 10^6}{T^2}\right) \frac{10^3}{M_{CO2}} . \qquad \text{(II.16)}$$

McPherson *et al*. (2008) compared the Redlich-Kwong equation of state with that of Span and Wagner (Span and Wagner, 1996). They show that the thermodynamic properties given by Span and Wagner (1996) are almost identical to the International Union of Pure and Applied Chemistry (IUPAC) (Angus *et al*., 1976) data sets over the $p_c - T$ range of CO_2 sequestration interest. However, the algorithm given by Span and Wagner (1996) for evaluating CO_2 properties has a very high computational cost, being around 100 times slower than that of the Redlich-Kwong equation of state (McPherson *et al*., 2008). Additionally, the Redlich-Kwong equation of state is more flexible and gives acceptable agreement with experimental data (McPherson *et al*., 2008). Therefore, we chose to use the Redlich-Kwong equation of state.

III. Potential calculation

Here we develop the mathematical formulation of the problem for the case in which CO_2 density varies linearly with pressure (Eq. (3.24)), and CO_2 viscosity and brine properties are constant.

First, we integrate Eq. (3.4) for the CO_2 phase, which yields

$$h_c = z - z_0 + \frac{1}{g\beta}\ln\left(1 + \frac{\beta}{\rho_0}\left(P_c - P_0\right)\right). \tag{III.1}$$

The inverse of Eq. (III.1) gives the CO_2 pressure as a function of the head as

$$P_c - P_0 = \frac{\rho_0}{\beta}\left(e^{g\beta(h_c-(z-z_0))} - 1\right). \tag{III.2}$$

Integrating Eq. (3.12) and using Eq. (III.2) gives the following expression for the CO_2 potential

$$\Phi_c = \frac{\pi k \rho_0^2}{\mu_c \beta} e^{-2g\beta(z-z_0)}\left(e^{2g\beta h_c} - 1\right). \tag{III.3}$$

Since the exponent $2g\beta h_c$ is small, $\left(e^{2g\beta h_c} - 1\right)$ can be approximated as $2g\beta h_c$. Therefore, the CO_2 potential can be expressed as

$$\Phi_c \approx 2\pi g k \frac{\rho_0^2}{\mu_c} h_c \, e^{-2g\beta(z-z_0)}, \tag{III.4}$$

where the potential is composed of a part corresponding to a constant CO_2 density (ρ_0) multiplied by a correction due to CO_2 compressibility (the exponential in the right-hand side of Eq. (III.4)). Combining Eq. (III.1) and (III.3) and operating, yields an expression of CO_2 pressure as a function of the potential

$$P_c - P_0 = \sqrt{\frac{\mu_c}{\pi k \beta}\Phi_c + \frac{\rho_0^2}{\beta^2} e^{-2g\beta(z-z_0)}} - \frac{\rho_0}{\beta}. \tag{III.5}$$

Note that the head (Eq. (III.1)) at the interface can be expressed as a function of the CO_2 density as

$$h_{ci} = z - z_0 + \frac{1}{g\beta}\ln\left(\frac{\rho_0 + \beta\left(P_{ci} - P_0\right)}{\rho_0}\right) = z - z_0 + \frac{1}{g\beta}\ln\left(\frac{\rho_{ci}}{\rho_0}\right), \tag{III.6}$$

where the subscript i indicates interface. Combining Eq. (III.3) with Eq. (III.6) yields the following expression for the CO_2 potential at the interface

$$\Phi_i = \frac{\pi k \rho_0^2}{\mu_c \beta}\left(\frac{\rho_{ci}^2}{\rho_0^2} - e^{-2g\beta(z-z_0)}\right). \tag{III.7}$$

In the brine phase, integration of Eq. (3.4) yields

$$h_w = z - z_0 + \frac{P_w - P_0}{\rho_w g}, \tag{III.8}$$

which is the expression of the head for an incompressible fluid. Integrating Eq. (3.12) gives the potential in the brine phase as

$$\Phi_w = 2\pi g k \frac{\rho_w^2}{\mu_w} h_w. \tag{III.9}$$

Combining Eq. (III.8) with (III.9), gives the following expression for the brine pressure

$$P_w - P_0 = \frac{\mu_w}{2\pi k \rho_w}\Phi_w - \left(z - z_0\right)\rho_w g. \tag{III.10}$$

Note that the brine pressure varies with the logarithm of the distance to the injection well (see the form of the potential in Eq. (3.16a)).

IV. CO_2 plume thickness calculation

A system of two equations with two unknowns has to be solved in step 4 of the time stepping algorithm of Chapter 3 when a mass flow rate is prescribed at the injection well. The unknowns are the head at the well and the thickness of the CO_2 plume at the well. The two equations are Eq. (3.23) and (3.8) accounting for the capillary entry pressure in (3.6).

Combining Eq. (3.23) with Eqs. (3.18), (III.3) and (III.7), after some algebra, gives the following expression for the head at the well as a function of the increment of the CO_2 plume thickness

$$e^{2g\beta h_c} = \frac{Q - A_1\Delta z_f + A_2 - A_3}{A_4}, \tag{IV.1}$$

where

$$Q = \frac{\mu_c\beta}{\pi k\rho_0^2} Q_m, \tag{IV.2a}$$

$$A_1 = \frac{\mu_c\beta}{\pi k\rho_0^2} \frac{\overline{\rho}_c \pi r_{if}^2 \varphi\left(1 - S_{rw}\right)}{\Delta t}, \tag{IV.2b}$$

$$A_2 = \sum_{j=1}^{m} \frac{\rho_{ci,j}^2 / \rho_0^2}{\ln\left(r_j / r_p\right)} \Delta z_j, \tag{IV.2c}$$

$$A_3 = \frac{\mu_c\beta}{\pi k\rho_0^2} \sum_{j=1}^{n} \frac{J_{cz,j+1} \ln\left(r_{j+1} / r_j\right)}{\ln\left(r_j / r_p\right)} \Delta z_j, \tag{IV.2d}$$

$$A_4 = \sum_{j=1}^{m} \frac{e^{-2g\beta\left(z_j - z_0\right)}}{\ln\left(r_j / r_p\right)} \Delta z_j. \tag{IV.2e}$$

Next, combining Eq. (3.6) with Eqs. (III.3), (III.5) and assuming hydrostatic conditions at the well give the second equation of the system of equations

$$e^{g\beta h_c} = p + \frac{\rho_w}{\rho_0} g\beta\Delta z_f, \tag{IV.3}$$

where

$$p = \frac{\beta}{\rho_0}\left(P_w\left(z_{f-1}\right) + P_{cc}\right) + 1, \tag{IV.4}$$

where $P_w\left(z_{f-1}\right)$ is the brine pressure evaluated at the depth reached by the CO_2 plume in the previous time step. The combination of Eq. (IV.1) and (IV.3) gives the following quadratic equation

$$\Delta z_f^2 + B\Delta z_f + C = 0\,, \tag{IV.5}$$

where

$$B = \frac{2p\rho_0}{g\beta\rho_w} + \frac{\rho_0^2 e^{-2g\beta\left(z_f - z_0\right)}}{\rho_w^2 g^2 \beta^2}\frac{A_1}{A_4}\,, \tag{IV.6a}$$

$$C = \frac{\rho_0^2}{\rho_w^2 g^2 \beta^2}\left(p^2 - \frac{Q + A_2 - A_3}{A_4}e^{-2g\beta\left(z_f - z_0\right)}\right). \tag{IV.6b}$$

Once Eq. (IV.5) is solved and the increment of the CO_2 plume thickness at the well in a given time step is known, the head at the well can be calculated from Eq. (IV.1) as

$$h_c\left(r_p\right) = \frac{1}{2g\beta}\exp\left(\frac{Q - A_1\Delta z_f + A_2 - A_3}{A_4}\right). \tag{IV.7}$$

V. Mean CO_2 density at a layer

The mean CO_2 density in a given layer has to be calculated in order to apply Eq. (3.23). Assuming that CO_2 density varies linearly with pressure (Eq. (3.24)), and using Eq. (III.5), (3.16c) and (III.7), after some algebra, the following expression for the CO_2 density is obtained

$$\rho_c = \sqrt{\rho_{ci}^2 + \frac{\mu_c \beta}{\pi k} J_c \ln \frac{r_j}{r}} \quad . \tag{V.1}$$

The mean CO_2 density in a layer is obtained from dividing the CO_2 mass in a given layer by the volume that it occupies

$$\overline{\rho} = \frac{1}{V} \int_{z_{j-1}}^{z_j} \int_{r_p}^{r_j} 2\pi r \varphi (1 - S_{rw}) \rho_c \, \mathrm{d}r \, \mathrm{d}z \, . \tag{V.2}$$

Introducing Eq. (V.1) in Eq. (V.2) and integrating yields

$$\begin{aligned} \overline{\rho} = & \frac{1}{\left(r_j^2 - r_p^2\right)} \left[r^2 \sqrt{a - b \ln r} - \frac{1}{2} \sqrt{\frac{\pi}{2}} \sqrt{b} e^{2a/b} erf\left(\sqrt{\frac{2}{b}} \sqrt{a - b \ln r} \right) \right]_{r_p}^{r_j} = \\ & \frac{1}{\left(r_j^2 - r_p^2\right)} \left[r_j^2 \rho_{ci} - r_p^2 \rho_{cp} + \frac{r_j^2}{2} \sqrt{\frac{b\pi}{2}} \exp\left(\frac{2\rho_{ci}^2}{b} \right) \left(erf\left(\sqrt{\frac{2}{b}} \rho_{ci} \right) - erf\left(\sqrt{\frac{2}{b}} \rho_{cp} \right) \right) \right] \end{aligned} , \tag{V.3}$$

where

$$a = \rho_{ci}^2 + \frac{\mu_c \beta}{\pi k} J_c \ln r_j \, , \tag{V.4a}$$

$$b = \frac{\mu_c \beta}{\pi k} J_c \, . \tag{V.4b}$$

VI. Coupled HM formulation for CO_2 flow

The balance equations required for the solution of the problems studied in Chapter 4 are presented in this appendix. Olivella *et al*. (1994) have presented the governing equations for non-isothermal multiphase flow of water and gas through porous deformable media. A detailed derivation is given there, and only a description of the modified formulation for gas (CO_2) flow is presented in this appendix.

The mass balance of solid present in the medium is written as

$$\frac{\partial}{\partial t}\left(\rho_s\left(1-\phi\right)\right)+\nabla\cdot\left(\mathbf{j}_s\right)=0\ , \tag{VI.1}$$

where ρ_s is the density of solid and $\mathbf{j}_s$ is the flux of solid. From this equation, an expression for porosity variation can be obtained if the flux of solid is written as the velocity of the solid multiplied by the volumetric fraction occupied by the solid phase and its density, i.e. $\mathbf{j}_s = \rho_s(1-\varphi)\,\mathrm{d}\,\mathbf{u}/\mathrm{d}\,t$,

$$\frac{D_s\varphi}{Dt}=\frac{\left(1-\varphi\right)}{\rho_s}\frac{D_s\rho_s}{Dt}+\left(1-\varphi\right)\nabla\cdot\frac{\mathrm{d}\,\mathbf{u}}{\mathrm{d}\,t}\,. \tag{VI.2}$$

The material derivative with respect to the solid is defined as

$$\frac{D_s\left(\bullet\right)}{Dt}=\frac{\partial\left(\bullet\right)}{\partial t}+\frac{\mathrm{d}\,\mathbf{u}}{\mathrm{d}\,t}\cdot\nabla\left(\bullet\right). \tag{VI.3}$$

Equation (VI.2) expresses the variation of porosity caused by volumetric deformation and solid density variation.

In the formulation required for the analysis in this paper, gas and liquid phases are considered. The total mass balance of a component i present in each phase (for instance dissolved CO_2 or evaporated water) is expressed as

$$\frac{\partial}{\partial t}\left(\omega_l^i\rho_l S_l\varphi+\omega_g^i\rho_g S_g\varphi\right)+\nabla\cdot\left(\mathbf{j}_l^i+\mathbf{j}_g^i\right)=f^i\ , \tag{VI.4}$$

where S_l , S_g are the phase degree of saturations; ω_l^i , ω_g^i are the mass fractions of the component i in each phase; ρ_l , ρ_g are the phase densities, $\mathbf{j}_l^i$, $\mathbf{j}_g^i$ are the mass fluxes of the component i in each phase and f^i is an external supply of mass

of component i . In this formulation the components are the water and CO_2. The mass flux of components is a combination of a non-advective flux (diffusion + dispersion) written as $\mathbf{i}_l^i$, $\mathbf{i}_g^i$, the advective Darcy flux written as $\mathbf{q}_l$, $\mathbf{q}_g$ and another advective term caused by the solid motion proportional to the solid velocity $\mathrm{d}\mathbf{u}/\mathrm{d}t$:

$$\frac{\partial}{\partial t}\left(\omega_l^i\rho_l S_l\varphi+\omega_g^i\rho_g S_g\varphi\right)+\nabla\cdot\left(\mathbf{i}_l^i+\mathbf{i}_g^i+\omega_l^i\rho_l\mathbf{q}_l+\omega_g^i\rho_g\mathbf{q}_g+\left(\omega_l^i\rho_l S_l+\omega_g^i\rho_g S_g\right)\varphi\frac{\mathrm{d}\mathbf{u}}{\mathrm{d}t}\right)=f^i\,. \tag{VI.5}$$

The use of the material derivative leads to

$$\begin{aligned}&\varphi\frac{D_s\left(\omega_l^i\rho_l S_l+\omega_g^i\rho_g S_g\right)}{Dt}+\left(\omega_l^i\rho_l S_l+\omega_g^i\rho_g S_g\right)\frac{D_s\varphi}{Dt}+\left(\omega_l^i\rho_l S_l+\omega_g^i\rho_g S_g\right)\varphi\nabla\cdot\frac{\mathrm{d}\mathbf{u}}{\mathrm{d}t}\\&+\nabla\cdot\left(\mathbf{i}_l^i+\mathbf{i}_g^i+\omega_l^i\rho_l\mathbf{q}_l+\omega_g^i\rho_g\mathbf{q}_g\right)=f^i\end{aligned}\,. \tag{VI.6}$$

The mass balance of solid is introduced in the mass balance of a component to obtain, after some algebra,

$$\begin{aligned}&\varphi\frac{D_s\left(\omega_l^i\rho_l S_l+\omega_g^i\rho_g S_g\right)}{Dt}+\left(\omega_l^i\rho_l S_l+\omega_g^i\rho_g S_g\right)\frac{(1-\varphi)}{\rho_s}\frac{D_s\rho_s}{Dt}\\&+\left(\omega_l^i\rho_l S_l+\omega_g^i\rho_g S_g\right)\nabla\cdot\frac{\mathrm{d}\mathbf{u}}{\mathrm{d}t}+\nabla\cdot\left(\mathbf{i}_l^i+\mathbf{i}_g^i+\omega_l^i\rho_l\mathbf{q}_l+\omega_g^i\rho_g\mathbf{q}_g\right)=f^i\end{aligned}\,. \tag{VI.7}$$

The volumetric deformation term ($\mathrm{d}\varepsilon_v/\mathrm{d}t=\nabla\cdot(\mathrm{d}\mathbf{u}/\mathrm{d}t)$) couples the mass balance equations with the deformations of the medium. This requires the coupled solution of the mechanical equations. If the inertial terms are neglected, the momentum balance for the porous medium reduces to the equilibrium of stresses

$$\nabla\cdot\boldsymbol{\sigma}+\mathbf{b}=\mathbf{0}\,, \tag{VI.8}$$

where $\boldsymbol{\sigma}$ is the stress tensor and $\mathbf{b}$ is the vector of body forces.

The simultaneous solution of the coupled equations given above produces the spatial and temporal evolution of displacements, liquid pressure and CO_2 pressure. These are considered as state variables or unknowns in this approach.

VII. Pressure evolution with time

Fluid pressure buildup can be divided into three parts. One corresponding to fluid pressure buildup in the brine phase (ΔP_1), another in the CO_2 phase (ΔP_3) and a third corresponding to a capillary fringe which is partially saturated with CO_2 (ΔP_2) (Figure 4.3). This capillary fringe defines the interface between CO_2 and brine. Assuming, for the purpose of pressure buildup calculations, that the interface is (sub)vertical, the pressure buildup for brine and CO_2 phases can be calculated using Thiem's solution (Thiem, 1906). Pressure loss across the capillary fringe is approximated by means of a leakage coefficient

$$\Delta P_1 = \frac{Q\mu_w}{2\pi kb} \ln \frac{R}{R_i}, \tag{VII.1}$$

$$\Delta P_2 = \frac{Q}{2\pi R_i \gamma}, \tag{VII.2}$$

$$\Delta P_3 = \frac{Q\mu_c}{2\pi kb} \ln \frac{R_i}{r_w}, \tag{VII.3}$$

where Q is the volumetric CO_2 flow rate, μ_w and μ_c are the viscosity of brine and CO_2, respectively, k is the intrinsic permeability of the aquifer, b is the aquifer thickness, R is the radius of influence, R_i is the radius of the interface between CO_2 and brine, r_w is the well radius and γ is a leakage coefficient. This leakage coefficient characterizes the pressure drop across the capillary fringe that can be observed in Figure 4.3. As the relative permeability to both CO_2 and aqueous phases drops significantly with saturation, displacement of the capillary fringe requires some extra energy. The leakage coefficient can be seen as the conductance of the capillary fringe. Consequently, it is derived from the harmonic average of effective permeability across the capillary fringe. Therefore it will be quite sensitive to the adopted relative permeability functions and to the thickness of the capillary fringe. Here, we assume γ approximately constant, which appears consistent with the reduction of ΔP_2 away from the injection well. However, the leakage coefficient probably decreases with distance from the well (see Figure 4.3).

The radius of influence is given by

$$R = \sqrt{\frac{2.25 k_w \rho_w g t}{\mu_w S_s}}, \tag{VII.4}$$

where ρ_w is the brine density, g is gravity, t is time and S_s is the specific storage coefficient. The radius of the interface between CO_2 and brine can be approximated as

$$R_i = \sqrt{\frac{Qt}{\pi b \theta_c}}, \tag{VII.5}$$

where θ_c is the volumetric content of CO_2. Note that both radii grow with the square root of time. Thus, ΔP_1 is time independent.

To analyze the time evolution of ΔP, we derive pressure buildup with respect to time

$$\frac{d}{dt}\left(\Delta P_1 + \Delta P_2 + \Delta P_3\right) = 0 + \frac{Q}{2\pi}\left(-\frac{1}{R_i^2 \gamma} + \frac{\mu_c}{k_c b R_i}\right)\frac{dR_i}{dt}. \tag{VII.6}$$

For small R_i the derivative is negative because the first term (negative) is inversely proportional to R_i^2 and will be greater than the other term (positive), which is inversely proportional to R_i. The fluid pressure buildup will increase when the capillary fringe is at such a distance that the pressure drop due to capillary forces does not affect the injection. The condition for this to occur is

$$R_i > \frac{k_c b}{\mu_c \gamma}, \tag{VII.7}$$

which may be quite large. In our simulations, pressure started to increase after some 10 years of injection, for which R_i equals 2200 m.

VIII. Flow equation

To derive properly the mass balance of water in deformable porous media, we have to account for the fact that the solid skeleton is in motion. Thus, we first consider the mass balance of solid

$$\frac{\partial\left((1-\phi)\rho_s\right)}{\partial t}+\nabla\cdot\left((1-\phi)\rho_s\frac{\mathrm{d}\mathbf{u}}{\mathrm{d}t}\right)=0\,, \tag{VIII.1}$$

where ϕ is porosity, ρ_s is the density of the solid, t is time and $\mathbf{u}$ is the displacement vector. Expanding Eq. (VIII.1) yields an expression for the porosity variation that reads

$$\frac{\mathrm{D}\phi}{\mathrm{D}t}=\frac{(1-\phi)}{\rho_s}\frac{D\rho_s}{Dt}+(1-\phi)\nabla\cdot\frac{\mathrm{d}\mathbf{u}}{\mathrm{d}t}\,, \tag{VIII.2}$$

where we have used the material derivative, which is defined as

$$\frac{\mathrm{D}(\bullet)}{\mathrm{D}t}=\frac{\partial(\bullet)}{\partial t}+\frac{\mathrm{d}\mathbf{u}}{\mathrm{d}t}\cdot\nabla(\bullet). \tag{VIII.3}$$

Eq. (VIII.2) shows that porosity may vary because of variations of the density of the solid and/or variations caused by volumetric strain.

Now, we write the total mass balance of water considering that the water flux is a combination of Darcy's law and an advection caused by solid motion

$$\frac{\partial(\phi\rho)}{\partial t}+\nabla\cdot\left(\rho\mathbf{q}+\phi\rho\frac{\mathrm{d}\mathbf{u}}{\mathrm{d}t}\right)=0\,, \tag{VIII.4}$$

where ρ is the water density and $\mathbf{q}$ is the volumetric water flux.

Expanding Eq. (VIII.4) and using material derivatives (Eq. (VIII.3)) yields

$$\phi\frac{\mathrm{D}\rho}{\mathrm{D}t}+\rho\frac{\mathrm{D}\phi}{\mathrm{D}t}+\rho\phi\nabla\cdot\frac{\mathrm{d}\mathbf{u}}{\mathrm{d}t}+\nabla\cdot(\rho\mathbf{q})=0\,. \tag{VIII.5}$$

The mass balance of solid and water are combined by introducing Eq. (VIII.2) in Eq. (VIII.5). Dividing by ρ and grouping the terms yields

$$\frac{\phi}{\rho}\frac{\mathrm{D}\rho}{\mathrm{D}t}+\frac{(1-\phi)}{\rho_s}\frac{\mathrm{D}\rho_s}{\mathrm{D}t}+\nabla\cdot\frac{\mathrm{d}\mathbf{u}}{\mathrm{d}t}+\frac{1}{\rho}\nabla\cdot(\rho\mathbf{q})=0\,. \tag{VIII.6}$$

Applying the chain rule to the material derivatives we obtain

$$\phi\beta\frac{\partial p}{\partial t}+(1-\phi)\frac{1}{K_s}\frac{\partial p}{\partial t}+\nabla\cdot\frac{\mathrm{d}\mathbf{u}}{\mathrm{d}t}+\frac{1}{\rho}\nabla\cdot(\rho\mathbf{q})=0 \tag{VIII.7}$$

where $\beta = (1/\rho)(\mathrm{d}\rho/\mathrm{d}p)$ is water compressibility and $1/K_s = (1/\rho_s)(\mathrm{d}\rho_s/\mathrm{d}p)$ is solid compressibility. The solid is usually assumed to be incompressible, so the second term of Eq. (VIII.7) can be neglected. Furthermore, the divergence of the solid velocity can be written as the time derivative of the divergence of the solid displacement. Hence, Eq. (VIII.7) gives

$$\phi\beta\frac{\partial p}{\partial t} + \frac{\mathrm{d}}{\mathrm{d}t}\nabla\cdot\mathbf{u} + \frac{\mathbf{q}}{\rho}\cdot\nabla\rho + \nabla\cdot\mathbf{q} = 0\,. \tag{VIII.8}$$

The third term of Eq. (VIII.8) can be neglected because is very small compared to the fourth term. Then, the expression for the flow equation presented in Eq. (5.9) is obtained

$$\phi\beta\frac{\partial p}{\partial t} + \frac{\mathrm{d}}{\mathrm{d}t}(\nabla\cdot\mathbf{u}) + \nabla\cdot\mathbf{q} = 0\,. \tag{VIII.9}$$

The second term of this equation is usually expressed in hydrology as a function of the soil compressibility and is combined with the first term to yield the specific storage coefficient. However, since we are interested in the coupling of the fluid and mechanical equations, the use of this form allows coupling this equation to the mechanical equation through the term containing the divergence of the solid displacement.

References

Abousleiman, Y.N., Hoang, S.K. and Tran, M.H. (2010). Mechanical characterization of small shale samples subjected to fluid exposure using the inclined direct shear testing device. *International Journal of Rock Mechanics and Mining Sciences* 47, 355–367.

Altunin, V. V. and Sakhabetdinov, M. A. (1972). Viscosity of liquid and gaseous carbon dioxide at temperatures 220-1300 K and pressure up to 120 bar. *Teploenergetika* 8, 85–89.

Angus, A., Armstrong, B. and Reuck, K.M. (ed) (1976). *International thermodynamics tables of the fluid state. Carbon dioxide*. International Union of Pure and Applied Chemistry. Pergamon Press, Oxford.

Aziz, K. and Settari, A. (ed) (2002). *Petroleum Reservoir Simulation*. Blitzprint Ltd., 2nd edition.

Bachu, S. (2003). Screening and ranking of sedimentary basins for sequestration of CO_2 in geological media in response to climate change. *Environmental Geology* 44, 277–289.

Bachu, S. and Adams, J.J. (2003). Sequestration of CO_2 in geological media in response to climate change: capacity of deep saline aquifers to sequester CO_2 in solution. *Energy Conversion & Management* 44, 3151–3175.

Barton, N., Bandis, S. and Bakhtar, K. (1985). Strength, deformation and conductivity coupling of rock joints. *International Journal of Rock Mechanics and Mining Sciences & Geomechical Abstracts* 22 (3), 121–140.

Bear, J. (ed) (1972). *Dynamics of Fluids in Porous Media*. Elsevier, New York.

Biot, M.A. (1956). Thermoelasticity and irreversible thermodynamics. *Journal of Applied Phisics* 27(3), 240–253.

Birkholzer, J. T., Zhou, Q. and Tsang, C.-F. (2009). Large-scale impact of CO_2 storage in deep saline aquifers: A sensitivity study on pressure response in stratified systems. *International Journal of Greenhouse Gas Control* 3, 181–194.

Birkholzer, J. T. and Zhou, Q. (2009). Basin-scale hydrogeologic impacts of CO_2 storage: Capacity and regulatory implications. *International Journal of Greenhouse Gas Control* 3, 745–756.

Bohnhoff, M., Zoback, M.D., Chiaramonte, L., Gerst, J.L. and Gupta, N. (2010). Seismic detection of CO_2 leakage along monitoring wellbores. *International Journal of Greenhouse Gas Control* 4 (4), 687–697.

Bolster, D., Barahona, M., Dentz, M., Fernandez-Garcia, D., Sanchez-Vila, X., Trinchero, P., Valhondo, C. and Tartakovsky, D.M. (2009a). Probabilistic risk analysis of groundwater remediation strategies. *Water Resources Research* 45, W06413, doi: 10.1029/2008WR007551.

Bolster, D., Dentz, M. and Carrera, J. (2009b). Effective two phase flow in heterogeneous media under temporal pressure fluctuations. *Water Resources Research* 45, W05408, doi: 1029/2008WR007460.

Brill, J. and Mukherjee, H. (1999). *Multiphase flow in wells*. SPE Monograph Vol. 17, Henry L. Doherty Memorial fund of AIME, Richardson, Texas.

Burton, M and Bryant, S.L. (2009). Surface dissolution: minimizing groundwater impact and leakage risk simultaneously. *Energy Procedia* 1, 3707–3714.

Butler, J. J. J. (1988). Pumping test in nonuniform aquifers – the radially symmetric case. *Journal of Hydrology* 101, 15–30.

Cai, M., Morioka, H., Kaiser, P.K., Tasaka, Y., Kurose, H., Minami, M. and Maejima, T. (2007). Back-analysis of rock mass strength parameters using AE monitoring data. *International Journal of Rock Mechanics and Mining Sciences* 44, 538–549.

Cantucci, B., Montegrossi, G., Vaselli, O., Tassi, F., Quattrocchi, F. and Perkins, E.H. (2009). Geochemical modeling of CO_2 storage in deep reservoirs: The Weyburn Project (Canada) case study. *Chemical Geology* 265, 181–197.

Cappa, F. and Rutqvist, J. (2011a). Modeling of coupled deformation and permeability evolution during fault reactivation induced by deep underground injection of CO_2. *International Journal of Greenhouse Gas Control* 5 (2), 336–346.

Cappa, F. and Rutqvist, J. (2011b). Impact of CO_2 geological sequestration on the nucleation of earthquakes. *Geophysical Research Letters* 38, L17313, doi: 10.1029/2011GL048487.

Carrera, J., Silva, O., Rötting, T., Carbonell, R., Vilarrasa, V., Pérez-Estaún, A. and CIUDEN's research group (2011a). Characterization and working programme of

Hontomín CO_2 injection site (Spain). Monitoring, hydrogeochemical characterization and injection tests. *6th Trondheim Carbon, Capture and Sequestration Conference,* 14-16 June, Trondheim, Norway.

Carrera, J., Silva, O. and Ayora, C. (2011b). Método y sistema de almacenamiento de gases solubles en formaciones geológicas permeables. *European patent application Nº EP11382321.5.*

Celia, M.A. and Nordbotten, J.M. (2009). Practical modeling approaches for geological storage of carbon dioxide. *Ground Water* 47 (5), 627–638.

Chen, Z., Huan, G. and Ma, Y. (ed) (2006). *Computational methods for multiphase flows in porous media*. SIAM, Philadelphia.

Chiaramonte, L., Zoback, M.D., Friedmann, J. and Stamp, V. (2008). Seal integrity and feasibility of CO_2 sequestration in the Teapot Dome EOR pilot: geomechanical site characterization. *Environmental Geology* 54, 1667–1675.

Colebrook, C.F. (1939). Turbulent flow in pipes with particular reference to the transition region between the smooth- and rough-pipe laws. *Journal of the Institution of Civil Engineers* 11, 133–156.

Cooper, H.H. and Jacob, C.E. (1946). A generalized graphical method for evaluating formation constants and summarizing well field history. *American Geophysical Union Transactions* 27, 526–534.

Cristescu, N. (ed) (1989). *Rock Rheology*. Kluwer Academic Publishers. Dordrecht.

Dake, L.P. (ed) (1978). *Fundamentals of Reservoir Engineering*. Elsevier, Oxford.

Dana, E. and Skoczylas, F. (2002). Experimental study of two-phase flow in three sandstones. II. Capillary pressure curve measurement and relative permeability pore space capillarity models. *International Journal of Multiphase Flow* 28, 1965–1981.

Dehandschutter, B., Vandycke, S., Sintubin, M., Vandenberghe, N. and Wouters, L. (2005). Brittle fractures and ductile shear bands in argillaceous sediments: inferences from Oligocene Boom Clay (Belgium). *Journal of Structural Geology* 27, 1095–1112.

Dentz, M. and Tartakovsky, D.M. (2009a). Abrupt-interface solution for carbon dioxide injection into porous media. *Transport In Porous Media* 79, 15–27.

Dentz, M. and Tartakovsky, D.M. (2009b). Response to “Comments on abrupt-interface solution for carbon dioxide injection into porous media by Dentz and Tartakovsky (2008)" by Lu *et al*. *Transport In Porous Media* 79, 39–41.

Dodds, K.J., Dewhurst, D.N., Siggins, A.F., Ciz, R., Urosevic, M., Gurevich, B. and Sherlock, D.H. (2007). Experimental and theoretical rock physics research with application to reservoirs, seals and fluid processes. *Journal of Petroleum Science and Engineering* 57, 16–36.

Doughty, C. and Pruess, K. (2004). Modeling Supercritical Carbon Dioxide Injection in Heterogeneous Media. *Vadose Zone Journal* 3, 837–847.

Doughty, C., Freifeld, B.M. and Trautz, R.C. (2006). Site characterization for CO_2 geologic storage and vice versa: the Frio brine pilot, Texas, USA as a case study. *Environmental Geology* 54, 1635–1656.

Ennis-King, J. and Paterson, L. (2005). The role of convective mixing in the long-term storage of carbon dioxide in deep saline formations. *Journal of Society of Petroleum Engineers* 10 (3), 349–356.

Eseme, E., Urai, J.L., Krooss, B.M. and Littke, R. (2007). Review of mechanical properties of oil shales: Implications for exploitation and basin modelling. *Oil Shale* 24 (2), 159–174.

Faust, C.R. and Mercer, J.W. (1979). Geothermal reservoir simulation. 1. Mathematical models for liquid – and vapour – dominated hydrothermal systems. *Water Resources Research* 15 (1), 23–30.

Ferronato, M., Gambolati, G., Janna, C. and Teatini, P. (2008). Numerical modelling of regional faults in land subsidence prediction above gas/oil reservoirs. *International Journal for Numerical and Analytical Methods in Geomechanics* 32, 633–657.

Ferronato, M., Gambolati, G., Janna, C. and Teatini, P. (2010). Geomechanical issues of anthropogenic CO_2 sequestration in exploited gas fields. *Energy Conversion & Management* 51, 1918–1928.

François, B., Laloui, L. and Laurent, C. (2009). Thermo-hydro-mechanical simulation of ATLAS in situ large scale test in Boom Clay. *Computers and Geotechnics* 36, 626–640.

Garcia, J.E. (2003). Fluid Dynamics of Carbon Dioxide Disposal into Saline Aquifers. *PhD thesis*. University of California, Berkeley.

Garcia, J.E. and Pruess, K. (2003). Flow instabilities during injection of CO_2 into saline aquifers. *Proceedings Tough Symposium 2003*, LBNL, Berkeley.

Gens, A., Vaunat, J., Garitte, B. and Wileveau, Y. (2007). In situ behaviour of a stiff layered clay subject to thermal loading: observations and interpretation. *Géotechnique* 57 (2), 207–228.

Ghassemi, A., Tarasovs, S. and Cheng, A.H.-D. (2007). A 3-D study of the effects of thermomechanical loads on fracture slip in enhanced geothermal reservoirs. *International Journal of Rock Mechanics and Mining Sciences* 44, 1132–1148.

Ghomian, Y., Pope, G.A. and Sepehrnoori, K. (2008). Reservoir simulation of CO_2 sequestration pilot in Frio brine formation, USA Gulf Coast. *Energy* 33, 1055–1067.

GHS (2009). Spreadsheet with CO_2 compressibility correction. http://www.h2ogeo.upc.es/publicaciones/2009/Transport$\%$20in$\%$20porous$\%$20media/Effects$\%$20of$\%$20CO2$\%$20Compressibility$\%$20on$\%$20CO2$\%$20Storage$\%$20in$\%$20Deep$\%$20Saline$\%$20Aquifers.xls.

GHS (Hydrogeology Group) (2012). Spreadsheet with the semianalytical solution for CO_2 injection. http://www.h2ogeo.upc.es/publicaciones/2011/Semianalytical_solution.xlsx

Giraud, A. and Rousset, G. (1996). Time-dependent behaviour of deep clays. *Engineering Geology* 41, 181–195

Goerke, U.-J., Park, C.-H., Wang, W., Singh, A.K. and Kolditz, O. (2011). Numerical simulation of multiphase hydromechanical processes induced by CO_2 injection into deep saline aquifers. *Oil & Gas Science and Technology* 66, 105–118.

Goodman, R.E. (ed.) (1989). *Introduction to Rock Mechanics*. John Wiley and Sons, New York.

Guglielmi, Y., Cappa, F. and Amitrano, D. (2008). High-definition analysis of fluid-induced seismicity related to the mesoscale hydromechanical properties of a fault zone. *Geophysical Research Letters* 35, L06306, doi:10.1029/2007GL033087.

Han, W.S., Stillman, G.A., Lu, M., Lu, C., McPherson, B.J. and Park, E. (2010). Evaluation of potential nonisothermal processes and heat transport during CO_2 sequestration. *Journal of Geophysical Research* 115, B07209, doi: 10.1029/2009JB006745.

Hantush, M.S. (1956). Analysis of data from pumping tests in leaky aquifers. *Transactions American Geophysical Union* 37 (6), 702–714.

Häring, M.O., Schanz, U., Ladner, F. and Dyer, B.C. (2008). Characterization of the Basel 1 enhanced geothermal system. *Geothermics* 37, 469–495.

Hasan, A.R. and Kabir, C.S. (ed) (2002). *Fluid flow and heat transfer in wellbores*. SPE Richardson, Texas.

Hassanzadeh, H., Pooladi-Darvish, M. and Keith, D.W. (2009). Accelerating CO_2 dissolution in saline aquifers for geological storage – mechanistic and sensitivity studies. *Energy & Fuels* 23, 3328–3336.

Heap, M.J., Faulkner, D.R., Meredith, P.G. and Vinciguerra, S. (2010). Elastic moduli evolution and accompanying stress changes with increasing crack damage: implications for stress changes around fault zones and volcanoes during deformation. *Geophysical Journal International* 183, 225–236.

Henninges, J., Liebscher, A., Bannach, A., Brandt, W., Hurter, S., Köhler, S., Möller, F. and CO2SINK Group (2011). *P-T-ρ* and two-phase fluid conditions with inverted density profile in observation wells at the CO_2 storage site at Ketsin (Germany). *Energy Procedia* 4, 6085–6090.

Hesse, M.A., Tchelepi, H.A., Cantwell, B.J. and Orr, Jr. F.M. (2007). Gravity currents in horizontal porous layers: Transition from early to late self-similarity. *Journal of Fluid Mechanics* 577, 363–383.

Hesse, M.A., Tchelepi, H.A. and Orr, Jr. F.M. (2008). Gravity currents with residual trapping. *Journal of Fluid Mechanics* 611, 35–60.

Hidalgo, J.J. and Carrera, J. (2009). Effect of dispersion on the onset of convection during CO_2 sequestration. *Journal of Fluid Mechanics* 640, 443–454.

Hitchon, B., Gunter, W. D., Gentzis, T. and Bailey, R. T. (1999). Sedimentary basins and greenhouse gases: a serendipitous association. *Energy Conversion & Management* 40, 825–843.

Houseworth, J.E. (2012). Matched boundary extrapolation solutions for CO_2 well-injection into a saline aquifer. *Transport In Porous Media* 91, 813–831.

Hsieh, P.A. and Bredehoeft, J.D. (1981). A reservoir analysis of the Denver earthquakes: A case of induced seismicity. *Journal of Geophysical Research* 86 (B2), 903–920.

Hsieh, P.A., Bredehoeft, J.D. and Farr, J.M. (1987). Determination of aquifer transmissivity from earth tide analysis. Water Resources Research 23 (10), 1824–1832.

Hsieh, P.A., Bredehoeft, J.D. and Rojstaczer, S.A. (1988). Response of well aquifer systems to earth tides: Problem revisited. *Water Resources Research* 24 (3), 468–472.

Hsieh, P.A. (1995). Deformation-induced changes in hydraulic head during ground-water withdrawal. *Ground Water* 34 (6), 1082–1089.

Hu, D.W., Zhou, H., Zhang, F. and Shao, J.F. (2010). Evolution of poroelastic properties and permeability in damaged sandstone. *International Journal of Rock Mechanics and Mining Sciences* 47, 962–973.

Huppert, H.E. and Woods, A.W. (1995). Gravity-driven flows in porous media. *Journal of Fluid Mechanics* 292, 55–69.

Ide, S. T., Jessen, K. and Orr Jr, F. M. (2007). Storage of CO_2 in saline aquifers: Effects of gravity, viscous, and capillary forces on amount and timing of trapping. *International Journal of Greenhouse Gas Control* 1, 481–491.

IEA (2010). Energy technology perspectives. Scenarios & strategies to 2050. Executive summary, International Energy Agency.

Jain, L. and Bryant, S.L. (2011). Optimal design of injection/extraction wells for the surface dissolution CO_2 storage strategy. *Energy Procedia* 4, 4299–4306.

Juanes, R., MacMinn, C.W. and Szulczewski, M.L. (2010). The footprint of the CO_2 plume during carbon dioxide storage in saline aquifers: Storage efficiency for capillary trapping at the basin scale. *Transport In Porous Media* 82, 19–30.

Jurado, A., de Gaspari, F., Vilarrasa, V., Bolster, D., Sanchez-Vila, X., Fernandez-Garcia, D. and Tartakovsky, D.M. (2012). Probabilistic analysis of groundwater-related risks at subsurface excavation sites. *Engineering Geology* 125, 35–44.

Katz, D.L. and Lee, R.L. (ed) (1990). *Natural gas engineering*. McGraw-Hill, New York.

Kikuta, K., Hongo, S., Tanase, D. and Ohsumi, T. (2004). Field test of CO_2 injection in Nagaoka, Japan. *In: Proceedings of the 7th International Conference on Greenhouse Gas Control Technologies*, September, Vancouver, Canada, 1367–1372.

Kim, J.-M. and Parizek, R.R. (1997). Numerical simulation of the Noordbergum effect resulting from groundwater pumping in a layered aquifer system. *Journal of Hydrology* 202, 231–243.

Klee, G., Bunger, A., Meyer, G., Rummel, F. and Shen, B. (2011) In situ stresses in borehole Blanche-1/South Australia derived from breakouts, core discing and hydraulic fracturing to 2 km depth. *Rock Mechanics Rock Engineering* 44, 531–540.

Kopp, A., Class, H. and Helmig, R. (2009). Investigation on CO_2 storage capacity in saline aquifers Part 1. Dimensional analysis of flow processes and reservoir characteristics. *Journal of Greenhouse Gas Control* 3, 263–276.

Korbol, R. and Kaddour, A. (1995). Sleipner vest CO_2 disposal - injection of removed CO_2 into the Utsira formation. *Energy Conversion & Management* 36 (6-9), 509–512.

Lake, L.W. (ed) (1989). *Enhanced Oil Recovery*. Prentice-Hall, Englewood Cliffs, New Jersey.

Law, D.H.S. and Bachu, S. (1996). Hydrogeological and numerical analysis of CO_2 disposal in deep aquifers in the Alberta sedimentary basin. *Energy Conversion & Management* 37(6-8), 1167–1174.

Ledesma, A., Gens, A. and Alonso, E.E. (1996). Parameter and variance estimation in geotechnical backanalysis using prior information. *International Journal for Numerical and Analytical Methods in Geomechanics* 20, 119–141.

Lindeberg, E. and Wessel-Berg, D. (1997). Vertical convection in an aquifer column under a gas cap of CO_2. *Energy Conversion & Management* 38, S229–S234.

Lu, C., Lee, S.-Y., Han, W.S., McPherson, B.J. and Lichtner, P.C. (2009). Comments on "Abrupt-interface solution for carbon dioxide injection into porous media" by M. Dentz and D. M. Tartakovsky. *Transport In Porous Media* 79, 29–37.

Lu, M. and Connell, L.D. (2008). Non-isothermal flow of carbon dioxide in injection wells during geological storage. *International Journal of Greenhouse Gas Control* 2, 248–258.

Lucier, A. and Zoback, M. (2008). Assessing the economic feasibility of regional deep saline aquifer CO_2 injection and storage: A geomechanics-based workflow applied to the Rose Run sandstone in Eastern Ohio, USA. *International Journal of Greenhouse Gas Control* 1, 230–247.

Lyle, S., Huppert, H.E., Hallworth, M., Bickle, M. and Chadwick, A. (2005). Axisymmetric gravity currents in a porous medium. *Journal of Fluid Mechanics* 543, 293–302.

MacMinn, C.W. and Juanes, R. (2009). Post-injection spreading and trapping of CO_2 in saline aquifers: impact of the plume shape at the end of injection. *Compututational Geoscience* 13, 483–491.

Mainguy, M. and Longuemare, P. (2002). Coupling fluid flow and rock mechanics: formulations of the partial coupling between reservoir and geomechanical simulators. *Oil & Gas Science and Technology* 57 (4), 355–367.

Majer, E.L., Baria, R., Stark, M., Oates, S., Bommer, J., Smith, B. and Asanuma, H. (2007). Induced seismicity associated with Enhanced Geothermal Systems. *Geothermics* 36, 185–222.

Mallikamas, W. and Rajaram, H. (2005). On the anisotropy of the aperture correlation and effective transmissivity in fractures generated by sliding between identical self-affine surfaces. *Geophysical Research Letters* 32, L11401, doi: 10.1029/2005GL022859.

Manceau, J.-C. and Rohmer, J. (2011). Analytical solution incorporating history-dependent processes for quick assessment of capillary trapping during CO_2 geological storage. *Transport In Porous Media* 90, 721–740.

Mathias, S.A., Hardisty, P.E., Trudell, M.R. and Zimmerman, R.W. (2009). Approximate solutions for pressure buildup during CO_2 injection in brine aquifers. *Transport In Porous Media* 79, 265–284.

Mathias, S.A., González Martínez de Miguel, G.J., Thatcher, K.E. and Zimmerman, R.W. (2011). Pressure buildup during CO_2 injection into a closed brine aquifer. *Transport In Porous Media* 89 (3), 383–397.

McCoy, S.T. and Rubin, E.S. (2008). An engineering-economic model of pipeline transport of CO_2 with application to carbon capture and storage. *International Journal of Greenhouse Gas Control* 2, 219–229.

McDermott, C.I., Bond, A.E., Wang, W. and Kolditz, O. (2011). Front tracking using a hybrid analytical finite element approach for two-phase flow applied to supercritical CO_2 replacing brine in a heterogeneous reservoir and caprock. *Transport In Porous Media* 90, 545–573.

McPherson, B. J. O. L. and Cole, B. S. (2000). Multiphase CO_2 flow, transport and sequestration in the Powder River Basin, Wyoming, USA. *Journal of Geochemical Exploration* 69-70, 65–69.

McPherson, B. J. O. L., Han, W.S. and Cole, B. S. (2008). Two equations of state assembled for basic analysis of multiphase CO_2 flow and in deep sedimentary basin conditions. *Computers and Geosciences* 34, 427–444.

Mertens, J., Bastiaens, W. and Dehandschutter, B. (2004). Characterisation of induced discontinuities in the Boom Clay around the underground excavations (URF, Mol, Belgium). *Applied Clay Science* 26, 413–428.

Michael, K., Golab, A., Shulakova, V., Ennis-king, J., Allinson, G., Sharma, A. and Aiken, T. (2010). Geological storage of CO_2 in saline aquifers – A review of the experience from existing storage operations. *International Journal of Greenhouse Gas Control* 4, 659–667.

Miller, S.A., Collettini, C., Chiaraluce, L., Cocco, M., Barchi, M. and Kaus, B.J.P. (2004). Aftershocks driven by a high-pressure CO_2 source at depth. *Nature* 427, 724–727.

Moeck, I., Kwiatek, G. and Zimmermann, G. (2009). Slip tendency analysis, fault reactivation potential and induced seismicity in a deep geothermal reservoir. *Journal of Structural Geology* 31, 1174–1182.

Moeck, I. and Backers, T. (2011). Fault reactivation potential as a critical factor during reservoir stimulation. *First Break* 29, 73–80.

Moran, M.J., Shapiro, H.N., Boettner, D.D. and Bailey, M.B. (ed) (2011). *Fundamentals of engineering thermodynamics*. 7th edition, John Wiley & Sons, Inc, USA.

Morris, J.P., McNab, W.W., Carroll, S.K., Hao, Y., Foxall, W. and Wagoner, J.L. (2009). “Injection and reservoir hazard management: the role of injection-induced mechanical deformation and geochemical alteration at In Salah CO_2 storage project: status report quarter end, June 2009" *LLNL Technical Report*, DOI 10.2172/964517.

Mukhopadhyay, S., Yang, S.-Y. and Yeh, H.-D. (2012). Pressure buildup during supercritical carbon dioxide injection from a partially penetrating borehole into gas reservoirs. *Transport In Porous Media* 91, 889–911.

Neuweiller, I., Attinger, S., Kinzelbach, W. and King, P. (2003). Large scale mixing for immiscible displacement in heterogeneous porous media. *Transport In Porous Media* 51, 287–314.

Neuzil, C.E. (1986). Groundwater flow in low-permeability environments. *Water Resources Research* 22(8), 1163–1195.

Nickalls, R.W.D. (1993). A new approach to solving the cubic: Cardan's solution revealed. *The Mathematical Gazette* 77, 354–359.

Nimtz, M., Klatt, M., Wiese, B., Kühn, M. and Krautz, H.J. (2010). Modelling of the CO_2 process – and transport chain in CCS systems – Examination of transport and storage processes. *Chemie der Erde* 70, 185–192.

Nooner, S.L., Eiken, O., Hermanrud, C., Sasagawa, G.S., Stenvold, T. and Zumberge, M.A. (2007). Constraints on the in situ density of CO_2 within the Utsira formation from time-lapse seafloor gravity measurements. *International Journal of Greenhouse Gas Control* 1, 198–214.

Nordbotten, J.M., Celia, M.A. and Bachu, S. (2005). Injection and storage of CO_2 in deep saline aquifers: analytical solution for CO_2 plume evolution during injection. *Transport In Porous Media* 58, 339–360.

Nordbotten, J.M. and Celia, M.A. (2006). Similarity solutions for fluid injection into confined aquifers. *Journal of Fluid Mechanics* 561, 307–327.

Nordbotten, J.M., Kavetski, D., Celia, M.A. and Bachu, S. (2009). A semi-analytical model estimating leakage associated with CO_2 storage in large-scale multi-layered geological systems with multiple leaky wells. *Environmental Science & Technology* 43(3), 743–749.

Olivella, S., Carrera, J., Gens, A. and Alonso E. E. (1994). Non-isothermal multiphase flow of brine and gas through saline media. *Transport In Porous Media* 15, 271–293.

Olivella, S., Gens, A., Carrera, J. and Alonso E. E. (1996). Numerical formulation for a simulator (CODE_BRIGHT) for the coupled analysis of saline media. *Engineering Computations* 13, 87–112.

Ortega, J.A., Ulm, F.-J. and Abousleiman, Y. (2010). The effect of particle shape and grain-scale properties of shale: A micromechanics approach. *International Journal for Numerical and Analytical Methods in Geomechanics* 34, 1124–1156.

Pan, L., Oldenburg, C.N., Wu, Y. and Pruess, K. (2009). Wellbore flow model for carbon dioxide and brine. *Energy Procedia* 1, 71–78.

Paterson, L., Lu, M., Connell, L.D. and Ennis-King, J. (2008). Numerical modeling of pressure and temperature profiles including phase transitions in carbon dioxide wells. *SPE Annual Technical Conference and Exhibition*, 21-24 September, Denver, USA.

Pau, G.S.H., Bell, J.B., Pruess, K., Almgren, A.S., Lijewski, M.J. and Zhang, K. (2010). High resolution simulation and characterization of density-driven flow in CO_2 storage in saline aquifers, *Advances in Water Resources* 33(4), 443–455.

Phillips, W.S., Rutledge, J.T., House, L.S. and Fehler, M.C. (2002). Induced microearthquake patterns in hydrocarbon and geothermal reservoirs: six case studies. *Pure and Applied Geophysics* 159, 345–369.

Plenefisch, T. and Bonjer, K.-P. (1997). The stress field in the Rhine Graben area inferred from earthquake focal mechanisms and estimation of frictional parameters. *Tectonophysics* 275, 71–97.

Preisig, M. and Prévost, J.H. (2011). Coupled multi-phasse thermo-poromechanical effects. Case study: CO_2 injection at In Salah, Algeria. *International Journal of Greenhouse Gas Control* 5 (4), 1055–1064.

Pruess, K. and Garcia, J. (2002). Multiphase flow dynamics during CO_2 disposal into saline aquifers. *Environmental Geology* 42, 282–295.

Pruess, K., Garcia, J.E., Kovscek, T., Oldenburg, C., Rutqvist, J., Steelfel, C. and Xu, T. (2004). Code intercomparison builds confidence in numerical simulation models for geologic disposal of CO_2. *Energy* 29, 1431–1444.

Pytharouli, S.I., Lunn, R.J., Shipton, Z.K., Kirkpatrick, J.D. and do Nascimento, A.F. (2011). Microseismicity illuminates open fractures in the shallow crust. *Geophysical Research Letters* 38, L02402, doi:10.1029/2010GL045875.

Rayward-Smith, W.J. and Woods, A.W. (2011). Some implications of cold CO_2 injection into deep saline aquifers. *Geophysical Research Letters* 38, L06407, doi:10.1029/2010GL046412.

Redlich, O. and Kwong, J.N.S. (1949). On the thermodynamics of solutions. V. An equation of state. Fugacities of gaseous solutions. *Chemical Reviews* 44, 233–244.

Riaz, A., Hesse, M.A., Tchelepi, H.A. and Orr, Jr. F.M. (2006). Onset of convection in a gravitationally unstable diffusive boundary layer in porous media. *Journal of Fluid Mechanics* 548, 87–111.

Rimmelé, G., Barlet-Gouédard, V. and Renard, F. (2009). Evolution of the petrophysical and mineralogical properties of two reservoir rocks under thermodynamic conditions relevant for CO2 geological storage at 3 km depth. *Oil and Gas Science and Technology* 65, 565–580.

Rodrigues, J.D. (1983). The Noordbergum effect and characterization of aquitards at the Rio Maior Mining Project. *Ground Water* 21 (2), 200–207.

Rubin, A.M., Gillard, D. and Got, J.-L. (1999). Streaks of microearthquakes along creeping faults. *Nature* 400, 635–641.

Rutledge, J.T. and Phillips, W.S. (2003). Hydraulic stimulation of natural fractures as revealed by induced microearthquakes, Carthage Cotton Valley gas field, east Texas. *Geophysics* 68 (2), 441–452.

Rutqvist, J. and Tsang, C.-F. (2002). A study of caprock hydromechanical changes with CO_2 injection into a brine formation. *Environmental Geology* 42, 296–305.

Rutqvist, J. and Stephansson, O. (2003). The role of hydromechanical coupling in fractures rock engineering. *Hydrogeology Journal* 11, 7–40.

Rutqvist, J., Birkholzer, J.T., Cappa, F. and Tsang, C.-F. (2007). Estimating maximum sustainable injection pressure during geological sequestration of CO_2 using coupled fluid flow and geomechanical fault-slip analysis. *Energy Conversion & Management* 48, 1798–1807.

Rutqvist, J., Birkholzer, J.T. and Tsang, C.-F. (2008). Coupled reservoir–geomechanical analysis of the potential for tensile and shear failure associated with CO_2 injection in multilayered reservoir–caprock systems. *Rock Mechanics and Mining Sciences* 45, 132–143.

Rutqvist, J., Vasco, D.W. and Myer, L. (2010). Coupled reservoir-geomechanical analysis of CO_2 injection and ground deformations at In Salah, Algeria. *International Journal of Greenhouse Gas Control* 4 (2), 225–230.

Rutqvist, J. (2012). The geomechanics of CO_2 storage in deep sedimentary formations. *Geotechnical and Geology Engineering*, doi: 10.1007/s10706-011-9491-0.

Saripalli, P. and McGrail, P. (2002). Semi-analytical approaches to modeling deep well injection of CO_2 for geological sequestration. *Energy Conversion & Management* 43, 185–198.

Saurot, J., Molez, L., Guéguen, Y. and Hoteit, N. (2007). Shale dynamic properties and anisotropy under triaxial loading: Experimental and theoretical investigations. *Physics and Chemistry of the Earth* 32, 896–906.

Schorlemmer, D., Wiemer, S. and Wyss, M. (2005). Variations in earthquake-size distribution across different stress regimes. *Nature* 437, 539–542.

Segall, P. and Fitzgerald, S.D. (1998). A note on induced stress changes in hydrocarbon and geothermal reservoirs. *Tectonophysics* 289, 117–128.

Settari, A. and Walters, D. A. (1999). Advances in coupled geomechanical and reservoir modeling with applications to reservoir compaction. *SPE Reservoir Simulator Symposium* 14-17 February, Houston, Texas, USA.

Shalabi, F.I., Cording, E.J. and Al-Hattamleh, O.H. (2007). Estimation of rock engineering properties using hardness tests. *Engineering Geology* 90, 138–147.

Silva, O., Vilarrasa, V. and Carrera, J. (2011). An efficient injection concept for CO_2 geological storage. *6th Trondheim Carbon, Capture and Sequestration Conference,* 14-16 June, Trondheim, Norway.

Singh, A.K., Goerke, U.-J. and Kolditz, O. (2011). Numerical simulation of non-isothermal compositional gas flow: Application to carbon dioxide injection into gas reservoirs. *Energy* 36, 3446–3458.

Smith, S.A., McLellan, P., Hawkes, C., Steadman, E.N. and Harju, J.A. (2009). Geomechanical testing and modelling of reservoir and cap rock integrity in an acid gas EOR/sequestration project, Zama, Alberta, Canada. *Energy Procedia* 1, 2169–2176.

Soltanzadeh, H. and Hawkes, C.D. (2009). Assessing fault reactivation tendency within and surrounding porous reservoirs during fluid production or injection. *International Journal of Rock Mechanics and Mining Sciences* 46, 1–7.

Sovova, H. and Prochazka, J. (1993). Calculations of compressed carbon dioxide viscosities. *Industrial & Engineering Chemistry Research* 32 (12), 3162–3169.

Span, R. and Wagner, W. (1996). A new equation of state for carbon dioxide covering the fluid region from the triple-point temperature to 1100 K at pressures up to 88 MPa. *Journal of Physical and Chemical Reference Data* 25 (6), 1509–1595.

Spycher, N., Pruess, K. and Ennis-king, J. (2003). CO_2-H_2O Mixtures in the Geological Sequestration of CO_2. I. Assessment and calculation of mutual solubilities from 12 to 100°C and up to 600 bar. *Geochimica et Cosmochimica Acta* 67, 3015–3031.

Stauffer, P.H., Viswanathan, H.S., Pawar, R.J. and Guthrie, G.D. (2009). A system model for geologic sequestration of carbon dioxide. *Environmental Science and Technology* 43 (3), 565–570.

Streit, J.E. and Hillis, R.R. (2004). Estimating fault stability and sustainable fluid pressures for underground storage of CO_2 in porous rock. *Energy* 29, 1445–1456.

Tartakovsky, D.M. (2007). Probabilistic risk analysis in subsurface hydrology. *Geophysical Research Letters* 34, L05404.

Tchelepi, H.A. and Orr, Jr. F.M. (1994). Interaction of viscous fingering, permeability inhomogeneity and gravity segregation in three dimensions. *SPE Reservoir Engineering* 9 (4), 266–271.

Tezuka, K. and Niitsuma, H. (2000). Stress estimated using microseismic clusters and its relationship to the fracture system of the Hijiori hot dry rock reservoir. *Engineering Geology* 56, 47–62.

Thiem, G. (ed) (1906). *Hydrologische Methode*. Leipzig, Gebhardt.

Thury, M. (2002). The characteristics of the Opalinus Clay investigated in the Mont Terri underground rock laboratory in Switzerland. *C. R. Physique* 3, 923–933.

Tran, D., Settari, A. and Nghiem, L. (2004). New iterative coupling between a reservoir simulator and a geomechanics module. *Society of Petroleum Engineers Journal, SPE/ISRM Rock Mechanics Conference*, 20-23 October, Irving, Texas, USA, 362–369.

Tsang, C.-F., Birkholzer, J.T. and Rutqvist, J. (2008). A comparative review of hydrologic issues involved in geologic storage of CO_2 and injection disposal of liquid waste. *Environmental Geology* 54, 1723–1737.

van der Kamp, G. and Gale, J.E. (1983). Theory of earth tide and barometric effects in porous formations with compressible grains. *Water Resources Research* 19 (2), 538–544.

van der Meer, L. H. G. and van Wees, J. D. (2006). Limitations to storage pressure in finite saline aquifers and the effect of CO2 solubility on storage pressure. *SPE Annual Technical Conference and Exhibition*, 24-27 September, San Antonio, Texas, USA.

van Genuchten, R. (1980). A closed-form equation for predicting the hydraulic conductivity of unsaturated soils. *Soil Science Society of America Journal* 44, 892–898.

Vardakos, S.S., Gutierrez, M.S. and Barton, N.R. (2007). Back-analysis of Shimizu No. 3 by distinct element modeling. *Tunnelling and Underground Space Technology* 22, 401–413.

Vasco, D.W., Ferretti, A. and Novali, F. (2008). Reservoir monitoring and characterization using satellite geodetic data: Interferometric Synthetic Aperture Radar observations from the Krechba field, Algeria. *Geophysics* 73 (6), WA113–WA122.

Vasco, D.W., Rucci, A., Ferretti, A., Novali, F., Bissell, C., Ringrose, P.S., Mathieson, A.S. and Wright, I.W. (2010). Satellite-based measurements of surface deformation reveal fluid flow associated with the geological storage of carbon dioxide. *Geophysical Research Letters* 37, L03303, doi:10.1029/2009GL041544.

Verdon, J.P., Kendall, J.M. and Maxwell, S.C. (2010). A comparison of passive seismic monitoring of fracture stimulation due to water versus CO_2 injection. *Geophysics* 75, MA1–MA7.

Verdon, J.P., Kendall, J.-M., White, D.J. and Angus, D.A. (2011). Linking microseismic event observations with geomechanical models to minimise the risks of storing CO_2 in geological formations. *Earth and Planetary Science Letters* 305, 143–152.

Verruijt, A. (1969). *Elastic storage of aquifers*. In: Flow through porous media. Edited by R.J.M. de Wiest. Academic Press, New York. pp. 331-376.

Vidal-Gilbert, S., Nauroy, J.-F. and Brosse, E. (2009). 3D geomechanical modelling for CO_2 geologic storage in the Dogger carbonates of the Paris Basin. *International Journal of Greenhouse Gas Control* 3, 288–299.

Vidal-Gilbert, S., Tenthorey, E., Dewhurst, D., Ennis-King, J., van Ruth, P. and Hillis, R. (2010). Geomechanical analysis of the Naylor Field, Otway Basin, Australia: Implications for CO_2 injection and storage. *International Journal of Greenhouse Gas Control* 4 (5), 827–839.

Vilarrasa, V., Bolster, D., Olivella, S. and Carrera, J. (2009). Coupled hydromechanical modeling of CO_2 sequestration in deep saline aquifers. *Geophysical Research Abstracts, Vol. 11, EGU General Assembly*, 19-24 April, Vienna, Austria.

Vilarrasa, V., Bolster, D., Dentz, M., Olivella, S. and Carrera, J. (2010a). Effects of CO_2 compressibility on CO_2 storage in deep saline aquifers. *Transport In Porous Media* 85, 619–639.

Vilarrasa, V., Bolster, D., Olivella, S. and Carrera, J. (2010b). Coupled hydromechanical modeling of CO_2 sequestration in deep saline aquifers. *International Journal of Greenhouse Gas Control* 4, 910-919.

Vilarrasa, V., Bolster, D., Dentz, M. and Carrera, J. (2010c). Semianalytical solution for CO_2 plume and pressure evolution during injection of compressible CO_2 in deep saline aquifers. *CCS Ready to go?*, 19-22 April, Rotterdam, Netherlands.

Vilarrasa, V., Bolster, D., Olivella, S. and Carrera, J. (2010d). Coupled hydromechanical modelling of radial CO_2 injection in deep saline aquifers. *Proceedings of 2nd Workshop of CODE_BRIGHT Users*, 6-7 May, UPC, Barcelona, Spain.

Vilarrasa, V., Olivella, S. and Carrera, J. (2010e). Coupled hydromechanical modelling of CO_2 injection in deep saline aquifers. *Proceedings of 1st Workshop on Advanced Scientific Results from IDAEA, CSIC*, 9-11 June, Blanes, Barcelona, Spain.

Vilarrasa, V., Olivella, S. and Carrera, J. (2010f). Caprock hydromechanical changes during CO_2 sequestration in deep saline aquifers. *XVIII International Conference on Computational Methods in Water Resources*, 21-24 June, Barcelona, Spain.

Vilarrasa, V., Olivella, S. and Carrera, J. (2010g). Effects of the initial stress state on the geomechanical stability of the caprock during CO_2 sequestration in deep saline

aquifers. *1st French-Spanish Symposium on Geological Storage of CO_2: Scientific Advances in the Geological Storage of CO_2*, 22-24 November, Pau, France.

Vilarrasa, V., Koyama, T., Neretnieks, I. and Jing, L. (2011a). Shear-induced flow channels in a single rock fracture and their effect on solute transport. *Transport In Porous Media* 87 (2), 503–523.

Vilarrasa, V., Olivella, S. and Carrera, J. (2011b). Geomechanical stability of the caprock during CO_2 sequestration in deep saline aquifers. *Energy Procedia* 4, 5306–5313.

Vilarrasa, V., Olivella, S. and Carrera, J. (2011c). Hydromechanical characterization test for CO_2 sequestration in deep saline aquifers. *Geophysical Research Abstracts, Vol. 13, EGU General Assembly*, 3-8 April, Vienna, Austria.

Vilarrasa, V., Olivella, S. and Carrera, J. (2011d). Hydromechanical behaviour of the aquifer and caprock under high pressure injection. *6th Trondheim Carbon, Capture and Sequestration Conference*, 14-16 June, Trondheim, Norway.

Vilarrasa, V., Olivella, S. and Carrera, J. (2011e). Coupled hydromechanical Processes during CO_2 sequestration in deep saline aquifers. *IV International Conference on Computational Methods for Coupled Problems in Science and Engineering*, 20-22 June, Kos Islands, Greece.

Vilarrasa, V., Carrera, J. and Olivella, S. (2012a). High pressure injection test for hydromechanical and onset of induced microseismicity characterization of CO_2 injection sites. *Geophysical Research Abstracts, Vol. 14, EGU General Assembly*, 22-27 April, Vienna, Austria.

Vilarrasa, V., Olivella, S., Silvia, O. and Carrera, J. (2012b). Numerical simulation of non-isothermal CO_2 injection using the thermo-hydro-mechanical code CODE_BRIGHT. *Geophysical Research Abstracts, Vol. 14, EGU General Assembly*, 22-27 April, Vienna, Austria.

Vilarrasa, V., Olivella, S., Silva, O. and Carrera, J. (2012c). Extension of CODE_BRIGHT to simulate non-isothermal CO_2 injection in deep saline aquifers. *Proceedings of 4th Workshop of CODE_BRIGHT Users*, 3 May, UPC, Barcelona, Spain.

Vilarrasa, V., Olivella, S., Silva, O. and Carrera, J. (2012d). Coupled thermo-hydro-mechanical modelling of CO_2 injection in deep saline aquifers. *Proceedings of 2nd*

Workshop on Advanced Scientific Results from IDAEA, CSIC, 14-16 May, Roquetes, Tarragona, Spain.

Wheatcraft, S. W. and Winterberg, F. (1985). Steady state flow passing through a cylinder of permeability different from the surrounding medium. *Water Resources Research* 21 (12), 1923–1929.

Wileveau, Y. and Bernier, F. (2008). Similarities in the hydromechanical response of Callovo-Oxfordian clay and Boom Clay during gallery excavation. *Physics and Chamistry of the Earth* 33, 5343–5349.

Xuan, R. and Sava, P. (2010). Probabilistic microearthquake location for reservoir monitoring. *Geophysics* 75 (3), MA9–MA26.

Yeo, I.W., De Freitas, M.H. and Zimmerman, R.W. (1998). Effect of shear displacement on the aperture and permeability of rock. *International Journal of Rock Mechanics and Mining Sciences* 35(8), 1051–1070.

Yin, S., Dusseault, M.B. and Rothenburg, L. (2009). Thermal reservoir modelling in petroleum geomechanics. *International Journal for Numerical and Analytical Methods in Geomechanics* 33, 449–485.

Zendehboudi, S., Khan, A., Carlisle, S. and Leonenko, Y. (2011). Ex situ dissolution of CO_2: a new engineering methodology based on mass-transfer perspective for enhancement of CO_2 sequestration. *Energy & Fuels* 25, 3323–3333.

Zhang, C. and Rothfuchs, T. (2004). Experimental study of the hydro-mechanical behaviour of the Callovo-Oxfordian argillite. *Applied Clay Science* 26, 325–336.

Zhang, L.Q., Yue, Z.Q., Yang, Z.F., Qi, J.X. and Liu, F.C. (2006). A displacement-based back-analysis method for rock mass modulus and horizontal in situ stress in tunnelling – Illustrated with a case study. *Tunnelling and Underground Space Technology* 21, 636–649.

Zhang, W., Li, Y., Xu, T., Cheng, H., Zheng, Y. and Peng, X. (2009). Long-term variations of CO_2 trapped in different mechanisms in deep saline formations: A case study of the Songliao Basin, China. *International Journal of Greenhouse Gas Control* 3, 161–180.

Zhou, Q., Birkholzer, J.T., Tsang, C.-F. and Rutqvist, J. (2008). A method for quick assessment of CO_2 storage capacity in closed and semi-closed saline formations. *International Journal of Greenhouse Gas Control* 2, 626–639.

Zienkiewicz, O.C. and Cormeau, I.C. (1974). Viscoplasticity, plasticity and creep in elastic solids: a unified numerical solution approach. *International Journal for Numerical Methods in Engineering* 8, 821–845.

Zienkiewicz, O.C. and Taylor, R.L. (ed) (2000). *The finite element method. Vol 2: Solid mechanics*. Oxford: Butterworth-Heinemann.

Zigrang, D.J. and Sylvester, N.D. (1985). A review of explicit friction factor equations. *Journal of Energy Resources Technology* 107(2), 280–283.

Zimmerman, R.W. (2000). Coupling in poroelasticity and thermoelasticity. *International Journal of Rock Mechanics and Mining Sciences* 37, 79–87.

Zoback, M.D., Barton, C.A., Brudy, M., Castillo, D.A., Finkbeiner, T., Grollimund, B.R., Moos, D.B., Peska, P., Ward, C.D. and Wiprut, D.J. (2003). Determination of stress orientation and magnitude in deep wells. *International Journal of Rock Mechanics and Mining Sciences* 40, 1049–1076.

Zoback, M.L. (1992). First and second order patterns of tectonic stress: the world stress map project. *Journal of Geophysical Research* 97, 11703–11728.